

# Low-Energy Defibrillation Using Resonant Drift Pacing

Thesis submitted in accordance with the requirements of  
the University of Liverpool for the degree of Doctor in Philosophy

by

Stuart William Morgan

February 2009

# Declaration

No part of the work referred to in this thesis has been submitted in support of an application for another degree or qualification of this or any other institution of learning. However some parts of the material contained herein has been previously published.

# Acknowledgements

I owe a huge debt of gratitude to Vadim Biktashev and Irina Biktasheva. I thank you both for allowing me to work on this truly inspiring project. I sincerely appreciate the enormous amount of hard work which you have put into carefully supervising me through my studies and I feel very privileged to have been your student over the past three years.

I am deeply grateful to Gernot Plank both for the use of CARP and for the hours of technical support which you have provided me, it has been a pleasure collaborating with you.

I thank Sergio Alonso, Blanca Rodriguez, and Natalia Trayanova for providing me with details from their own numerical simulations.

I am also grateful to Andy Foulkes and Ibrahim Idris for their valuable comments during our group seminars and to all my friends in the department for their moral support throughout.

A special note to my family who are always there for me. In particular my Mum, who's cherished memory gives me constant motivation to succeed. Also to Dad, without you I would never have the opportunities which lie before me.

For Anna, the most precious person in my life. Words can not express my appreciation for all of the love and support which you have given me during my research. You believed in me when I did not believe in myself: I would never have reached this milestone without you!

This studentship was supported by EPSRC grant EP/D500338/1.

# Abstract

This thesis explores the feasibility of and seeks to further develop a method of low-energy defibrillation through mathematical modelling and computational experiments.

Normally, the contraction of heart muscle is synchronized by a wave of electric excitation which propagates in an orderly fashion through the heart. If propagation of this wave is temporarily blocked it may form a re-entrant circuit. This re-entrant wave overrides the normal heart rhythm causing rapid and uncoordinated contractions which disrupts the heart's function of pumping blood.

It has previously been suggested that delivery of properly timed multiple weak shocks can be used for low-energy defibrillation. If the shocks are applied via a feedback protocol, the re-entrant circuits move until they are terminated at an inexcitable piece of tissue. This is the meaning of the term *resonant drift pacing*. Resonant drift pacing works on simple mathematical models but, until now, it has not been tested on the most detailed models of cardiac tissue.

We assess resonant drift pacing as a method for low-energy defibrillation through numerical simulations of both bidomain and monodomain descriptions of cardiac tissue. We use rectangular geometry as well as anatomically realistic geometry of rabbit ventricles. Termination of re-entry is achieved with high probability at a fraction of the conventional defibrillation shock strength.

To explain reasons when resonant drift pacing fail, we further develop the existing theory of resonant drift by extending it into three dimensions. This new theory, and the simulations, reveal reasons when resonant drift pacing has not been successful and we suggest modifications to overcome the difficulties.

# Publications and presentations

## Journal publications

These journal publications are based on work contained within this thesis;

1. **Morgan, S. W.**, Plank, G., Biktasheva, I.V., and Biktashev, V.N. “Low-energy defibrillation in human cardiac tissue: a simulation study.” *Biophysical Journal* **96**: 1364-1373, 2009.
2. **Morgan, S. W.** , Biktasheva, I. V., and Biktashev, V. N. “Control of scroll wave turbulence using resonant perturbations.” *Phys. Rev. E* **78**: 046207, 2008.

## Conference proceedings

The following papers and abstracts have been published in conference proceedings;

1. **Morgan, S. W.**, Plank, G., Biktasheva, I.V., and Biktashev, V.N. “Feedback control of resonant drift as a tool for low voltage defibrillation.” *Europace*, 10 (Supp. 1):i140, 2008. (Cardiostim 2008)
2. Biktasheva, I.V., **Morgan, S. W.**, Plank ,G., and Biktashev, V.N. “Feedback control of resonant drift as a tool for low voltage defibrillation” *Computers in Cardiology 2008* **35**:501-504, 2008.

## Presentations

I have given the following presentations at conferences;

1. “Feedback control of resonant drift as a tool for low-voltage defibrillation.” CARDIOSTIM (16th world congress in cardiac electrophysiology and cardiac techniques) in Nice (France), 20th June 2008.

2. “Using resonant perturbations to control scroll wave turbulence.” Departmental seminar, 21st May 2008.
3. “Low voltage defibrillation using resonant drift pacing.” Poster for the NCRG (Northern Cardiovascular Research Group) meeting in Liverpool, 29th April 2008.
4. “Termination of scroll wave turbulence in excitable media by resonant drift.” BAMC (British Applied Mathematics Colloquium) in Manchester, 1st April 2008.
5. “Feedback control of resonant drift: a bidomain study.” Departmental seminar, 22nd May 2007.
6. “Feedback control of resonant drift: a bidomain study.” Poster for the International Workshop on Non-Linear Dynamics in Excitable Media in Ghent (Belgium), 17th April 2007.
7. “Feedback control of resonant drift: a bidomain study.” Poster for the University of Liverpool Poster Day, 14th March 2007.
8. “The bidomain model of cardiac electrophysiology and resonant drift.” Departmental seminar, 17th May 2006.

# Contents

<b>Abstract</b>	<b>iii</b>
<b>Publications and presentations</b>	<b>iv</b>
<b>Table of Abbreviations</b>	<b>x</b>
<b>List of Figures</b>	<b>xiv</b>
<b>List of Tables</b>	<b>xv</b>
<b>1 Introduction</b>	<b>1</b>
1.1 Motivation . . . . .	1
1.2 Thesis outline . . . . .	3
<b>2 Literature review</b>	<b>6</b>
2.1 Physiological background . . . . .	6
2.1.1 Properties of cardiac cells . . . . .	6
2.1.2 Action potential propagation . . . . .	7
2.1.3 Cardiac arrhythmias . . . . .	8
2.1.4 Defibrillation . . . . .	9
2.2 Single cell models . . . . .	10
2.2.1 Single cell modelling overview . . . . .	10
2.2.2 The Hodgkin-Huxley model . . . . .	12
2.2.3 Development of ionic current models . . . . .	14
2.2.4 Modified Beeler-Reuter-Drouhard-Roberge model . . . . .	15
2.2.5 Modified Courtemanche <i>et al.</i> 1998 human atrial cell model .	21
2.3 Tissue models . . . . .	23
2.3.1 Bidomain model . . . . .	24

2.3.2	Monodomain model . . . . .	26
2.3.3	Comparison of monodomain and bidomain models . . . . .	27
2.4	Whole-ventricle anatomical models . . . . .	29
2.5	Numerical methods . . . . .	30
2.5.1	Cardiac Arrhythmias Research Package . . . . .	30
2.5.2	Solving the bidomain equations . . . . .	30
2.5.3	Solving the monodomain equations . . . . .	31
2.5.4	Solving the linear system . . . . .	31
2.5.5	Parallel computing . . . . .	32
2.6	The Barkley model . . . . .	32
2.6.1	Model definition . . . . .	32
2.6.2	Numerical algorithm . . . . .	33
2.7	Theory of resonant drift . . . . .	34
2.7.1	Phenomenological description of resonant drift . . . . .	35
2.7.2	Interaction with boundaries . . . . .	38
2.7.3	Feedback controlled stimulation . . . . .	39
2.8	Dynamics of three-dimensional scroll waves . . . . .	41
2.8.1	Equations of motion . . . . .	42
2.8.2	Filament tension . . . . .	43
2.8.3	Solution of the equations of motion: untwisted scroll rings . .	43
2.9	Scroll wave turbulence . . . . .	44
2.9.1	Control of scroll wave turbulence using a non-resonant perturbation . . . . .	45
2.10	Summary . . . . .	45
<b>3</b>	<b>Resonant drift in the bidomain model</b>	<b>46</b>
3.1	Methodology . . . . .	47
3.1.1	Governing equations . . . . .	47
3.1.2	Numerical methods and parameters . . . . .	47
3.1.3	Visualization . . . . .	49
3.1.4	Generation of re-entry patterns . . . . .	50
3.1.5	Single shock defibrillation procedure . . . . .	51
3.1.6	Resonant drift pacing procedure . . . . .	51
3.2	Results . . . . .	52



3.2.1	Single shock defibrillation results . . . . .	52
3.2.2	Resonant drift pacing results . . . . .	52
3.2.3	Effect of fluctuations on resonant drift pacing . . . . .	61
3.2.4	Direction of drift . . . . .	62
3.2.5	Using a time delay to induce success . . . . .	62
3.3	Summary . . . . .	64
<b>4</b>	<b>Control of scroll wave turbulence using resonant drift</b>	<b>67</b>
4.1	Methodology . . . . .	68
4.1.1	Governing equations . . . . .	68
4.1.2	Numerical methods . . . . .	68
4.1.3	Generation of turbulence . . . . .	69
4.1.4	Resonant frequency . . . . .	69
4.1.5	Forcing . . . . .	72
4.2	Results . . . . .	75
4.2.1	Elimination of the turbulence . . . . .	75
4.2.2	Windows of resonant frequencies . . . . .	76
4.2.3	Termination times . . . . .	78
4.2.4	Resonant vs non-resonant stimulation . . . . .	86
4.2.5	Feedback controlled vs constant frequency stimulation . . . . .	87
4.3	Summary . . . . .	88
<b>5</b>	<b>Theory of resonant drift in three-dimensions</b>	<b>91</b>
5.1	The theory of filament dynamics . . . . .	91
5.1.1	Change of coordinates to the filament frame of reference . . . . .	93
5.1.2	Evolutionary equation for the scroll perturbation . . . . .	94
5.1.3	The equations of motion . . . . .	96
5.2	Some coefficients of the equations of motion vanish . . . . .	98
5.3	Effect of resonant perturbation on scroll rings . . . . .	102
5.4	Effect of resonant perturbation on helical scroll waves . . . . .	104
5.5	Vector equations . . . . .	108
5.5.1	Vector equation for filament $\mathbf{R}$ . . . . .	108
5.5.2	Vector equation for the phase $\Phi$ . . . . .	109
5.5.3	Scalar equation for the phase $\phi$ . . . . .	111

5.6	Summary . . . . .	112
<b>6</b>	<b>Resonant drift in a whole-ventricle anatomical model</b>	<b>113</b>
6.1	Methodology . . . . .	114
6.1.1	Governing equations . . . . .	114
6.1.2	Numerical methods and parameters . . . . .	114
6.1.3	Visualization . . . . .	116
6.1.4	Generation of re-entry patterns . . . . .	116
6.1.5	Single shock defibrillation procedure . . . . .	117
6.1.6	Resonant drift pacing procedure . . . . .	117
6.1.7	Constant frequency stimulation procedure . . . . .	118
6.2	Results . . . . .	119
6.2.1	Single shock defibrillation results . . . . .	119
6.2.2	Resonant drift pacing results . . . . .	120
6.2.3	Using a time delay to induce success . . . . .	125
6.2.4	Effect of conductivity fluctuations on resonant drift pacing . . . . .	125
6.2.5	Constant frequency perturbation results . . . . .	128
6.3	Summary . . . . .	129
<b>7</b>	<b>Conclusions</b>	<b>130</b>
7.1	Main results . . . . .	130
7.2	Clinical implications . . . . .	132
7.3	Further directions of research . . . . .	133
<b>A</b>	<b>Modified Beeler-Reuter-Drouhard-Roberge model</b>	<b>134</b>
<b>B</b>	<b>Modified Courtemanche model</b>	<b>138</b>
<b>C</b>	<b>Calculations from Chapter 5</b>	<b>147</b>
C.1	Reaction-diffusion system expressed in the filament frame of reference	147
C.1.1	The gradient operator $\nabla\alpha$ . . . . .	147
C.1.2	The Laplacian $\Delta_3\alpha$ . . . . .	149
C.1.3	Time derivative . . . . .	150
C.2	Existence equation for a rigidly rotating spiral wave . . . . .	151
C.3	Orders of magnitude . . . . .	152
C.4	Eigenvalues and eigenfunctions of $L$ . . . . .	153

C.5	Orthogonality of $\mathbf{Y}_i$ to $\mathbf{V}_j$ . . . . .	154
C.6	Some coefficients of the motion equations are zero . . . . .	155
C.7	Non-zero coefficients . . . . .	157
C.8	Terms due to perturbation . . . . .	159
C.9	Derivatives $\mathbf{N}_t$ and $\mathbf{B}_t$ . . . . .	161
C.10	Covariant form of the motion equations . . . . .	167
<b>Bibliography</b>		<b>177</b>

# Table of Abbreviations

Abbreviation	Explanation
RDP	Resonant Drift Pacing
SSD	Single Shock Defibrillation
CARP	Cardiac Arrhythmia Research Package
ICD	Implantable Cardiac Defibrillator
ATP	Antitachycardia Pacing
BZ	Belousov-Zhabotinsky
ACh	Acetylcholine
PDE	Partial Differential Equation
ODE	Ordinary Differential Equation
UCSD	University of California Sandiego
LV	Left Ventricle
RV	Right Ventricle
BRDR	Beeler-Reuter-Drouhard-Roberge

Table 1: Abbreviations used in this thesis

# List of Figures

2.1	Diagram of the heart chambers . . . . .	8
2.2	Defibrillation shock waveforms . . . . .	9
2.3	Equivalent electrical circuit model of a cell's membrane. . . . .	11
2.4	Cardiac action potential from a modified BRDR model. . . . .	21
2.5	Cardiac action potentials from a modified Courtemanche model. . .	23
2.6	Equivalent electrical circuit of a bidomain model . . . . .	24
2.7	Equivalent electrical circuit of a monodomain model . . . . .	26
2.8	Virtual electrodes and conductivity fluctuations. . . . .	28
2.9	Visualisation of the UCSD rabbit ventricle. . . . .	29
2.10	Rigidly rotating spiral wave . . . . .	36
2.11	Resonantly drifting spiral wave with imprecise resonance . . . . .	37
2.12	Resonantly drifting spiral wave with precise resonance . . . . .	38
2.13	Resonant repulsion near the right edge boundary . . . . .	39
2.14	Successful termination of a spiral wave using resonant drift pacing .	40
2.15	Scroll wave filaments . . . . .	42
3.1	Meandering and stationary rotating re-entry in the bidomain model.	49
3.2	Initiation of a re-entrant wave. . . . .	50
3.3	Illustration of the feedback algorithm and location of the registration electrodes. . . . .	53
3.4	Single shock defibrillation images . . . . .	54
3.5	Single shock defibrillation results . . . . .	55
3.6	Resonant drift pacing of a meandering re-entry with $A = 1 \times 10^6 \mu\text{A}/\text{cm}^3$	57
3.7	Resonant drift pacing of a meandering re-entry with $A = 2 \times 10^6 \mu\text{A}/\text{cm}^3$	57
3.8	Resonant drift pacing with horizontal line registering electrode. . . .	58
3.9	Resonant drift pacing with vertical line registering electrode. . . . .	58

3.10	Resonant drift pacing results for meandering re-entry. . . . .	59
3.11	Resonant drift pacing results for stationary rotating re-entry. . . . .	60
3.12	Infinite loop in resonant drift pacing: $A = 10 \times 10^6 \mu\text{A}/\text{cm}^3$ . . . . .	61
3.13	Infinite loop in resonant drift pacing $A = 2 \times 10^6 \mu\text{A}/\text{cm}^3$ . . . . .	61
3.14	Resonant drift pacing of a meandering re-entry with no fluctuations. . . . .	62
3.15	Altering the direction of drift using a time delay. . . . .	63
3.16	Using a time delay to escape an infinite loop. . . . .	64
4.1	Development of scroll wave turbulence from an initial scroll ring. . . . .	70
4.2	The effect of forcing on the mean frequency of the turbulence $\tilde{\omega}_0(A, \Omega)$ and definitions of the resonant windows. . . . .	71
4.3	Different locations for the recording point. . . . .	75
4.4	Examples of successful and unsuccessful elimination of turbulence un- der modulation of medium excitability. . . . .	76
4.5	Modulation of medium excitability: termination times . . . . .	79
4.6	Modulation of medium excitability: termination time against forcing amplitude and untuning of the resonance . . . . .	80
4.7	Turbulence termination using a single pulse. . . . .	81
4.8	Applied current forcing: Termination time for the amplitude $A = 0.3$ . . . . .	82
4.9	Applied current forcing: termination times using constant and feed- back controlled frequencies. . . . .	83
4.10	Applied current forcing: termination times using constant and feed- back controlled frequencies. . . . .	84
4.11	Applied current forcing: evolution of the turbulence. . . . .	85
4.12	Applied current forcing: termination time against forcing amplitude $A$ and untuning of the resonance . . . . .	86
4.13	‘Snake instability’ . . . . .	89
5.1	Normal $\mathbf{N}$ , tangent $\mathbf{T}$ , and binormal $\mathbf{B}$ vectors . . . . .	92
6.1	Surface view and translucent view of re-entry in rabbit ventricles . . . . .	116
6.2	Generation of re-entry in rabbit ventricle . . . . .	117
6.3	Single shock defibrillation in the rabbit ventricle . . . . .	119
6.4	Resonant drift pacing in rabbit ventricles with recording point at the apex of right ventricle. . . . .	122

6.5	Wavefronts triggering shocks in the rabbit ventricle . . . . .	123
6.6	Resonant drift pacing in rabbit ventricles with recording point at the base of left ventricle. . . . .	124
6.7	Helical filament in rabbit ventricles . . . . .	125
6.8	Using a time delay to induce success in rabbit ventricles. . . . .	126
6.9	Resonant drift pacing in rabbit ventricles with no fluctuations . . . .	127
6.10	Constant frequency stimulation in the rabbit ventricle . . . . .	128

# List of Tables

1	Abbreviations used in this thesis . . . . .	xi
3.1	Summary of numerical parameters for Chapter 3 . . . . .	49
4.1	Summary of numerical parameters for Chapter 4 . . . . .	69
6.1	Summary of numerical parameters for Chapter 6 . . . . .	115
6.2	Resonant drift pacing results in UCSD rabbit geometry. . . . .	120
A.1	Values of the constants used in our modified BRDR model . . . . .	137
B.1	Values of the constants used in our modified Courtemanche model . .	146



# Chapter 1

## Introduction

### 1.1 Motivation

There are more than one hundred thousand premature cardiac deaths every year in the UK alone. Most of these are associated with re-entrant cardiac arrhythmias. Normally, the contraction of the heart muscle is synchronized by a wave of electric excitation which propagates in an orderly fashion through the heart. If propagation of this wave is temporarily blocked it may form a re-entrant circuit. This re-entrant wave overrides the normal heart rhythm, hijacking control over the cardiac muscle causing rapid and uncoordinated contractions which disrupts the heart's function of pumping blood. Milder forms of re-entrant arrhythmias seriously decrease quality of life. The extreme form is ventricular fibrillation, which is related to persistent re-entrant waves in the larger chambers of the heart and is usually fatal.

The last line of defence against re-entrant arrhythmias and fibrillation is electrical defibrillation, which is a powerful electric shock aiming at 'resetting' all the excitable cells in the heart to the same state and thus stopping any electric activity, including the re-entrant wave. The traditional method of delivery is through large electrodes applied to the chest of the patient. It is also one of the functions of the implantable cardiac defibrillators (ICD's), which are used by high-risk cardiac patients, and can deliver defibrillating shocks automatically when they detect dangerous patterns of activity.

Unfortunately, defibrillation is not always effective. Shocks have to be extremely powerful in order to ensure excitation of all cells in the heart, such strong shocks are extremely painful and cause damage to the heart and surrounding tissues. Thus there is a high demand in clinics on alternative methods of defibrillation which would

work with smaller voltages. Such methods exist and are sometimes attempted by the implantable devices, or on the operating table, and then high-energy shocks are delivered only if the milder methods fail. They fail too often, so the search for more efficient low-energy defibrillation algorithms continues.

It has been suggested that delivery of properly timed multiple weak shocks can be used for low-energy defibrillation. If shocks are timed to be in resonance with the re-entry, the locations of re-entrant waves move, cycle after cycle, until they are terminated at an inexcitable piece of tissue. This is the meaning of the term *resonant drift* [4, 24]. The problem of using resonant drift to eliminate re-entrant waves from cardiac tissue is choosing the correct choice of frequency for stimulation to ensure resonance. This problem can be overcome by taking feedback from the re-entrant wave itself [16, 18, 17], so that the stimulus is applied precisely at the times that the excitation wavefront reaches a particular recording point in the medium. I will refer to this feedback algorithm as *resonant drift pacing*.

Resonant drift pacing works nicely on simple mathematical models [15, 18, 17]. Real cardiac tissue is much more complicated than the models on which the method has been tried so far and experimentalists doubt so much that it will work they do not want to risk the expenses and lives of experimental animals to try it. The theory of resonant drift is not developed enough, so when the resonant drift pacing does not work there has been no obvious way to say why and thus no ways to see how to modify the experiment to make it work.

There are significant issues which could effect the use of resonant drift pacing as a tool for low-energy defibrillation. Ventricular fibrillation is believed to be associated with multiple re-entrant sources [34] and it is unknown whether the feedback control strategy can terminate them all. The ventricles are three-dimensional (3D). In 3D we have scroll waves, which are the 3D extension of 2D spiral waves and the effectiveness of feedback control in 3D is not yet understood. The effect of cardiac anisotropy on resonant drift also remains a mystery, as does the anatomy of the heart.

Before resonant drift pacing can be used as a method for low-energy defibrillation each of these points need to be investigated. This thesis looks at each of them in turn and makes suggestions for how to overcome any difficulties that arise.

## 1.2 Thesis outline

The aims of this project are to assess the effectiveness of using resonant drift pacing as a method for low-energy defibrillation through mathematical modelling and numerical experiments. We further develop the theory of resonant drift, by extending the existing theory into three dimensions. We also test resonant drift pacing using computer simulations of the most realistic mathematical models of heart known to date, in order to foresee possible difficulties that may be encountered by experimentalists, and suggest ways to overcome those difficulties.

The outline of this thesis is as follows;

**Chapter 2** We review the relevant literature used and referred to throughout this thesis.

We explain the equations which are used to model the ionic currents of a single cell. In particular, the classical Hodgkin-Huxley model [37] as well as the Courtemanche human atrial model [22] and Beeler-Reuter-Drouhard-Roberge model [12, 28]. In our numerical simulations, we use a number of modifications to these models which are also discussed.

The monodomain and bidomain models of cardiac tissue are introduced in section 2.3 and compared in section 2.3.3. We then discuss whole ventricle anatomical models (section 2.4) and the numerical issues involved in solving cardiac equations (section 2.5). As well as realistic cardiac models, in this thesis we use the Barkley model of excitable media which is introduced in section 2.6.

The phenomenon of resonant drift and its feedback control in 2D is described in more detail in section 2.7. We then discuss the equations of motion of unperturbed scroll waves (section 2.8) and the methods which have so far been employed to control scroll wave turbulence (section 2.9).

Chapters 3-6 contain original results obtained by the author.

**Chapter 3** We test resonant drift pacing using an anisotropic bidomain model of cardiac tissue, solved over a rectangular domain. This is currently the most up-to-date cardiac model available and takes into account both intra- and extra-cellular regions. For the ionic current kinetics we use a modified version of the Courtemanche

human atrial model. This model describes 13 currents making it one of the most complete models available. We use different locations for the registration electrode to record the feedback signals and also vary the time delay of shock application.

The results show that in this model setting, resonant drift pacing can be used to move the re-entrant waves. Termination can be achieved with high probability, at a fraction of the conventional single shock defibrillation strength, by moving the re-entrant waves until they hit an in-excitable boundary, or annihilate with each other. The direction of the drift can be managed by choosing the location of the electrodes and using a time delay of shock application.

Difficulties occur due to new wavefronts being initiated from the shock electrodes. However, our numerical experiments allow a detailed insight into this problem and can be used as a tool to suggest solutions.

**Chapter 4** We test resonant drift pacing in a three-dimensional model of excitable media using the Barkley model. It has previously been shown by Alonso *et al.* [7, 8] that scroll wave turbulence can be controlled using periodic, low amplitude, perturbations with a *non-resonant* frequency. In this study we verify those results and show that applying perturbations in resonance with the scroll wave turbulence, either using a constant frequency or using resonant drift pacing, terminates the scrolls with higher probability, and faster, than was shown by Alonso *et al.*.

We have found that the resonance between the forcing and the scrolls is characterised not by a single resonant frequency but by a *resonant window* which depends on the type of forcing and its amplitude. Our results also show that fastest termination is achieved when the forcing is applied with a constant frequency chosen within the resonant window.

**Chapter 5** We present a theoretical description of resonant drift in 3D. Using asymptotic methods we derive equations of motion for a perturbed scroll wave filament. The equations describe how the scrolls phase evolves in time and the motion of the filament in the tangent and binormal planes. We present these new equations of motion using both a scalar and vector formulation. This work builds upon the work of Keener [41] and Biktashev, Holden, and Zhang [19] who produced equations of motion for an unperturbed scroll wave.

To illustrate how our new equations of motion can be used we apply them to the

special cases of circular and helical filaments.

**Chapter 6** We test resonant drift pacing using a three-dimensional anisotropic bidomain model solved over an anatomically realistic finite element mesh of a rabbit ventricle. This study looks at the effect that the complicated geometry of the heart chambers, the 3D nature of the heart, the bidomain nature of cardiac tissue, and cardiac anisotropy has on the success of resonant drift pacing.

The results show that in this model setting, resonant drift pacing terminates re-entry with high probability at a fraction of the conventional single shock defibrillation strength. We found that the most efficient location for the registration electrode is in the apex of the right ventricle. The intensity of the microscopic fluctuations of intracellular conductivity has little effect on the outcome of resonant drift pacing. When resonant drift pacing fails to terminate re-entry we found that adjusting the time delay of shock application can induce success.

**Chapter 7** We summarise the work and present our conclusions.

## Chapter 2

# Literature review

This chapter is a review of the relevant literature used and referred to throughout this thesis. We discuss the physiological background, the techniques used to model cardiac cells, the models of cardiac tissue which are currently available, and the numerical methods used to solve them. We introduce the Barkley model of excitable media and the phenomena of resonant drift and how it can potentially be employed as a method of low-energy defibrillation by employing a feedback mechanism. We also describe the current theory for the motion of scroll waves and existing attempts which have been made to terminate scroll wave turbulence using low amplitudes.

Claude Bernard [13] wrote in 1865 “Cette application des mathématiques aux phénomènes naturels est le but de toute science” (The application of mathematics to natural science is the aim of all science), but cautioned that it was too early to achieve that in physiology. The topics introduced in this chapter highlight the amazing advances made in this field over the past 50 years.

## 2.1 Physiological background

### 2.1.1 Properties of cardiac cells

Cardiac cells have a surface membrane which allow the movement of charged ions (such as sodium  $\text{Na}^+$ , potassium  $\text{K}^+$ , and calcium  $\text{Ca}^{2+}$ ) through it. This flow of ions constitutes an electrical current and will alter the *potential difference*,  $V_m$ , across the cell membrane. Proteins in the membrane act as specific channels for each of the ionic species to move through. These channels have gates which are sensitive to potential difference. When a cell is at rest these *voltage-gated channels* are closed, and the potential difference between the inside of the cell and the outside

is called the *resting potential* (for human atrial cells the resting potential is about  $-80\text{mV}$ , but is different between different regions of the heart). There are many types of ions present in a cardiac cell, for brevity in this introduction we will only describe the movement of the most important.

When a membrane is depolarised above a *threshold potential* (about  $-50\text{mV}$ ), sodium-ion channels open. The positively charged sodium ions move freely into the cell causing a net positive charge into the cell. This event is followed by the opening of potassium-ion and calcium-ion channels causing a few positively charged ions to move out of the cell, starting the re-polarisation. Finally, more potassium-ion channels open resulting in a net positive charge out of the cell. This results in the complete re-polarisation of the cell membrane back to the resting potential.

Such movement of charged ions is called an action potential and is an important characteristic of cardiac cells. The shape of an action potential will vary between cell types (see Fig. 2.4 and Fig. 2.5). Cells which are able to cycle through an action potential are called *excitable*.

A feature of the action potential is that of refractoriness. Once an action potential has been elicited, the voltage-gated sodium ion channels remain closed for a certain length of time, the *absolute refractory period*. A subsequent action potential can not be initiated during this period.

We will now discuss how the action potential propagates in an orderly fashion through the heart, enabling contraction of cardiac tissue.

### 2.1.2 Action potential propagation

The action potential is first initiated by cells in the sinoatrial node (the pacemaker of the heart). Cells in the sinoatrial node are self-excitable, meaning they periodically produce an action potential without stimulation. During the rapid depolarisation of a cell, positively charged ions are driven through the membrane of neighbouring cells. Such movement of ions brings the potential of the resting neighbouring cells to the threshold potential, resulting in an action potential being elicited. This process repeats itself as positively charged ions from the newly depolarised cells diffuse into, and subsequently depolarise, adjacent cells. A chain reaction follows and the action potential propagates through the heart.

Excitation spreads from the sinoatrial node to atrial muscle causing the atria to

contract (see Fig. 2.1). The atria and ventricles are separated by a ring of fibrous tissue and the action potential can only be transmitted from the atria to the ventricles by passing through the atrioventricular node. The action potential passes through the atrioventricular node to the bundles of His, which are made up of Purkinje fibres. The Purkinje fibres rapidly transmit the action potential to all regions of the left and right ventricles. Finally the action potential propagates quickly across the ventricular tissue causing the ventricles contract. It is contraction of the ventricles which pumps blood to the lungs for oxygenation and then around the body.

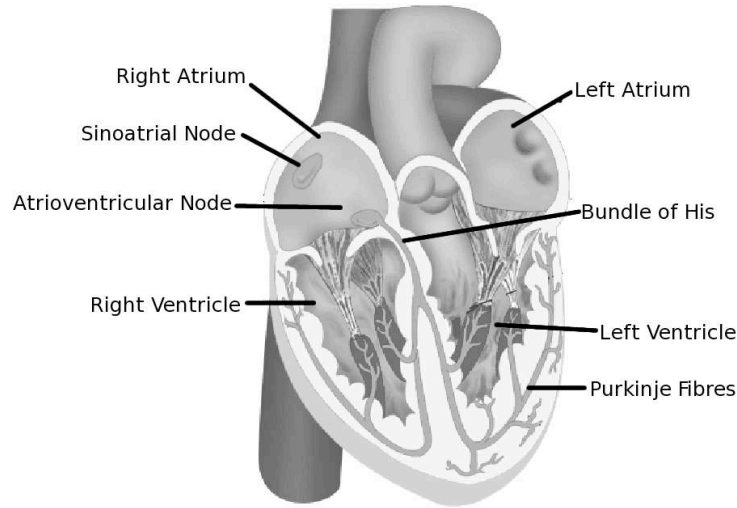


Figure 2.1: Diagram of the heart chambers.

### 2.1.3 Cardiac arrhythmias

As a result of temporary block of action potential propagation, the excitation wave may form a re-entrant circuit which captures control over cardiac muscle causing rapid and uncoordinated contractions of different parts of the heart. There are more than 100,000 premature cardiac deaths every year in the UK [93]. Most of these are associated with re-entrant cardiac arrhythmias.

Milder forms of arrhythmias such as paroxysmal tachycardia or atrial flutter seriously decrease quality of life. The extreme form is ventricular fibrillation which is related to persistent re-entrant waves in the largest chambers of the heart and, without intervention, usually leads to death. Causes of cardiac arrhythmias include ischemia, drug toxicity, and electric shocks [93].



### 2.1.4 Defibrillation

In clinical practice, electrical defibrillation is used to treat re-entrant arrhythmias and fibrillation. The traditional approach is delivery of a powerful electric shock through a large plate electrode applied to the chest of a patient. For high risk patients an implantable cardiac defibrillator (ICD) is used, which automatically detects abnormal patterns of activity and delivers defibrillating shocks automatically when necessary. The powerful shocks required for single shock defibrillation can cause collateral damage to the heart and surrounding tissues. Such shocks are also extremely painful with many patients reporting psychological side effects [21, 40].

Although ICD therapy has improved over the years, no major break-through has been achieved in terms of reducing the energy required for single shock defibrillation to a level where these adverse side effects could be avoided. Most efforts have been focused on different optimizations of the shock waveform (see Fig. 2.2). Empirically, it has been demonstrated that biphasic waveforms [82] defibrillate at a lower threshold than monophasic waveforms and that truncated exponential pulses further increase the efficiency [74]. However, even with these optimized waveforms the delivered shock energies are still more than one order of magnitude too large to render painless defibrillation.

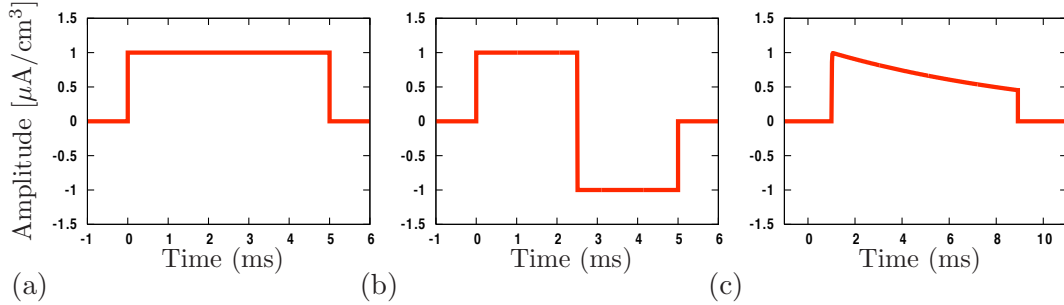


Figure 2.2: Defibrillation shock waveforms. (a) Rectangular monophasic. (b) Rectangular biphasic. (c) Truncated exponential monophasic. The data for these graphs were generated using CARP [81].

Several approaches to minimize defibrillation energy requirements by employing smarter protocols are under examination, however, so far antitachycardia pacing (ATP) is the only approach that gained clinical significance.

ATP relies on the delivery of a series of weak shocks at a frequency which is higher than the intrinsic frequency of the arrhythmia. In the case of ATP failure, a high-energy defibrillation shock has to be applied. Although the mechanisms which are

responsible for ATP failure are not fully understood, an evident weakness inherent to the method is that an empirically chosen fixed pacing frequency is likely to be suboptimal depending on the arrhythmia. No arrhythmia-specific input is used to initialize the ATP sequence, or to adjust the ATP sequence as a function of the alterations of the arrhythmia.

Most new ideas for low-energy defibrillation are theoretical and tested only in numerical simulations, or in the Belousov-Zhabotinsky (BZ) chemical reaction medium [86, 92]. There are only few cases where experimentalists have attempted a direct verification of their use in cardiac tissue.

## 2.2 Single cell models

### 2.2.1 Single cell modelling overview

The 1952 Hodgkin-Huxley equations [37] provide the earliest model of excitable cells. These equations describe current flow through  $\text{Na}^+$  and  $\text{K}^+$  channels in a giant squid axon. The Hodgkin-Huxley model was the first mathematical reconstruction of experimentally determined kinetics of ion channel gating which correctly predicted the shape of the action potential. Such was the impact of the model that Hodgkin and Huxley received the Nobel Prize for Physiology and Medicine in 1963 for their achievement.

In 1960, Noble [58] adapted the Hodgkin-Huxley equations to simulate  $\text{Na}^+$  and  $\text{K}^+$  currents in cardiac cells. The current generation of cell models have been modified to describe the kinetics of over 23 currents. At the time of writing, there are over 300 models of cardiac cells listed in the model repository at [www.cellml.org/models](http://www.cellml.org/models), each differ in complexity, the type of cardiac cell which they model, and the underlying biology.

In this section we will explain the framework for the formulation of an action potential model of a single cell.

#### Total membrane current

The total current flow through a membrane,  $I_m$  can be separated into an ionic current  $I_{ion}$  and a capacitance current  $I_C$  (see Fig. 2.3),

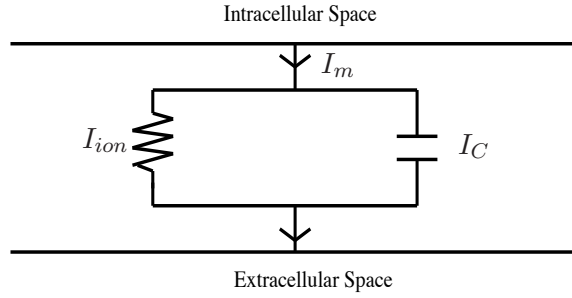


Figure 2.3: Equivalent electrical circuit model of a cell's membrane. This diagram is the author's own artwork.

$$I_m = I_C + I_{ion} = C_m \frac{\partial V_m}{\partial t} + \sum_k i_k, \quad (2.1)$$

where  $C_m$  is the capacitance of the cell membrane per unit area,  $V_m$  the transmembrane voltage,  $I_C$  is the capacitance current, and  $I_{ion}$  is the total current carried by all the ionic species,  $i_k$ .

### Electrochemical gradient of an ion

The flow of an ion species across a cell membrane depends on the concentration of that ion on either side of the membrane, i.e. *the chemical gradient* for that ion, and on the potential across the membrane, i.e. *the electrical gradient*. The net force acting on an ionic species is called *the electrochemical gradient* which is the difference between the membrane potential  $V_m$  and the equilibrium potential  $E_k$  for that ion, i.e.  $(V_m - E_k)$ . The sign of the electrochemical gradient determines the direction of the ionic current across the membrane.

The equilibrium potential  $E_k$  is the potential at which the chemical and electrical gradients are equal and opposite. It is given by the Nernst equation

$$E_k = \frac{RT}{zF} \ln \left( \frac{[k]_e}{[k]_i} \right), \quad (2.2)$$

where  $R$  is the universal gas constant,  $T$  the absolute temperature,  $z$  the valence of the ion,  $F$  Faraday's constant and  $[k]_e$  and  $[k]_i$  are the extracellular and intracellular ion concentrations.

## The ionic currents

The amplitude of an ionic current  $i_k$  depends on the conductance of the membrane to the ion  $g_k$ , as well as the electrochemical gradient,

$$i_k = g_k(V_m - E_k). \quad (2.3)$$

## The ionic conductances and gated membrane channels

The conductance  $g_k$  of the membrane to ion species  $k$  is the product of the conductance of a single channel  $\gamma$ , the number of channels per cell  $N$ , and the probability  $n$  of the channel being open,

$$g_k = \gamma N n = \bar{g}_k n. \quad (2.4)$$

The probability  $n$  of the channel being open depends on a gating process. Each channel is controlled by a gate that can either be in an open state or a closed state. The gates move between the two states with an opening rate constant  $\alpha_n$  and a closing rate constant  $\beta_n$ . The exact values for  $\alpha_n$  and  $\beta_n$  depend only on the instantaneous value of the membrane potential  $V_m$  and can be determined from experimental data. If we define the fraction of gates in the closed state as  $1 - n$ , then the rate of opening is  $\alpha_n(1 - n)$  and the rate of closing is  $\beta_n n$ .

The rate of change of  $n$  is determined by the difference in the rates of opening and closing,

$$\frac{dn}{dt} = \alpha_n(1 - n) - \beta_n n. \quad (2.5)$$

### 2.2.2 The Hodgkin-Huxley model

Hodgkin and Huxley used a voltage-clamp technique to separate the total membrane current,  $I_m$ , into a sodium current, a potassium current, and a ‘leakage’ current carried by other ions. The Hodgkin-Huxley system of equations [37] in full is

$$I_m = C_m \frac{\partial V_m}{\partial t} + i_K + i_{Na} + i_l, \quad (2.6)$$

where the individual ionic currents are given by the formulae

$$i_K = \bar{g}_K n^4 (V_m - E_K),$$

$$i_{\text{Na}} = \bar{g}_{\text{Na}} m^3 h (V_m - E_{\text{Na}}),$$

$$i_l = \bar{g}_l (V_m - E_l),$$

$$\frac{dn}{dt} = \alpha_n (1 - n) - \beta_n n,$$

$$\frac{dm}{dt} = \alpha_m (1 - m) - \beta_m m,$$

$$\frac{dh}{dt} = \alpha_h (1 - h) - \beta_h h,$$

and the rate constants  $\alpha$  and  $\beta$  were measured experimentally,

$$\begin{aligned} \alpha_n &= \frac{0.01(V_m + 10)}{\exp\left(\frac{V_m + 10}{10}\right) - 1}, & \beta_n &= 0.125 \exp\left(\frac{V_m}{80}\right), \\ \alpha_m &= \frac{0.1(V_m + 25)}{\exp\left(\frac{V_m + 25}{10}\right) - 1}, & \beta_m &= 4 \exp\left(\frac{V_m}{18}\right), \\ \alpha_h &= 0.07 \exp\left(\frac{V_m}{20}\right), & \beta_h &= \frac{1}{\exp\left(\frac{V_m + 30}{10}\right) + 1}. \end{aligned}$$

The following values were taken,

$$\bar{g}_{\text{Na}} = 120, \quad E_{\text{Na}} = -115,$$

$$\bar{g}_{\text{K}} = 36, \quad E_{\text{K}} = 12,$$

$$\bar{g}_l = 0.3, \quad E_l = -10.613,$$

$$C_m = 1.0.$$

The value of the dimensionless quantities  $n, m$  and  $h$  only change in time after a change of membrane potential  $V_m$ . For the potassium conductance, the probability of the  $\text{K}^+$  ion channel being open is given by  $n^4$ . This is due to the fact that the potassium ion channel gate will only open when four particles (constituting the gate to this channel) occupy a certain region of the membrane. Similarly, the probability of the sodium,  $\text{Na}^+$ , ion channel being open is given by  $m^3 h$ . Therefore the sodium ion channel gate is open when three particles of one type, and one of another type, occupy a certain region of the membrane.

The units of measurement for membrane potential  $V_m$  is given in mV, current density in  $\mu\text{A}/\text{cm}^2$ , conductance in  $\text{m.mho}/\text{cm}^2$ , and time in ms. The expression for the  $\alpha$  and  $\beta$ 's were calculated at temperature  $6.3^\circ\text{C}$ .

### 2.2.3 Development of ionic current models

Following the success of the 1952 Hodgkin-Huxley equations, in 1962 Denis Noble published one of the first mathematical models of a cardiac cell [58]. By adapting the equations of the original Hodgkin-Huxley model, Noble described the action potential and pace-maker potential of the Purkinje fibres of the heart.

The potassium-current,  $i_K$ , equations differ from those of Hodgkin and Huxley in that the potassium ions are assumed to flow through two types of channel in the membrane. By contrast, the sodium current equations,  $i_{Na}$ , are very similar to those of Hodgkin and Huxley. For both the potassium current and the sodium current, the rate constants were varied according to experimental data obtained from the Purkinje fibres. Calcium currents had not yet been discovered in 1962 so they were not included into Noble's 1962 model.

Following Noble's 1962 model of cardiac action potentials in Purkinje fibres, the next significant development in cardiac membrane modelling occurred when McAllister, Noble, and Tsien published a paper [51] in 1975 which described nine ionic currents of cardiac Purkinje fibres based on new experimental data. The description of the kinetics of the currents was still based on the Hodgkin-Huxley formalism, but the extra currents incorporated some significant new changes. The McAllister-Noble-Tsien model includes an inward calcium current (which had been discovered since the 1962 Noble model) along with a sodium current, three potassium currents, one chloride current, and three background currents. A total of 10 variables are used, consisting of the voltage and nine gates.

The 1977 Beeler Reuter model [12] was the first ionic model of the action potential of ventricular myocardial fibres in mammals. This model incorporates four ionic currents; sodium, calcium, and two potassium currents. Not all of the ionic currents of the Purkinje fibre model are present in ventricular tissue and so this model is simpler than McAllister, Noble, and Tsien's model.

Drouhard and Roberge (1987) revised the Hodgkin-Huxley formulation for sodium current activation and inactivation gates. Such modifications were made possible due to the availability of more accurate measurements of the sodium current. These modifications to the sodium current were then substituted into the earlier Beeler-Reuter model to produce the Beeler-Reuter-Drouhard-Roberge model [28].

Following the Drouhard-Roberge modifications, the Beeler-Reuter model was

then further modified by Skouibine, Trayanova, and Moore [71] to handle potentials outside the range of normal physiological activity, allowing the model to be used in defibrillation studies. They modified the rate constants  $\alpha$  and  $\beta$  to ensure that the high energy defibrillation shocks don't produce non-physiologically realistic solutions. In addition, electroporation was introduced into the model. Electroporation protects a cell when the transmembrane potential  $V_m$  exceeds a critical value (e.g. via a defibrillating shock). Conductive pores are formed which shunt the excess current across the membrane, limiting the growth of  $V_m$  and preventing damage to the membrane.

Luo and Rudy developed a model to study the action potential of the ventricular cells of a guinea-pig. In 1991 [48], they produced a model by collecting recent experimental data which had been obtained since the publication of the Beeler-Reuter model. This model describes the dynamics of two sodium currents, three potassium currents, and a background current. The focus of the model was to correctly predict the depolarisation and repolarisation phases of the action potential. In 1994 [49, 50], Luo and Rudy developed a second phase model of mammalian ventricular cells, based on recent experimental data. The emphasis in their second phase model was to further develop the calcium changes during the action potential.

In 2004, Courtemanche *et al.* [22] noticed that models of atrial cells had only been produced using animal data and saw the need for a model based on human data. They then developed a model of the action potential based on current ionic data obtained directly in human atrial cells. When human data were insufficient, they supplemented with animal data. The Courtemanche model builds mostly on the work of Luo and Rudy.

In this thesis we will present results from our own numerical simulations using modified versions of the Courtemanche human atrial [22] and the Beeler-Reuter-Drouhard-Roberge [12, 28] model, which will now be discussed.

#### **2.2.4 Modified Beeler-Reuter-Drouhard-Roberge model**

##### **Beeler-Reuter model**

The Beeler-Reuter [12] model is a mathematical model of the action potential of mammalian ventricular myocardial fibres. The model incorporates four individual ionic currents; one carried by sodium ions  $i_{Na}$ , one by calcium ions  $i_s$ , and two by

potassium ions  $i_{K1}$ ,  $i_{x1}$ . The general formulation for the ionic currents follow the concepts introduced by Hodgkin and Huxley [37], where the total membrane current is described by the formula

$$I_m = C_m \frac{\partial V_m}{\partial t} + i_{K1} + i_{x1} + i_{Na} + i_s. \quad (2.7)$$

The potassium current  $i_{Na}$  is primarily responsible for the rapid upstroke of the action potential, while the other currents determine the configuration of the plateau of the action potential and the re-polarization phase.

The individual currents are described by the equations

$$i_{K1} = 1.4 \frac{\exp(0.04[V_m + 85]) - 1}{\exp(0.08[V_m + 53]) + \exp[0.04(V_m + 53)]} + 0.07 \frac{V_m + 23}{1 - \exp[-0.04(V_m + 23)]},$$

$$i_{x1} = \frac{0.8x_1(\exp[0.04(V_m + 77)] - 1)}{\exp[0.04(V_m + 35)]},$$

$$i_{Na} = (\bar{g}_{Na}m^3hj + g_{NaC})(V_m - E_{Na}),$$

$$i_s = \bar{g}_s df(V_m - E_s),$$

where the values,

$$E_{Na} = 50 \quad E_s = -82.3 - 13.0287 \ln[Ca]_i,$$

were chosen, and the calcium concentration is calculated using

$$\frac{d[Ca]_i}{dt} = -10^{-7}i_s + 0.07(10^{-7} - [Ca]_i).$$

The values for the gating variables are found from solving the ODE's

$$\frac{dy}{dt} = \alpha_y(1 - y) - \beta_y y, \quad y = x_1, m, h, j, d, f.$$

The rate constants were calculated experimentally and are given by the following expressions

$$\alpha_{x1} = \frac{0.0005 \exp[0.083(V_m + 50)]}{\exp[0.057(V_m + 50)] + 1}, \quad \beta_{x1} = \frac{0.0013 \exp[-0.06(V_m + 20)]}{\exp[-0.04(V_m + 20)] + 1},$$

$$\alpha_m = \frac{-1(V_m + 47)}{\exp[-0.1(V_m + 47)] - 1}, \quad \beta_m = 40 \exp[-0.056(V_m + 72)],$$



$$\begin{aligned}
\alpha_h &= 0.126 \exp[-0.25(V_m + 77)], & \beta_h &= \frac{1.7}{\exp[-0.082(V_m + 22.5)] + 1} \\
\alpha_j &= \frac{0.055 \exp[-0.25(V_m + 78)]}{\exp[-0.2(V_m + 78)] + 1}, & \beta_j &= \frac{0.3}{\exp[-0.1(V_m + 32)] + 1}, \\
\alpha_d &= \frac{0.095 \exp[-0.01(V_m - 5)]}{\exp[-0.072(V_m - 5)] + 1}, & \beta_d &= \frac{0.07 \exp[-0.017(V_m + 44)]}{\exp[0.05(V_m + 44)] + 1}, \\
\alpha_f &= \frac{0.012 \exp[-0.008(V_m + 28)]}{\exp[0.15(V_m + 28)] + 1}, & \beta_f &= \frac{0.0065 \exp[-0.02(V_m + 30)]}{\exp[-0.2(V_m + C_3)] + 1}.
\end{aligned}$$

The following values were also chosen

$$\begin{aligned}
\bar{g}_{\text{Na}} &= 4, & g_{\text{NaC}} &= 0.003, \\
g_s &= 0.09, & C_m &= 1.0.
\end{aligned}$$

The units of measurement for membrane potential  $V_m$  is given in mV, current density in  $\mu\text{A}/\text{cm}^2$ , conductance in  $\text{m.mho}/\text{cm}^2$ , time in ms, membrane capacity in  $\mu\text{F}/\text{cm}^2$ ,  $[\text{Ca}]_i$  in mole/l, rate constants in  $\text{ms}^{-1}$ , and  $x_1, m, h, j, d, f$  are dimensionless.

### Beeler-Reuter-Drouhard-Roberge model

In 1987, Jean-Pierre Drouhard and Fernand Roberge published [28] a revised formulation of the Hodgkin-Huxley representation of the sodium current in ventricular myocardial cells. Their modifications ensured that the action potential upstroke is much faster than in the the original Hodgkin-Huxley model, which was in agreement with experimental observations. The Drouhard-Roberge model was substituted into the original Beeler-Reuter model to form the Beeler-Reuter-Drouhard-Roberge model, where the total membrane current is given by the formula,

$$I_m = C_m \frac{\partial V_m}{\partial t} + i_{K_1} + i_{x_1} + \tilde{i}_{\text{Na}} + i_s. \quad (2.8)$$

The modified sodium current  $\tilde{i}_{\text{Na}}$  (which differs to the Hodgkin Huxley formulation only by the values of the rate constants  $\alpha_m, \alpha_h, \beta_m$  and  $\beta_h$ ) was defined as

$$\tilde{i}_{\text{Na}} = m^3 h \bar{g}_{\text{Na}} (V_m - E_{\text{Na}}),$$

where

$$\frac{dm}{dt} = \alpha_m(1 - m) - \beta_m m,$$

$$\frac{dh}{dt} = \alpha_h(1 - h) - \beta_h h,$$

and the rate constants  $\alpha_m$  and  $\beta_m$  were found experimentally to be

$$\alpha_m = \frac{0.9(V_m + 42.65)}{1 - \exp[-0.22(V_m + 42.65)]},$$

$$\beta_m = 1.437 \exp[-0.085(V_m + 39.75)],$$

$$\alpha_h = 0.1 \exp[-0.193(V_m + 79.65)],$$

$$\beta_h = \frac{1.7}{1 + \exp[-0.095(V_m + 20.5)]}.$$

The values  $\bar{g}_{\text{Na}} = 15 \text{mS/cm}^2$  and  $E_{\text{Na}} = 40 \text{mV}$  were chosen as a reasonable compromise between available experimental measurements.

### Modifications to the Beeler-Reuter-Drouhard-Roberge model

The Beeler-Reuter-Drouhard-Roberge model was then further modified by Skouibine, Trayanova, and Moore [71] to handle potentials outside the range of normal physiological activity, allowing the model to be used in defibrillation studies.

The first modification was to introduce an electroporation current,  $i_{ep}$  into the expression for the transmembrane current,

$$I_m = C_m \frac{\partial V_m}{\partial t} + i_{K_1} + i_{x_1} + \tilde{i}_{\text{Na}} + i_s + i_{ep}.$$

For defibrillation studies an electroporation current  $i_{ep}$  should be included to prevent  $V_m$  from rising to non-physiologically high values during the shocks. The formulation which Skouibine *et al* used for  $i_{ep}$  differs from the formulation used in our studies. Skouibine used a formulation proposed by Krassowska in 1995 [45] but we chose to use a more detailed formulation proposed by Debruin and Krassowska in 1997 [25]. It is this more detailed formulation which we describe here.

The  $i_{ep}$  component of the transmembrane current is due to the movement of ions through the shock-induced pores,

$$i_{ep} = g_p N V_m,$$

where  $g_p$  is the conductance of a single pore and  $N$  is the number of pores per unit area.  $N(V_m, t)$  is governed by a first order differential equation,

$$\frac{dN}{dt} = \alpha e^{\beta(V_m)^2} \left( 1 - \frac{N}{N_0} e^{-q\beta(V_m)^2} \right),$$

where  $N_0$  is the number of pores per unit area when  $V_m = 0$  mV, and  $\alpha$ ,  $\beta$ , and  $q$  are constants with the values  $\alpha = 200.0 \text{ cm}^{-2} \text{ ms}^{-1}$ ,  $\beta = 6.25 \times 10^{-5} \text{ mV}^{-2}$ ,  $N_0 = 1.5 \times 10^5 \text{ cm}^{-2}$ , and  $q = 2.46$ .

The conductance  $g_p$  is modelled as an instantaneous function of transmembrane potential,

$$g_p(V_m) = \frac{\pi h \sigma}{4} (e^{v_m} - 1) \left( e^{v_m} \frac{w_0 e^{(w_0 - n v_m)} - n v_m}{w_0 - n v_m} - \frac{w_0 e^{(w_0 + n v_m)} + n v_m}{w_0 + n v_m} \right)^{-1},$$

where  $h$  is the thickness of the membrane,  $\sigma$  is the conductivity of the aqueous solution that fills the pore,  $w_0$  is the energy barrier inside the pore, and  $n$  is the relative entrance length of the pore. Also,  $v_m$  is the non-dimensional transmembrane potential  $v_m \equiv V_m(e/KT)$ , where  $e$  is the charge on an electron,  $K$  is the Boltzmann constant, and  $T$  is the absolute temperature.

The second modification was to shorten the action potential duration by decreasing the time constants of the slow inward currents (by a factor  $k$ ) as suggested by Leon, Roberge, and Vinet [47]. This was done because the action potential duration in a fibrillating ventricle is considerably shorter than a normal action potential,

$$\alpha_d = 0.095 \frac{\exp[-0.01(V_m - 5)]}{\exp[-0.072(V_m - 5)] + 1} k,$$

$$\beta_d = 0.07 \frac{\exp[-0.017(V_m + 44)]}{\exp[-0.05(V_m + 44)] + 1} k,$$

$$\alpha_f = 0.012 \frac{\exp[-0.008(V_m + 28)]}{\exp[-0.15(V_m - 28)] + 1} k,$$

$$\beta_f = 0.0065 \frac{\exp[-0.06(V_m + 30)]}{\exp[-0.2(V_m + 30)] + 1} k.$$

The equations for the membrane kinetics were also modified before using defibrillating strength high-amplitude shocks. In the Beeler-Reuter-Drouhard-Roberge model, when  $V_m$  exceeds the limits  $-85 \text{ mV} < V_m < 100 \text{ mV}$  due to a strong depolarization or hyperpolarization, the solutions become unstable and lead to non-physiological results. Skouibine *et al* [71] traced the source of this instability back to the equations for the rate coefficients  $\alpha_{x1,m,h}$  and  $\beta_{x1,m,h}$ . The values of these coefficients grow exponentially outside the range  $-85 \text{ mV} < V_m < 100 \text{ mV}$  at the sites of delivery and withdrawal of current.

To overcome this problem, Skouibine *et al.* revised the equations for the rate constants  $\alpha_{x1,m,h}$  and  $\beta_{x1,m,h}$  to ensure that,

- the sodium activation gates  $m$  remain closed ( $m = 0$ ) for  $V_m \leq -85\text{mV}$  and open ( $m = 1$ ) for  $V_m \geq 100\text{mV}$ ,
- the sodium inactivation gates  $h$  are open ( $h = 1$ ) for  $V_m \leq -90\text{mV}$ ,
- the outward rectifier current activation gate  $x_1$  stays open for  $V_m \geq 400\text{mV}$ .

The new equations for  $\alpha_{x1,m,h}$  and  $\beta_{x1,m,h}$  are

$$\alpha_m = \begin{cases} 0.9 \frac{V_m + 42.65}{1 - \exp[-0.22V_m - 9.3830]}, & V_m < 100\text{mV} \\ 890.9437890 \frac{\exp[0.0486479V_m - 4.8647916]}{1 + 5.93962526 \exp[0.0486479V_m - 4.8647916]}, & V_m \geq 100\text{mV} \end{cases}$$

$$\beta_m = \begin{cases} 1.437 \exp[-0.085V_m - 3.37875], & V_m \leq -85\text{mV} \\ \frac{100}{1 + 0.4864082 \exp[0.2597504V_m + 22.0787804]}, & V_m > -85\text{mV} \end{cases}$$

$$\alpha_h = \begin{cases} 0.1 \exp[-0.193V_m - 15.37245], & V_m \leq -90\text{mV} \\ -12.0662845 - 0.1422598V_m, & V_m > -90\text{mV} \end{cases}$$

$$\beta_h = \frac{1.7}{1 + \exp[-0.095V_m - 1.9475]}$$

$$\alpha_{x_1} = \begin{cases} 0.0005 \frac{\exp[0.083V_m + 4.150]}{1 + \exp[0.057V_m + 2.850]}, & V_m < 400\text{mV} \\ 151.7994692 \frac{\exp[0.0654979V_m - 26.1871448]}{1 + 1.5179947 \exp[0.0654679V_m - 26.1871448]}, & V_m \geq 400\text{mV} \end{cases}$$

$$\beta_{x_1} = 0.0013 \frac{\exp[-0.06V_m - 1.20]}{1 + \exp[-0.04V_m - 0.80]}.$$

The final alteration was to modify the original equation for the intracellular calcium concentration  $[Ca]_i$ . This was because the solution given by the original equations in [12] drops below 0 when  $V_m$  exceeds 200mV. Skouibine *et al.* chose to keep  $[Ca]_i$  constant for  $V_m \geq 200\text{mV}$ .

$$\frac{d[Ca]_i}{dt} = \begin{cases} -10^{-7}i_s + 0.07(10^{-7} - [Ca]_i), & V_m < 200\text{mV} \\ 0, & V_m \geq 200\text{mV} \end{cases}$$

Figure 2.4 shows the action potential of this model. See Appendix A for the complete system of equations of this modified version of the Beeler-Reuter-Drouhard-Roberge model.

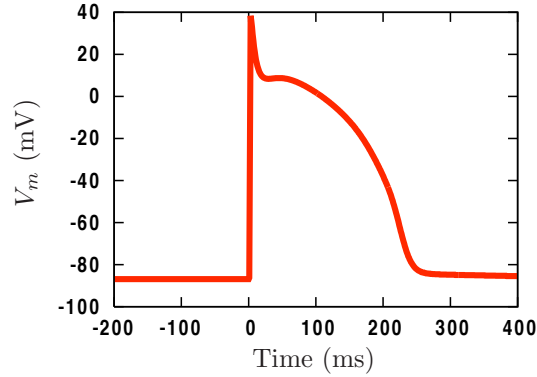


Figure 2.4: Cardiac action potential from a modified Beeler-Reuter-Drouhard-Roberge model. The data for this graph were generated using CARP [81].

### 2.2.5 Modified Courtemanche *et al.* 1998 human atrial cell model

Courtemanche, Ramirez, and Nattel [22] developed a model describing the action potential of cells in a human atrium. The model built on the classical work of Luo and Rudy [48, 49, 50] who developed a model of the action potential of guinea pig ventricular cells.

The expression for transmembrane current is

$$\begin{aligned} I_m = C_m \frac{\partial V_m}{\partial t} &+ i_{Na} + i_{K1} + i_{to} + i_{Kur} + i_{Kr} + i_{Ks} + i_{Ca,L} \\ &+ i_{p,Ca} + i_{NaK} + i_{NaCa} + i_{b,Na} + i_{b,Ca}, \end{aligned} \quad (2.9)$$

where the ionic gating variables are all governed by Hodgkin-Huxley type differential equations,

$$\frac{dy}{dt} = \alpha_y(1 - y) - \beta_y y,$$

with  $y$  representing the appropriate gating variable.

Several modifications have been suggested for the Courtemanche model. To allow comparisons between our results and those from [62] we used the formulation for electroporation proposed by Krassowska in 1995 [45],

$$i_{ep} = G(V_m, t)V_m,$$

where

$$\frac{dG}{dt} = a \exp[b(V_m - V_{rest})^2](1 - \exp[-c(V_m - V_{rest})^2]),$$

with the constants taking the values  $a = 2.5 \times 10^{-3} \text{mS}/(\text{cm}^2 \text{ms})$ ,  $b = 2.5 \times 10^{-5} \text{mV}^{-2}$ , and  $c = 10^{-9} \text{mV}^{-2}$ .

In addition to electroporation, an acetylcholine (ACh) dependent potassium current  $i_{K(ACh)}$  has been added by Kneller *et al.* [44]. ACh is a chemical transmitter in both the central and parasympathetic nervous system which is present in humans and many other organisms. ACh stimulates muscle contractions and excites nerves where an increase in ACh causes a decreased heart rate.

The new current  $i_{K(ACh)}$  is formulated as follows:

$$i_{K(ACh)} = \left[ \frac{10}{1 + \frac{9.13652}{[ACh]^{0.477811}}} \right] \left[ 0.0517 + \frac{0.4516}{1 + \exp \left[ \frac{V_m + 59.53}{17.18} \right]} \right] (V - E_k)$$

Xie *et al.* [91] modified the equations describing the  $i_{Ca,L}$ ,  $i_{Ks}$ , and  $i_{Kr}$  currents. They found that by blocking  $i_{Ca,L}$  by 65% coupled with a ninefold increase of the  $i_{Ks}$  and  $i_{Kr}$  currents allows the generation of a stationary rotating re-entrant spiral wave. Without these modifications to the currents, a re-entrant spiral wave generated using the original Courtemanche model tends to meander and self-terminate.

For the purpose of testing resonant drift pacing as a method for low-energy defibrillation we chose to incorporate electroporation and the ACh dependent potassium current to enable us to assess its effectiveness. These modifications were also used by Plank *et al.* for a single shock defibrillation study [62]. The choice of model was therefore important to allow comparisons with this previous published work. Further, we also included the modifications suggested by Xie to generate a stationary rotating re-entry.

Figures 2.5(a) and (b) show the action potential for this model with and without Xie’s modifications respectively. See Appendix B for the full detailed model used in this thesis.

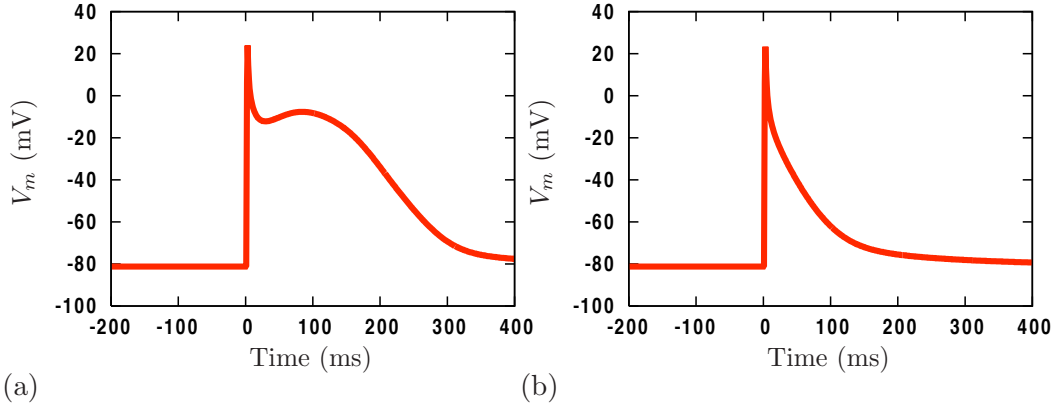


Figure 2.5: Action potentials from the modified Courtemanche human atrial model; (a) without and (b) with the modifications due to Xie *et al.* The data for these graphs were generated using CARP [81].

## 2.3 Tissue models

An action potential propagates from one cell to the next due to the depolarising local current flow ahead of the action potential upstroke. During the rapid depolarisation of a cell, positively charged ions are carried through the membrane of neighbouring cells. Such movement of ions brings the potential of the resting neighbouring cells to the threshold potential which opens  $\text{Na}^+$  and  $\text{Ca}^{2+}$  channels, resulting in an action potential being elicited. This process repeats itself as positively charged ions from the newly depolarised cells are carried into, and subsequently depolarise, adjacent cells. A chain reaction follows and the action potential propagates through the tissue.

Current models of cardiac tissue vary in complexity. The *bidomain model* of cardiac tissue describes current flow and electric potential distribution in both the intracellular (inside the cell) and extracellular (outside the cell) regions. The *monodomain model* is essentially a reduced version of the bidomain model which only describes the currents in the intracellular region.

### 2.3.1 Bidomain model

The bidomain model is currently the most complete description of cardiac electrical activity. The principle for the model was first published in 1969 [68] but the model was not expressed formally until 1978 [77, 53]. Later, the bidomain model was expressed as a ‘reaction-diffusion’ type model [66].

The bidomain model describes current flow and electric potential distribution in both the intracellular and extracellular regions of cardiac tissue linking them through transmembrane current (see Fig. 2.6). Mathematically, the difference between the intracellular and extracellular domains is the assignment of different conductivities in each domain. The transmembrane potential  $V_m$  in the bidomain model is the

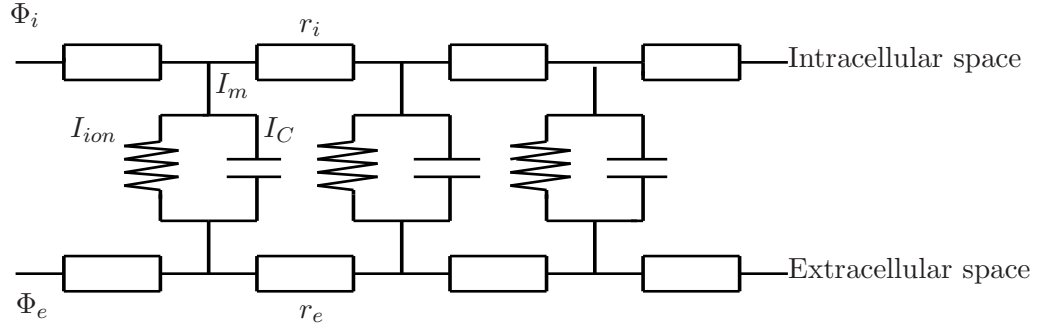


Figure 2.6: Equivalent electrical circuit of a bidomain model. This diagram is the author’s own artwork.

difference between the intracellular,  $\Phi_i$ , and extracellular,  $\Phi_e$ , potentials,

$$V_m = \Phi_i - \Phi_e. \quad (2.10)$$

The potential in each domain satisfies the equations,

$$\nabla \cdot (\sigma_i \nabla \Phi_i) = \beta I_m, \quad (2.11)$$

$$\nabla \cdot (\sigma_e \nabla \Phi_e) = -\beta I_m + I_e, \quad (2.12)$$

where  $\beta$  is the membrane surface-to-volume ratio, i.e. the amount of membrane found in a given volume of tissue, and  $I_e$  is an extracellular current density stimulus.  $\sigma_i$  and  $\sigma_e$  are the intracellular and the extracellular conductivity tensors.

The conductivity tensors can fluctuate at a microscopic level. Intracellular conductivity fluctuations are modelled [62] according to the formula

$$\sigma_{ij} = \bar{\sigma}_{ij}(1 + F\eta),$$



where  $\eta \in [-1, 1]$  are independent equidistributed random numbers. The actual value of  $F$  would vary depending on species, age, and gender. The intracellular  $\Phi_i$  and extracellular  $\Phi_e$  potentials are related through the transmembrane current  $I_m$ . The transmembrane current consists of a capacitive part, an ionic part  $I_{ion}$ , and an imposed transmembrane current density stimulation  $I_{trans}$ ,

$$I_m = C_m \frac{\partial V_m}{\partial t} + I_{ion} - I_{trans}, \quad (2.13)$$

where  $C_m$  is the membrane capacitance per unit area.

The tissue equations (2.11), (2.12), and the membrane equation (2.13), constitute the bidomain model. This formulation is a coupled system of equations since the intracellular and extracellular potentials are solved simultaneously.

By using (2.10), (2.11), (2.12), and (2.13), the bidomain model can be expressed as a decoupled system consisting of a parabolic PDE and an elliptic PDE,

$$C_m \frac{\partial V_m}{\partial t} = -I_{ion} + \frac{1}{\beta} \nabla \cdot (\sigma_i \nabla V_m) + \frac{1}{\beta} \nabla \cdot (\sigma_i \nabla \Phi_e) + I_{trans} \quad (2.14)$$

$$\nabla \cdot ((\sigma_i + \sigma_e) \nabla \Phi_e) = -\nabla \cdot (\sigma_i \nabla V_m) + I_e, \quad (2.15)$$

where the independent variables are  $V_m$  and  $\phi_e$ .

### Conductive bath

The bidomain model permits the inclusion of a conductive bath perfusing the tissue. The potential in the bath  $\Phi_o$  satisfies Laplace's equation,

$$\nabla \cdot (\sigma_o \nabla \Phi_o) = 0, \quad (2.16)$$

where  $\sigma_o$  is the bath conductivity and  $\Phi_o$  is the bath potential. At the tissue-bath interface, the extracellular and bath potentials are equal,

$$\Phi_e = \Phi_o. \quad (2.17)$$

### Boundary conditions

To obtain a solution for the potentials in a bidomain model, boundary conditions must be applied. These conditions should define the interfaces which occur naturally, i.e. the outer surface of the heart. The most commonly applied are Neumann (no-flux) boundary conditions.

When a problem is posed without the conductive bath, the following conditions are imposed

$$\mathbf{n}^T \sigma_i \nabla \Phi_i = 0, \quad (2.18)$$

$$\mathbf{n}^T \sigma_e \nabla \Phi_e = 0, \quad (2.19)$$

where  $\mathbf{n}$  is a vector normal to the domain boundary. This condition means that no current flows out of the edges of the domain.

When a conductive bath is included, at the tissue-bath interface the normal current is continuous, but the intracellular current density is zero,

$$\mathbf{n}^T \sigma_e \nabla \Phi_e = \mathbf{n}^T \sigma_o \nabla \Phi_o, \quad (2.20)$$

$$\mathbf{n}^T \sigma_i \nabla \Phi_i = 0. \quad (2.21)$$

### 2.3.2 Monodomain model

In general, the ratio of conductivities along and across the fibres in the intracellular and extracellular domains is not the same. This case refers to unequal anisotropy. In the absence of external electric current,  $I_e$ , for the special case where there is equal anisotropy, the bidomain equations reduce to a monodomain formulation. The monodomain model provides the simplest description of action potential propagation. It describes only current flow through the intracellular region of cardiac tissue (see Fig. 2.7). The general form of the model is

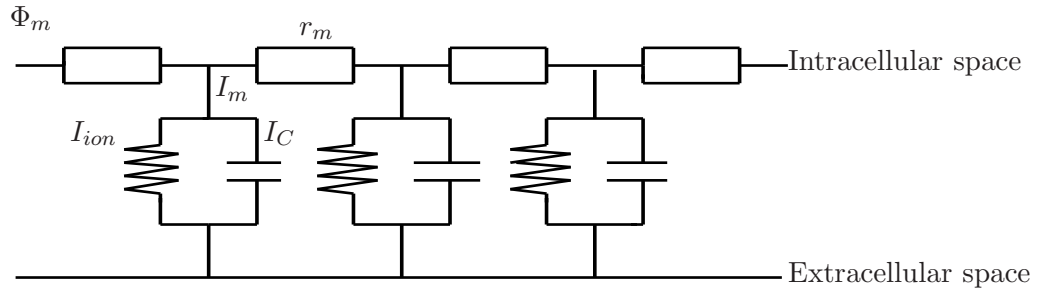


Figure 2.7: Equivalent electrical circuit of a monodomain model. This diagram is the author’s own artwork.

$$C_m \frac{\partial V_m}{\partial t} = \frac{1}{\beta} \nabla \cdot (\sigma_m \nabla V_m) - I_{ion} + I_{trans}. \quad (2.22)$$

Here,  $C_m$  is the capacitance of the cell membrane per unit area,  $V_m$  the transmembrane voltage,  $\nabla$  is the gradient operator,  $\sigma_m$  is a diffusion matrix which introduces

anisotropy into the model, for models of isotropic tissue  $\sigma_m$  is a scalar quantity.  $I_{ion}$  represents the current flow which is carried by ions.  $I_{trans}$  is a transmembrane current source.

The conductivities in the monodomain model are linked to the conductivities in the bidomain model by

$$\sigma_m = \frac{\sigma_i \sigma_e}{\sigma_i + \sigma_e}$$

### Boundary conditions

Similar to the bidomain model, the most commonly applied boundary conditions in the monodomain model are Neumann (no-flux) boundary conditions,

$$\mathbf{n}^T \sigma_m \nabla V_m = 0, \quad (2.23)$$

where  $\mathbf{n}$  is a vector normal to the domain boundary. This condition means that no current flows out of the edges of the domain.

### 2.3.3 Comparison of monodomain and bidomain models

The bidomain model considers both the extracellular and intracellular spaces explicitly, providing a more detailed model of cardiac tissue than the monodomain model. However, a study by Potse *et al* [64] compared the potentials resulting from normal depolarisation and repolarisation in a monodomain and bidomain model (made comparable due to the choice of ionic kinetics). They concluded that in the absence of stimulation, propagating action potentials can be studied without substantial loss of accuracy using a monodomain model.

The more detailed description of cardiac tissue offered by the bidomain equations is necessary to model certain phenomena. During defibrillation, current is injected into the extracellular space and the unequal anisotropy of the intracellular and extracellular domains produce patterns of polarisation and depolarisation in the vicinity of the stimulus. Such patterns of polarisation are called *virtual electrodes* (see Fig. 2.8) and were first observed in numerical simulations using a passive (i.e. ionic currents not accounted for) bidomain model [69]. Optical mapping studies [85] confirmed the existence of the theoretical predictions of virtual electrodes.

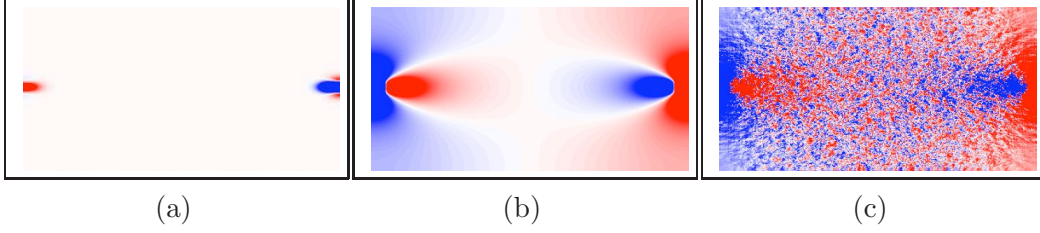


Figure 2.8: The effect of applying shocks to passive tissue via an anode (left) and a cathode (right). The tissue is described using a: (a) monodomain model, (b) bidomain model, (c) bidomain model with 50% conductivity fluctuations. Shocks were applied as transmembrane current  $I_{trans}$  in the monodomain model, and as extracellular current  $I_e$  in the bidomain model. In (b) and (c) virtual electrodes can be seen. In (c) the conductivity fluctuations cause a ‘salt-and-pepper’ effect. The colours represent values of  $V_m$ : red is positive potential, white is zero potential (resting tissue), blue is negative potential. The figures are the author’s own visualisation using CARP [81].

Mathematically, virtual electrodes can be explained by re-arranging the bidomain equations [70, 72]. First express (2.14) as

$$I_{ion} + C_m \frac{\partial V_m}{\partial t} - \frac{1}{\beta} \nabla \cdot (\sigma_i \nabla V_m) = \frac{1}{\beta} \nabla \cdot (\sigma_i \nabla \Phi_e). \quad (2.24)$$

The right hand side of (2.24) is called the *activating function*. By ignoring  $I_{trans}$  and expressing equation (2.15) as

$$\Phi_e = -(\nabla \cdot (\sigma_i + \sigma_e \nabla))^{-1} (\nabla \cdot (\sigma_i \nabla)) V_m + (\nabla \cdot ((\sigma_i + \sigma_e) \nabla))^{-1} I_e, \quad (2.25)$$

it can be seen that the activating function is in fact a function depending on  $I_e$ . When a stimulus,  $I_e$ , is applied to passive tissue initially  $V_m = 0$  and  $I_{ion} = 0$  everywhere on the domain, causing (2.24) to become;

$$C_m \frac{\partial V_m}{\partial t} = \frac{1}{\beta} \nabla \cdot (\sigma_i \nabla \Phi_e). \quad (2.26)$$

From (2.26) it can be seen that the activating function starts the initial change in transmembrane potential, causing the patterns of polarisation and depolarisation called virtual electrodes.

Virtual electrodes play an important role in the success of defibrillation through their interaction with the re-entrant wave fronts far away from the location of the shock [29, 75]. However for some timings and amplitudes the shock may fail to defibrillate because the virtual electrodes induce new re-entrant wavefronts [30].

## 2.4 Whole-ventricle anatomical models

Recent advances in computer power have seen the rise of whole-ventricle models of cardiac tissue which include the 3D geometry of the ventricles, together with a description of the orientation of fibres. Currently used and available models are of whole rabbit [78], canine [57], and pig [73] ventricles.

The model geometry of the whole rabbit ventricle (called the University of California San Diego (UCSD) rabbit anatomy) was obtained by fixing a rabbit heart mechanically and filling it with silicone. The ventricles were then sliced and each slice was imaged. Each image was then separated into regions where fibre orientation was determined. Data obtained from the images were fitted to a finite element mesh describing the 3D geometry. The models of the canine and pig ventricles were obtained in a similar way. More recent developments have been anatomical models based on non-invasive magnetic resource imaging (MRI) data [36]. Fig 2.9 is a visualisation of the UCSD rabbit anatomy.

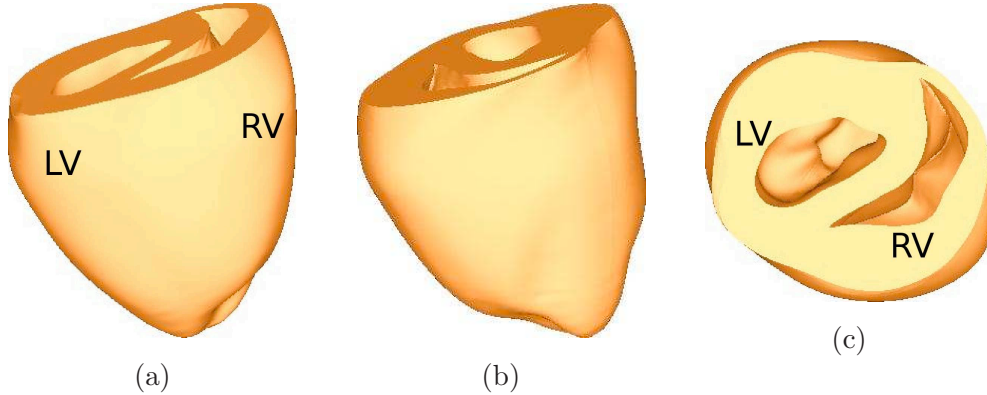


Figure 2.9: Visualisation of the UCSD rabbit ventricle. LV denotes left ventricle and RV denotes right ventricle. This figure is the author's own visualisation using CARP [81].

Trayanova *et al.* have used the UCSD rabbit anatomy for a series of studies into single shock defibrillation [75, 5]. For their defibrillation studies they use the Beeler-Reuter-Drouhard-Roberge ionic model modified for high amplitude shocks by Skouibine *et al.* [71]. In addition they use a bidomain model to describe the tissue with a conductive bath. Virtual large plate electrodes were positioned in the conductive bath to apply the defibrillating shocks. The shock waveforms used in the defibrillation studies include truncated exponential monophasic and biphasic shocks

[65].

In Chapter 6, we present our numerical simulations using a bidomain model with the UCSD rabbit anatomy. To allow comparison with previously published work, we base our model on that of Trayanova *et al.* as described above.

## 2.5 Numerical methods

### 2.5.1 Cardiac Arrhythmias Research Package

The bidomain equations are the most complete description of cardiac electrical activity. Their numerical solution is, however, computationally demanding because the elliptic equation must be solved for each time step of the parabolic equation [79]. The monodomain equation is more computationally efficient because it does not contain the elliptic equation.

To solve both the monodomain and bidomain equations we have used the Cardiac Arrhythmias Research Package (CARP) [81]. In this section we will explain the numerical methods which have been used for the simulations presented in this thesis.

### 2.5.2 Solving the bidomain equations

The bidomain equations (2.14)-(2.15) have  $V_m$  and  $\phi_e$  as independent variables. The numerical solution is a three step scheme which involves finding the solution of a parabolic PDE (2.14), an elliptic PDE (2.15), and a nonlinear system of ODEs for  $I_{ion}$ , at each time step.

#### Time discretisation

Firstly, using the Crank-Nicholson method for the time discretisation of the parabolic equation yields

$$\left(1 - \frac{\Delta t}{2\beta C_m} \nabla(\sigma_i \nabla)\right) V_m^{n+1} = \left(1 - \frac{\Delta t}{2\beta C_m} \nabla(\sigma_i \nabla)\right) V_m^n + \frac{\Delta t}{2\beta C_m} \nabla(\sigma_i \nabla \Phi_e^n) - I_{ion}(V_m^n, \mathbf{u}^n) + I_{trans}. \quad (2.27)$$

The non-linear system of ODE's can be discretised using a forward Euler scheme,

$$\mathbf{u}^n = \mathbf{u}^{n-1} + \Delta t f(\mathbf{u}^n, V_m^n), \quad (2.28)$$

and the elliptic equation is discretised as

$$\nabla \cdot ((\bar{\sigma}_i + \bar{\sigma}_e) \nabla \Phi_e^n) = -\nabla \cdot (\bar{\sigma}_i \nabla V_m^n) - I_e. \quad (2.29)$$

## Spatial discretisation

Equations (2.27),(2.28),(2.29) provide the time discretisation implemented in CARP for the bidomain equations. Spatial discretisation is further needed to allow numerical computation. Several approaches are possible for spatial discretisation. Finite differences are popular [64] for its ease of implementation. However, to enable accurate models of the complex geometry of the heart, finite elements are widely used [75, 62]. The finite element approach is employed in CARP using triangular shaped elements in 2D and tetrahedral shaped elements in 3D.

### 2.5.3 Solving the monodomain equations

The solution of the monodomain equations is similar to the solution of the bidomain equations, with the exception that there is no elliptic equation. This makes solving the monodomain equations an easier task which requires less computational resources.

### 2.5.4 Solving the linear system

As with most numerical schemes, the discretisation methods implemented by CARP lead to the solution of a linear system of the form,

$$\mathbf{Ax} = \mathbf{b}, \tag{2.30}$$

which needs to be solved at every time step  $\Delta t$ . Both *direct* and *iterative* solution methods are implemented in CARP. Direct methods solve the linear system (2.30) by direct matrix manipulation and results in an exact solution. Gaussian elimination, lower-upper (LU) decomposition, and Cholesky decomposition are all examples of direct solution methods. Iterative methods (such as the conjugate gradient method) start with an approximate solution and attempt to reduce the error.

For relatively small problems, direct solvers have been shown to be computationally the fastest approach [84, 63]. However, direct methods tend to require the inversion of a large matrix and the memory requirements in doing so are considerable. For large problems (such as the simulation of a whole 3D ventricle), direct solvers are not always suitable because of such memory requirements. Iterative methods do not have this problem and so are favoured for such large problems.

Preconditioning has been shown to increase the speed for iterative methods [64], and so the preconditioned conjugate gradient method has become the standard

choice for an iterative solver of the bidomain equations. Preconditioning changes the linear system (2.30) into a problem of the form,

$$\mathbf{B}^{-1}\mathbf{A}\mathbf{B}^{-T}(\mathbf{B}^T\mathbf{x}) = \mathbf{B}^{-1}\mathbf{b}, \quad (2.31)$$

where  $\mathbf{M} = \mathbf{B}\mathbf{B}^T$  is the preconditioner of  $\mathbf{A}$ . Weber dos Santos *et al.* [84] compared a multigrid (MG) preconditioner against the traditional incomplete lower upper (ILU) and concluded that for 3D simulations, the MG preconditioner performed faster than the ILU preconditioner. Multigrid methods are based upon several discretisations of the same problem domain. A solution is obtained on a coarse discretisation, and then extrapolated to a discretisation of higher resolution.

In this thesis we use the LU decomposition, direct solution method for 2D problems, and the Conjugate gradient method with a MG preconditioner for 3D simulations of the whole ventricle.

### 2.5.5 Parallel computing

To reduce computation time, CARP can be executed in parallel. Parallel computing allows independent parts of a calculation to be carried out at the same time on different processors, before combining the output. The parallel implementation of CARP makes use of the following libraries;

- *SuperLU* [26] for the LU decomposition method,
- *PETSc* (portable, extensible toolkit for scientific computation) [9], which contains many functions such as the manipulation of parallel sparse matrices and parallel preconditioners.
- *MPI* (message passing interface library) [2] to allow processors to communicate with each other.

## 2.6 The Barkley model

### 2.6.1 Model definition

The Barkley model, and associated numerical algorithm, were originally proposed as a method for performing very fast numerical simulations of spiral waves in two dimensions and scroll waves in three dimensions [10, 27]. The model is a two-variable system of reaction-diffusion equations modeling the dynamics of an excitable



medium,

$$u_t = f(u, v) + \Delta u, \quad (2.32)$$

$$v_t = g(u, v), \quad (2.33)$$

where the functions  $f(u, v)$  and  $g(u, v)$  express the local kinetics of the two variables  $u$  and  $v$ . The local kinetics are modelled using the equations

$$f(u, v) = \frac{1}{\varepsilon} u(1 - u) \left( u - u^{th}(v) \right), \quad (2.34)$$

$$g(u, v) = u - v, \quad (2.35)$$

where  $u^{th} = \frac{v + b}{a}$ , and  $a$ ,  $b$ , and  $\varepsilon$  are parameters with  $\varepsilon \ll 1$ . The variables  $u$  and  $v$  are known as the excitation and recovery variables respectively.

The Barkley model is a simplification to the Fitzhugh-Nagumo model [31], which itself was designed as a simplified version of the Hodgkin-Huxley model. The advantage of the Barkley model over other models of excitable media is that the reaction terms permit very fast numerical simulations of spiral waves and scroll waves.

### 2.6.2 Numerical algorithm

Two open source computer programs EZspiral and EZscroll [11] implement the Barkley model in two and three dimensions, respectively. The programs are written in the C programming language. Here we give an overview of the numerical methods used in these programs.

#### Reaction terms

By ignoring the diffusion term, Barkley considered the ODE for the reaction terms in the model,

$$u_t = f(u, v), \quad (2.36)$$

$$v_t = g(u, v). \quad (2.37)$$

The two important aspects of the numerical scheme are that  $u$  becomes zero whenever it is very small, and the use of a semi-implicit scheme to allow large time steps.

With explicit Euler time-stepping,  $\frac{\Delta t}{\varepsilon} \approx 1$  is the maximum time step for obtaining accurate solutions [27]. To enable the use of larger time steps, in both EZspiral and EZscroll, Dowle *et al* use a semi-implicit method to solve  $f(u, v)$ .

## Diffusion terms

In EZspiral, Barkley implements a five-point, and a nine-point, finite-difference Laplacian formula on a square lattice. In EZscroll, both seven-point and nineteen-point formulas are implemented on a regular cubic lattice.

There are several advantage of using the nineteen-point formula over the seven-point formula for 3D simulations. Firstly, Dowle *et al.* [27] showed that the stability limit,  $\Delta t_{max}$ , is much larger for the nineteen-point formula than for the seven-point formula. It should be noted however, that the nineteen-point formula does take more computation than the seven-point formula. The second advantage is that stability limit,  $\Delta t_{max}$ , is identical for both the nineteen-point formula in 3D and the nine-point formula in 2D. This is particularly useful for considering simulations in both 2D and 3D when the same time step  $\Delta t$  is required for a given grid spacing  $h$ , independent of the space dimension.

## 2.7 Theory of resonant drift

Rotating spiral waves are a typical example of self-organised spatio-temporal patterns which occur in many different reaction-diffusion systems. They have been observed in chemical Belousov-Zhabotinsky (BZ) reaction [86, 92] and also in biological systems such as the colonies of *Dictyostylium Discoideum* [33], in the calcium waves within frog eggs, in the retina of the eye, and cardiac tissue [23]. These are all examples of excitable media.

A spiral wave is created from certain initial conditions, or if a single propagating wave is broken down. In many cases such self-sustained activity destroys the normal functions of biological media, which is not desirable. For example, such self-sustained re-entrant activity in cardiac muscle is termed a cardiac arrhythmia and often precedes death. This provides motivation for the study of spiral wave dynamics and efficient methods for their control.

In this section we review the phenomenon of resonant drift and how it could potentially be applied as a new method for low-energy defibrillation.

Davydov *et al.* [24] considered a simplified model of spiral waves and demonstrated that if the parameters of the model are changed periodically with frequency close to the rotation frequency of the spiral wave, then the spiral wave drifts in space along a circular trajectory. In the case of a precise resonance between the forcing

frequency and the frequency of the spiral, the spiral wave drifts along a straight line. This theoretical prediction was supported by numerical simulations of the FitzHugh-Nagumo model and was confirmed by Agladze *et al.* [4] through experiments in BZ reaction. This phenomenon is termed resonant drift and has since been reproduced in a monodomain model of atrial tissue [17]. It was suggested that resonant drift could be used to drive a re-entrant cardiac arrhythmia to an inexcitable boundary, or an inexcitable piece of cardiac tissue, which would lead to the termination of the re-entry. If this is possible in a real heart, then resonant drift will provide cardiologists with a new strategy for low-energy defibrillation.

Biktashev and Holden produced a phenomenological description for the resonant drift in terms of ODE's for the center of rotation and rotation phase of a spiral wave. This system was originally derived using the symmetry properties of a spiral wave [15], and later using an asymptotic approach [18]. We will now describe the main outcomes from their research.

### 2.7.1 Phenomenological description of resonant drift

Spiral waves are a solution to a reaction-diffusion equation of the form

$$\mathbf{u}_t = \mathbf{f}(\mathbf{u}) + \mathbf{D}\Delta\mathbf{u} + \mathbf{h}. \quad (2.38)$$

Here  $\mathbf{u} = \mathbf{u}(x, y, t) \in \mathbb{R}^l$  is a vector function (e.g. the vector of the transmembrane voltage and the activation and inactivation variables of the ionic channels),  $\mathbf{f} \in \mathbb{R}^l$  is a non linear function (e.g. the ionic currents),  $\mathbf{D} \in \mathbb{R}^{l \times l}$  is a diffusion matrix, and  $\mathbf{h} = \mathbf{h}(\mathbf{u}, x, y, t) \in \mathbb{R}^l$  denotes a small perturbation which is assumed to be uniformly bounded.

We assume that (2.38) with no perturbation ( $\mathbf{h}(\mathbf{u}, x, y, t) = 0$ ) supports rigidly rotating (i.e. constant frequency) spiral waves (see Fig. 2.10) which are solutions of the form

$$\mathbf{u}(x, y, t) = \mathbf{V}(r, \theta - \omega t), \quad (2.39)$$

where  $\omega$  is the angular frequency of the rigidly rotating spiral wave,  $\mathbf{V}(r, \theta - \omega t)$  is  $2\pi$  periodic with respect to  $\omega$ , and  $r$  and  $\theta$  are polar co-ordinates in the  $(x, y)$  plane. Typically, spiral wave solutions only exist for a unique value of  $\omega$ , up to the sign.

Rigidly rotating spiral wave solutions have an important symmetry property; they are invariant with respect to spatial displacement, rotation, and time. This

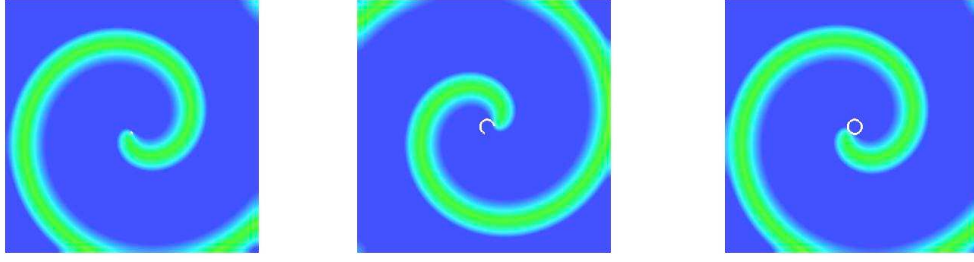


Figure 2.10: Rigidly rotating spiral wave. The trajectory of the tip is shown in white. These images were generated by the author using EZspiral.

invariance property allows one to say that there is a three-dimensional (3D) manifold of solutions to the unperturbed system,

$$\mathbf{V}(x, y, t) = \mathbf{V}(r(x - X, y - Y), \theta(x - X, y - Y) - \omega t + \phi), \quad (2.40)$$

where  $X$ ,  $Y$ , and  $\phi$  correspond to small shifts in space and rotation respectively. It should be noted here that a shift in time  $t$  is equivalent to a rotation by  $\phi$  and so does not contribute to a dimension of the manifold of spiral wave solutions.

Biktashev and Holden [15, 18] derived equations for the drift of a spiral wave solution to (2.38) with  $\mathbf{h} \neq 0$ . That is, they derived the following equations of motion for  $X$ ,  $Y$ , and  $\phi$ ,

$$\frac{d\phi}{dt} = \omega(X, Y) - \Omega \quad (2.41)$$

$$\frac{dX}{dt} = v(X, Y) \cos(\phi) + C_x(X, Y) \quad (2.42)$$

$$\frac{dY}{dt} = v(X, Y) \sin(\phi) + C_y(X, Y) \quad (2.43)$$

where  $\omega(X, Y)$  is the frequency of the spiral wave solution which may depend on the position of the spiral,  $(X, Y)$ , due to the spatial dependence of the perturbation  $\mathbf{h}(x, y, t)$ . Further,  $\Omega$  is the frequency of the perturbation,  $X$  and  $Y$  are the coordinates for the center of rotation,  $\phi$  is the phase of rotation,  $v(X, Y)$  is the velocity of the drift, and  $C_x(X, Y)$  and  $C_y(X, Y)$  describe the drift of the spiral which would happen without external perturbation (i.e. due to inhomogeneity of the medium or interactions with other spirals or the boundaries).

### Solutions of the phenomenological system

Assume that  $\omega(X, Y) = \omega$  and  $v(X, Y) = v$  are constant and  $C_x(X, Y) = C_y(X, Y) = 0$ . We shall consider two solutions to the phenomenological system.

### Imprecise resonance

Consider the case when  $\omega - \Omega = A \neq 0$  where  $A$  is constant. From (2.41) we have the solution

$$\phi = At + \phi_0,$$

where  $\phi_0$  is a constant of integration. Solving (2.42) and (2.43) we get the solutions

$$X = \frac{v}{A} \sin(At + \phi_0) + X_0, \quad (2.44)$$

$$Y = -\frac{v}{A} \cos(At + \phi_0) + Y_0, \quad (2.45)$$

where  $X_0$  and  $Y_0$  are constants. Thus it can be seen from (2.44) and (2.45) that the trajectories of the drifting spiral are circles with radius  $\frac{v}{A}$  and centre  $(X, Y) = (X_0, Y_0)$  (see Fig. 2.11),

$$(X - X_0)^2 + (Y - Y_0)^2 = \frac{v^2}{A^2}.$$

It should also be noted that since the distance traveled for one complete trajectory around the circle is  $\left| \frac{2\pi v}{\omega - \Omega} \right|$  then the time taken for one trajectory is  $\left| \frac{2\pi}{\omega - \Omega} \right|$ .

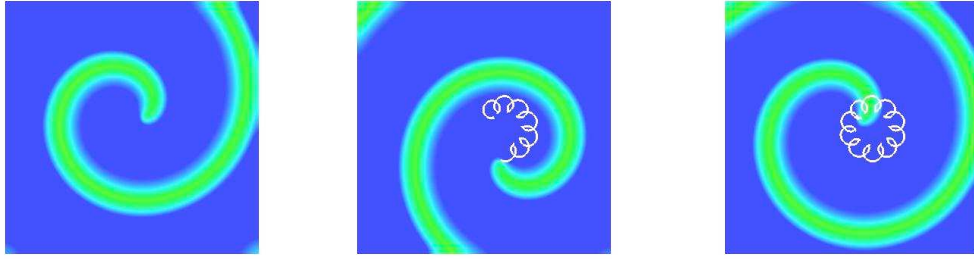


Figure 2.11: Resonantly drifting spiral wave with imprecise resonance,  $\omega \neq \Omega$ . The trajectory of the tip is shown in white. These images were generated by the author using EZspiral.

### Precise resonance

Consider the case when  $\omega - \Omega = 0$ . From (2.41) we have the solution

$$\phi = \phi_0,$$

where  $\phi_0$  is a constant. Solving (2.42) and (2.43) we get the solutions

$$X = v \cos(\phi_0)t + X_0, \quad (2.46)$$

$$Y = v \sin(\phi_0)t + Y_0, \quad (2.47)$$

where  $X_0$  and  $Y_0$  are constants. Thus it can be seen from (2.46) and (2.47) that the trajectories of the drifting spiral are straight lines with direction  $\phi_0 = \tan^{-1} \left( \frac{Y - Y_0}{X - X_0} \right)$ , (see Fig. 2.12).

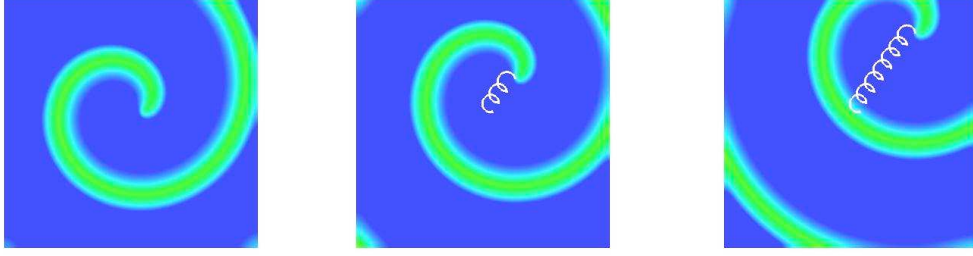


Figure 2.12: Resonantly drifting spiral wave with precise resonance,  $\omega = \Omega$ . The trajectory of the tip is shown in white. These images were generated by the author using EZspiral.

### 2.7.2 Interaction with boundaries

As proposed by Biktashev and Holden [15, 18], the phenomenological system (2.41), (2.42) and (2.43) describes the motion of the resonant drift for the center of rotation of a spiral wave. Where, by neglecting the influence of  $C_x(X, Y)$  and  $C_y(X, Y)$ , and assuming that  $\omega(X, Y) = \omega$ , if  $\omega - \Omega = A \neq 0$  the trajectories of the drift are circles and if  $\omega - \Omega = 0$  the trajectories are straight lines.

To use resonant drift as a tool for defibrillation one needs to ensure that the trajectory of the drifting spiral will reach an in-excitable boundary and terminate. There are problems associated with this. Firstly, since the spiral's rotation frequency,  $\omega(X, Y)$ , is a function of  $X$  and  $Y$  there may be no exact resonance for the whole medium, thus the drift trajectory can not be straight along the whole medium if the frequency of the perturbation,  $\Omega$ , remains constant. Secondly, as Biktashev and Holden observed through numerical experiments [15, 18],  $\omega(X, Y)$  changes regularly in the vicinity of a boundary. This causes a repulsion effect which we will now describe.

Suppose that far from a boundary the frequency of the stimulus is sufficiently close to the frequency of the rotating spiral  $\Omega \cong \omega(X, Y)$ , so that each stimulus is applied at the same phase of rotation and so each shift is in the same direction, causing the direction of the drift trajectory to be a straight line. As the spiral

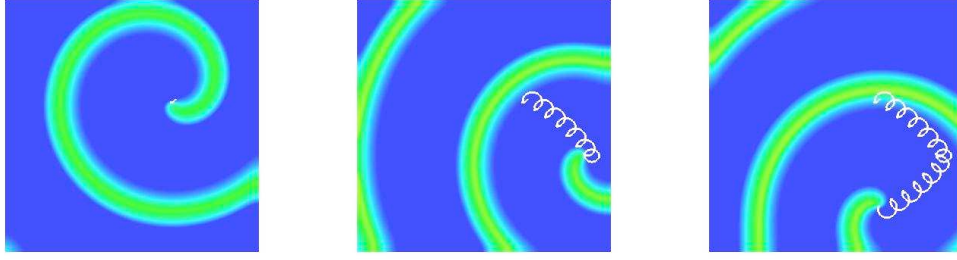


Figure 2.13: Resonant repulsion near the right edge boundary. The trajectory of the tip is shown in white. These images were generated by the author using EZspiral.

approaches a boundary its frequency of rotation increases and so subsequent stimuli occur at later and later phases which changes the direction of shifts. This process continues until the spiral is moving away from the boundary, thus the motion of the spiral acts as if it has been repelled from an in-excitable boundary (see Fig. 2.13).

### 2.7.3 Feedback controlled stimulation

The problems of using resonant drift to eliminate re-entrant waves from cardiac tissue are the choice of frequency for stimulation and resonant repulsion from boundaries. Resonant repulsion is related to the change in the resonant frequency as the spiral drifts through different regions of the medium. To overcome the problem of resonant repulsion away from an in-excitable boundary, Biktashev and Holden suggested changing the forcing frequency as the frequency of the spiral changes. This can be done by taking feedback from the spiral wave itself [16, 18, 17] so that the stimulus is applied precisely at the times that the excitation wavefront reaches a particular recording point,  $(x_r, y_r)$ , in the medium. To do this one considers the phase difference  $\phi$  by a fixed dependence on the current position of the spiral,

$$\phi(t) = \Phi_{fb}(X, Y, x_r, y_r). \quad (2.48)$$

If one assumes that the shape of the spiral is described by an Archimedian spiral then one may write

$$\Phi_{fb}(X, Y, x_r, y_r) = \theta(X - x_r, Y - y_r) + \frac{2\pi\rho(X - x_r, Y - y_r)}{\lambda}$$

where  $\rho$  and  $\theta$  are polar coordinates, and  $\lambda$  is the asymptotic wavelength. Instead of the previous system of ODE's describing the motion of the drifting spiral we get

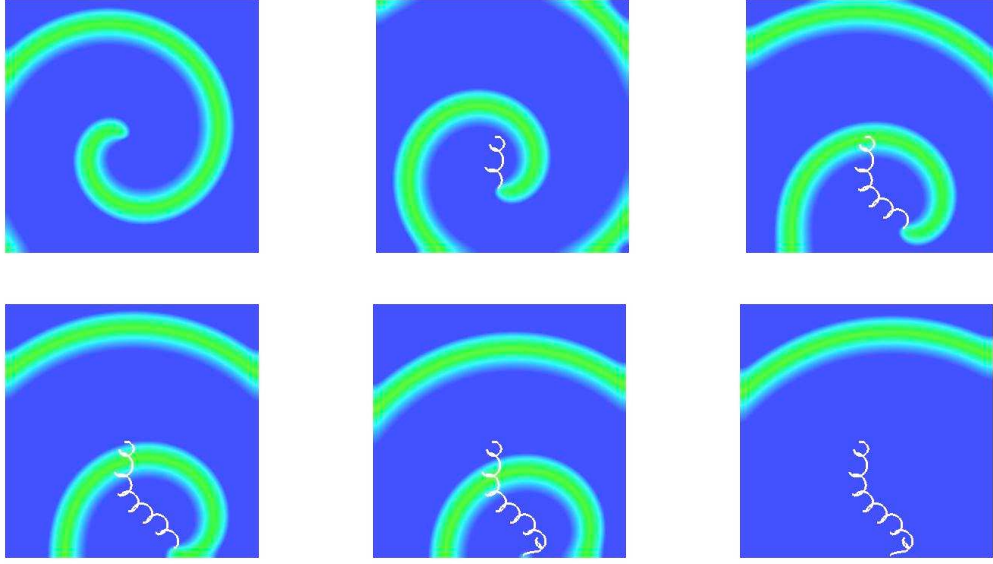


Figure 2.14: Successful termination of a spiral wave using resonant drift pacing. These images were generated by the author using EZspiral.

the system

$$\Phi(X, Y, x_r, y_r) = \theta(X - x_r, Y - y_r) + \frac{2\pi\rho(X - x_r, Y - y_r)}{\lambda}, \quad (2.49)$$

$$\frac{dY}{dt} = v(X, Y) \cos(\Phi_{fb}) + C_x(X, Y), \quad (2.50)$$

$$\frac{dX}{dt} = v(X, Y) \sin(\Phi_{fb}) + C_y(X, Y). \quad (2.51)$$

A successful termination of a spiral wave using feedback controlled stimulation is presented in Fig. 2.14. In contrast to the case of constant frequency stimulation with a resonant frequency  $\omega = \Omega$ , the trajectory of the spiral wave is a curve, not a straight line. This is due to the changing phase distance from the tip of the spiral to the recording point.

In cardiac tissue, the recording point can be realised by a simple device that consists of a recording electrode which measures the voltage at a point in the tissue and triggers a shock from a stimulating electrode upon the arrival of a re-entrant spiral wave at this point. It could also be programmed with a timer which controls a delay time,  $t_{delay}$ , between the detection of a re-entrant spiral wave by the registration electrode and a shock from the stimulating electrode [16].

Numerical simulations using a reaction diffusion system have show that the stimulation amplitude necessary for extinguishing spiral waves by the feedback control



of resonant drift (i.e. resonant drift pacing (RDP)) can be by an order of magnitude less than that required for single shock defibrillation [17, 60].

RDP has previously been tested using a 2D model of isotropic homogeneous atrial tissue [17]. However RDP has not yet been tested using an isotropic inhomogeneous bidomain model of cardiac tissue. We present the results of our own numerical simulations of RDP in such a model in Chapters 3 and 6.

### **Different types of feedback**

Zykov *et al.* have used a registration electrode in the form of a straight line [94, 67]. In experiments using the BZ reaction, spiral waves drift along the line electrode until they reach an in-excitable boundary, at which point they terminate. Another approach introduced by Zykov *et al.* is ‘global feedback’ [96] which requires finding an integral of the distribution of excitation over the entire medium and forcing the medium on the basis of this information. However, although global feedback has been shown to have similar efficiency compared with a single recording electrode [60], due to its abstract nature, implementing global feedback in a defibrillator could be problematic.

## **2.8 Dynamics of three-dimensional scroll waves**

Scroll waves are the three-dimensional extension of spiral waves. They have been observed in BZ reaction [87, 88], in numerical simulations of excitable media [61, 14], and also in cardiac tissue [35, 34]. In any cross section a scroll wave has the shape of a spiral. So a scroll wave can be viewed as a stacking of spiral waves, rotating around a *filament* which occupies the center of the scroll (see Fig. 2.15).

As the wave rotates, the filament generally moves through space according to certain laws of motion. These equations of motion were first published by Keener in 1988 [41] and their properties discussed in a series of papers following the original publication [42, 43]. Biktashev, Holden, and Zhang [19] simplified Keener’s equations of motion by showing that some of the coefficients are zero.

Investigating the properties of 3D scroll waves provide insights into processes in the cardiac tissue of mammals whose heart wall is thick enough for 3D effects to be significant (i.e. human ventricular tissue [46]).

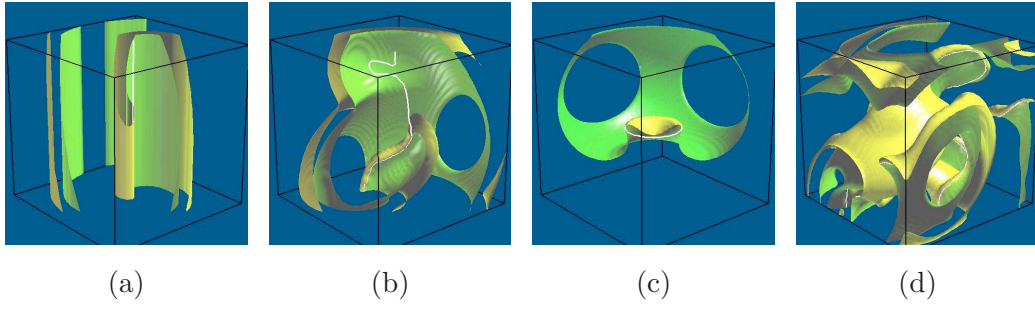


Figure 2.15: Scroll wave filaments with (a) Straight filament, (b) twisted and bent filament, (c) untwisted scroll ring, (d) scroll wave turbulence. These images were generated by the author using EZscroll. The white lines represent the filaments, the yellow surfaces are the wavefronts, and the green surfaces are the wave backs.

### 2.8.1 Equations of motion

In 1988, Keener [41] derived equations of motion, which were later simplified by Biktashev, Holden, and Zhang [19], for the filament of an unperturbed scroll wave solution of a 3D reaction-diffusion system,

$$\mathbf{u}_t = \mathbf{D}\Delta_3\mathbf{u} + f(\mathbf{u}), \quad (2.52)$$

where  $\mathbf{u} = \mathbf{u}(x, y, z, t)$  is a function of time and space,  $\mathbf{D}$  is the diagonal matrix of diffusion coefficients, and  $\Delta_3\mathbf{u} = \mathbf{u}_{xx} + \mathbf{u}_{yy} + \mathbf{u}_{zz}$  is the Laplacian operator in 3D.

The following equations are the equations of motion for a scroll wave filament [19],

$$\phi_t = \mathbf{N}_t \cdot \mathbf{B} + \mathbf{R}_t \cdot \mathbf{T}(\phi_s - \tau) + b_1(\phi_{ss} - \tau_s) + a_1(\phi_s - \tau)^2, \quad (2.53)$$

$$\mathbf{R}_t \cdot \mathbf{N} = b_2\kappa, \quad (2.54)$$

$$\mathbf{R}_t \cdot \mathbf{B} = c_3\kappa, \quad (2.55)$$

where  $\mathbf{N}$  is the normal vector,  $\mathbf{B}$  the binormal vector, and  $\mathbf{T}$  the tangent vector to a point  $\mathbf{R}$  on the filament,  $\phi$  is the rotation phase of the scroll,  $s$  is the arc-length coordinate along the filament,  $t$  is time,  $\tau$  is the torsion of the filament and  $\kappa$  is the curvature of the filament. The coefficients  $a_1, b_1, b_2$ , and  $c_3$  will be discussed in detail in Chapter 5.

In this section we have only presented the results from [41, 19]. Further details of the calculations can be found in Chapter 5 where we derive equations of motion

for the filament of a scroll wave solution to (2.52) with a perturbation.

### 2.8.2 Filament tension

Biktashev, Holden, and Zhang [19] considered the total length of the filament defined at each  $t$ ,

$$S(t) \equiv \int ds = \int |\mathbf{R}_\sigma(\sigma, t)| d\sigma \quad (2.56)$$

where  $\sigma$  is a new parameter introduced in [19] such that points with equal  $\sigma$  move perpendicular to the filament. It was shown then that

$$\frac{dS}{dt} = -b_2 \int_{s_0}^{s_1} \kappa^2 ds.$$

So, if the filament is not straight and  $b_2 > 0$  then its total length tends to zero.

This allows the introduction of a property of scroll waves, called the *filament tension*. The filament tension is determined by the coefficient  $b_2$  and its sign uniquely determines whether the length of the filament increases or decreases in time.

If a filament shortens in time then it is said to have a *positive* filament tension. Scroll waves with positive filament tension therefore either collapse or stabilise to a straight shape. In a bounded medium, the contraction of a filament with positive tension can lead to the self termination of the scroll wave.

If a filament lengthens in time then it is said to have a *negative* filament tension. It has been demonstrated [14, 7] that in a medium of sufficiently big size, the elongation of a filament with negative tension will lead to *scroll wave turbulence* (see Fig. 2.15(d)).

### 2.8.3 Solution of the equations of motion: untwisted scroll rings

Keener [41] considered a solution of his system of equations for an untwisted scroll ring. Here we re-tell that story but using the simplified system of equations (2.53), (2.54), and (2.55). Assume that  $\phi(s, t)$  is the same everywhere on the ring and consider the following parametrisation

$$\mathbf{R}(\sigma, t) = \begin{pmatrix} a(t) \cos \sigma \\ a(t) \sin \sigma \\ -z_*(t) \end{pmatrix},$$

where  $a(t)$  is the radius of the ring and  $z_*(t)$  allows movement along the  $z$  axis. Since  $|\mathbf{R}_\sigma(s, t)| = a(t)$ , by using the Frenet-Serret equations (see (5.3)-(5.6)) it can be seen that

$$\mathbf{T} = \begin{pmatrix} -\sin \sigma \\ \cos \sigma \\ 0 \end{pmatrix}, \quad \mathbf{N} = \begin{pmatrix} \cos \sigma \\ \sin \sigma \\ 0 \end{pmatrix}, \quad \mathbf{B} = \begin{pmatrix} 0 \\ 0 \\ 1 \end{pmatrix},$$

where  $\kappa = -\frac{1}{a}$  and  $\tau = 0$ . Taking derivative of  $\mathbf{R}$  with respect to time  $t$ ,

$$\mathbf{R}_t = \begin{pmatrix} a_t \cos \sigma \\ a_t \sin \sigma \\ -z_{*t} \end{pmatrix}$$

allows one to deduce that  $\mathbf{R}_t \cdot \mathbf{N} = a_t$  and  $\mathbf{R}_t \cdot \mathbf{B} = -z_t$ . Substitution into the equations of motion (2.53), (2.54), and (2.55) yields

$$\begin{aligned} \frac{d\phi}{dt} &= 0, \\ \frac{da}{dt} &= -\frac{b_2}{a}, \\ \frac{dz_*}{dr} &= \frac{c_3}{a}. \end{aligned}$$

Using the initial conditions  $\phi(0) = \phi_0$ ,  $a(0) = a_0$  and  $z(0) = z_0$  these equations allow the solution

$$\begin{aligned} \phi(t) &= \phi_0, \\ a(t) &= (a_0^2 - 2b_2 t)^{\frac{1}{2}}, \\ z_*(t) &= z_0 + \frac{c_3}{b_2}(a_0 - a(t)). \end{aligned}$$

So if  $b_2$  is positive then the lifetime of the scroll ring is  $T = \frac{a_0^2}{2b_2}$  during which time the ring drifts a distance of  $Z = \frac{c_3 a_0}{b_2}$ . If  $b_2$  is negative then the ring expands.

## 2.9 Scroll wave turbulence

Scroll wave turbulence is a self sustained regime in 3D excitable media. A chaotic wave pattern develops through the negative-tension of scroll wave filaments, which tend to spontaneously elongate, bend, and loop, producing an expanding tangle that fills the entire domain. It has suggested that scroll wave turbulence could provide an explanation for the development of fibrillation and the occurrence of sudden cardiac death in healthy people [89, 14].

### 2.9.1 Control of scroll wave turbulence using a non-resonant perturbation

The three dimensional nature of a ventricle, and the existence of scroll wave turbulence presents a challenge to the idea of using resonant drift pacing as a tool for low-energy defibrillation.

Theoretical progress in this area has, to date, been limited. However, Alonso *et al.* [7, 6] considered the effect of applying a periodic non resonant forcing on scroll wave turbulence. By numerical simulations of the Barkley model, they showed that a periodic modulation of the mediums excitability with a constant frequency chosen slightly higher than the frequency of the scroll waves can control the turbulence in the medium. They proposed a theory of this effect based on a kinematic description of the scroll waves [8]. They concluded that a faster than resonant stimulation can change the filament tension from negative to positive, which causes the collapse of each of the scrolls in the medium.

The data published by Alonso *et al.* indeed looks like a convincing way to control scroll wave turbulence. However, in many of their simulations although the turbulence was controlled, the scrolls were not terminated. Instead the filaments stabilised to a straight line connecting opposite ends of the domain. Considering cardiac defibrillation, to enable the heart to function normally again, all scroll waves would need to be terminated and not merely controlled into a straight shape.

The effect of applying a resonant perturbation to scroll wave turbulence has not yet been studied and is the subject of investigation in Chapter 4 of this thesis.

## 2.10 Summary

In this Chapter we have described the literature relevant to this thesis. We have introduced the physiological background of this thesis and the models of cardiac cells and cardiac tissue which we use. We discuss the phenomenon of resonant drift in two-dimensions and explain how it can potentially be employed as a method of low-energy defibrillation. We finally describe the existing equations of motion of scroll waves and the methods which have previously been employed to control scroll wave turbulence.

## Chapter 3

# Resonant drift in the bidomain model

The first simulation study presented in this thesis begins the investigation into the effectiveness of using resonant drift pacing for low-energy defibrillation. Previous studies of resonant drift pacing have used a completely unrealistic description of the action of electric current on cardiac tissue [17]. Here we use an anisotropic bidomain model of cardiac tissue with microscopic intracellular conductivity fluctuations and realistic cellular kinetics. Shocks are applied by injecting current into, and withdrawing from, the extracellular space. Such a description was used in simulations before, but only for high-energy single-shock defibrillation [62].

The results show that, in this model setting, resonant drift pacing can be used to move the cores of the re-entrant waves. Termination can be achieved with high probability, at a fraction of the conventional single shock defibrillation strength, by moving the cores until they hit an anatomical boundary, or annihilate with each other. We show that in a realistically anisotropic model, direction of movement depends on electrode location and time delays of the shock application. Knowing the electrode location and the anatomy of the heart, the best delay could be estimated to move the core in the direction of a suitable anatomical structure or boundary which is likely to terminate the re-entrant wave.

## 3.1 Methodology

### 3.1.1 Governing equations

The bidomain equations (2.14)-(2.15) of cardiac tissue are most widely used to study defibrillation-related phenomena [65]. The bidomain model was discussed in section 2.3.1, for the readers' convenience we reproduce the equations here,

$$\begin{aligned} C_m \frac{\partial V_m}{\partial t} &= -I_{ion} + \frac{1}{\beta} \nabla \cdot (\sigma_i \nabla V_m) + \frac{1}{\beta} \nabla \cdot (\sigma_e \nabla \Phi_e), \\ \nabla \cdot ((\sigma_i + \sigma_e) \nabla \Phi_e) &= -\nabla \cdot (\sigma_i \nabla V_m) + I_e, \end{aligned}$$

where  $V_m = \Phi_i - \Phi_e$  is the transmembrane potential,  $\Phi_i$  and  $\Phi_e$  are the intracellular and extracellular potential distributions,  $\beta$  is the average cell's surface to volume ratio,  $C_m$  is the membrane capacitance per unit area,  $\sigma_i$  and  $\sigma_e$  are the intracellular and extracellular conductivity tensors respectively,  $I_e$  is the extracellular current, and  $I_{ion}$  is the ionic current density through the membrane.

In the absence of external electric current  $I_e$ , if variations of  $\Phi_e$  are negligible compared to  $\Phi_i$ , or if the anisotropy ratios in both domains are the same, then the bidomain equations can be replaced by the simpler monodomain equation (see section 2.3.2)

$$C_m \frac{\partial V_m}{\partial t} = -I_{ion} + \frac{1}{\beta} \nabla \cdot (\sigma_m \nabla V_m),$$

where  $\sigma_m$  is the membrane's conductivity. A recent comparison of the monodomain and bidomain models suggests that they yield very similar results as long as no strong electric fields are applied [64].

To allow comparison with [62], for the ionic currents,  $I_{ion}$ , we have used the Courtemanche *et al.* human atrial model [22] with the alterations described in section 3.1.4. This model is very detailed, taking into account all major ionic transport mechanisms as well as intracellular calcium handling. The complete model used in this study can be found in Appendix B.

An explanation of the parameters used in our simulations are given in Section 3.1.2 and a summary is given in Table 3.1.

### 3.1.2 Numerical methods and parameters

All simulations were performed by the Cardiac Arrhythmias Research Package (CARP) [81, 80, 63]. We used a numerical setup similar to Plank *et al.* [62]. We used a thin

sheet of cardiac tissue  $4 \times 2 \times 0.02 \text{ cm}^3$  with the space discretisation step  $0.01 \text{ cm}$ . All cardiac muscle fibres were oriented in the  $x$  direction (i.e. conductivity in the  $x$  direction is greater than in the  $y$  and  $z$  directions). To ensure that no current flows out of the edges of the domain, no-flux boundary conditions were imposed.

For single shock defibrillation, a bidomain formulation was used during the shock and 10 ms after the shock with a time step of  $1 \mu\text{s}$ . A monodomain formulation was then used to observe the post-shock evolution of  $V_m$  for a further 500 ms with a time step of  $10 \mu\text{s}$ . For resonant drift pacing, a bidomain formulation was used throughout with a time step  $10 \mu\text{s}$ .

The intracellular conductivities in all bidomain calculations were fluctuating according to

$$\sigma_{ij} = \bar{\sigma}_{ij}(1 + F\eta), \quad (3.1)$$

where  $j = x, y, z$ . The fluctuation intensity was fixed to  $F = 0.5$  and  $\eta \in [-1, 1]$  are independent equidistributed random numbers. The choice of  $F = 0.5$  was made after analysing the data published in [62]. To investigate the effect that intracellular conductivity fluctuations have on resonant drift pacing, we tried setting  $F = 0.0$  (see Fig. 3.14).

As in [62], we set the intracellular conductivity along the fibre axis to  $\bar{\sigma}_{ix} = 0.174 \text{ S/m}$ , and across the fibre axis to  $\bar{\sigma}_{iy} = \bar{\sigma}_{iz} = 0.019 \text{ S/m}$ . The extracellular conductivities were set to  $\sigma_{ex} = 0.625 \text{ S/m}$ ,  $\sigma_{ey} = \sigma_{ez} = 0.236 \text{ S/m}$ . When the monodomain model was used, the conductivities were set to be,  $\sigma_{mx} = 0.146 \text{ S/m}$ ,  $\sigma_{my} = \sigma_{mz} = 0.0182 \text{ S/m}$ . In addition, we set  $\beta = 1400 \text{ cm}^{-1}$  and  $C_m = 1.0 \mu\text{F/cm}^2$  throughout.

All simulations presented in this chapter were calculated on a Beowulf cluster at The University of Liverpool.

Quantity	Value
Surface to volume ratio	$\beta = 1400 \text{ cm}^{-1}$
Membrane capacitance per unit area	$C_m = 1.0 \mu\text{F/cm}^2$
Extracellular conductivity tensor	$\sigma_e$
... along the fibres	$\sigma_{ex} = 0.625 \text{ S/m}$
<i>continued on next page ...</i>	



... continued from previous page	
Quantity	Value
... across the fibres	$\sigma_{ey} = \sigma_{ez} = 0.236 \text{ S/m}$
Intracellular conductivity tensor	$\bar{\sigma}_{ij}(1 + F\eta(x, y, z))$
... along the fibres	$\bar{\sigma}_{ix} = 0.174 \text{ S/m}$
... across the fibres	$\bar{\sigma}_{iy} = 0.019 \text{ S/m}$
... fluctuation intensity	$F = 0.5$
... noise	$\eta(x, y, z) \in [-1, 1]$
Monodomain conductivity tensor	$\sigma_m$
... along the fibres	$\sigma_{mx} = 0.146 \text{ S/m}$
... across the fibres	$\sigma_{my} = 0.0182 \text{ S/m}$
Time discretisation step	$\Delta t = 10 \mu\text{s}$ and $\Delta t = 1 \mu\text{s}$
Space discretisation step	$0.01 \text{ cm}$
Tissue size	$(x, y, z) = (4 \text{ cm}, 2 \text{ cm}, 0.01 \text{ cm})$

Table 3.1: Summary of numerical parameters for Chapter 3

### 3.1.3 Visualization

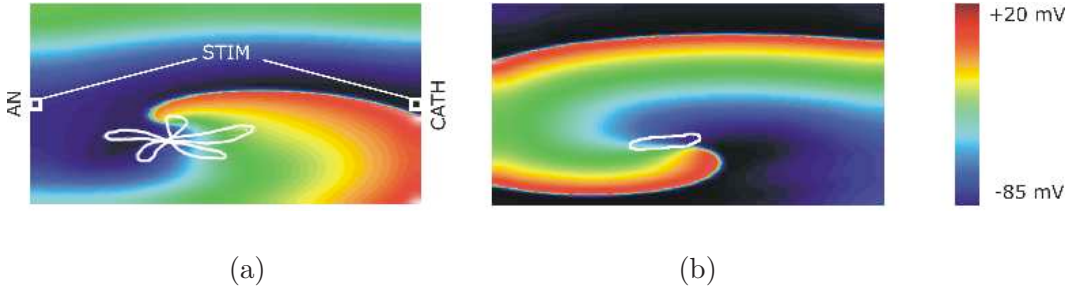


Figure 3.1: (a) Meandering re-entry with the trajectory of the tip and illustration of the location of the stimulating electrodes, (b) Stationary rotating re-entry with the trajectory of the tip.

We used CARP’s transmembrane voltage  $V_m(x, y, t)$  output to visualize the results of simulations, using the colour-coding shown in Fig. 3.1.

The same information was used to detect the wave tips. The wavefront at time  $t$  was defined as  $V_m = -23.75\text{mV}$ . Then the wavetips for that time were defined as the intersections of the front at time  $t$  with the front at time  $t - 3\text{ms}$ .

To visualize drift we used a “stroboscopic” method, i.e. we showed positions of the tip synchronized with the signals detected by the registration electrodes.

For meandering spirals this required further refinement since the stroboscopic selection of tips produced a congested picture, even without any stimulation: so a five-petal meandering pattern (as shown in Fig. 3.1(b)) produced five clusters of tips. With stimulation, the tip picture becomes even more complicated and unreadable. So we showed only every  $N$ -th stroboscopic tip position. Since the meandering patterns were affected by stimulation, we found that the optimal value for  $N$  was different from 5; we used  $N = 3$ .

### 3.1.4 Generation of re-entry patterns

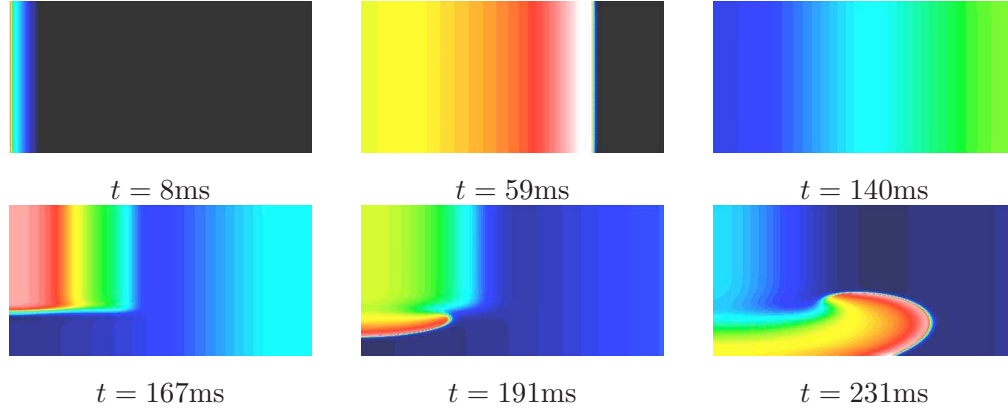


Figure 3.2: Initiation of a re-entrant wave. A planar wave front is initiated at  $t = 0\text{ms}$  by stimulating the left edge of the tissue. After  $t = 160\text{ms}$  the upper left quadrant of the tissue is stimulated and, due to the refractory period of the initial planar wave, causes a re-entrant wave to form.

To initiate re-entry, we used an S1-S2 protocol (see Fig. 3.2). We used two alterations of the Courtemanche human atrial model [22] of the ionic currents,  $I_{ion}$ :

- (i) To prevent  $V_m$  from rising to non-physiological values during the defibrillation shocks an electroporation current,  $i_{ep}$ , was included (see [62] and references therein). In addition, a formulation for a spatially invariant acetylcholine-dependent potassium current,  $i_{K(ACH)}$ , was added [44, 62]. This ionic model was used to generate a meandering re-entry, see Fig. 3.1(a).
- (ii) In addition to electroporation and  $i_{K(ACH)}$ , we used a 65% block of the slow inward L-type current  $i_{Ca,L}$ , coupled with a nine-fold increase in the slow delayed outward current  $i_{Ks}$ , and the rapid delayed outward current  $i_{Kr}$ , as suggested by Xie *et al.* [91]. This ionic model was used to generate a stationary rotating re-entry, see Fig. 3.1(b).

### 3.1.5 Single shock defibrillation procedure

Monophasic current shocks were injected (CATH) into, and withdrawn (AN) from, the extracellular space via volumes  $0.1 \times 0.1 \times 0.02 \text{ cm}^3$ , “stimulating electrodes”, centered along the left and right edges of the slab (Fig. 3.1(a), STIM). The shocks,  $I_e$ , had rectangular monophasic waveform, duration  $\Delta = 5 \text{ ms}$ , and varied amplitude  $A$ ,

$$I_e(x, y, z, t) = A\Theta(t - t_0)\Theta(t_0 + \Delta - t) [\chi_a(x, y, z) - \chi_c(x, y, z)].$$

Here  $\Theta()$  is the Heaviside step function,  $t_0$  is the time of the shock application, and  $\chi_a(x, y, z)$  and  $\chi_c(x, y, z)$  are equal to 1 within the anode and cathode electrodes and equal to 0 otherwise. For our domain  $(x, y, z) = (4 \text{ cm}, 2 \text{ cm}, 0.02 \text{ cm})$ , centered at  $(0, 0, 0)$ , we used,

$$\chi_a(x, y, z) = \begin{cases} 1, & x \in [-2, -1.9], y \in [-0.05, 0.05], z \in [-0.01, 0.01] \\ 0, & \text{otherwise} \end{cases}$$

and

$$\chi_c(x, y, z) = \begin{cases} 1, & x \in [1.9, 2], y \in [-0.05, 0.05], z \in [-0.01, 0.01] \\ 0, & \text{otherwise} \end{cases}$$

where all stated coordinates are in cm. Shocks were applied at twelve different timings  $t_0$ , separated by 10 ms intervals, after the same initial conditions. This covered an entire single rotor cycle, 120 ms. A single shock was deemed successful if no re-entry was detectable at the moment 500 ms after its end. We define the single shock defibrillation success threshold as the shock amplitude which gives a 50% success rate across the twelve timings.

### 3.1.6 Resonant drift pacing procedure

Repetitive low-amplitude shocks of the same waveform and via the same *stimulating* electrodes as above, were applied at the time moments determined by signals received via *registration* electrodes.

Six different locations for the registration electrodes were used: “point” electrodes  $0.02 \times 0.02 \times 0.02 \text{ cm}^3$  in the top left, top right, bottom left and bottom right corners and “line” electrodes [94] (of cross-section  $0.02 \times 0.02 \text{ cm}^2$ ) through the whole medium either horizontally, along the fibres or vertically, across the fibres, see Fig. 3.3(c).

A shock was applied immediately,  $t_{delay} = 0$ , when the average potential of the registration electrode exceeded  $-55$  mV, see Fig. 3.3(a). To investigate the direction of drift, we tried a delay of  $t_{delay} = 30$  ms, about a quarter of the re-entry period, see Fig. 3.3(b).

To allow post-shock evolution, the registration electrodes were de-activated for a “blanking time”  $t_{blank} = 50$  ms after a shock application.

For the meandering re-entry, resonant drift pacing was considered successful if the re-entry was terminated sooner than its self-termination time, 16000 ms. For the stationary-rotating re-entry, this time was extended to 30000 ms.

## 3.2 Results

### 3.2.1 Single shock defibrillation results

We have varied the timings, and strength  $A$ , of the single shocks to assess the variability of the outcomes. Consistent with previous observations [62], there were three typical single shock defibrillation outcomes for both the meandering and stationary-rotating patterns:

- Strong enough shocks annihilated re-entry immediately (Fig. 3.4(a)).
- Weaker shocks led to multiple wavebreaks (Fig. 3.4(b)).
- Weaker still shocks only shift re-entry in space (Fig. 3.4(c)).

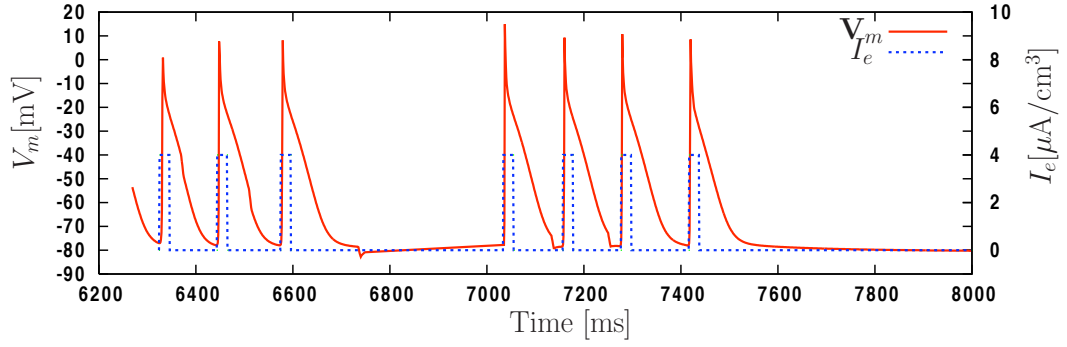
We have found the 50% single shock defibrillation success threshold to be  $A = 14 \times 10^6 \mu\text{A}/\text{cm}^3$ , and  $18 \times 10^6 \mu\text{A}/\text{cm}^3$  for the meandering and stationary-rotating patterns respectively (see Fig. 3.5).

### 3.2.2 Resonant drift pacing results

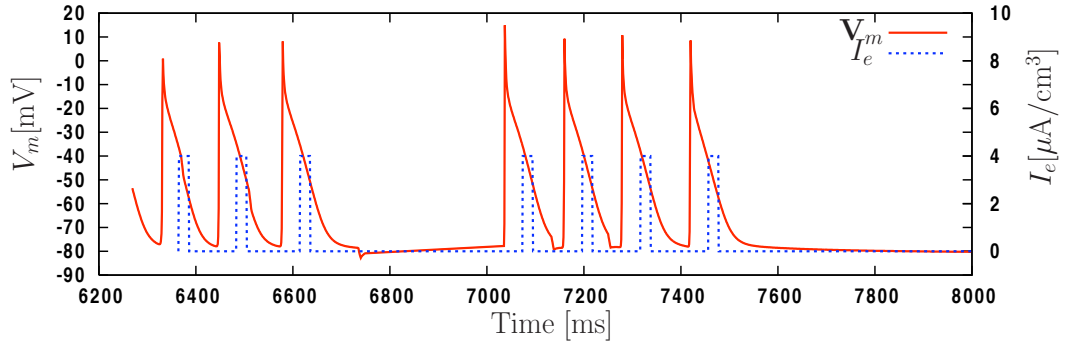
The time taken for termination of all re-entrant activity using resonant drift pacing with different locations of the registration electrode is shown in Fig. 3.10, for the meandering re-entry, and Fig. 3.11 for the stationary rotating re-entry.

#### Meandering re-entry

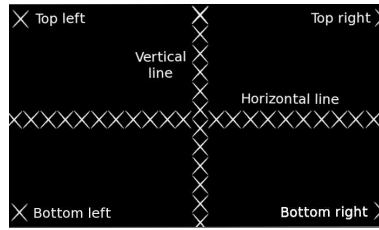
**Point registration electrodes.** Depending on the shock strength, the following outcomes were observed.



(a)



(b)



(c)

Figure 3.3: Illustration of the feedback algorithm with (a)  $t_{\text{delay}} = 0\text{ms}$  and (b)  $t_{\text{delay}} = 30\text{ms}$ . (c) Locations used for the registration electrode.

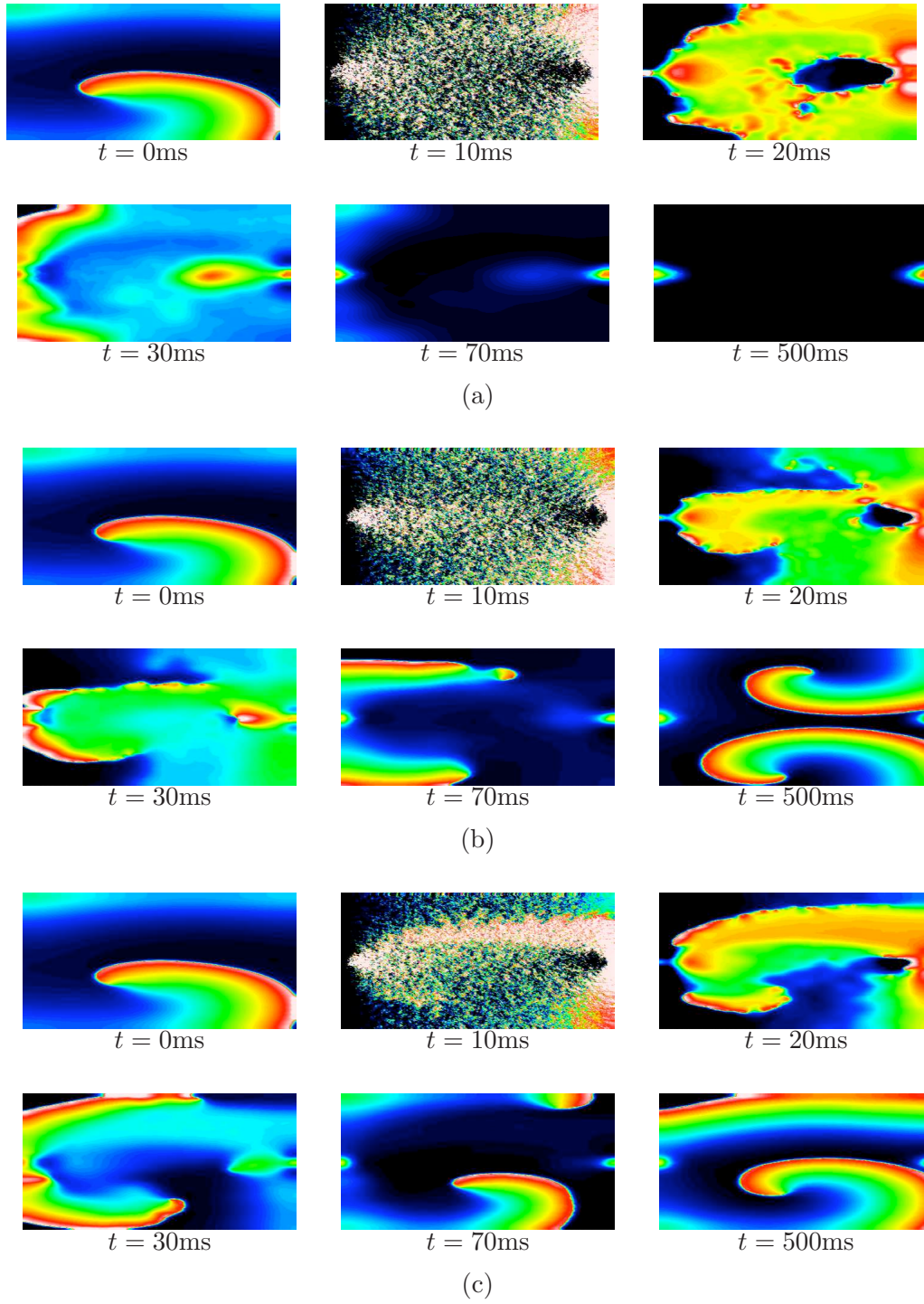


Figure 3.4: Single shock defibrillation: (a) Termination,  $A = 16 \times 10^6 \mu\text{A}/\text{cm}^3$  applied at time  $t = 10$ . (b) Breakup,  $A = 14 \times 10^6 \mu\text{A}/\text{cm}^3$  applied at time  $t = 10$ . (c) Displacement,  $A = 10 \times 10^6 \mu\text{A}/\text{cm}^3$  applied at time  $t = 10$ .

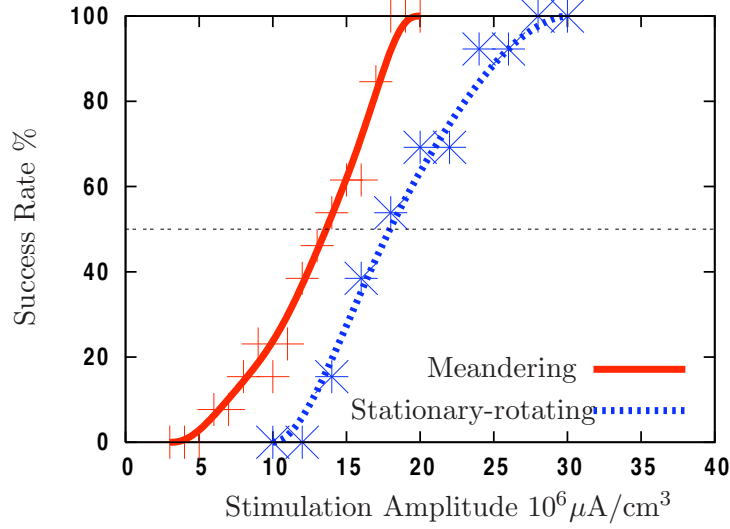


Figure 3.5: Single shock defibrillation: Percentage of successful terminations (from the 12 initial conditions used for each shock amplitude) as function of shock amplitude  $A$ . The raw data is plotted as markers, and a smooth curve (Bezier approximation) is drawn through them. The horizontal dashed line indicates the 50% success rate threshold for SSD.

- The original re-entry drifted, roughly towards the registration electrode, until termination on an in-excitable boundary, see Fig. 3.6.
- Secondary meandering patterns are generated from stimulating electrode; both the original and newly generated re-entries drifted. An example is shown in Fig. 3.7. The original re-entry “A” was terminated by the first 24 shocks. However, a secondary meandering pattern “C” was generated by a shock in the process. After “A” terminated, it was “C” that triggered the subsequent shocks. A third meandering pattern, “B” was generated by a further shock. Due to the proximity of “B” to the registration electrode, it took over the control of the shock applications. Re-entry “B” drifted to the boundary and terminated after a further 15 shocks. Then “C” was again the solitary meandering pattern and took over the control. A fourth meandering pattern, “D” was generated by a shock and, due to its proximity to the registration electrode, took over the control. After 3 shocks, “D” collided with “C” and they annihilated each other without reaching an inexcitable boundary.

Pak *et al.* [59] tested a stimulation protocol similar to resonant drift pacing in optical mapping experiments with real rabbit ventricles. They were successful at

defibrillating with shock strengths an order of magnitude lower than single shock defibrillation, but saw no evidence of annihilation at the ventricular boundaries. Mutual annihilation of “C” and “D” in Fig. 3.7 suggests a plausible explanation.

### Line registration electrodes

- *Horizontal:* With the registration electrode along the fibres, the re-entry drifted at a small angle to it (see Fig. 3.8).
- *Vertical:* With the registration electrode across the fibres, the drift was usually more complicated. An example is shown in Fig. 3.9. The re-entry initially drifts upwards along the electrode. After 21 shocks, the drift turns downwards, until it reaches an inexcitable boundary after a further 109 shocks and terminates. The trajectory of the drift crosses itself, which is not allowed in the asymptotic theory of drift of rigidly rotating spiral waves [16], so may be a new feature due to meander.

Termination times using different locations of the registration electrode is shown in Fig. 3.10 for the meandering re-entry.

It can be seen that resonant drift pacing can successfully terminate meandering patterns using amplitudes 14 times lower than the single shock defibrillation success threshold. Termination was achieved in all of our resonant drift pacing simulations with the meandering pattern.

Among the registration electrodes, the vertical line was the most successful, as it produced the largest proportion of successful terminations in the fastest time, and the top right was the least successful location. The vertical line was more successful than the horizontal line, possibly because the drift path in our simulations was shorter in the vertical direction than in the horizontal, even with account of fibre orientation.

We conclude that the termination time depends on the mutual position of the registration electrode, anode, cathode, initial position of the re-entry, tissue size and fibre orientation.

For amplitude  $A = 1 \times 10^6$ , re-entry termination time for the meandering pattern in most cases was longer than its self-termination time 16000 ms. Thus, we did not consider lower values for the stimulation amplitudes.



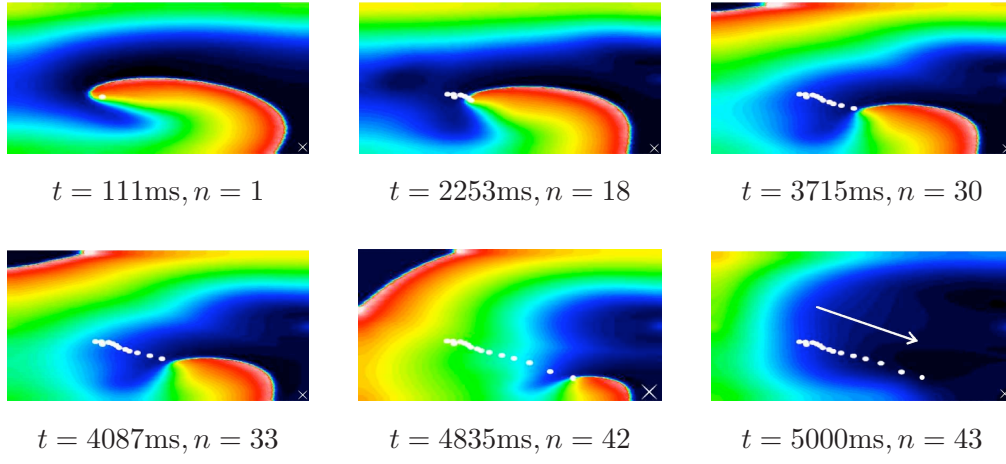


Figure 3.6: Resonant drift pacing of a meandering re-entry with  $A = 1 \times 10^6 \mu\text{A}/\text{cm}^3$ : Re-entry drifts to an inexcitable boundary where it is terminated. Here and below, the location of the registration electrode is shown with a cross and  $n$  denotes the number of shocks applied so far.

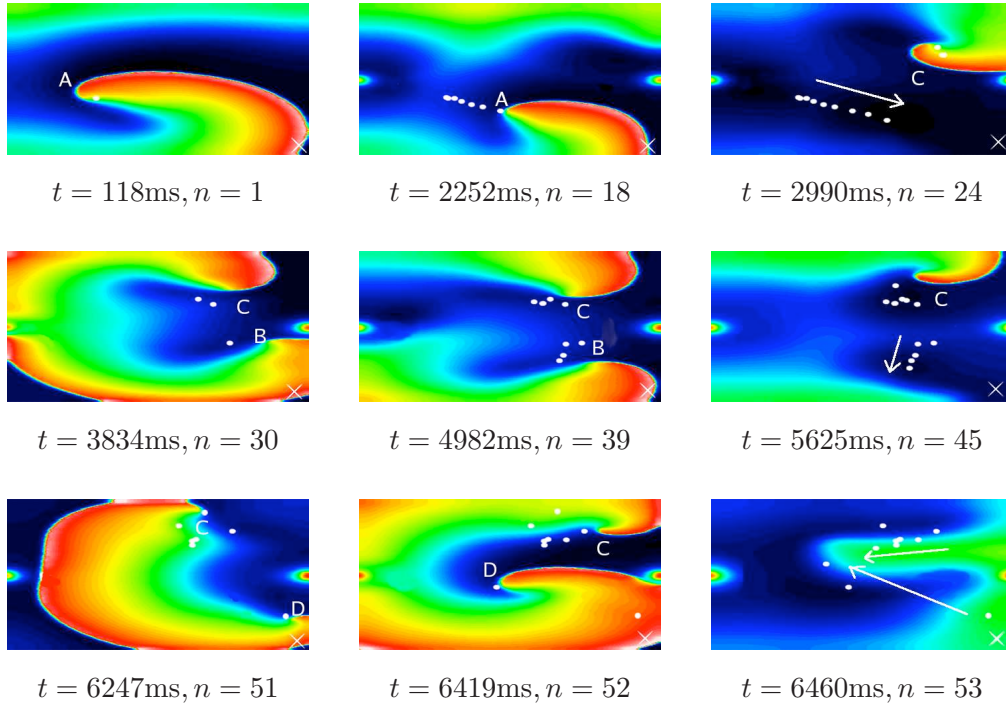


Figure 3.7: Resonant drift pacing of meandering re-entry with  $A = 2 \times 10^6 \mu\text{A}/\text{cm}^3$ : Original re-entry  $A$  drifts resonantly to an inexcitable boundary where it is terminated. Additional re-entrant patterns ( $B, C$ , and  $D$ ) are generated by the shock electrodes. In turn, they trigger shock applications.  $B$  drifts to a boundary and terminates, whilst  $C$  and  $D$  collide with each other and terminate before reaching a boundary.

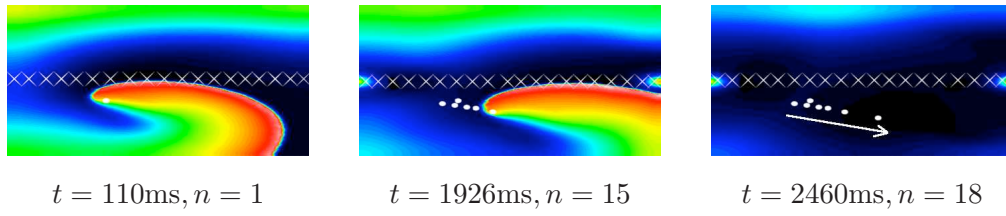


Figure 3.8: Resonant drift pacing with horizontal line registering electrode with  $A = 2 \times 10^6 \mu\text{A}/\text{cm}^3$ : Re-entry drifts resonantly at an angle to the line electrode until it reaches an inexcitable boundary and terminates.

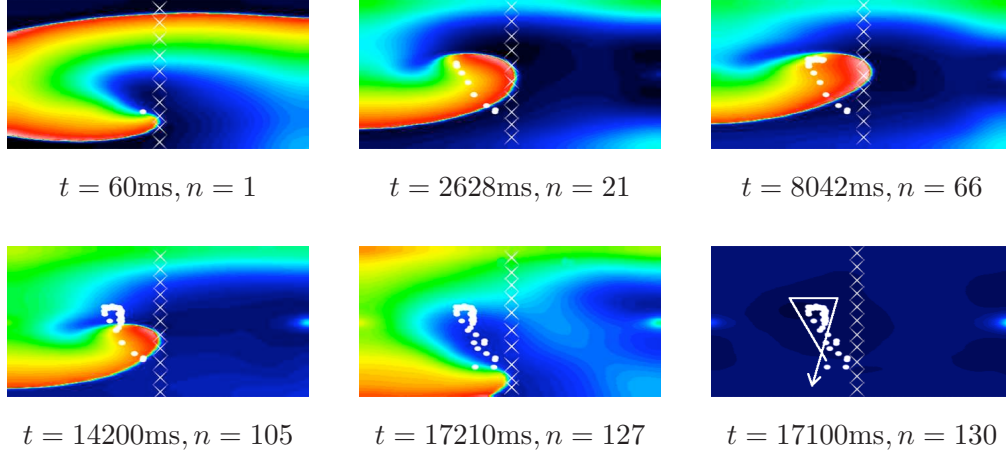
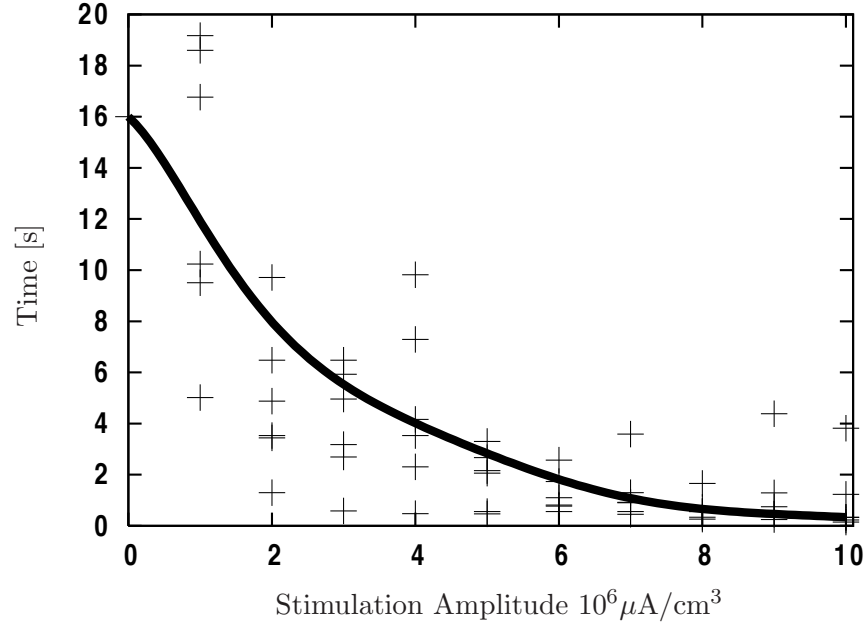


Figure 3.9: Resonant drift pacing with vertical line registering electrode,  $A = 1 \times 10^6 \mu\text{A}/\text{cm}^3$ . The re-entry drifts upwards for 21 shocks, before changing direction and reaches the boundary after a further 109 shocks.

### Stationary rotating re-entry

Figure 3.11 shows the times taken for annihilation of all re-entrant waves for the different locations of the registration electrode. Resonant drift pacing can terminate stationary-rotating patterns using amplitudes 18 times lower than the single shock success threshold. The combination of shock strength with the location of the registration electrode affects the probability of success and the time taken for termination.

Termination of stationary rotating re-entry was not always observed within the 30000 ms limit. Sometimes the algorithm gets caught in an infinite loop (Fig. 3.12 and Fig. 3.13), when the original re-entrant pattern has been terminated, but shocks produce new wavefronts which trigger further stimulation producing further wavefronts and so on. Such loops are discussed further in section 3.2.5.

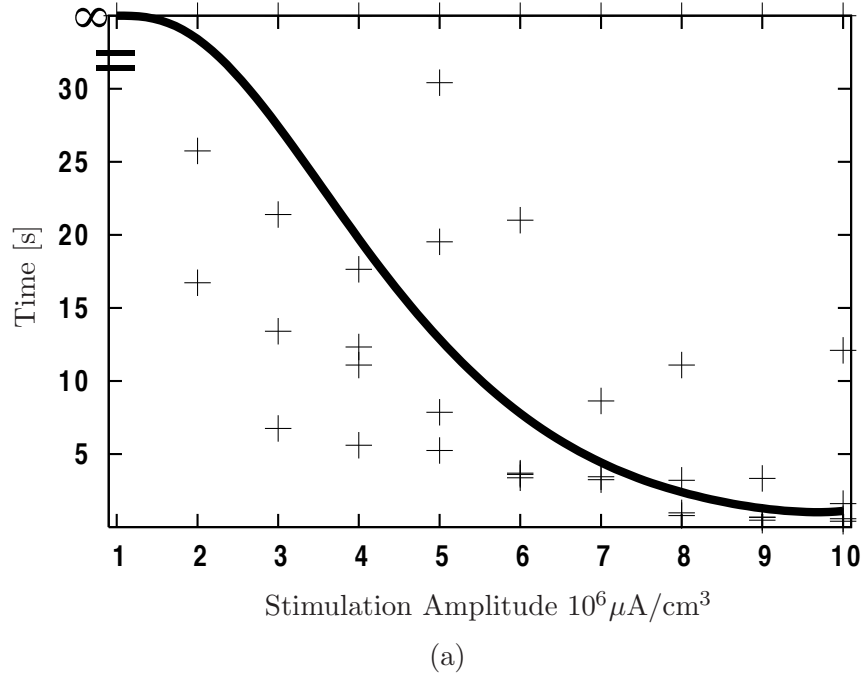


(a)

$A$	Bottom left	Bottom right	Top left	Top right	Vertical line	Horizontal line
1	19169	5013	16763	10239	17600	9510
2	1297	6478	4880	9712	3530	2440
3	5930	2689	6474	4960	580	3180
4	9820	3530	4160	2310	480	7290
5	2060	560	2160	2670	470	3300
6	2570	560	1100	1730	770	810
7	900	920	1300	3590	450	560
8	1660	340	720	1330	260	560
9	460	1290	750	4385	250	460
10	230	330	1230	3820	150	340

(b)

Figure 3.10: Resonant drift pacing results for meandering re-entry. (a) Termination time as a function of shock amplitude  $A$ . (b) Raw data with termination time in ms and amplitude  $A$  in  $\mu\text{A}/\text{cm}^3$ .



$A$	Bottom left	Bottom right	Top left	Top right	Vertical line	Horizontal line
1	$\infty$	$\infty$	$\infty$	$\infty$	$\infty$	$\infty$
2	$\infty$	$\infty$	$\infty$	$\infty$	25750	16720
3	$\infty$	21390	$\infty$	$\infty$	13410	6760
4	$\infty$	12330	$\infty$	17640	11090	5600
5	$\infty$	19530	$\infty$	29420	7860	5250
6	$\infty$	3370	$\infty$	21000	3690	3610
7	$\infty$	3250	$\infty$	8630	3450	2280
8	$\infty$	790	$\infty$	3210	11090	980
9	$\infty$	480	$\infty$	3340	670	670
10	$\infty$	400	$\infty$	1610	12100	570

(b)

Figure 3.11: Resonant drift pacing results for stationary rotating re-entry. (a) Termination time as a function of shock amplitude  $A$ . (b) Raw data with termination time in ms and amplitude  $A$  in  $\mu\text{A}/\text{cm}^3$ .  $\infty$  denotes the simulation got caught in an infinite loop.

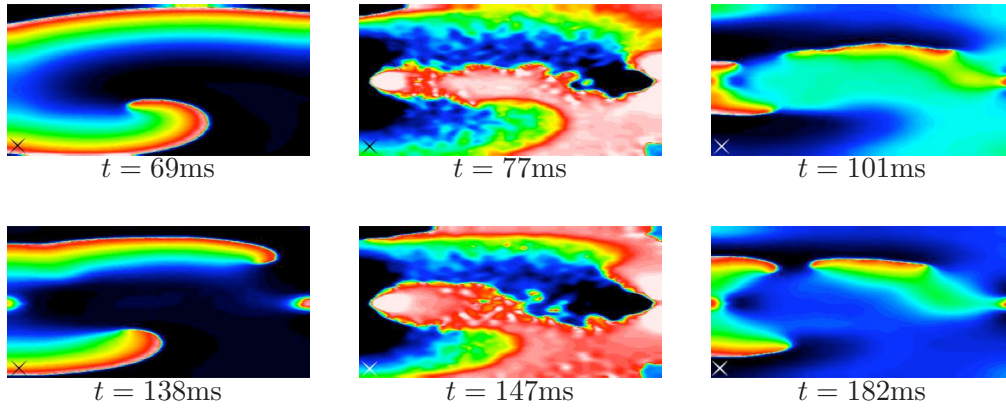


Figure 3.12: Infinite loop in resonant drift pacing:  $A = 10 \times 10^6 \mu\text{A}/\text{cm}^3$ . New waves are initiated by shocks which repeatedly trigger another shock application.

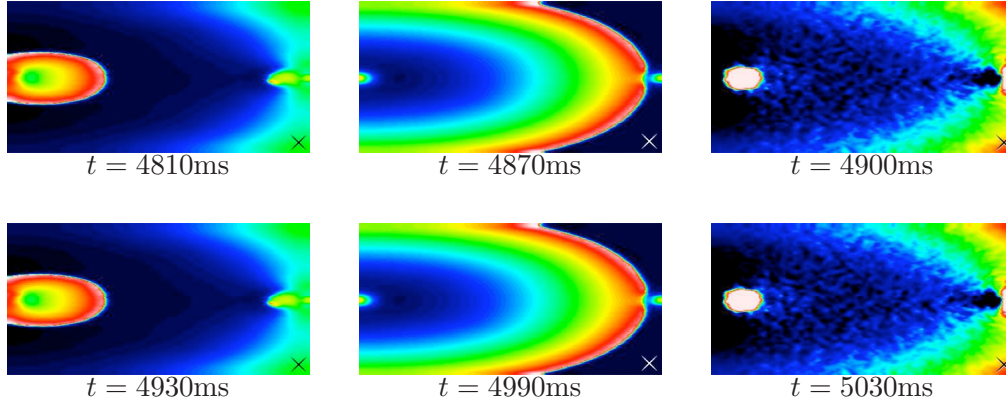


Figure 3.13: Infinite loop in resonant drift pacing:  $A = 2 \times 10^6 \mu\text{A}/\text{cm}^3$ . New waves are initiated by shocks which repeatedly trigger another shock application.

### 3.2.3 Effect of fluctuations on resonant drift pacing

The effect of varying the fluctuation intensity on single shock defibrillation was investigated in [62]. It was shown that, for a single rotor re-entry, the actual fluctuation intensity made no qualitative difference on the success or failure of a shock. To investigate whether the fluctuation intensity effects the outcome of resonant drift pacing we set the fluctuation intensity to be zero,  $F = 0.0$ , so that the intracellular conductivities remained constant,  $\sigma_{ij} = \bar{\sigma}_{ij}$ .

Fig. 3.14 shows the effect of applying resonant drift pacing to the meandering re-entry, with a “point” registration electrode in the bottom right location, and a shock amplitude  $A = 1 \times 10^6 \mu\text{A}/\text{cm}^3$ . This simulation is equivalent to Fig. 3.6 with no conductivity fluctuations. It can be seen that when  $F = 0.0$ , there is little difference to the outcome of resonant drift pacing compared to the case when  $F = 0.5$ .

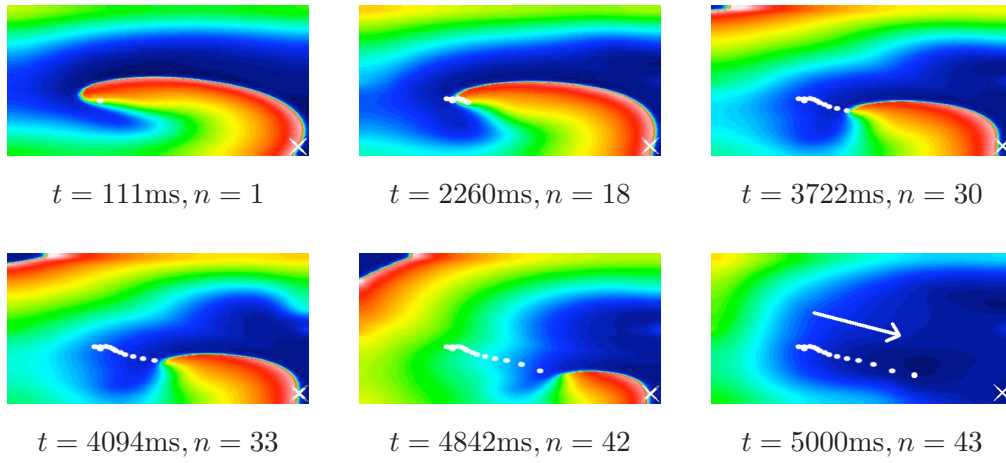


Figure 3.14: Resonant drift pacing of a meandering re-entry with  $A = 1 \times 10^6 \mu\text{A}/\text{cm}^3$  and **no intracellular conductivity fluctuations**: Re-entry drifts to an inexcitable boundary where it is terminated. Here and below, the location of the registration electrode is shown with a cross and  $n$  denotes the number of shocks applied so far.

### 3.2.4 Direction of drift

The theory of feedback-controlled resonant drift of spiral waves in reaction-diffusion systems [16, 18] predicts that the drift direction depends, among other things, on the delay of the stimulation with respect to the registered signals. A delay by a certain fraction of a spiral's period causes a change in the drift direction by the same fraction of  $360^\circ$ . We have verified that it works in this realistically anisotropic bidomain model as well.

Fig. 3.15 shows fragments of two such simulations, with the same initial conditions and different values of  $t_{\text{delay}}$ , 0 and 30 ms, which is about a quarter of the re-entry period. The direction of the drift in these two cases differs by about  $90^\circ$ , in agreement with [16, 18].

### 3.2.5 Using a time delay to induce success

We have mentioned in section 3.2.2 that resonant drift pacing may fail through an infinite loop of wavefront eliminations and creations. If newly created wavefronts are unbroken as in Fig. 3.13 then the re-entrant activity will vanish if the stimulation is stopped at any time, *i.e.* the success is achieved.

A genuine failure happens when newly created waves are broken and form new re-entries, as in Fig. 3.12. The chances of getting in such a loop depend on the drift trajectory, which depends on the location of the registration and stimulation

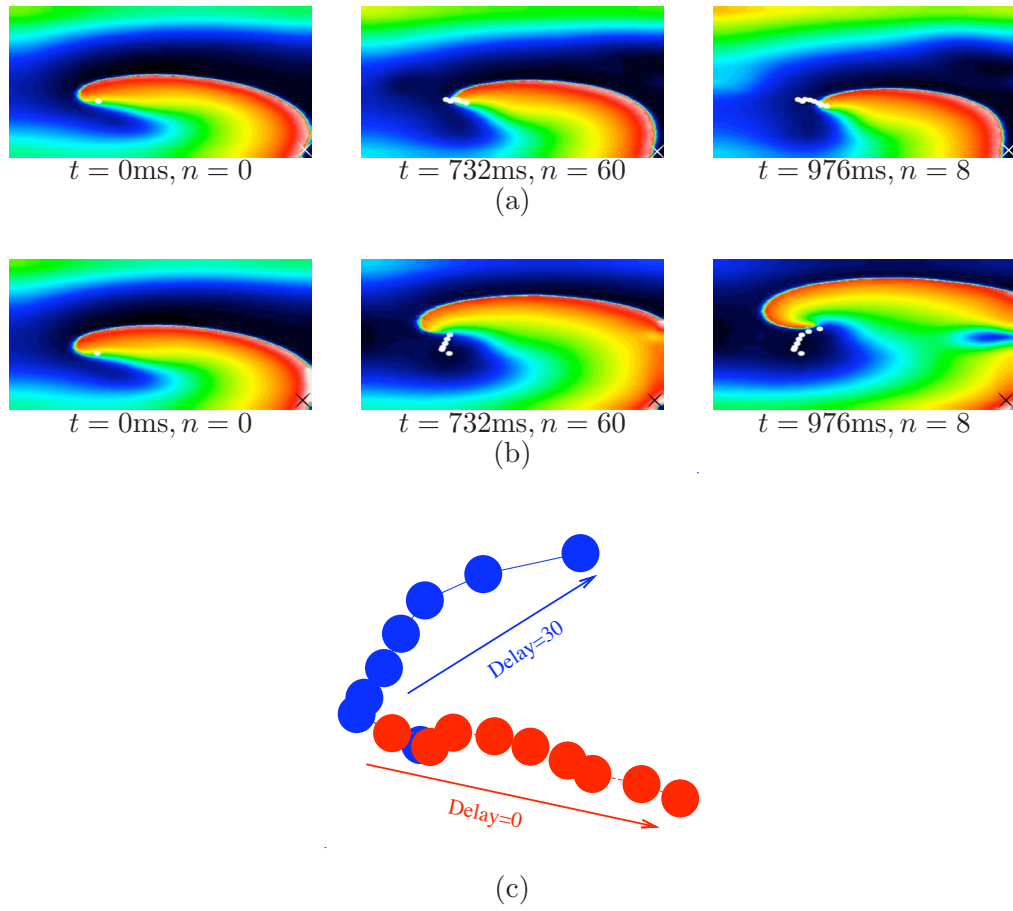


Figure 3.15: Resonant drift of a meandering pattern with: (a)  $t_{\text{delay}} = 0\text{ms}$ ,  $A = 1 \times 10^6 \mu\text{A}/\text{cm}^3$ . (b)  $t_{\text{delay}} = 30\text{ms}$ ,  $A = 1 \times 10^6 \mu\text{A}/\text{cm}^3$ . (c) Enlarged tip trajectories from (a) and (b).

electrodes and the feedback delay. Hence such loops should be avoidable by an appropriate choice of the electrode locations and/or of  $t_{\text{delay}}$ . In a real-life situation, such choice would require plenty of information and may be difficult to make. Not all theoretical solutions (*e.g.* optimal positions of the electrodes) may be possible to implement in practice. Further, the optimal parameters may vary from one arrhythmia episode to another so difficult to predict *a priori*.

Of all the mentioned parameters,  $t_{\text{delay}}$  is the easiest to change, and it may even be adjusted in real time, during pacing. Hence we propose that a change of the feedback delay may be used to discontinue an infinite loop *even after it has already started*.

To demonstrate the feasibility of this approach, we re-ran the simulation presented in Fig 3.12. Originally with  $t_{\text{delay}} = 0\text{ms}$  it gave an elimination/creation loop



which still persisted after 30000 ms. Now we increased  $t_{delay}$  to 30 ms at  $t = 1000$  ms. This broke the loop and terminated the re-entry, see Fig. 3.16.

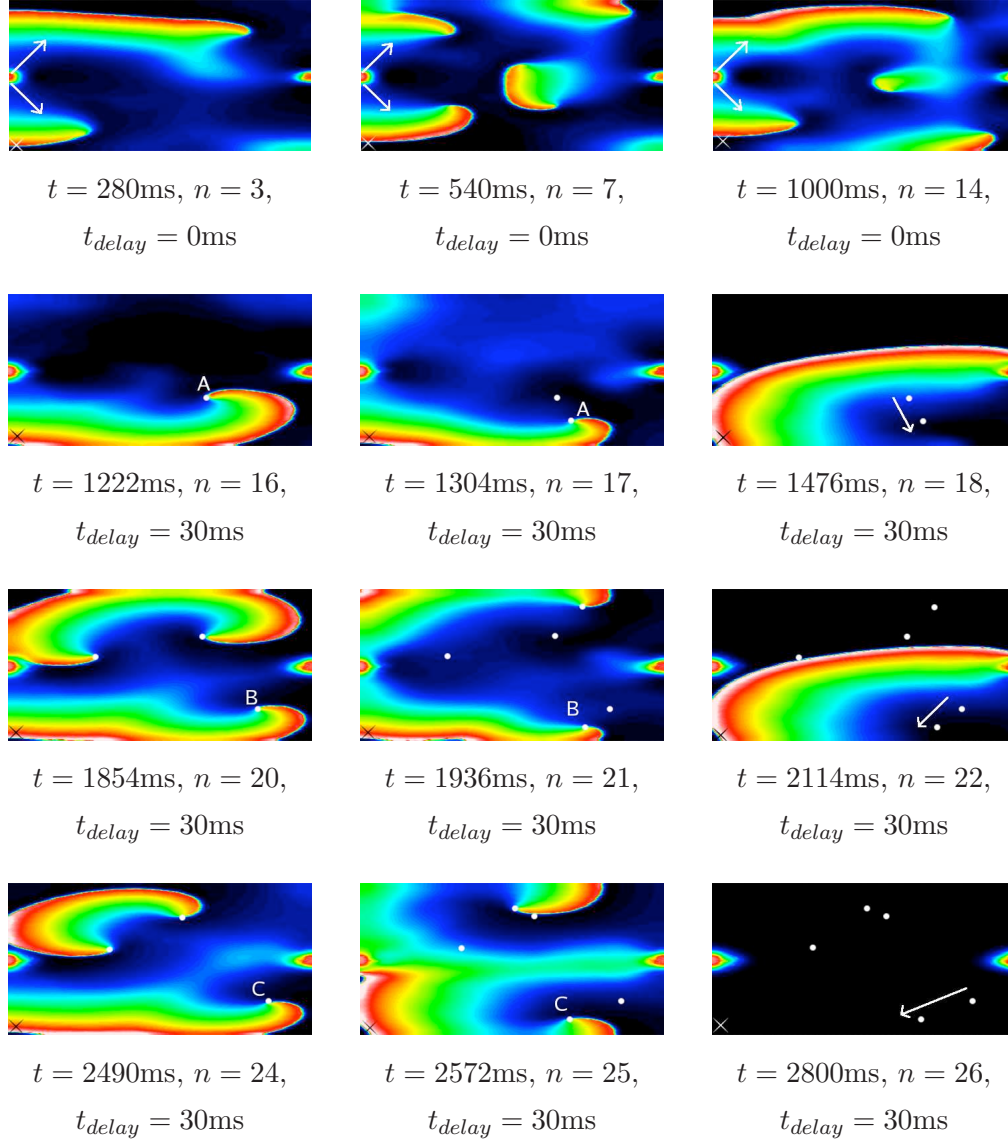


Figure 3.16: Using a time delay to escape an infinite loop: the re-entry from Fig. 3.12 is extinguished. Arrows illustrate the generation of new wavefronts and the direction of drift.

### 3.3 Summary

The goal of this simulation study was to investigate the effectiveness of using resonant drift pacing for low-energy defibrillation. Previously, the use of resonant drift had only been studied experimentally in the Belousov-Zhabotinsky reaction medium



and in simulations of simplified models ([94, 17, 60]).

The mechanisms by which external electric fields effect excitation and propagation via non-uniformity of the electric field, and the heterogeneity of the the tissue conductivities, has only been only been achieved in recent years. This investigation studies the implications of using resonant drift pacing as a method for low-energy defibrillation via these mechanisms.

In our simulations, resonant drift pacing eliminated re-entry, with high probability, at amplitudes much lower than single shock defibrillation. If we allow 10 s for low-energy re-entry termination the required shock strength with resonant drift pacing is 12 and 15 times smaller than with a single shock, respectively for the meandering and stationary-rotating patterns. Our data suggests that microscopic fluctuations of the intracellular conductivity do not effect the outcome of resonant drift pacing. However, the success depends on a number of details, which these numerical experiments help to uncover, *e.g.* mutual location of the stimulating and registering electrodes. It appears that “line” registration electrodes work better than “point” electrodes.

In our simulations, the drift tended to be towards the point registration electrode, or along the line registration electrode. A delay between triggering the registration electrode and the shock delivery changes the drift direction. So the choice of the location of the registration electrode and the delay in the feedback can be used to select a desirable direction. This idea has already been explained theoretically and tested in an isotropic model [16, 18], however our data shows that the direction of drift can be controlled using a delay in a realistically anisotropic bidomain model.

We demonstrated that the intensity of the intracellular conductivity fluctuations actually makes little difference to the outcome of resonant drift pacing.

The direction of drift may play a pivotal role in low-energy defibrillation. *E.g.* in a whole ventricle, a drift towards the apex would be desirable because a drift in the circumferential direction could be without ever reaching an inexcitable obstacle. We investigate resonant drift pacing with a whole ventricle model in Chapter 6.

Difficulties occurred due to new wavefronts being initiated from the shock electrodes. For resonant drift pacing to be most effective we would like to alleviate this difficulty (initiation of excitation waves has been theoretically discussed for a one-dimensional problem [38, 39] but further work would be required before applying it

to this complex 2D model). However, our numerical experiments allow a detailed insight into this problem and they can be used as a tool to suggest solutions, *e.g.* by adjusting the time delay.

## Chapter 4

# Control of scroll wave turbulence using resonant drift

Alonso *et al.* [7] considered the effect of applying a periodic *non-resonant* forcing on scroll wave turbulence. By numerical simulations of Barkley’s model they showed that periodic modulation of the medium’s excitability, with constant frequency higher than the frequency of the scroll waves, can control the turbulence in the medium. They went on to propose a theory of this effect based on the kinematic description of the scroll waves [8]. Their interpretation is that faster-than-resonant stimulation can effectively change the filament tension from negative to positive, thus disrupting the mechanism supporting the multiplication of scroll filaments and compelling them to collapse.

However, to our knowledge, the possibility of eliminating scroll turbulence by *resonant* stimulation has not been investigated so far. This was the task set for the study presented in this chapter.

Uniform modulation of the medium’s excitability is easily achievable in the light-sensitive BZ reaction, though it may be not practical in cardiac tissue. In this study we compare suppression of the scroll wave turbulence using

- (1) modulation of the medium’s excitability, as used by Alonso *et al.* in [7, 6],
- (2) an “applied transmembrane current” forcing, as in [18].

Keeping in mind single shock cardiac defibrillation used in clinical practice, we also compare repetitive forcing of constant and feedback controlled frequencies to a single pulse.

Our results show that resonant perturbation ensures the quickest termination of the scroll wave turbulence. Feedback controlled perturbation is as effective as constant frequency resonant perturbation, but offers the advantage of not having to know the correct frequency *a priori*. The resonant and feedback-controlled forcing suppress the 3D turbulence using amplitudes one order of magnitude lower than that of a single pulse currently used in clinical practice to terminate fibrillation.

## 4.1 Methodology

### 4.1.1 Governing equations

The 3D numerical simulations presented here were performed using the Barkley model of excitable media [10, 27]. We introduced this model in section 2.6 but repeat the equations here for the readers' convenience,

$$\begin{aligned} u_t &= \frac{1}{\varepsilon} u(1-u) \left( u - \frac{v+b(t)}{a} \right) + \nabla^2 u + h(t), \\ v_t &= u - v, \end{aligned}$$

where  $\varepsilon$  is a small parameter,  $\varepsilon \ll 1$ , characterising mutual time scales of the fast  $u$  and slow  $v$  variables, and  $a$  and  $b$  specify the kinetic properties of the system. Parameter  $b$  determines the excitation threshold and thus controls the excitability of the medium. The term  $h(t)$  represents an “applied transmembrane current” and corresponds to the activating function in the bidomain model.

An explanation of the parameters used in the simulations of Barkley's model is given in Section 4.1.2 and a summary is given in Table 4.1

### 4.1.2 Numerical methods

For numerical simulations we used EZscroll software [11] by Barkley *et al.* [10, 27] modified appropriately to describe the stimulation. We used a 19-points finite difference approximation of the Laplacian with equal discretisation steps  $\Delta x$  in all three spatial directions, and an implicit first order Euler time stepping with a time step  $\Delta t$ . Simulations were run in a box  $(x, y, z) \in [0, L]^3$  with Neumann boundary conditions. In most simulations, we used  $\Delta x = 2/3$ ,  $\Delta t = 1/30$  and  $L = 60$ .

In all simulations the model parameters were chosen as  $a = 1.1$ ,  $b = 0.19$  (or the average value of  $b(t)$  when it varied), and  $\varepsilon = 0.02$ , as in [7]. At this set of parameters scroll waves will have negative filament tension.

The choice of parameters was the same as in [7] to allow comparison, with the exception of the discretisation steps. We used cruder discretisation steps which allowed us to perform more simulations within reasonable CPU time. We also performed selected control simulations with  $\Delta x = 0.4$ ,  $\Delta t = 0.01$  and  $L = 60$ , as in [7]; the results were quantitatively somewhat different but qualitatively similar (see section 4.1.4 for details).

Quantity	Value
Small parameter	$\varepsilon = 0.02$
Parameter $a$	$a = 1.1$
Parameter $b$	$b = 0.19$
Space discretisation step	$\Delta x = 2/3$
Time discretisation step	$\Delta t = 1/30$
Box size	$(x, y, z) \in [0, L]^3$ , $L = 60$

Table 4.1: Summary of numerical parameters for Chapter 4

### 4.1.3 Generation of turbulence

The development of scroll wave turbulence is presented in Fig. 4.1. Starting at  $t = 0$  with the standard EZscroll scroll ring initial conditions in an unperturbed medium, the negative tension of the initial scroll ring caused elongation and bending of the filament. Interaction with the boundaries caused the filament to fragment and soon a complex tangle of many filaments filling the volume was observed.

The turbulent state of the system was saved at five different times  $t = 240, 245, 250, 255, 260$ , and then each state used as an initial condition in our simulations.

### 4.1.4 Resonant frequency

There are different ways to define resonance between the forcing and the turbulence it is aimed to control. We considered three different frequencies to which the forcing frequency can be compared:

- The rotation frequency of an unforced scroll around its filament  $\omega_0$ . It is also the frequency of a 2D spiral wave in a large enough medium.
- The mean frequency of the unforced turbulence  $\bar{\omega}_0$ . It is different from  $\omega_0$  due to interaction of scrolls with each other and with boundaries. This difference

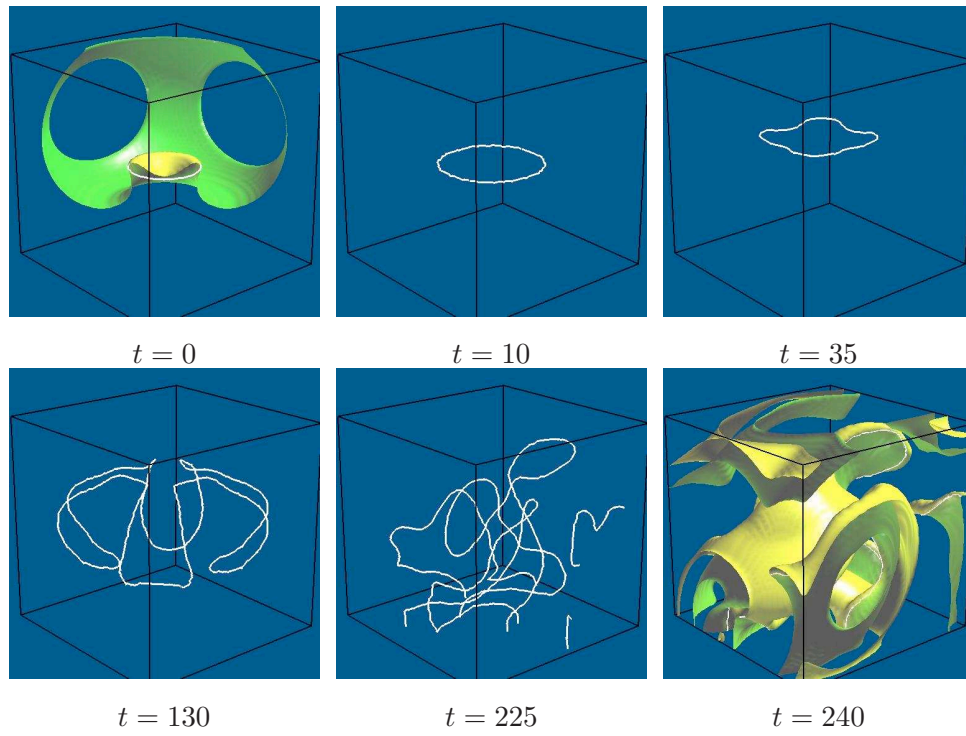


Figure 4.1: Development of scroll wave turbulence from an initial scroll ring. The white lines show the filaments of the scroll waves.

can be significant as this interaction is the only factor that stops the filaments' growth in length and number.

- The mean frequency of the forced turbulence  $\tilde{\omega}_0(A, \Omega)$ , which depends on the forcing amplitude  $A$ , and the forcing frequency  $\Omega$  (see Fig. 4.2(a,b)). By definition,  $\tilde{\omega}_0(0, \Omega) = \bar{\omega}_0$  for any  $\Omega$ . The difference between  $\tilde{\omega}_0$  and  $\bar{\omega}_0$  is less obvious from the theoretical viewpoint than the difference between  $\bar{\omega}_0$  and  $\omega_0$ , as the theory of resonant drift of the scroll wave turbulence is yet to be developed. Yet we suppose that it is  $\tilde{\omega}_0$  that is to be compared to the forcing frequency to determine resonance, since it represents the *de facto* state of the controlled system regardless of the detailed mechanisms that brought it into that state.

The frequency  $\omega_0$  was measured for a single straight scroll. The frequencies  $\bar{\omega}_0$  and  $\tilde{\omega}_0(A, \Omega)$  were both measured by recording the intervals  $T_j$  between the moments  $t_j^r$  in which wavefronts passed through a recording point  $(x_r, y_r, z_r)$ ,

$$T_j = t_{j+1}^r - t_j^r.$$

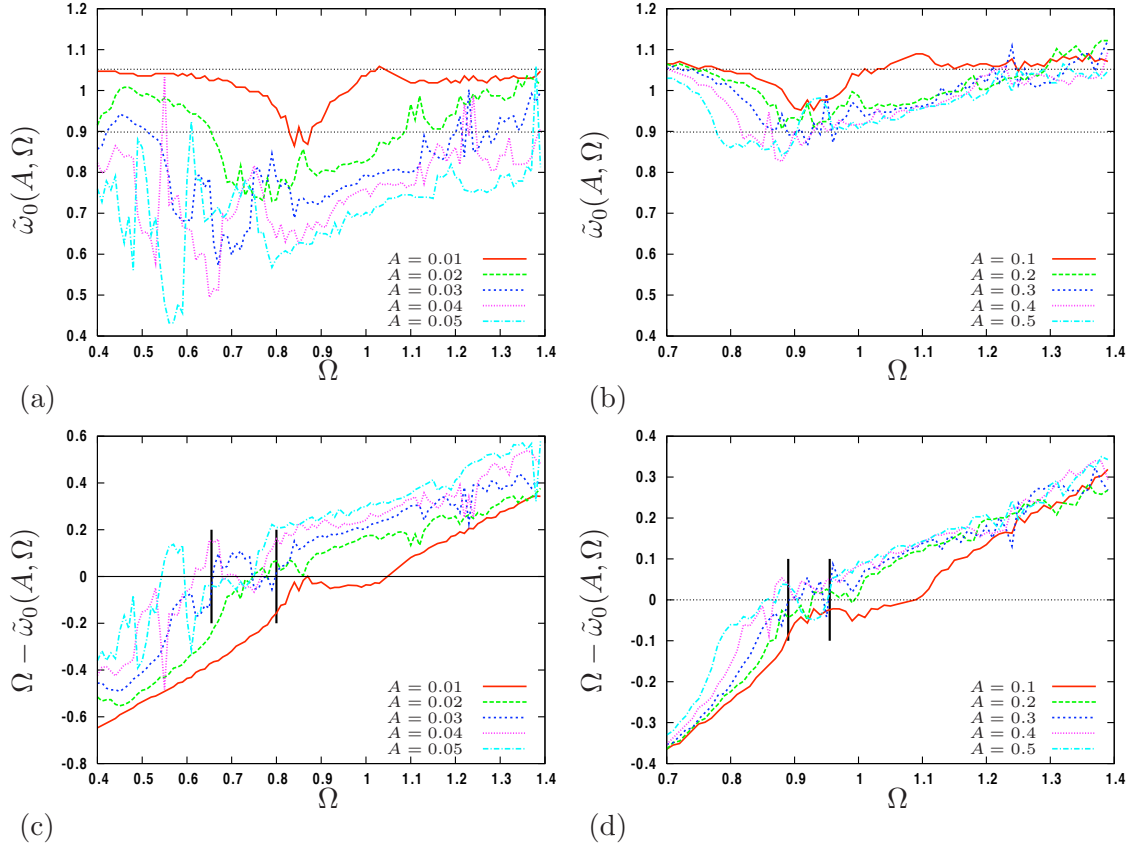


Figure 4.2: The mean frequency  $\tilde{\omega}_0(A, \Omega)$  of the perturbed turbulence (measured at the point  $(x_r, y_r, z_r) = (0, 0, 0)$ ), against forcing frequency  $\Omega$  at different forcing amplitudes  $A$  due to (a) modulation of the medium's excitability and (b) applied transmembrane current forcing. In (a) and (b) the line  $\tilde{\omega}_0 = 1.05$  is the mean frequency of the unperturbed turbulence, and the line  $\omega_0 = 0.9$  is the frequency of the single scroll. The **resonant windows** can be seen from the deviation of the mean frequency  $\tilde{\omega}_0(A, \Omega)$  from the forcing frequency  $\Omega$  due to (c) modulation of excitability and (d) applied current forcing. In (c) and (d) the line  $\Omega - \tilde{\omega}_0(A, \Omega) = 0$  is drawn to highlight the resonant windows. The vertical brackets illustrate the corresponding resonant windows at forcing amplitude  $A = 0.03$  for (c) and  $A = 0.3$  for (d).

The mean frequency for the entire simulation was then calculated as the average,

$$\tilde{\omega}_0 = \frac{2\pi N}{\sum_{j=1}^N T_j},$$

for all  $N$  intervals recorded, and similarly for  $\bar{\omega}_0$ . For  $\bar{\omega}_0$  the simulation was run for  $t \in [0, 5000]$ . For  $\tilde{\omega}_0(A, \Omega)$  the simulation was run for  $t \in [0, 5000]$  or until all scrolls were terminated if it happened sooner.

For our crude discretisation steps  $\Delta x = 2/3$ ,  $\Delta t = 1/30$  and  $L = 40$ , when modulating the medium's excitability we have observed  $\omega_0 = 0.90$ ,  $\bar{\omega}_0 = 1.05$  and  $\tilde{\omega}_0(0.03, \omega_0) = 0.74$ . The finer discretisation steps  $\Delta x = 0.40$ ,  $\Delta t = 0.01$  and  $L = 60$  produced  $\omega_0 = 1.20$ ,  $\bar{\omega}_0 = 1.27$  and  $\tilde{\omega}_0(0.03, \omega_0) = 1.01$ . That is, the cruder discretisation slows down the scroll waves overall, compared to the finer discretisation, but the relationship between the key frequencies remains similar.

#### 4.1.5 Forcing

We investigated the application of the following types of forcing on scroll wave turbulence;

1. Modulation of the medium's excitability, *i.e.* variation of parameter  $b(t)$  around its average value  $b_0$ .
  - (a) Repetitive stimulation
    - i. Constant frequency
2. Applied transmembrane current,  $h(t)$ 
  - (a) Single pulse
  - (b) Repetitive stimulation
    - i. Constant frequency
    - ii. Feedback controlled

#### Modulation of the medium's excitability

The medium's excitability in the model is defined by parameter  $b$ . Following [7, 8], we introduced into the model a spatially-uniform forcing by applying a periodic modulation of the parameter  $b$  in time, while keeping the applied current term zero,

$$b(t) = b_0 + A \cos(\Omega t), \quad h(t) = 0, \quad (4.1)$$



where  $b_0 = 0.19$ ,  $A$  is the forcing amplitude, and  $\Omega$  is the forcing frequency. Since  $b$  determines the excitation threshold, varying its value will vary the excitability of the medium.

Starting from the five different turbulent initial conditions, the simulations were performed at different values of  $A$  and  $\Omega$ , and the time taken for elimination of the turbulence was recorded. If any scrolls remained after  $t = 5000$  then the experiment was stopped and considered to have failed to eliminate the turbulence.

### Applied transmembrane current

Here, simulations were performed with

$$b(t) = b_0 = 0.19, \quad h(t) \neq 0.$$

**(a) Single pulse.** Simulations were started from the saved initial conditions at  $t = t_0$  and a single rectangular monophasic pulse of time duration  $\Delta = 0.3$  was applied,

$$h(t) = A \Theta(t - t_0) \Theta(t_0 + \Delta - t),$$

where  $\Theta()$  is the Heaviside step function. After the shock, evolution of the filaments was observed for a further 250 units of time. If no filaments remained at the end of this period, the shock was considered to be a success, and otherwise it was deemed to be unsuccessful.

Shocks of different amplitudes  $A$  were tested, and the success threshold was defined as the amplitude which gives a 50% success rate over the five initial conditions used.

**(b) Repetitive stimulation.** The stimulus  $h(t)$  was set to be a repetitive series of rectangular monophasic pulses of amplitude  $A$  and duration  $\Delta = 0.3$ ,

$$h(t) = A \sum_{j=1}^N \Theta(t - t_j^s) \Theta(t_j^s + \Delta - t).$$

We studied the effect of repetitive stimulation with both constant and feedback-controlled frequencies.

i. **Constant frequency**

Simulations were started from the saved initial conditions at  $t = t_0$ , and periodic pulses were applied at times  $t_j^s$  where

$$t_j^s = t_0 + j \frac{2\pi}{\Omega},$$

for  $j = 0, 1, 2, \dots$ . Experiments were repeated for different forcing frequencies  $\Omega$  and amplitudes  $A$ , and the time taken to eliminate the turbulence in each experiment was recorded. If any scrolls remained after  $t = 5000$  then the experiment was stopped and considered to have failed to eliminate the turbulence.

ii. **Feedback controlled**

The stimulus  $h(t)$  was set to be a repetitive series of rectangular pulses with timings  $t_j^s$  determined by taking feedback from the turbulence itself. Feedback is taken from a recording point  $(x_r, y_r, z_r)$  so that a pulse is applied every time that a wave passes through this point. That is, subject to the following conditions

$$u(x_r, y_r, z_r, t_{j-1}^r) = 0 \quad \text{and} \quad u(x_r, y_r, z_r, t_j^r) > 0,$$

a shock is applied at time  $t_j^s$  where

$$t_j^s = t_j^r + t_{\text{delay}}.$$

We also investigated the effect of different time delays  $t_{\text{delay}}$  for applying a pulse after a wavefront has passed through the recording point. Delays ranging from  $t_{\text{delay}} = 0.0$  to  $t_{\text{delay}} = 6.0$  were used, with increments of 0.1.

Different locations were used for the recording point (see Fig. 4.3):

- in the **corner** of the domain,  $(x_r, y_r, z_r) = (0, 0, 0)$ ,
- in the **center** of the domain,  $(x_r, y_r, z_r) = (L/2, L/2, L/2)$ ,
- in the center of a **face** of the domain,  $(x_r, y_r, z_r) = (L/2, L/2, 0)$ ,
- in the center of an **edge** of the domain,  $(x_r, y_r, z_r) = (L/2, 0, 0)$ .

Experiments were repeated for different locations for the recording point, different values of time delay  $t_{\text{delay}}$ , and amplitude  $A$  and the time taken for the elimination of the turbulence recorded. If any scrolls remained after  $t = 5000$  time steps then the experiment was stopped and considered to have failed to eliminate the turbulence.

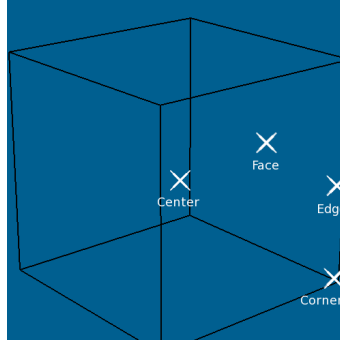


Figure 4.3: Different locations for the recording point.

## 4.2 Results

### 4.2.1 Elimination of the turbulence

Fig. 4.4 illustrates the main result of our study: a resonant stimulation can eliminate scroll wave turbulence, and does it quicker and more reliably than a non-resonant stimulation. The figure shows evolution of the turbulence due to modulation of the medium’s excitability at three different forcing frequencies at a fixed amplitude. The forcing frequency  $\Omega = 0.8$  is within the “resonant window” (see below for a formal definition), and the turbulence is terminated quickly within  $t = 41$ . The forcing frequency  $\Omega = 1.22$  is above-resonant, and although the turbulence is terminated, it takes much longer,  $t = 2089$ . The forcing frequency  $\Omega = 1.13$  is also above the resonant window, and it leads to stabilisation of vortices’ in the center of the medium rather than their termination.

We note here that the mechanism of “taming” of scroll wave turbulence suggested by Alonso *et al.* [7, 8] is based on inversion of the filament tension from negative to positive. The sequence shown in Fig. 4.4(c) illustrates why this is *not* sufficient for defibrillation: the scroll filaments stabilise with a straight shape, which is consistent with their effective tension being positive, but it does *not* lead to their elimination.

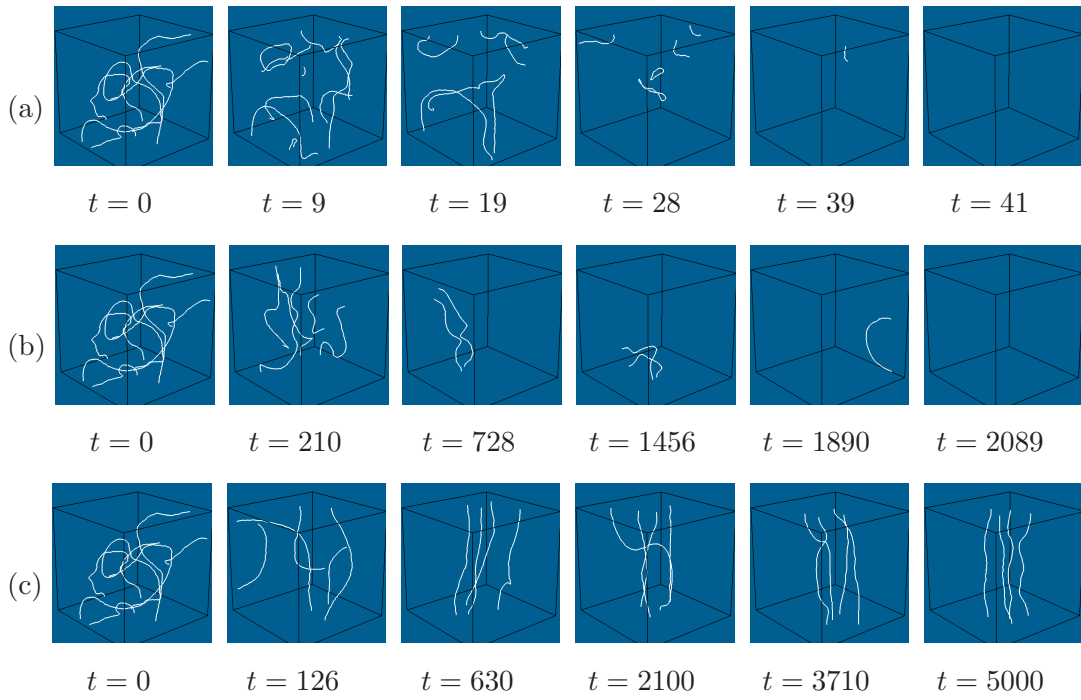


Figure 4.4: **Examples of successful and unsuccessful elimination of turbulence.** Evolution of the turbulence under modulation of medium excitability with (a)  $\Omega = 0.8$ , (b)  $\Omega = 1.22$ , (c)  $\Omega = 1.13$  at fixed amplitude  $A = 0.03$ .

In the following subsections, we analyse in more details the empirical conditions required for successful termination of the turbulence.

#### 4.2.2 Windows of resonant frequencies

For both the modulation of the medium's excitability and applied transmembrane current forcing, we have varied the frequency  $\Omega$  and amplitude  $A$  to assess their effects on termination of the turbulence. We observed very different effects of the modulation of excitability and of the applied current forcing on the mean frequency of the turbulence  $\tilde{\omega}_0(A, \Omega)$ . In this section we define a resonant window of frequencies for each amplitude and forcing type.

##### Modulation of excitability

As the amplitude of the modulation increases, the mean frequency of the turbulence  $\tilde{\omega}_0(A, \Omega)$  decreases dramatically (see Fig. 4.2(a)). When using the largest forcing amplitude ( $A = 0.05$ ), the frequency of the turbulence reduced to less than half that of the frequency of the unperturbed turbulence.

Resonant windows can be identified in Fig. 4.2(c). We define the resonant window

to be the range of forcing frequencies  $\Omega$ , for which  $\Omega \approx \tilde{\omega}_0(A, \Omega)$ . The upper and lower bounds for the resonant window can be seen as the first and last points where  $\Omega - \tilde{\omega}_0(A, \Omega) = 0$ . The resonant window is taken to be this range and a further 0.01 either side of this range.

There is a different resonant window for each amplitude. As the amplitude increases, the size of the resonant window increases and shifts towards lower forcing frequencies.

The above definition of the resonant window should be used with caution for the lowest amplitudes. E.g. for  $A = 0.01$  in Fig.4.2(c) the window must be between 0.873 and 1.045. However, most of this interval corresponds to a “false resonance”, when  $\Omega \approx \tilde{\omega}_0$  but that does not lead to termination. Termination of the turbulence at this forcing amplitude is observed in the narrow vicinity of  $\Omega = 0.873$  only. Applying a forcing with frequency in the vicinity of  $\Omega = 1.045$  maintains the turbulence.

### **Applied transmembrane current**

As the amplitude of the applied current forcing increases, the mean frequency of the turbulence  $\tilde{\omega}_0(A, \Omega)$  decreases. Even for the largest forcing amplitude  $A = 0.5$ , the reduction in the frequency of the turbulence due to the applied current forcing is not more than 20% of the frequency of the unperturbed turbulence.

Resonant windows for applied current forcing can be identified in Fig.4.2(d). The resonant windows were defined in the same way as in section 4.2.2. There is a different resonant window for each amplitude, although for all forcing amplitudes that we tested, the resonant windows are in the vicinity of the frequency of a straight scroll  $\omega_0 = 0.9$ .

For the lowest amplitude  $A = 0.1$  in Fig.4.2(d) there is no obvious resonant window. However, the resonant termination of the turbulence at this forcing amplitude is observed in the narrow vicinity of 0.870. The interval of frequencies above that and up until 1.09 corresponds to the “false resonance”.

### **Note on resonant windows**

Existence of resonant windows rather than unique resonant frequencies may be a purely statistical phenomenon due to fluctuations of frequencies of the scroll turbulence, or may be an indication that the forced turbulence adjusts its frequency in

response to the forcing. Nothing like this has been reported for resonant drift in 2D, thus we may be dealing with a specifically three-dimensional phenomenon. However, 3D scrolls have additional degrees of freedom compared to 2D spirals, *e.g.* twisted scrolls can rotate faster than straight scrolls [52]. This might offer an explanation of cases of false resonance, when formally defined resonant windows are abnormally extended towards higher frequencies but are not associated with fast and reliable termination, see *e.g.* the case of  $A = 0.01$  in Fig. 4.2(a,c) and Fig. 4.5(a). Indeed, in case of strong twist, different parts of the same filament have different phases and are forced in different directions, which does not result in an overall directed movement and does not bring about termination.

### 4.2.3 Termination times

#### Modulation of the medium's excitability

Fig. 4.5 presents the turbulence termination times due to modulation of the medium's excitability at five different forcing amplitudes. The vertical brackets show the windows of resonant frequencies for each amplitude, as in Fig. 4.2. From these data, it can be seen that termination of turbulence is fastest when the forcing frequency  $\Omega$  is within the resonant window. The turbulence can be terminated with a frequency outside of the resonant window. Although, further away from the resonant window, average termination time increases and the probability of success decreases.

Fig. 4.6 shows a plot of termination time against (a) fixed forcing amplitude  $A$ , and (b) untuning of the resonance  $\delta$  defined as

$$\delta = \frac{|\Omega - \tilde{\omega}_0(A, \Omega)|}{\sigma},$$

where  $\sigma$  is the standard deviation of the turbulence frequency recorded throughout a simulation,

$$\sigma = 2\pi \left( \frac{1}{N} \sum_{j=1}^N T_j^{-2} - \left( \frac{1}{N} \sum_{j=1}^N T_j^{-1} \right)^2 \right)^{1/2}.$$

The strength of resonance is a measure of how close the forcing frequency is to the frequency of the scroll wave turbulence.

It can be seen from Fig. 4.6(a) that increasing  $A$  reduces the termination time. The reduction is not very pronounced at larger  $A$ ; one should bear in mind here that the data in this graph are for *all* frequencies, resonant or not. Fig. 4.6(b)

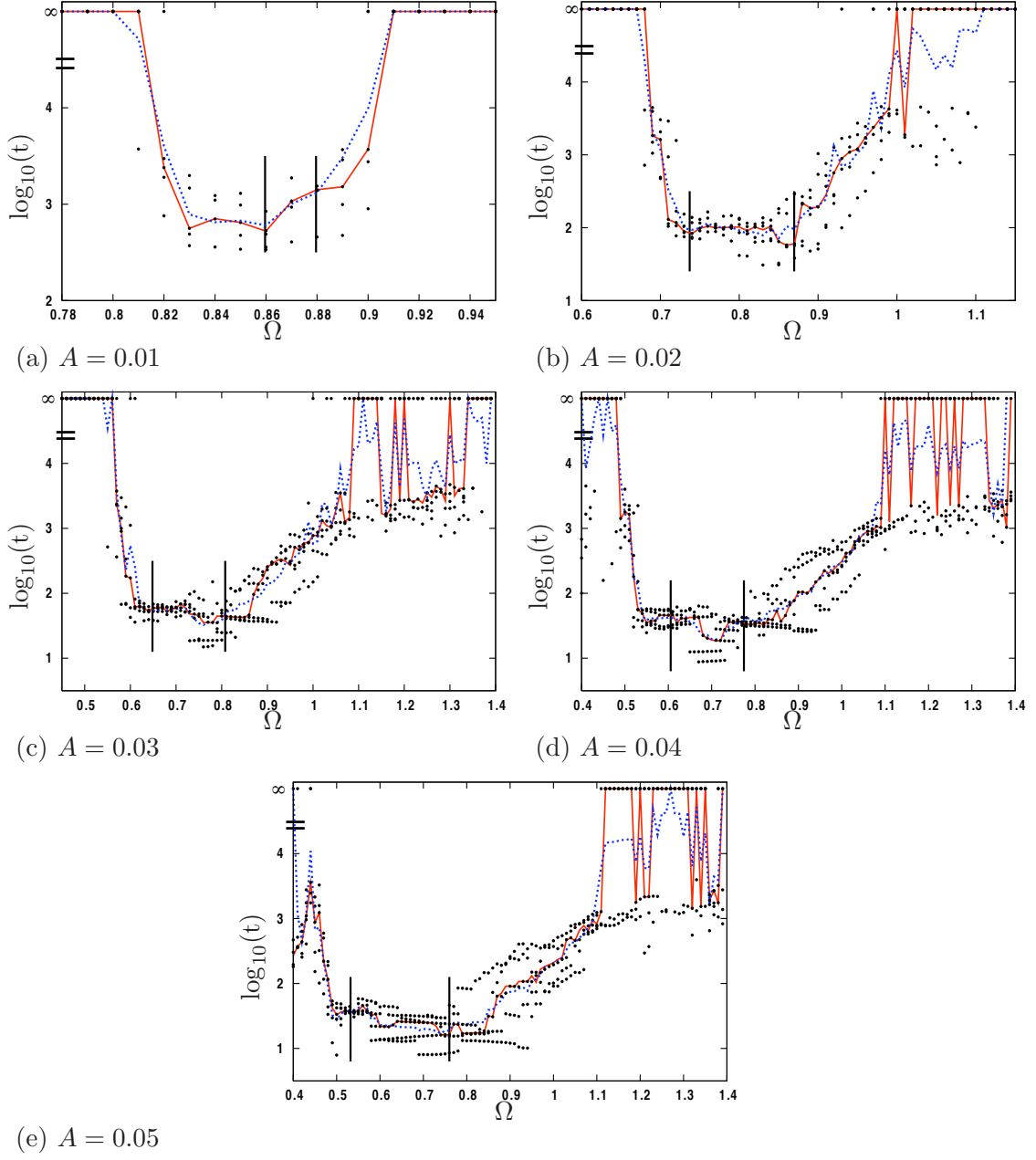


Figure 4.5: **Modulation of medium's excitability:** termination times at different amplitudes: (a)  $A = 0.01$ , (b)  $A = 0.02$ , (c)  $A = 0.03$ , (d)  $A = 0.04$ , and (e)  $A = 0.05$ . Black dots: termination times for individual simulations. Red solid line: median values of the termination times at every fixed frequency. Blue dashed line: same, mean values. For averaging and visualization purposes, we assign value  $t = 10^5$  to the failures. Black vertical brackets: the windows of resonant frequencies for each amplitude.

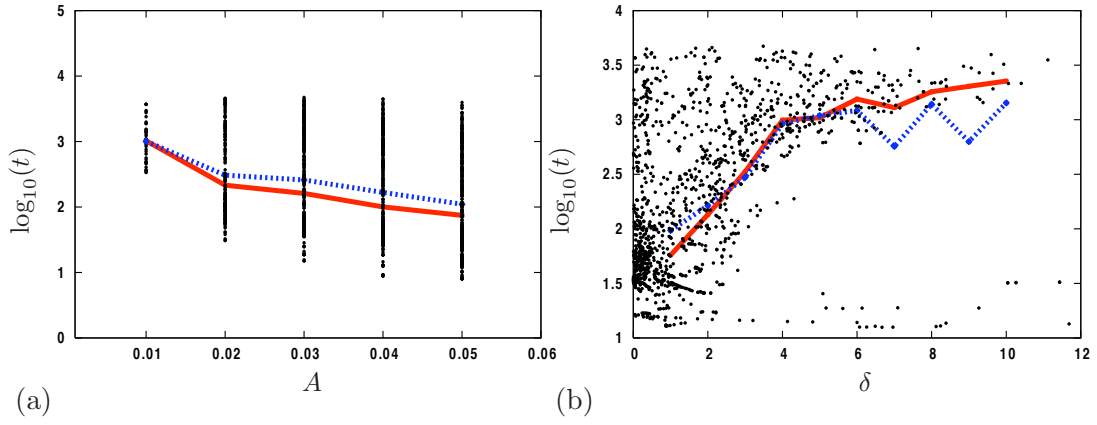


Figure 4.6: **Modulation of medium's excitability:** termination time against (a) fixed forcing amplitude  $A$ , (b) untuning of the resonance  $\delta$ . The dots represent termination times for individual simulations. The solid line goes through the median values of the termination times at either (a) or (b), and the dashed line through the geometric mean values.

shows that at smaller  $\delta$ , *i.e.* a better resonance, the time taken to eliminate the turbulence reduces. Here the data are for all forcing amplitudes, large and small. Comparing Fig. 4.6(a) and Fig. 4.6(b), and taking into account that reliable forcing amplitudes for the turbulence termination seems to be  $A \geq 0.02$ , termination times are more sensitive to the quality of resonance than to the forcing amplitude.

### Applied transmembrane current forcing

**(a) Single pulse.** The single pulse stimulation was tested having in mind the current clinical practice for cardiac defibrillation is by means of a single electric pulse of large amplitude. We defined the single pulse success threshold as the amplitude at which the turbulence is terminated in more than 50% of the experiments. In our setup, this success threshold was found to be  $A = 4.3$ . Fig. 4.7 shows an example of successful defibrillation with a single pulse shock at amplitude  $A = 4.3$ .

**(b) Repetitive pulses.** Fig. 4.8 presents the turbulence termination times, both for constant-frequency and feedback-controlled applied current forcing. The solid-line and dashed-line curves show the dependence of the termination times on the applied current forcing frequency  $\Omega$ , at fixed amplitude  $A = 0.3$ . The vertical brackets show the window of resonant frequencies as in Fig. 4.2(d). The dashed horizontal straight line shows the geometric mean termination time for the feedback controlled



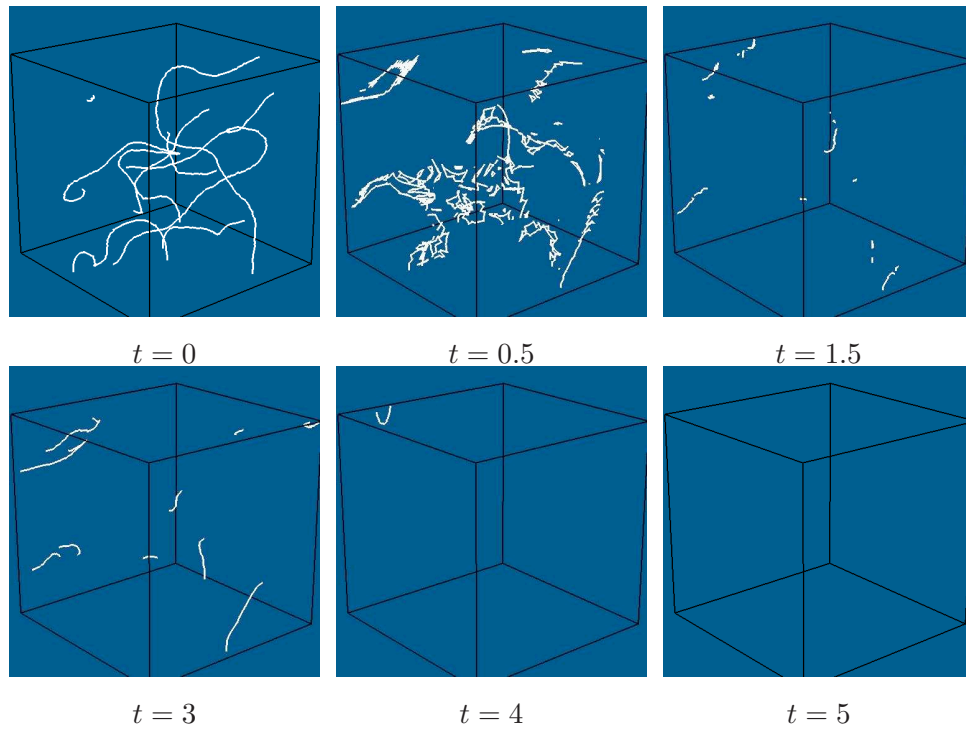


Figure 4.7: **Single pulse:** termination of the turbulence at forcing amplitude  $A = 4.3$ .

stimulation, and the solid horizontal line shows the corresponding median termination time. From these data, it can be seen that forcing frequencies within the resonant window ensure the fastest termination of turbulence. The turbulence can be terminated with a frequency outside of the resonant window but there the probability of the turbulence termination decreases. The individual experiments with failed termination are depicted as  $\log_{10}(\text{Time}) = \infty$ , and counted for the sake of averaging as  $\log_{10}(\text{Time}) = 5$ . Further away from resonant frequencies the turbulence termination time rapidly increases.

Figures 4.9 and 4.10 illustrates the effects of the stimulation amplitude  $A$ . The left panels in it are similar to Fig. 4.8 and present the turbulence termination time dependence on the applied current forcing frequency  $\Omega$ , at five different amplitudes  $A = 0.1, 0.2, 0.4, 0.5$ . The histograms on the right show the distributions of termination times for feedback controlled experiments, for the four different locations of the recording point. All the observations made for Fig. 4.8 are valid for the forcing amplitudes in figures 4.9 and 4.10.

For amplitudes  $A > 0.2$  in feedback controlled experiments, the average termination time is close to the average termination time achieved at resonant frequencies.

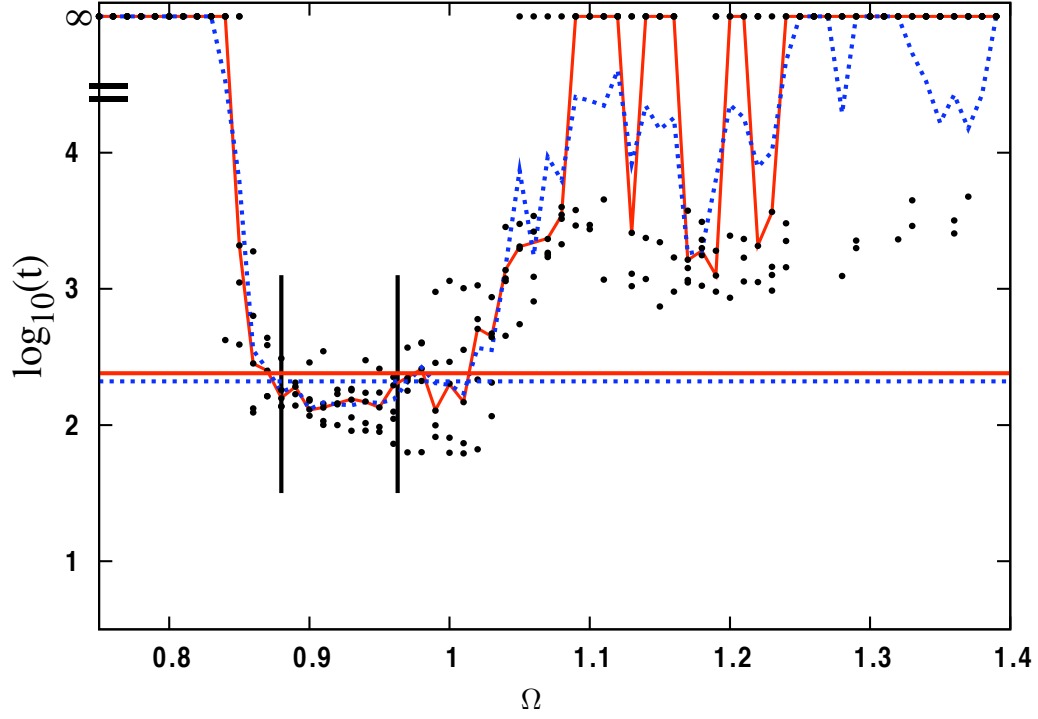


Figure 4.8: **Applied current forcing:** termination time for the amplitude  $A = 0.3$ . The black dots represent termination times for individual simulations. The red solid line goes through the median values of the termination times at a fixed frequency, and the blue dashed line through the geometric mean values. The horizontal straight lines show the median (red solid line) and geometric mean (blue dashed line) termination times for the feedback experiments. The vertical brackets designate the window of resonant frequency.

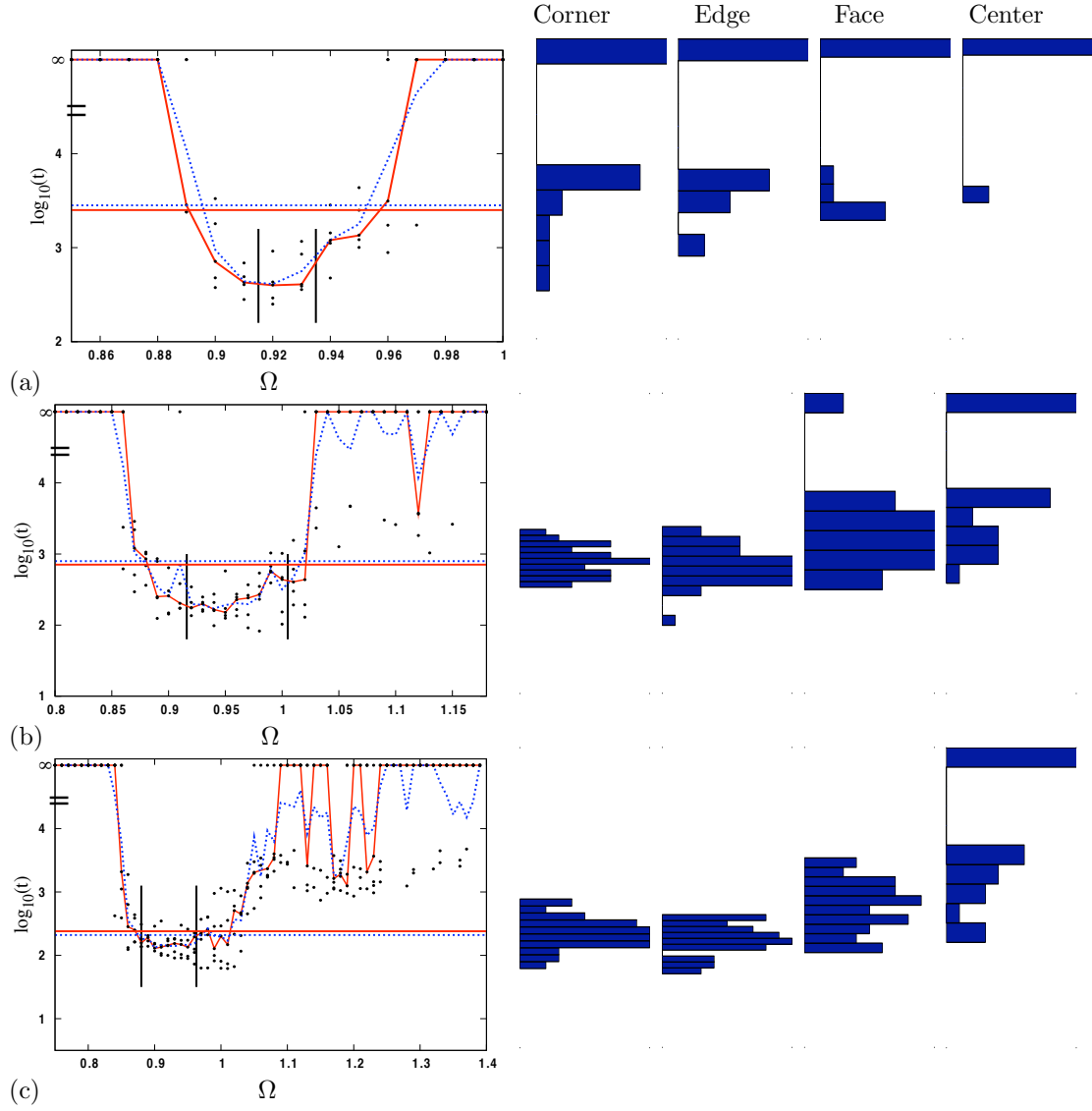


Figure 4.9: **Applied current forcing:** termination times for the amplitudes (a)  $A = 0.1$ , (b)  $A = 0.2$ , (c)  $A = 0.3$ . The left panels are as in Fig.4.8. The histograms on the right are distribution of termination times for feedback controlled experiments, at different locations for the recording point (they are rotated  $90^\circ$  clockwise and flipped in the vertical direction, to bring their abscissa axes in line with the ordinata axes of the graphs on the left).

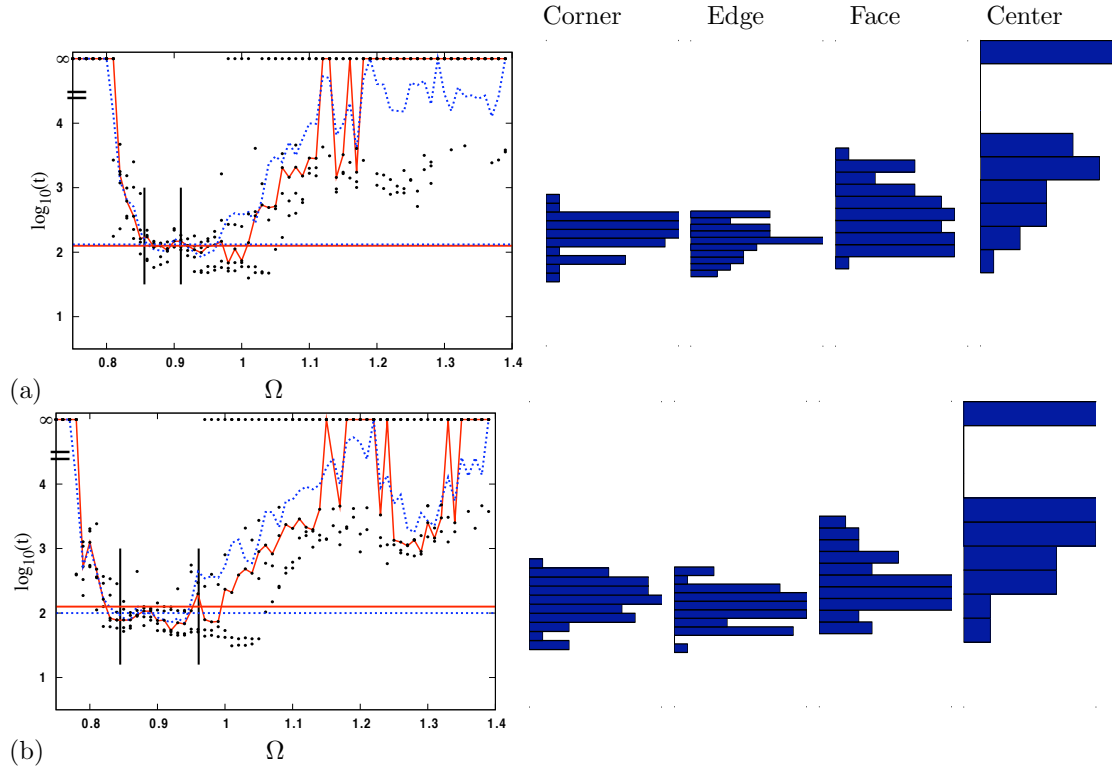


Figure 4.10: **Applied current forcing:** termination times (as in Fig. 4.9) for the amplitudes (a)  $A = 0.4$ , (b)  $A = 0.5$ .

For lower amplitudes, the success probability using feedback-controlled controlled stimulation falls down, in the same way as it does for the constant-frequency forcing.

The location of the recording point used for the feedback is also important for a successful termination. The most successful locations, in the 3D experiments, appear to be the corner or the edge of the medium. The center location for the recording point appears to be the worst for all forcing amplitudes tested.

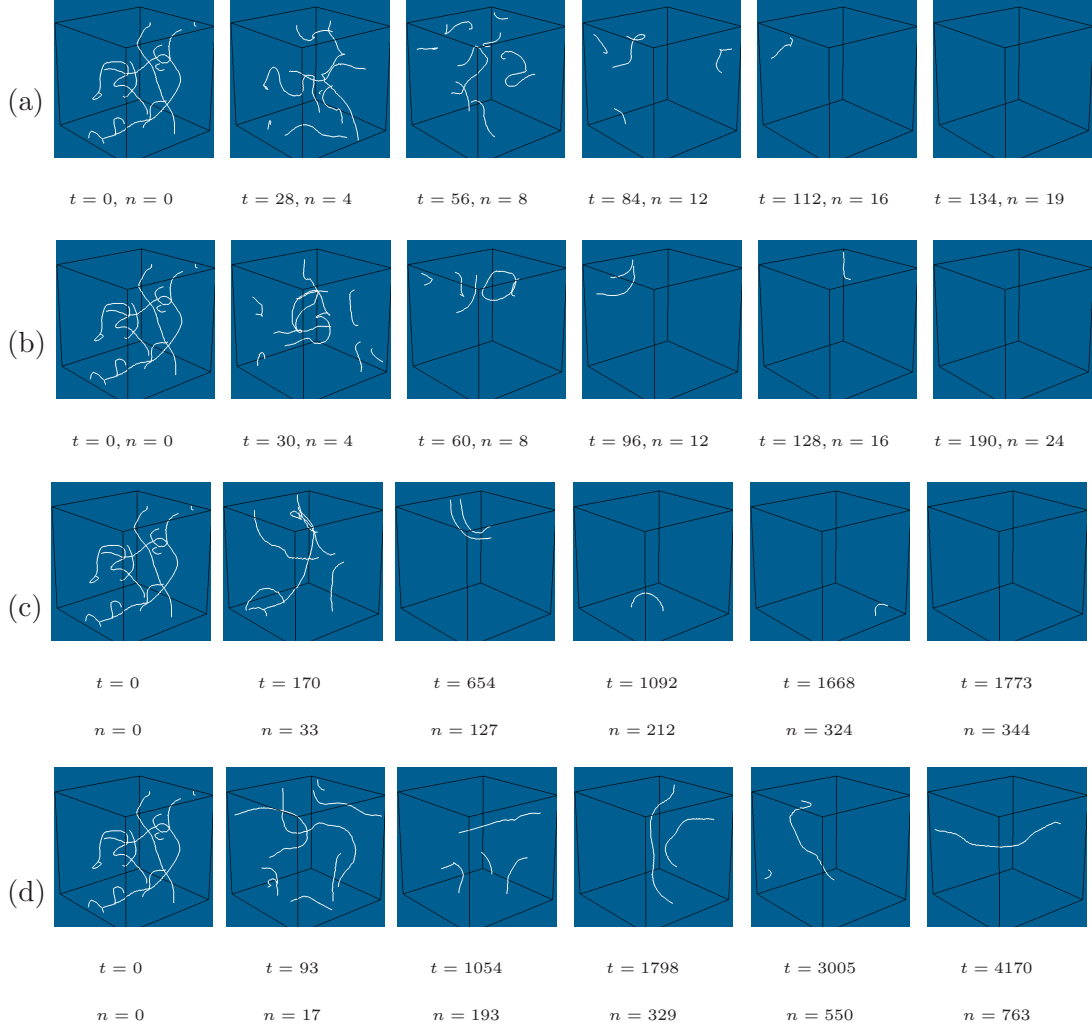


Figure 4.11: **Applied current forcing:** evolution of the turbulence using (a)  $\Omega = 0.9$  (b) feedback (c)  $\Omega = 1.22$  (d)  $\Omega = 1.15$  at fixed amplitude  $A = 0.3$ .

Fig. 4.11 shows evolution of the turbulence due to applied current forcing at different forcing frequencies  $\Omega = 0.9, 1.22, 1.15$ , and the feedback controlled, at the fixed amplitude  $A = 0.3$ . The forcing frequency  $\Omega = 0.9$  is within the resonant window, and the turbulence is terminated quickly by  $t = 134$  (series a). The feedback

controlled stimulation terminates the turbulence by  $t = 190$  (series b). The forcing frequency  $\Omega = 1.22$  is above-resonant, although the turbulence is terminated it takes ten times longer, to  $t = 1773$  (series c). The forcing frequency  $\Omega = 1.15$  is also above the resonant window. Simulation with that frequency leads to stabilisation of a filament in the center of the medium (series d), similar to what was observed for faster-than-resonant modulation of excitability, see Fig. 4.4(c).

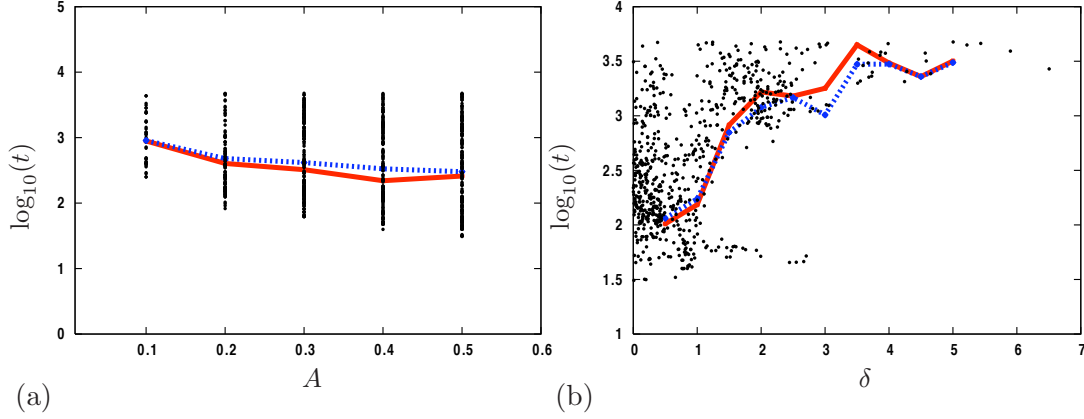


Figure 4.12: **Applied current forcing:** termination time against (a) fixed forcing amplitude  $A$ , (b) untuning of the resonance  $\delta$ . The dots represent termination times for individual simulations. The solid line goes through the median values of the termination times at either (a) or (b), and the dashed line through the geometric mean values.

Fig. 4.12 is similar to Fig. 4.6 and shows plots of termination time against (a) fixed forcing amplitude  $A$ , and (b) untuning of the resonance  $\delta$ , defined in the same way as for the modulation of excitability forcing. It can be seen from Fig. 4.12(a) that increasing the amplitude  $A$  reduces the termination time. Fig. 4.12(b) shows that reducing the untuning  $\delta$  also reduces the termination time. Comparing Fig. 4.12(a) and Fig. 4.12(b), and taking into account that reliable forcing amplitudes for the turbulence termination seems to be  $A \geq 0.2$ , termination times are more sensitive to the untuning of resonance  $\delta$  than to the change of forcing amplitude  $A$ .

#### 4.2.4 Resonant vs non-resonant stimulation

It has been previously shown [7] in Barkley's model with the same model parameters as we used here, that scroll wave turbulence can be controlled by a weak *non-resonant* modulation of the medium's excitability. A theory was presented in [8] explaining that this control of turbulence was due to an inversion of the filament tension from

negative to positive, which can happen if the frequency of forcing is higher than the frequency of the scrolls. It was argued that such stimulation causes the filaments to collapse and could therefore be used for termination of the scroll wave turbulence. We have seen, however, that positive tension may lead to stabilization rather than termination of scrolls, see Fig. 4.4(c) and 4.11(d).

In [7] an above-resonant frequency forcing was used to control the turbulence. More specifically, their forcing frequency  $\Omega$  was almost equal to (1% higher than) the frequency of a straight scroll,  $\omega_0$ . The frequency of a forced turbulence is significantly lower than the frequency of a straight scroll, *e.g.*  $\tilde{\omega}_0(A, \omega_0) < \omega_0$ , thus forcing with frequency  $\omega_0$  is above-resonant. This is true both for the finer discretisation steps used in [7] and cruder discretisation steps used in a majority of our simulations.

To make a specific comparison, let us consider excitability modulation with amplitude  $A = 0.03$  (same as in [7]) and frequency  $\Omega = 0.91$  which is about 1% higher than  $\omega_0$ . As can be seen from Fig. 4.5(c), such forcing gives a mean turbulence termination time of  $t = 251$  (compare with termination time  $t = 1510$  in the example shown in [7]). Within the resonant window for this amplitude as defined in this chapter, the mean termination time is between  $t = 71$  and  $t = 32$ , *i.e.* 3 to 7 times faster than using above-resonant forcing frequency as in [7].

So, a direct like-for-like comparison shows that although the above-resonant frequency stimulation suggested in [7] works in principle, the resonant stimulation works more reliably and much faster.

It has also been reported by Wu *et al.* [90] that using a travelling-wave modulation of the mediums excitability can control scroll wave turbulence faster than the modulation used by Alonso *et al.* [7]. Fig.6 in [90] clearly shows that the optimum forcing frequency is below the rotation frequency of an unforced scroll  $\omega_0$ . We have shown in our study that resonant windows can be defined as the deviation of the mean frequency  $\tilde{\omega}(A, \Omega)$  from the forcing frequency. If Wu *et al.* define resonant windows in the same way then the optimum forcing frequency for control using travelling-wave modulation would probably sit within a resonant window.

#### 4.2.5 Feedback controlled vs constant frequency stimulation

Typically, the average termination time using feedback is close to that achieved at resonant constant frequencies. At the lowest stimulation amplitudes, both feedback-

controlled and constant-frequency termination times increase, and the probability of success decreases.

For a range of frequencies within or near the resonant window, the termination was achieved, on average, quicker with constant frequency than with feedback. To elucidate a possible reason for this difference, we have considered a two-dimensional version of the Barkley model, with the same model parameters and applied the same feedback controlled forcing as in our 3D simulations. We have found that applying a forcing with feedback in this case causes the spiral wave to drift along a rather complicated “snaky” trajectory, shown in Fig. 4.13(a). This behaviour is similar to that described recently by Zykov *et al.* [95, 67], and is caused by an instability, related to the delay between a change of the position or phase of the spiral and its detection by the feedback electrode, due to the distance between them and a finite speed of the waves. Indeed, in Fig. 4.13 the spiral core is over one wavelength away from the recording point. It can be seen from Fig. 4.13(a) at  $t = 600$  that this resonantly drifting spiral does not terminate at the boundary. Instead, it embarks on a continuous loop near the recording point in the medium.

According to Zykov *et al.* this ‘snake instability’ should disappear at lower amplitudes. Indeed, this is what happened in our simulations, see Fig. 4.13(b,c). This result suggests that in some conditions, smaller stimulation amplitudes may achieve termination quicker than large amplitudes. In our present setting, however, further reduction of amplitude did not help termination. For  $A = 0.001$ , the spiral entered a continuous loop in the vicinity of the recording point. For  $A = 0.0001$ , when the spiral wave reached a boundary, it drifted along it faster than its resonant drift in the center of the domain. So, reducing the amplitude is not necessarily a satisfactory solution to the problem of the ‘snake instability’ interference with terminating the spiral wave. However, in known computer models and experimental observations, scroll waves are apparently rather large in the scale of the heart chambers and are typically no more than one wavelength away from a boundary. Thus the ‘snake instability’ may not be a problem in a real heart.

### 4.3 Summary

Our 3D experiments show that the termination with a feedback-controlled forcing is achievable even at relatively weak amplitudes (see Fig. 4.9 and Fig. 4.10).



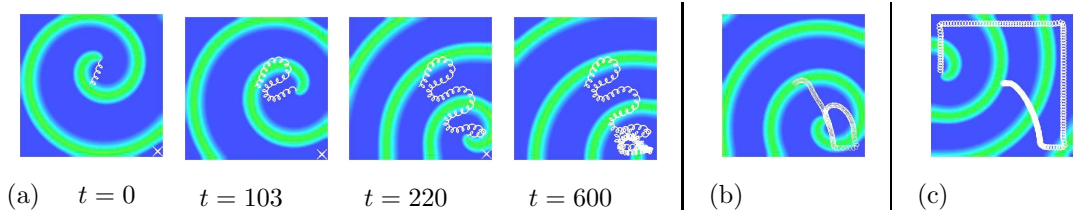


Figure 4.13: ‘**Snake instability**’: Applied current forcing with feedback controlled frequency applied with amplitude (a)  $A = 0.01$ , (b)  $A = 0.001$ , (c)  $A = 0.0001$  Model parameters  $a = 1.1$ ,  $b = 0.19$ ,  $\varepsilon = 0.02$  were used. The domain has dimensions  $L_x = L_y = 40$  with  $\Delta t = 0.0083$  and  $\Delta x = 1/3$ . The same numerical methods were employed as with our 3D simulations, with the exception of a nine-point finite difference scheme for the Laplacian. In all cases, the recording point was located in the bottom right corner.

We have found that the resonance between the forcing and the scrolls is characterised not by a single resonant frequency, but by a resonant window which depends on the type of forcing and its amplitude. For the modulation of the medium’s excitability, larger amplitudes corresponded to wider resonant windows, shifted towards lower forcing frequencies. For the applied transmembrane current forcing, the resonant windows did vary in size and location, but for the amplitudes that we tested they remained close to the frequency of a single straight scroll,  $\omega_0 \approx 0.9$ .

We have shown that termination of scroll wave turbulence can be achieved by repetitive stimulation. This is despite the fact that scroll waves continue to grow and multiply while we drive them to elimination. We have studied two different methods of forcing, the modulation of medium’s excitability and the applied transmembrane currents forcing. For a successful termination, the amplitude of the repetitive forcing should be higher than a certain threshold. However, this threshold is still much lower than that required for termination by a single shock. The termination is achieved with the highest probability, and in the quickest time, when using a resonant forcing frequency, *i.e.* when the frequency of stimulation,  $\Omega$ , is close to the *de facto* frequency of the forced scroll waves,  $\tilde{\omega}_0(A, \Omega)$ . Namely, we have shown that for both types of forcing, the turbulence termination becomes faster for smaller values of the untuning of the resonance  $\delta$  (see Fig. 4.6(b) and Fig. 4.12(b)).

Our results also show that the location of the recording point is important for a successful feedback-controlled termination, which is in good agreement with [60]. The most successful locations appear to be the corner or the edge of the medium.

The center location for the recording point appears to be the worst for all forcing amplitudes tested. It has been shown in 2D experiments [94] that a line of recording points is a robust approach. Therefore, if the same holds for 3D, a line of recording points down one edge of the medium may be the optimal choice.

## Chapter 5

# Theory of resonant drift in three-dimensions

The aim of this chapter is to derive equations of motion for a perturbed, general twisted non-planar scroll wave filament. This theory will build upon the previously published work by Keener [41] and Biktashev, Holden, and Zhang [19]. We apply the theory to the particular cases of a scroll ring and a helical scroll wave.

### 5.1 The theory of filament dynamics

We aim to study the behaviour of solutions of the perturbed three dimensional (3D) reaction diffusion system

$$\mathbf{u}_t = \mathbf{D}\Delta_3\mathbf{u} + \mathbf{f}(\mathbf{u}) + \mathbf{h}(t), \quad (5.1)$$

where  $\mathbf{u} = \mathbf{u}(x, y, z, t)$  is a vector function of time and space,  $\mathbf{D}$  is the diagonal matrix of diffusion coefficients,  $\mathbf{h}(t)$  is a time dependent perturbation, and  $\Delta_3\mathbf{u} = \mathbf{u}_{xx} + \mathbf{u}_{yy} + \mathbf{u}_{zz}$  is the Laplacian operator in 3D. I will refer to the coordinate system  $(x, y, z, t)$  as the *laboratory coordinate system*.

In this chapter subscripts denotes partial differentiation, unless otherwise specified.

An assumption we make on the properties of (5.1) is that when  $\mathbf{h}(t) = 0$  we have a two-dimensional solution in the form of a rigidly rotating spiral wave,

$$\hat{\mathbf{u}}(x, y, t) = \mathbf{V}(\hat{r}, \hat{\theta} - \omega t), \quad (5.2)$$

where  $\mathbf{V}$  is  $2\pi$ -periodic with respect to  $\hat{\theta}$  and the solution is asymptotically stable up to the natural invariance due to space and time homogeneity. Here  $\hat{r}$  and  $\hat{\theta}$  are polar coordinates in the laboratory coordinate system where  $x = \hat{r} \cos(\hat{\theta})$  and  $y = \hat{r} \sin(\hat{\theta})$ .

Scroll waves can be viewed as a slowly varying stacking of two dimensional spiral waves. At any moment in time we can view the 3D solutions of (5.1) as a scroll wave which is rotating around some slowly moving curve in three dimensional space. This curve is the filament of the scroll wave and is denoted by the position vector  $\mathbf{R}(s, t')$ . To describe the filament, we introduce a *filament coordinate system*  $(s, p, q, t')^T$  which co-moves with the filament (see Fig. 5.1), where;

$s$  is the arc-length coordinate along the filament,

$p$  is the coordinate along the normal vector  $\mathbf{N}$  at the point  $\mathbf{R}$ ,

$q$  is the coordinate along the binormal vector  $\mathbf{B}$  at the point  $\mathbf{R}$ ,

$t'$  is time in the filament coordinate system.

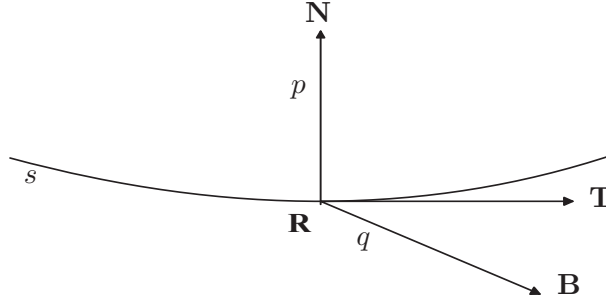


Figure 5.1: Normal  $\mathbf{N}$ , tangent  $\mathbf{T}$ , and binormal  $\mathbf{B}$  vectors to a point on a filament  $\mathbf{R}$ .

We denote the filament curvature by  $\kappa(s, t')$  (a measure of the deviation from a straight line) and its torsion by  $\tau(s, t')$  (a measure of the deviation from a plane).

3D solutions of (5.1) are assumed to be close to (5.2) in every cross section perpendicular to  $\mathbf{R}(s, t')$ . Define  $\mathbf{N}(s, t')$  as the normal vector to  $\mathbf{R}(s, t')$ ,  $\mathbf{T}(s, t')$  as the tangent vector, and  $\mathbf{B}(s, t')$  as the binormal vector ( $\mathbf{B}(s, t') = \mathbf{T}(s, t') \times \mathbf{N}(s, t')$ ). The following equations, called the *Frenet-Serret equations*, hold between the three vectors  $\mathbf{B}(s, t')$ ,  $\mathbf{T}(s, t')$  and  $\mathbf{N}(s, t')$  at fixed  $t'$ ,

$$\frac{\partial}{\partial s} \mathbf{R}(s, t') = \mathbf{T}(s, t') \quad (5.3)$$

$$\frac{\partial}{\partial s} \mathbf{T}(s, t') = \kappa(s, t') \mathbf{N}(s, t') \quad (5.4)$$

$$\frac{\partial}{\partial s} \mathbf{N}(s, t') = -\kappa(s, t') \mathbf{T}(s, t') + \tau(s, t') \mathbf{B}(s, t') \quad (5.5)$$

$$\frac{\partial}{\partial s} \mathbf{B}(s, t') = -\tau(s, t') \mathbf{N}(s, t') \quad (5.6)$$

Three-dimensional solutions to (5.1) are sought in the the filament coordinate system in the form

$$\mathbf{u}(s, p, q, t') = \mathbf{V}(r, \theta + \phi(s, t') - \omega t') + \mathbf{w}(s, p, q, t'), \quad (5.7)$$

here  $r, \theta$  are polar coordinates in the filament coordinate system ( $p = r \cos(\theta), q = r \sin(\theta)$ ),  $\mathbf{V}$  is the two-dimensional spiral wave solution given by (5.2),  $\phi(s, t')$  is the spiral rotation phase that varies slowly with  $s$  and  $t'$ , and  $\mathbf{w}(s, p, q, t')$  is a small correction term (due to perturbation) which we also assume to vary slowly with  $s$  and  $t'$ .

### 5.1.1 Change of coordinates to the filament frame of reference

To derive the equations of motion we first need to express (5.1) in terms of the filament coordinate system. Therefore we make the change of coordinates

$$(x, y, z, t) \rightarrow (s, p, q, t'),$$

where

$$\begin{aligned} t &= t', \\ \mathbf{X} &= (x, y, z)^T = \mathbf{R}(s, t') + p \mathbf{N}(s, t') + q \mathbf{B}(s, t'). \end{aligned}$$

In the filament system of coordinates the three dimensional Laplacian can be expressed as (see Appendix C.1 and [41])

$$\Delta_3 \alpha = H(H\alpha) - \frac{\kappa}{(1 - \kappa p)} \alpha_p + \alpha_{pp} + \alpha_{qq} \quad (5.8)$$

where the differential operator  $H$  is defined as

$$H\alpha = \frac{1}{(1 - \kappa p)} (\alpha_s - \tau \alpha_\theta).$$

This coordinate system is allowed to move with time, so we must make the following change of time derivatives

$$\alpha_t = \alpha_{t'} - \mathbf{T} \cdot \mathbf{X}_{t'} H\alpha - \mathbf{R}_{t'} \cdot (\mathbf{N}\alpha_p + \mathbf{B}\alpha_q) - \mathbf{B} \cdot \mathbf{N}_{t'}(\alpha_\theta) \quad (5.9)$$

### 5.1.2 Evolutionary equation for the scroll perturbation

The next step is to substitute (5.7) into (5.1), with the Laplacian and time derivative expressed in the filament coordinate system. Using (5.8) and (5.9), the following relations,

$\mathbf{u}_t(s, p, q, t')$	$= \mathbf{V}_t(r, \tilde{\theta}) + \mathbf{w}_t(s, p, q, t'),$
$f(\mathbf{u}(s, p, q, t'))$	$= f(\mathbf{V}(r, \tilde{\theta})) + \mathbf{F}(\mathbf{V}(r, \tilde{\theta}))\mathbf{w}(s, p, q, t') + \dots,$
$\Delta_3 \mathbf{u}(s, p, q, t')$	$= \Delta_3 \mathbf{V}(r, \tilde{\theta}) + \Delta_3 \mathbf{w}(s, p, q, t'),$
$\mathbf{h}(t)$	$= \mathbf{h}(t'),$
$\mathbf{V}_{t'}(r, \tilde{\theta} - \omega t')$	$= \mathbf{V}_{\tilde{\theta}}(r, \tilde{\theta}) \left( \phi_{t'}(s, t') - \omega \right),$
$H\mathbf{V}$	$= (\phi_s - \tau) \mathbf{V}_\theta,$
$H(H\mathbf{V})$	$= (\phi_s - \tau)_s \mathbf{V}_\theta + (\phi_s - \tau)^2 \mathbf{V}_{\theta\theta},$

where  $\tilde{\theta} = \theta + \phi(s, t') - \omega t'$  and  $\mathbf{F}(\mathbf{V}) = \frac{\partial}{\partial \mathbf{u}} f(\mathbf{V})$ , one can write the evolutionary equation for the scroll perturbation  $\mathbf{w}$ ,

$$L\mathbf{w} = G[\mathbf{V}, \mathbf{R}]. \quad (5.10)$$

The left hand side of (5.10) is

$$\begin{aligned} L\mathbf{w} = & \mathbf{w}_{t'} - (H\mathbf{w})\mathbf{T} \cdot \mathbf{X}_{t'} - \mathbf{R}_{t'} \cdot (\mathbf{N}\mathbf{w}_p + \mathbf{B}\mathbf{w}_q) - \mathbf{B} \cdot \mathbf{N}_{t'}(\mathbf{w}_\theta) \\ & - \mathbf{D}H(H\mathbf{w}) + \mathbf{D}\kappa\mathbf{w}_p - \mathbf{D}\mathbf{w}_{pp} - \mathbf{D}\mathbf{w}_{qq} - \mathbf{F}(\mathbf{V})\mathbf{w}, \end{aligned}$$

and the right hand side is

$$\begin{aligned} G[\mathbf{V}, \mathbf{R}] = & -\mathbf{V}_\theta \phi_{t'} + \mathbf{T} \cdot \mathbf{X}_{t'} (\phi_s - \tau) \mathbf{V}_\theta + \mathbf{R}_{t'} \cdot (\mathbf{N}\mathbf{V}_p + \mathbf{B}\mathbf{V}_q) + \mathbf{N}_{t'} \cdot \mathbf{B}\mathbf{V}_\theta \\ & + \mathbf{D}(\phi_{ss} - \tau_s) \mathbf{V}_\theta + \mathbf{D}(\phi_s - \tau)^2 \mathbf{V}_{\theta\theta} + \mathbf{D}\kappa\mathbf{V}_p + \mathbf{h}(t'). \end{aligned} \quad (5.11)$$

**Note:** To derive (5.11), since we assumed that 2D spiral wave solutions exist, we used the equation for the existence spiral wave (see Appendix C.2 and [18]),

$$\mathbf{D}(\mathbf{V}_{pp} + \mathbf{V}_{qq}) + \omega \mathbf{V}_\theta + \mathbf{f}(\mathbf{V}) = 0.$$

We also made the assumption that  $1 - \kappa p \approx 1$ . This was originally done by Keener [41] and can be explained by assuming that at any point in time,  $\kappa(s, t')$  is small. Therefore, in the vicinity of the scroll wave filament, the product  $\kappa p$  can be neglected.

By using the ansatz from [19] regarding the order of magnitude of the terms in (5.11), we introduce a small scaling parameter  $\epsilon$ , so that

$$\begin{aligned} \mathbf{R}(s, t) &= \epsilon^{-1} \hat{\mathbf{R}}(\epsilon s, \epsilon^2 t), \\ \phi(s, t) &= \hat{\phi}(\epsilon s, \epsilon^2 t). \end{aligned}$$

This means that variation in time is of order  $\epsilon^2$ , and variation in space is of order  $\epsilon$ . One can see (Appendix C.3) that  $\mathbf{w}, \kappa, \tau, \mathbf{R}_t, \mathbf{N}_t, \mathbf{B}_t$ , and  $\mathbf{T}_t$  have order  $\epsilon$  and all other terms have order  $\epsilon^2$ . Therefore,  $L\mathbf{w}$  can be separated into two parts  $L\mathbf{w} = L_0\mathbf{w} + L_1\mathbf{w}$ , where  $L_0\mathbf{w}$  is of the order  $\epsilon$  and  $L_1\mathbf{w}$  is of the order  $\epsilon^2$ . Neglecting  $L_1\mathbf{w}$  yields

$$L\mathbf{w} = \mathbf{w}_{t'} - \mathbf{D}\mathbf{w}_{pp} - \mathbf{D}\mathbf{w}_{qq} - \mathbf{F}(\mathbf{V})\mathbf{w},$$

where the linear operator  $L$  is

$$L\alpha = \alpha_{t'} - \mathbf{D}\Delta_2\alpha - \mathbf{F}(\mathbf{V})\alpha, \quad (5.12)$$

which has eigenfunctions  $\mathbf{V}_p = \frac{\partial \mathbf{V}}{\partial p}$ ,  $\mathbf{V}_q = \frac{\partial \mathbf{V}}{\partial q}$ , and  $\mathbf{V}_\theta = \frac{\partial \mathbf{V}}{\partial \theta}$  each with eigenvalue 0 (see Appendix C.4). Note that in (5.12) we have a two-dimensional Laplacian  $\Delta_2$ . This is due to the fact that the second derivative in  $s$  has order  $\epsilon^2$  and so we neglect it, thus moving from  $\Delta_3$  to  $\Delta_2$ . It should also be noted, that after dropping the  $s$  derivative the problem depends only on  $p$  and  $q$ , with  $s$  now appearing as a parameter.

### 5.1.3 The equations of motion

Assume that all time dependent variables in  $G[\mathbf{V}, \mathbf{R}]$ , except  $\mathbf{V}$ , vary slowly in time and  $\mathbf{V}$  is approximately periodic. Then  $G[\mathbf{V}, \mathbf{R}]$  can be considered to be approximately periodic within any time interval much shorter than  $\epsilon^{-1}$ . Similarly, we must assume that  $\mathbf{w}(s, p, q, t')$  is approximately periodic. We can then consider a periodic problem and proceed to find periodic solutions.

The *Fredholm Alternative* [32] says that periodic in time solutions  $\mathbf{w}$  to (5.10) exist if  $G[\mathbf{V}, \mathbf{R}]$  is orthogonal to the null space of the adjoint operator  $L^+$ , defined with respect to the natural inner product involving integration over the time period (as in [41]),

$$\langle m(r, \theta, t), n(r, \theta, t) \rangle = \int_{t-\frac{\pi}{\omega}}^{t+\frac{\pi}{\omega}} d\eta \oint d\theta \int_0^\infty r dr (m(r, \theta, \eta) \cdot n(r, \theta, \eta)), \quad (5.13)$$

where

$$(m(r, \theta, \eta) \cdot n(r, \theta, \eta)) = \sum_{i=0}^j \bar{m}_i n_i. \quad (5.14)$$

The adjoint operator of (5.12),  $L^+$ , can be written as

$$L^+ \alpha = -\alpha_{t'} - \mathbf{D}^T \Delta_2 \alpha - \mathbf{F}^T(\mathbf{V}) \alpha. \quad (5.15)$$

We assume that there are three linearly independent eigenfunctions  $\mathbf{Y}_p$ ,  $\mathbf{Y}_q$ , and  $\mathbf{Y}_\theta$  (where the subscripts on  $\mathbf{Y}$  do not denote partial differentiation) that span the null space of the adjoint operator  $L^+$ . These functions are normalised so that

$$\langle \mathbf{Y}_i, \mathbf{V}_j \rangle = \delta_{ij}, \quad (5.16)$$

where  $\delta_{ij}$  is the Kronecker delta symbol, and  $i, j = p, q, \theta$ .

With respect to our problem, the Fredholm Theorem says that (5.10) has a solution if and only if  $\langle \mathbf{Y}_i, G[\mathbf{V}, \mathbf{R}] \rangle = 0$  for  $i = p, q, \theta$ ,



$$\begin{aligned}
\langle \mathbf{Y}_i, G \rangle &= 0 \\
&= -\langle \mathbf{Y}_i, (\phi_{t'}) \mathbf{V}_\theta \rangle + \langle \mathbf{Y}_i, \mathbf{X}_{t'} \cdot \mathbf{T}(\phi_s - \tau) \mathbf{V}_\theta \rangle + \langle \mathbf{Y}_i, \mathbf{R}_{t'} \cdot \mathbf{N} \mathbf{V}_p \rangle \\
&\quad + \langle \mathbf{Y}_i, \mathbf{R}_{t'} \cdot \mathbf{B} \mathbf{V}_q \rangle + \langle \mathbf{Y}_i, \mathbf{N}_{t'} \cdot \mathbf{B} \mathbf{V}_\theta \rangle + \langle \mathbf{Y}_i, \mathbf{D}(\phi_{ss} - \tau_s) \mathbf{V}_\theta \rangle \\
&\quad + \langle \mathbf{Y}_i, \mathbf{D}(\phi_s - \tau)^2 \mathbf{V}_{\theta\theta} \rangle - \langle \mathbf{Y}_i, \mathbf{D}\kappa \mathbf{V}_p \rangle + \langle \mathbf{Y}_i, \mathbf{h}(t') \rangle \quad (5.17)
\end{aligned}$$

From (5.17) we can derive the following motion equations

$$\begin{aligned}
\phi_{t'} &= \mathbf{N}_{t'} \cdot \mathbf{B} + \mathbf{R}_{t'} \cdot \mathbf{T}(\phi_s - \tau) + d_1 \mathbf{N}_{t'} \cdot \mathbf{T}(\phi_s - \tau) + d_2 \mathbf{B}_{t'} \cdot \mathbf{T}(\phi_s - \tau) \\
&\quad + b_1(\phi_{ss} - \tau_s) + a_1(\phi_s - \tau)^2 - c_1\kappa + e_1, \quad (5.18)
\end{aligned}$$

$$\mathbf{R}_{t'} \cdot \mathbf{N} = b_2\kappa - c_2(\phi_{ss} - \tau_s) - a_2(\phi_s - \tau)^2 + e_2, \quad (5.19)$$

$$\mathbf{R}_{t'} \cdot \mathbf{B} = c_3\kappa - c_4(\phi_{ss} - \tau_s) - a_3(\phi_s - \tau)^2 + e_3. \quad (5.20)$$

To derive (5.18), (5.19), and (5.20) we made the assumption that the time derivatives (e.g.  $\phi_{t'}$ ) vary slowly in time and so can be removed from the integral and be treated as constant.

The coefficients are

$$\begin{aligned}
a_1 &= \langle \mathbf{Y}_\theta, \mathbf{D}\mathbf{V}_{\theta\theta} \rangle, \quad a_2 = \langle \mathbf{Y}_p, \mathbf{D}\mathbf{V}_{\theta\theta} \rangle, \quad a_3 = \langle \mathbf{Y}_q, \mathbf{D}\mathbf{V}_{\theta\theta} \rangle, \\
b_1 &= \langle \mathbf{Y}_\theta, \mathbf{D}\mathbf{V}_\theta \rangle, \quad b_2 = \langle \mathbf{Y}_p, \mathbf{D}\mathbf{V}_p \rangle, \quad c_1 = \langle \mathbf{Y}_\theta, \mathbf{D}\mathbf{V}_p \rangle, \\
c_2 &= \langle \mathbf{Y}_p, \mathbf{D}\mathbf{V}_p \rangle, \quad c_3 = \langle \mathbf{Y}_q, \mathbf{D}\mathbf{V}_p \rangle, \quad c_4 = \langle \mathbf{Y}_q, \mathbf{D}\mathbf{V}_\theta \rangle, \\
d_1 &= \langle \mathbf{Y}_\theta, p\mathbf{V}_\theta \rangle, \quad d_2 = \langle \mathbf{Y}_\theta, q\mathbf{V}_\theta \rangle, \\
e_1 &= \langle \mathbf{Y}_\theta, \mathbf{h}(t') \rangle, \quad e_2 = \langle \mathbf{Y}_p, \mathbf{h}(t') \rangle, \quad e_3 = \langle \mathbf{Y}_q, \mathbf{h}(t') \rangle.
\end{aligned}$$

Equation (5.18) differs from the corresponding equation published by Keener, and later used by Biktashev, Holden and Zhang, by the terms  $d_1 \mathbf{N}_{t'} \cdot \mathbf{T}(\phi_s - \tau)$ ,  $d_2 \mathbf{B}_{t'} \cdot \mathbf{T}(\phi_s - \tau)$ , and  $e_1$ . The term  $e_1$  is due to the perturbation. I will later show that the coefficients,  $d_1$  and  $d_2$ , of the additional terms are equal to zero and so do not effect the equations of motion.

Equations (5.19) and (5.20) differ from Keener's equations only by the terms  $e_2$  and  $e_3$  respectively. These terms are both due to the perturbation term  $\mathbf{h}(t)$  introduced in (5.1).

## 5.2 Some coefficients of the equations of motion vanish

As shown in [19], some of the coefficients of the evolution equations derived above are always zero. I will now review the relevant section of that paper and show which of the coefficients can be set to zero.

The eigenfunctions,  $\mathbf{V}_p, \mathbf{V}_q, \mathbf{V}_\theta$ , of  $L$  can be written explicitly,

$$\begin{aligned}\mathbf{V}_p(r, \theta - \omega t' + \phi) &= \mathbf{V}_r(r, \theta - \omega t' + \phi) \cos(\theta) - \frac{1}{r} \mathbf{V}_{\tilde{\theta}}(r, \theta - \omega t' + \phi) \sin(\theta) \\ \mathbf{V}_q(r, \theta - \omega t' + \phi) &= \mathbf{V}_r(r, \theta - \omega t' + \phi) \sin(\theta) + \frac{1}{r} \mathbf{V}_{\tilde{\theta}}(r, \theta - \omega t' + \phi) \cos(\theta) \\ \mathbf{V}_\theta(r, \theta - \omega t' + \phi) &= \mathbf{V}_{\tilde{\theta}}(r, \theta - \omega t' + \phi)\end{aligned}$$

(where  $\phi(s, t') = \phi$  and  $\tilde{\theta} = \theta - \omega t' + \phi$ ). The eigenfunctions of  $L^+$ ,  $\mathbf{Y}_p, \mathbf{Y}_q, \mathbf{Y}_\theta$ , can not be written explicitly. This makes it impossible to find the coefficients  $a_i, b_i, c_i, d_i, e_i$  analytically. However, recent developments suggest that it may be possible to calculate these coefficients numerically [20]. Here, we study the symmetry of the problem to deduce useful conclusions.

We change to a coordinate system which co-moves with the scroll wave (called the *scroll coordinate system*),

$$(r, \theta, t') \rightarrow (\rho, \tilde{\theta}, \tilde{t}),$$

where

$$\begin{aligned}\tilde{t} &= t', \\ \rho &= r, \\ \tilde{\theta} &= \theta - \omega \tilde{t} + \phi.\end{aligned}$$

In the scroll coordinate system,  $\phi(s, \tilde{t}) = \phi$  is taken to be constant since we made the assumption that it varies slowly in time. The arguments of  $\mathbf{V}$  and  $\mathbf{w}$  in this frame of reference are

$$\begin{aligned}\mathbf{V}(r, \theta - \omega t' + \phi) &= \tilde{\mathbf{V}}(\rho, \tilde{\theta}), \\ \mathbf{w}(s, p, q, t') &= \tilde{\mathbf{w}}(\rho, \tilde{\theta}, \tilde{t}),\end{aligned}$$

and the linear operators  $L$  and  $L^+$  become

$$\begin{aligned}\tilde{L}\tilde{\mathbf{w}} &= \tilde{\mathbf{w}}_{\tilde{t}} - \omega\tilde{\mathbf{w}}_{\tilde{\theta}} - \mathbf{D}\tilde{\Delta}_2\tilde{\mathbf{w}} - \tilde{F}(\mathbf{V}(\rho, \tilde{\theta}))\tilde{\mathbf{w}} \\ &= \tilde{\mathbf{w}}_{\tilde{t}} - \tilde{M}\tilde{\mathbf{w}},\end{aligned}\tag{5.21}$$

$$\begin{aligned}\tilde{L}^+\tilde{\mathbf{w}} &= -\tilde{\mathbf{w}}_{\tilde{t}} + \omega\tilde{\mathbf{w}}_{\tilde{\theta}} - \mathbf{D}^T\tilde{\Delta}_2\tilde{\mathbf{w}} - \tilde{F}^T(\mathbf{V}(\rho, \tilde{\theta}))\tilde{\mathbf{w}} \\ &= -\tilde{\mathbf{w}}_{\tilde{t}} - \tilde{M}^+\tilde{\mathbf{w}},\end{aligned}\tag{5.22}$$

where  $\tilde{M}^+$  is the adjoint of  $\tilde{M}$  with respect to the scalar product (5.14). Written explicitly,

$$\tilde{M}\tilde{\mathbf{w}} = \omega\tilde{\mathbf{w}}_{\tilde{\theta}} + \mathbf{D}\tilde{\Delta}_2\tilde{\mathbf{w}} + \tilde{F}(\mathbf{V}(\rho, \tilde{\theta}))\tilde{\mathbf{w}},\tag{5.23}$$

$$\tilde{M}^+\tilde{\mathbf{w}} = -\omega\tilde{\mathbf{w}}_{\tilde{\theta}} + \mathbf{D}^T\tilde{\Delta}_2\tilde{\mathbf{w}} + \tilde{F}^T(\mathbf{V}(\rho, \tilde{\theta}))\tilde{\mathbf{w}}.\tag{5.24}$$

Here, the tilde denotes the functions depending on  $\rho, \tilde{\theta}, \tilde{t}$  instead of  $r, \theta, t$ . In this rotating coordinate system, the eigenfunctions of  $\tilde{L}$  are expressed as

$$\begin{aligned}\tilde{\mathbf{V}}_p &= \tilde{\mathbf{V}}_\rho(\rho, \tilde{\theta}) \cos(\tilde{\theta} + \omega\tilde{t} - \phi) - \frac{1}{\rho}\tilde{\mathbf{V}}_{\tilde{\theta}}(\rho, \tilde{\theta}) \sin(\tilde{\theta} + \omega\tilde{t} - \phi) \\ \tilde{\mathbf{V}}_q &= \tilde{\mathbf{V}}_\rho(\rho, \tilde{\theta}) \sin(\tilde{\theta} + \omega\tilde{t} - \phi) + \frac{1}{\rho}\tilde{\mathbf{V}}_{\tilde{\theta}}(\rho, \tilde{\theta}) \cos(\tilde{\theta} + \omega\tilde{t} - \phi) \\ \tilde{\mathbf{V}}_\theta &= \tilde{\mathbf{V}}_{\tilde{\theta}}(\rho, \tilde{\theta})\end{aligned}$$

If we denote

$$\begin{aligned}\tilde{\mathbf{V}}_+(\rho, \tilde{\theta}) &= e^{i\tilde{\theta}} \left( \tilde{\mathbf{V}}_\rho(\rho, \tilde{\theta}) + \frac{i}{\rho}\tilde{\mathbf{V}}_{\tilde{\theta}}(\rho, \tilde{\theta}) \right), \\ \tilde{\mathbf{V}}_-(\rho, \tilde{\theta}) &= e^{-i\tilde{\theta}} \left( \tilde{\mathbf{V}}_\rho(\rho, \tilde{\theta}) - \frac{i}{\rho}\tilde{\mathbf{V}}_{\tilde{\theta}}(\rho, \tilde{\theta}) \right),\end{aligned}$$

then one can express the eigenfunctions  $\tilde{\mathbf{V}}_p, \tilde{\mathbf{V}}_q, \tilde{\mathbf{V}}_\theta$  can be written as follows

$$\begin{aligned}\tilde{\mathbf{V}}_p &= \text{Re} \left( e^{i(\omega\tilde{t}-\phi)} \tilde{\mathbf{V}}_+(\rho, \tilde{\theta}) \right) = \frac{1}{2} \left( e^{i(\omega\tilde{t}-\phi)} \tilde{\mathbf{V}}_+ + e^{-i(\omega\tilde{t}-\phi)} \tilde{\mathbf{V}}_-(\rho, \tilde{\theta}) \right) \\ \tilde{\mathbf{V}}_q &= \text{Im} \left( e^{i(\omega\tilde{t}-\phi)} \tilde{\mathbf{V}}_+(\rho, \tilde{\theta}) \right) = \frac{1}{2i} \left( e^{i(\omega\tilde{t}-\phi)} \tilde{\mathbf{V}}_+ - e^{-i(\omega\tilde{t}-\phi)} \tilde{\mathbf{V}}_-(\rho, \tilde{\theta}) \right) \\ \tilde{\mathbf{V}}_\theta &= \tilde{\mathbf{V}}_0(\rho, \tilde{\theta})\end{aligned}$$

Substituting  $\tilde{\mathbf{V}}_0(\rho, \tilde{\theta})$  into (5.21) yields

$$\tilde{M}\tilde{\mathbf{V}}_0 = 0$$

which proves that  $\tilde{V}_0$  is an eigenfunction of  $\tilde{M}$  with eigenvalue 0. By defining

$$\begin{aligned}\tilde{\mathbf{V}}_p + i\tilde{\mathbf{V}}_q &= e^{i(\omega\tilde{t}-\phi)}\tilde{\mathbf{V}}_+(\rho, \tilde{\theta}), \\ \tilde{\mathbf{V}}_p - i\tilde{\mathbf{V}}_q &= e^{-i(\omega\tilde{t}-\phi)}\tilde{\mathbf{V}}_-(\rho, \tilde{\theta}),\end{aligned}$$

and through substitution into (5.21), it can be seen that

$$\begin{aligned}\tilde{M}\tilde{\mathbf{V}}_+ &= i\omega\tilde{\mathbf{V}}_+, \\ \tilde{M}\tilde{\mathbf{V}}_- &= -i\omega\tilde{\mathbf{V}}_-, \end{aligned}$$

which implies that  $\tilde{\mathbf{V}}_+$  is an eigenfunction of  $\tilde{M}$  with eigenvalue  $i\omega$  and that  $\tilde{\mathbf{V}}_-$  is an eigenfunction of  $\tilde{M}$  with eigenvalue  $-i\omega$ .

The eigenvalues of  $\tilde{M}^+$  should be the same as the eigenvalues of  $\tilde{M}$ . We will label the eigenfunctions of  $\tilde{M}^+$  as  $\tilde{\mathbf{Y}}_+$ ,  $\tilde{\mathbf{Y}}_-$  and  $\tilde{\mathbf{Y}}_0$ , which have eigenvalues  $-i\omega$ ,  $+i\omega$  and 0 respectively.

It can be checked that  $e^{i(\omega\tilde{t}-\phi)}\tilde{\mathbf{Y}}_+$ ,  $e^{-i(\omega\tilde{t}-\phi)}\tilde{\mathbf{Y}}_-$ , and  $\tilde{\mathbf{Y}}_0$  are eigenfunctions of  $\tilde{L}^+$ , each with eigenvalue 0. Since these eigenfunctions have eigenvalue 0, a combination of them also results in an eigenfunction of  $\tilde{L}^+$  with eigenvalue 0. Hence, one can say that the following are eigenfunctions of  $\tilde{L}^+$  with eigenvalue 0,

$$\begin{aligned}\tilde{\mathbf{Y}}_p &= \text{Re} \left( e^{i(\omega\tilde{t}-\phi)}\tilde{\mathbf{Y}}_+(\rho, \tilde{\theta}) \right) = \left( e^{i(\omega\tilde{t}-\phi)}\tilde{\mathbf{Y}}_+(\rho, \tilde{\theta}) + e^{-i(\omega\tilde{t}-\phi)}\tilde{\mathbf{Y}}_-(\rho, \tilde{\theta}) \right), \\ \tilde{\mathbf{Y}}_q &= \text{Im} \left( e^{i(\omega\tilde{t}-\phi)}\tilde{\mathbf{Y}}_+(\rho, \tilde{\theta}) \right) = -i \left( e^{i(\omega\tilde{t}-\phi)}\tilde{\mathbf{Y}}_+(\rho, \tilde{\theta}) - e^{-i(\omega\tilde{t}-\phi)}\tilde{\mathbf{Y}}_-(\rho, \tilde{\theta}) \right), \\ \tilde{\mathbf{Y}}_\theta &= \tilde{\mathbf{Y}}_0(\rho, \tilde{\theta}).\end{aligned}$$

It is now left to express the inner product in the scroll system of coordinates  $(\rho, \tilde{\theta}, \tilde{t})$ ,

$$\langle \tilde{m}(\rho, \tilde{\theta}, \tilde{t}), \tilde{n}(\rho, \tilde{\theta}, \tilde{t}) \rangle = \int_{\tilde{t}-\frac{\pi}{\omega}}^{\tilde{t}+\frac{\pi}{\omega}} d\tilde{\eta} \oint d\tilde{\theta} \int_0^\infty \rho d\rho (\tilde{m}(\rho, \tilde{\theta}, \tilde{\eta}) \cdot \tilde{n}(\rho, \tilde{\theta}, \tilde{\eta})), \quad (5.25)$$

where

$$(\tilde{m}(\rho, \tilde{\theta}, \tilde{t}), \tilde{n}(\rho, \tilde{\theta}, \tilde{t})) = \sum_{i=0}^j \tilde{m}_i \tilde{n}_i. \quad (5.26)$$

We should also check the orthogonality condition (5.16) holds (see Appendix C.5). It can then be seen that the coefficients  $a_2 = a_3 = d_1 = d_2 = c_1 = c_2 = c_4 = 0$  (see Appendix C.6).

The equations of motion (5.18), (5.19), and (5.20) can now be simplified to

$$\phi_{t'} = \mathbf{N}_{t'} \cdot \mathbf{B} + \mathbf{R}_{t'} \cdot \mathbf{T}(\phi_s - \tau) + b_1(\phi_{ss} - \tau_s) + a_1(\phi_s - \tau)^2 + e_1, \quad (5.27)$$

$$\mathbf{R}_{t'} \cdot \mathbf{N} = b_2\kappa + e_2, \quad (5.28)$$

$$\mathbf{R}_{t'} \cdot \mathbf{B} = c_3\kappa + e_3, \quad (5.29)$$

where

$$a_1 = \langle \mathbf{Y}_\theta, \mathbf{D}\mathbf{V}_{\theta\theta} \rangle, c_3 = \langle \mathbf{Y}_q, \mathbf{D}\mathbf{V}_p \rangle,$$

$$b_1 = \langle \mathbf{Y}_\theta, \mathbf{D}\mathbf{V}_\theta \rangle, b_2 = \langle \mathbf{Y}_p, \mathbf{D}\mathbf{V}_p \rangle,$$

$$e_1 = \langle \mathbf{Y}_\theta, h \rangle, e_2 = \langle \mathbf{Y}_p, h \rangle, e_3 = \langle \mathbf{Y}_q, h \rangle.$$

Where the integrals  $a_1, b_1, b_2$  and  $c_3$  (see Appendix C.7) are

$$\begin{aligned} a_1 &= \frac{2\pi}{\omega} \oint d\tilde{\theta} \int_0^\infty \rho d\rho \left[ \tilde{\mathbf{Y}}_\theta(\rho, \tilde{\theta}) \cdot \mathbf{D}\tilde{\mathbf{V}}_{\theta\theta}(\rho, \tilde{\theta}) \right], \\ b_1 &= \frac{2\pi}{\omega} \oint d\tilde{\theta} \int_0^\infty \rho d\rho \left[ \tilde{\mathbf{Y}}_\theta(\rho, \tilde{\theta}) \cdot \mathbf{D}\tilde{\mathbf{V}}_\theta(\rho, \tilde{\theta}) \right], \\ b_2 + ic_3 &= \frac{2\pi}{\omega} \oint d\tilde{\theta} \int_0^\infty \rho d\rho \left[ \tilde{\mathbf{Y}}_+(\rho, \tilde{\theta}) \cdot \mathbf{D}\tilde{\mathbf{V}}_+(\rho, \tilde{\theta}) \right]. \end{aligned} \quad (5.30)$$

If the perturbation is chosen to be periodic in time  $\mathbf{h}(t) = \mathbf{H}(\Omega t' - \phi_*)$  (where  $\mathbf{H}(\chi) = \mathbf{H}(\chi + 2\pi)$ ) then we have the following expressions for  $e_1, e_2$  and  $e_3$  (see Appendix C.8),

$$e_1 = \frac{H_0}{\Omega}, \quad (5.31)$$

$$e_2 = \frac{H_1}{\Omega} \cos(\beta - \phi(s, t')), \quad (5.32)$$

$$e_3 = \frac{H_1}{\Omega} \sin(\beta - \phi(s, t')), \quad (5.33)$$

where  $\beta = (\omega - \Omega)t' + \phi_*$ , and  $\chi = \Omega t' - \phi_*$ , and

$$\begin{aligned} H_0 &= \left[ \oint d\chi \mathbf{H}(\chi) \right] \cdot \left[ \oint d\tilde{\theta} \int_0^\infty \rho d\rho \tilde{\mathbf{Y}}_0(\rho, \tilde{\theta}) \right] \\ &= 2\pi \tilde{\mathbf{H}}_0 \cdot \left[ \oint d\tilde{\theta} \int_0^\infty \rho d\rho \tilde{\mathbf{Y}}_0(\rho, \tilde{\theta}) \right], \end{aligned} \quad (5.34)$$

$$\begin{aligned} H_1 &= \left[ \oint d\chi e^{i\chi} \mathbf{H}(\chi) \right] \cdot \left[ \oint d\tilde{\theta} \int_0^\infty \rho d\rho \tilde{\mathbf{Y}}_+(\rho, \tilde{\theta}) \right] \\ &= 2\pi \tilde{\mathbf{H}}_1 \cdot \left[ \oint d\tilde{\theta} \int_0^\infty \rho d\rho \tilde{\mathbf{Y}}_+(\rho, \tilde{\theta}) \right]. \end{aligned} \quad (5.35)$$

Here,  $\tilde{\mathbf{H}}_0$  and  $\tilde{\mathbf{H}}_1$  are Fourier coefficients of  $\mathbf{H}(\chi)$ ,

$$\begin{aligned} \mathbf{H}(\chi) &= \sum_{n=-\infty}^{+\infty} \tilde{\mathbf{H}}_n e^{in\chi}, \\ \tilde{\mathbf{H}}_n &= \frac{1}{2\pi} \oint \mathbf{H}(\chi) e^{-in\chi} d\chi. \end{aligned}$$

### 5.3 Effect of resonant perturbation on scroll rings

Here I will consider a solution of the system (5.27), (5.28), and (5.29) for an untwisted scroll ring.

Firstly, the arc-length coordinate  $s$  might not be sufficient because the length of the filament may change with time. Biktashev, Holden, and Zhang [19] introduced a new parameter  $\sigma$  so that points with equal  $\sigma$  move perpendicular to the filament. Therefore,

$$\mathbf{R}_s(\sigma, t) = \frac{\partial \mathbf{R}}{\partial \sigma} \frac{\partial \sigma}{\partial s}.$$

By defining  $v = \frac{\partial s}{\partial \sigma}$ , we obtain the arc length differential operator,

$$\mathbf{R}_s(\sigma, t) = v^{-1} \frac{\partial \mathbf{R}}{\partial \sigma}(\sigma, t).$$

Further, since  $|\partial \mathbf{R}| = \partial s$  this implies that  $|\mathbf{R}_s| = 1$ . Then  $v^{-1}|\mathbf{R}_\sigma| = 1$  and so,

$$v = |\mathbf{R}_\sigma(\sigma, t)|$$

Assume that  $\phi = \phi(t)$  and consider the following parametrisation for a scroll ring

$$\mathbf{R}(\sigma, t) = \begin{pmatrix} a(t) \cos \sigma \\ a(t) \sin \sigma \\ -z_*(t) \end{pmatrix}.$$

Since  $|\mathbf{R}_\sigma| = a(t)$ , by using the Frenet-Serret equations (5.3)-(5.6) it can be seen that;

$$\mathbf{T} = \begin{pmatrix} -\sin \sigma \\ \cos \sigma \\ 0 \end{pmatrix}, \quad \mathbf{N} = \begin{pmatrix} \cos \sigma \\ \sin \sigma \\ 0 \end{pmatrix}, \quad \mathbf{B} = \begin{pmatrix} 0 \\ 0 \\ 1 \end{pmatrix},$$

where  $\kappa = -\frac{1}{a}$  and  $\tau = 0$ . Since  $a = a(t)$  it follows that  $\tau_s = \kappa_s = \kappa_{ss} = 0$ . Taking derivatives of  $\mathbf{R}$  and  $\mathbf{N}$  with respect to  $t$ ,

$$\mathbf{R}_t = \begin{pmatrix} a_t \cos \sigma \\ a_t \sin \sigma \\ -z_{*t} \end{pmatrix}, \quad \mathbf{N}_t = \begin{pmatrix} 0 \\ 0 \\ 0 \end{pmatrix},$$

allows one to deduce that  $\mathbf{R}_t \cdot \mathbf{N} = a_t$ ,  $\mathbf{R}_t \cdot \mathbf{B} = -z_{*t}$  and  $\mathbf{R}_t \cdot \mathbf{T} = \mathbf{N}_t \cdot \mathbf{B} = 0$ . Also, since  $\phi = \phi(t)$  it follows that  $\phi_s = \phi_{ss} = 0$ . Substitution into the motion equations (5.27)-(5.29) gives

$$\phi_t = \frac{H_0}{\Omega}, \quad (5.36)$$

$$a_t = -\frac{b_2}{a} + \frac{H_1}{\Omega} \cos(\beta - \phi), \quad (5.37)$$

$$z_{*t} = \frac{c_3}{a} + \frac{H_1}{\Omega} \sin(\beta - \phi). \quad (5.38)$$

From (5.36),  $\phi(t) = \frac{H_0}{\Omega}t + \phi_0$ . Substitution into (5.37), and recalling  $\beta = (\omega - \Omega)t + \phi_*$ , yields,

$$a_t = -\frac{b_2}{a} + \frac{H_1}{\Omega} \cos \left( t \left[ \omega - \Omega - \frac{H_0}{\Omega} \right] + \hat{\phi} \right), \quad (5.39)$$

where  $\hat{\phi} = \phi_* - \phi_0$ .

In the absence of perturbation, for a ring with initial radius  $a(0) = a_0$ , it can be seen that for filaments of negative tension (i.e. negative  $b_2$ ) the ring will expand. For filaments of positive tension (i.e. positive  $b_2$ ) the ring will collapse. This is in good agreement with the kinematic theory published by Alonso *et al.* [8].

With perturbation, the fate of a ring with initial radius  $a(0) = a_0$  will depend on the value of the sign and value of the perturbation term  $\frac{H_1}{\Omega} \cos \left( t \left[ \omega - \Omega - \frac{H_0}{\Omega} \right] + \hat{\phi} \right)$ . So, for filaments with negative tension the ring will expand unless the perturbation term is negative and large compared to  $\frac{b_2}{a}$ , in which case it will collapse. For filaments with positive filament tension, the ring will collapse unless the perturbation term is positive and large compared to  $\frac{b_2}{a}$ , in which case it will expand

## 5.4 Effect of resonant perturbation on helical scroll waves

In Chapter 4 we saw that, for the same amplitude, constant frequency forcing sometimes terminated scroll wave turbulence faster than resonant drift pacing. We hypothesised that this could be due to the existence of scrolls with strong twist, in which case different parts of the same filament have different phases and may be forced in different directions, which does not result in an overall directed movement and does not bring about termination. Instead of moving the filament, the forcing creates a filament of helical shape. We are interested in what our new theory may say about helical scroll waves under resonant forcing.

We consider a solution of the system (5.27), (5.28), and (5.29) for a stationary helical scroll wave to obtain some analytical evidence to back up this hypothesis. Assume that  $\phi = \phi(t)$  and consider the following parametrisation of a helical scroll wave

$$\mathbf{R}(\sigma, t) = \begin{pmatrix} a(t) \cos(\sigma - \sigma_*(t)) \\ a(t) \sin(\sigma - \sigma_*(t)) \\ b\sigma - z_*(t) \end{pmatrix},$$

where  $a(t)$  is the radius of the helix,  $b$  is the length of each of the coils in the helix,  $\sigma_*(t)$  is the phase of the helix, and  $z_*(t)$  allows linear growth along the z-axis. It follows from this choice of parametrisation that  $\mathbf{R}_t \cdot \mathbf{T} = 0$ , and so we can combine (5.28) and (5.29)

$$\begin{aligned} \mathbf{R}_t &= (\mathbf{R}_t \cdot \mathbf{N}) \cdot \mathbf{N} + (\mathbf{R}_t \cdot \mathbf{B}) \cdot \mathbf{B} \\ &= (b_2\kappa + e_2)\mathbf{N} + (c_3\kappa + e_3)\mathbf{B}. \end{aligned} \tag{5.40}$$

Since  $|\mathbf{R}_\sigma(s, t)| = (a^2(t) + b^2)^{\frac{1}{2}}$ , by using the Frenet-Serret equations (5.3) - (5.6) it can be seen that



$$\mathbf{T} = \begin{pmatrix} -a(a^2 + b^2)^{-\frac{1}{2}} \sin(\sigma - \sigma_*) \\ a(a^2 + b^2)^{-\frac{1}{2}} \cos(\sigma - \sigma_*) \\ b(a^2 + b^2)^{-\frac{1}{2}} \end{pmatrix}, \quad \mathbf{N} = \begin{pmatrix} -\cos(\sigma - \sigma_*) \\ -\sin(\sigma - \sigma_*) \\ 0 \end{pmatrix},$$

$$\mathbf{B} = \begin{pmatrix} -b(a^2 + b^2)^{-\frac{1}{2}} \sin(\sigma - \sigma_*) \\ b(a^2 + b^2)^{-\frac{1}{2}} \cos(\sigma - \sigma_*) \\ a(a^2 + b^2)^{-\frac{1}{2}} \end{pmatrix},$$

from here we deduce that

$$\begin{aligned} \kappa &= a(a^2 + b^2)^{-1}, \\ \tau &= -b(a^2 + b^2)^{-1}. \end{aligned}$$

Taking derivative of  $\mathbf{R}$  with respect to time  $t$ ,

$$\mathbf{R}_t = \begin{pmatrix} a_t \cos(\sigma - \sigma_*) + \sigma_{*t} a \sin(\sigma - \sigma_*) \\ a_t \sin(\sigma - \sigma_*) - \sigma_{*t} a \cos(\sigma - \sigma_*) \\ -z_{*t} \end{pmatrix},$$

and taking derivative of  $\mathbf{N}$  with respect to time  $t$ ,

$$\mathbf{N}_t = \begin{pmatrix} -\sigma_{*t} \sin(\sigma - \sigma_*) \\ \sigma_{*t} \cos(\sigma - \sigma_*) \\ 0 \end{pmatrix}$$

it follows that

$$\mathbf{N}_t \cdot \mathbf{B} = \sigma_{*t} b(a^2 + b^2)^{-\frac{1}{2}}.$$

It should also be noted that from the ansatz  $\phi(s, t) = \phi(t)$  that  $\phi_s = \phi_{ss} = 0$ , and from the above derivations of  $\kappa$  and  $\tau$  that  $\tau_s = \kappa_s = \kappa_{ss} = 0$ .

Substitution into (5.27) gives

$$\phi_t = \sigma_{*t} b(a^2 + b^2)^{-\frac{1}{2}} + a_1 \tau^2 + e_1. \quad (5.41)$$

By substitution into (5.40), the three components of vector  $\mathbf{R}_t$  are

$$\begin{aligned} &a_t \cos(\sigma - \sigma_*) + a \sigma_{*t} \sin(\sigma - \sigma_*) = \\ &-(b_2 \kappa + e_2) \cos(\sigma - \sigma_*) - b(a^2 + b^2)^{-\frac{1}{2}} (c_3 \kappa + e_3) \sin(\sigma - \sigma_*), \end{aligned} \quad (5.42)$$

and

$$\begin{aligned} & a_t \sin(\sigma - \sigma_*) - a\sigma_{*t} \cos(\sigma - \sigma_*) = \\ & -(b_2\kappa + e_2) \sin(\sigma - \sigma_*) + b(a^2 + b^2)^{-\frac{1}{2}}(c_3\kappa + e_3) \cos(\sigma - \sigma_*), \end{aligned} \quad (5.43)$$

and

$$-z_{*t} = a(a^2 + b^2)^{-\frac{1}{2}}(c_3\kappa + e_3). \quad (5.44)$$

By computing (5.42)  $\cos(\sigma - \sigma_*) + (5.43) \sin(\sigma - \sigma_*)$  and (5.42)  $\sin(\sigma - \sigma_*) - (5.43) \cos(\sigma - \sigma_*)$  we arrive at the system of equations

$$\phi_t = \sigma_{*t} b(a^2 + b^2)^{-\frac{1}{2}} + a_1\tau^2 + e_1, \quad (5.45)$$

$$a_t = -(b_2\kappa + e_2), \quad (5.46)$$

$$\sigma_{*t} = -ba^{-1}(a^2 + b^2)^{-\frac{1}{2}}(c_3\kappa + e_3), \quad (5.47)$$

$$-z_{*t} = a(a^2 + b^2)^{-\frac{1}{2}}(c_3\kappa + e_3). \quad (5.48)$$

By substituting (5.47) into (5.45), and using the equations (5.31)-(5.33) and the calculated values of  $\kappa$  and  $\tau$ , we find the coupled system for  $\phi_t$  and  $a_t$ ,

$$\phi_t = \frac{H_1}{\Omega} b^2 a^{-1} (a^2 + b^2)^{-1} \sin(\phi - \beta) + \frac{H_0}{\Omega} + b^2 (a^2 + b^2)^{-2} (a_1 - c_3), \quad (5.49)$$

$$a_t = -\frac{H_1}{\Omega} \cos(\beta - \phi) - b_2 a (a^2 + b^2)^{-1}, \quad (5.50)$$

where  $\beta = (\omega - \Omega)t + \phi_*$ .

One can deduce useful results when considering a relative equilibrium, i.e. we will look for solutions which don't change in time (such as a *stationary* helix), that is where all time derivative are constant. Consider the case when  $\phi(t) = \phi$  and  $a(t) = a$  are constant, then  $\phi - \beta = \phi_1$  is constant. It follows that,

$$\phi = (\omega - \Omega)t + \phi_* + \phi_1$$

and,

$$\phi_t = (\omega - \Omega),$$

where  $\phi_t$  is constant since we assume that  $\omega$  is constant. Substitution into (5.49) yields

$$\omega - \Omega = \frac{H_1}{\Omega} b^2 a^{-1} (a^2 + b^2)^{-1} \sin(\phi_1) + \frac{H_0}{\Omega} + b^2 (a^2 + b^2)^{-2} (a_1 - c_3), \quad (5.51)$$

Since  $a(t) = a$  is constant, then (5.50) becomes

$$0 = -\frac{H_1}{\Omega} \cos(\phi_1) - b_2 a (a^2 + b^2)^{-1}. \quad (5.52)$$

Re-arrangement of (5.51) and (5.52) produces

$$\sin^2(\phi_1) = \left( \omega - \Omega - \frac{H_0}{\Omega} - \frac{b^2(a_1 - c_3)}{(a^2 + b^2)^2} \right)^2 \frac{\Omega^2 a^2 (a^2 + b^2)^2}{H_1^2 b^4}, \quad (5.53)$$

and

$$\cos^2(\phi_1) = \frac{b_2^2 a^2 \Omega^2}{(a^2 + b^2)^2 H_1^2}. \quad (5.54)$$

Combining (5.53) and (5.54) produces,

$$\left( \omega - \Omega - \frac{H_0}{\Omega} - \frac{b^2(a_1 - c_3)}{(a^2 + b^2)^2} \right)^2 \frac{\Omega^2 a^2 (a^2 + b^2)^2}{H_1^2 b^4} + \frac{b_2^2 a^2 \Omega^2}{(a^2 + b^2)^2 H_1^2} = 1. \quad (5.55)$$

Define  $c^2 = (a^2 + b^2)$ ,

$$\left( \omega - \Omega - \frac{H_0}{\Omega} - \frac{b^2}{c^4} (a_1 - c_3) \right)^2 \frac{\Omega^2 a^2 c^4}{H_1^2 b^4} + \frac{b_2^2 a^2 \Omega^2}{c^4 H_1^2} = 1. \quad (5.56)$$

Define  $A = \frac{\Omega^2}{H_1^2}$ ,  $B = \omega - \Omega - \frac{H_0}{\Omega}$ ,  $D = -(a_1 - c_3)$ , and  $E = \frac{\Omega^2 b_2^2}{H_1^2}$ , and expand as follows,

$$\begin{aligned} \left( B + D \frac{b^2}{c^4} \right)^2 \frac{A a^2 c^4}{b^4} + \frac{E a^2}{c^4} &= 1, \\ \left( B^2 + 2BD \frac{b^2}{c^4} + D^2 \frac{b^4}{c^8} \right) \frac{A a^2 c^4}{b^4} + \frac{E a^2}{c^4} &= 1, \\ \frac{AB^2 a^2 c^4}{b^4} + \frac{2BD A a^2}{b^2} + \frac{D^2 A a^2}{c^4} + \frac{E a^2}{c^4} &= 1, \\ \frac{AB^2 a^2 c^8}{b^4} + \frac{2BD A a^2 c^4}{b^2} + D^2 A a^2 + E a^2 - c^4 &= 0. \end{aligned}$$

Since  $a^2 = (c^2 - b^2)$ , we can re-write this as the following quintic equation for  $c^2$

$$(c^2 - b^2)(AB^2c^8b^{-4} + 2BDAc^4b^{-2} + D^2A + E) - c^4 = 0, \quad (5.57)$$

There are too many unknown parameters in (5.57) for an exhaustive parametric study. If numerical values of parameters  $a_1, b_2, b_3, c_3, e_1, e_2$  and  $e_3$  are known, then solutions of this algebraic equation can be found. Such solutions would provide equilibria for the system (5.49)-(5.50) i.e. a stationary helical scroll wave solution for the original problem. Therefore it would confirm that a stationary helical filament subjected to resonant perturbations remains stationary. Such solutions could provide an explanation for the ‘false resonance’ phenomenon observed in Chapter 4 and give a reason why resonant drift pacing in 3D is not always successful.

## 5.5 Vector equations

As the examples of a scroll ring and helix demonstrate, the equations (5.27)-(5.29) are perfectly usable. Yet their form may be inconvenient for some applications due to the term  $\mathbf{N}_t \cdot \mathbf{B}$ . We will now transform those equations into a fully resolved form without time derivatives on the right hand side.

We re-write the equations of motion in a fully covariant form by introducing a unit phase vector  $\Phi(s, t)$  (as in [42]) instead of a scalar  $\phi(s, t)$ ,

$$\Phi(s, t) = \mathbf{N}(s, t) \cos \phi(s, t) - \mathbf{B}(s, t) \sin \phi(s, t).$$

It is convenient to introduce  $\Psi(s, t) = (\mathbf{T}(s, t) \times \Phi(s, t))$  where

$$\Psi(s, t) = \mathbf{N}(s, t) \sin \phi(s, t) + \mathbf{B}(s, t) \cos \phi(s, t).$$

### 5.5.1 Vector equation for filament $\mathbf{R}$

Firstly, for the equation the filament  $\mathbf{R}$ , recall (5.40)

$$\begin{aligned} \mathbf{R}_t &= (b_2\kappa + e_2) \cdot \mathbf{N} + (c_3\kappa + e_3) \cdot \mathbf{B} \\ &= b_2\kappa\mathbf{N} + c_3\kappa\mathbf{B} + e_2\mathbf{N} + e_3\mathbf{B}, \end{aligned}$$

and (5.32)-(5.33)

$$\begin{aligned} e_2 &= \frac{H_1}{\Omega} \cos(\beta - \phi(s, t)), \\ e_3 &= \frac{H_1}{\Omega} \sin(\beta - \phi(s, t)), \end{aligned}$$

where  $\beta = (\omega - \Omega)t + \phi_*$ . Equations (5.32) and (5.33) can be re-written as.

$$e_2 \mathbf{N} + e_3 \mathbf{B} = \frac{H_1}{\Omega} (\Phi \cos \beta + \Psi \sin \beta). \quad (5.58)$$

In addition, from the Frenet-Serret equations (5.3) - (5.6), one can deduce that

$$\kappa \mathbf{N} = \mathbf{R}_{ss}, \quad (5.59)$$

$$\kappa \mathbf{B} = \mathbf{R}_s \times \mathbf{R}_{ss}. \quad (5.60)$$

Substitution of (5.58), (5.59), and (5.60) into (5.40) produces the vector equation for  $\mathbf{R}_t$

$$\mathbf{R}_{t'} = b_2 \mathbf{R}_{ss} + c_3 (\mathbf{R}_s \times \mathbf{R}_{ss}) + \frac{H_1}{\Omega} (\Phi \cos \beta + \Psi \sin \beta). \quad (5.61)$$

### 5.5.2 Vector equation for the phase $\Phi$

If  $\Phi(s, t) = \mathbf{N}(s, t) \cos \phi(s, t) - \mathbf{B}(s, t) \sin \phi(s, t)$ , then the time derivative is

$$\Phi_t = \mathbf{N}_t \cos \phi - \mathbf{B}_t \sin \phi - \phi_t (\mathbf{N} \sin \phi + \mathbf{B} \cos \phi).$$

The equation for  $\phi_t$  has been found above (equation (5.27)), and since  $(\mathbf{R}_t \cdot \mathbf{T}) = 0$ , we have

$$\begin{aligned} \Phi_t &= \mathbf{N}_t \cos \phi - \mathbf{B}_t \sin \phi - (\mathbf{N}_t \cdot \mathbf{B})(\mathbf{B} \cos \phi + \mathbf{N} \sin \phi) \\ &\quad - b_1 (\phi_{ss} - \tau_s)(\mathbf{B} \cos \phi + \mathbf{N} \sin \phi) - a_1 (\phi_s - \tau)^2 (\mathbf{B} \cos \phi + \mathbf{N} \sin \phi) \\ &\quad - e_1 (\mathbf{B} \cos \phi + \mathbf{N} \sin \phi). \end{aligned} \quad (5.62)$$

The next step is to express (5.62) in a covariant form. Firstly consider the derivatives  $\mathbf{N}_t$  and  $\mathbf{B}_t$  (see Appendix (C.9) for details of the calculations),

$$\begin{aligned}
\mathbf{N}_t &= \mathbf{B}\kappa^{-1} \left( \frac{H_1}{\Omega} ((\tau_s - \phi_{ss}) \cos(\phi - \beta) + (\tau - \phi_s)^2 \sin(\phi - \beta)) \right. \\
&\quad \left. + c_3 \kappa_{ss} + b_2 \kappa \tau_s + 2b_2 \tau \kappa_s - c_3 \kappa \tau^2 \right) \\
&\quad - \mathbf{T} \left( \frac{H_1}{\Omega} (\tau - \phi_s) \sin(\phi - \beta) + b_2 \kappa_s - \tau c_3 \kappa \right),
\end{aligned}$$

and

$$\begin{aligned}
\mathbf{B}_t &= -\mathbf{N}\kappa^{-1} \left( \frac{H_1}{\Omega} ((\tau_s - \phi_{ss}) \cos(\phi - \beta) + (\tau - \phi_s)^2 \sin(\phi - \beta)) \right. \\
&\quad \left. + c_3 \kappa_{ss} + b_2 \kappa \tau_s + 2b_2 \tau \kappa_s - c_3 \kappa \tau^2 \right) \\
&\quad - \mathbf{T} \left( \frac{H_1}{\Omega} (\tau - \phi_s) \cos(\phi - \beta) + c_3 \kappa_s + b_2 \tau \kappa \right).
\end{aligned}$$

It can then be seen that

$$\begin{aligned}
(\mathbf{N}_t \cdot \mathbf{B}) &= \kappa^{-1} \left( \frac{H_1}{\Omega} ((\tau_s - \phi_{ss}) \cos(\phi - \beta) + (\tau - \phi_s)^2 \sin(\phi - \beta)) \right. \\
&\quad \left. + c_3 \kappa_{ss} + b_2 \kappa \tau_s + 2b_2 \tau \kappa_s - c_3 \kappa \tau^2 \right), \tag{5.63}
\end{aligned}$$

and so

$$\begin{aligned}
(\mathbf{N}_t - (\mathbf{N}_t \cdot \mathbf{B}) \cdot \mathbf{B}) \cos \phi &= -\mathbf{T} \left[ \frac{H_1}{\Omega} (\tau - \phi_s) \sin(\phi - \beta) + b_2 \kappa_s - \tau c_3 \kappa \right] \cos \phi, \\
-(\mathbf{B}_t + (\mathbf{N}_t \cdot \mathbf{B}) \cdot \mathbf{N}) \sin \phi &= \mathbf{T} \left[ \frac{H_1}{\Omega} (\tau - \phi_s) \cos(\phi - \beta) + c_3 \kappa_s + b_2 \tau \kappa \right] \sin \phi.
\end{aligned}$$

Using the identity

$$\cos(\phi - \beta) \sin \phi - \sin(\phi - \beta) \cos \beta = \sin \beta,$$

substitution into (5.62) yields

$$\begin{aligned}
\Phi_t &= \mathbf{T} (c_3 \kappa_s + b_2 \tau \kappa) \sin \phi - \mathbf{T} (b_2 \kappa_s - \tau c_3 \kappa) \cos \phi + \mathbf{T} \frac{H_1}{\Omega} (\tau - \phi_s) \sin(\beta) \\
&\quad - b_1 (\phi_{ss} - \tau_s) (\mathbf{B} \cos \phi + \mathbf{N} \sin \phi) - a_1 (\phi_s - \tau)^2 (\mathbf{B} \cos \phi + \mathbf{N} \sin \phi) \\
&\quad - e_1 (\mathbf{B} \cos \phi + \mathbf{N} \sin \phi). \tag{5.64}
\end{aligned}$$

The second step in expressing  $\Phi_t$  in a covariant form requires a new expression for the following terms (see Appendix (C.10) for details of the calculations),

$$\begin{aligned}
(\phi_s - \tau) &= -(\Psi \cdot \Phi_s), \\
(\phi_s - \tau)^2 &= (\Psi \cdot \Phi_s)^2, \\
(\phi_{ss} - \tau_s) &= (\Psi \cdot \Phi_s)_s \Psi, \\
b_2 \mathbf{T}(\tau \kappa \sin \phi - \kappa_s \cos \phi) &= -b_2 \mathbf{R}_s(\Psi \cdot (\mathbf{R}_s \times \mathbf{R}_{ss})), \\
c_3 \mathbf{T}(\tau \kappa \cos \phi + \kappa_s \sin \phi) &= -c_3 \mathbf{R}_s(\Phi \cdot (\mathbf{R}_s \times \mathbf{R}_{ss})).
\end{aligned}$$

This leads to the following vector equation for the scroll phase  $\Phi_t$

$$\begin{aligned}
\Phi_t &= -b_2 \mathbf{R}_s(\Psi \cdot (\mathbf{R}_s \times \mathbf{R}_{ss})) - c_3 \mathbf{R}_s(\Phi \cdot (\mathbf{R}_s \times \mathbf{R}_{ss})) - a_1 \Psi(\Psi \cdot \Phi_s)^2 \\
&\quad + b_1 \Psi(\Psi \cdot \Phi_s)_s + \frac{H_1}{\Omega} \mathbf{R}_s(\Psi \cdot \Phi_s) \sin \beta - \frac{H_0}{\Omega} \Psi,
\end{aligned} \tag{5.65}$$

where  $\beta = (\omega - \Omega)t + \phi_*$ .

### 5.5.3 Scalar equation for the phase $\phi$

With the information obtained, it is also possible to derive a scalar equation for the scroll phase  $\phi$  in a fully resolved form without time derivatives. By substitution of (5.63) into (5.27), and recalling that due to the choice of parameter  $\sigma$  that  $\mathbf{R}_t \cdot \mathbf{T} = 0$ , we find that

$$\begin{aligned}
\phi_t &= \kappa^{-1} \frac{H_1}{\Omega} \left( (\tau_s - \phi_{ss}) \cos(\phi - \beta) + (\tau - \phi_s)^2 \sin(\phi - \beta) \right) + \frac{H_0}{\Omega} + b_2 \tau_s \\
&\quad + c_3 \kappa^{-1} \kappa_{ss} + 2b_2 \kappa^{-1} \tau \kappa_s - c_3 \tau^2 + b_1(\phi_{ss} - \tau_s) + a_1(\phi_s - \tau)^2.
\end{aligned} \tag{5.66}$$

It should be noted here that (5.66) is singular at the points of inflection of the filament,  $\kappa = 0$ . Even for smooth filaments, the directions of  $\mathbf{N}$  and  $\mathbf{B}$  may change discontinuously as we go along the filament through an inflexion point, which would mean a discontinuous change in the scalar phase  $\phi$  even if the scroll is perfectly smooth. Therefore a singularity at  $\kappa = 0$  in (5.66) is expectable. Note that the equation for the vector phase  $\Phi$  (5.65) is free from any singularities and is equivalent to (5.66) wherever  $\kappa \neq 0$ .

$\kappa$  appears in the denominator of many terms and it may be possible that  $\kappa = 0$ , i.e. for straight scrolls. However, in the vector form (5.65),  $\kappa$  does not appear in the denominator, so we can see that it does effect the phase.

## 5.6 Summary

We have developed equations of motion for a perturbed general, twisted, scroll wave. These new equations build upon the work by Keener [41] and Biktashev, Holden, and Zhang [19]. The additional terms in our equations describe the effects of the resonant drift pacing. We present the equations in both fully resolved scalar and vector forms.

This new theory applied to the particular cases of a scroll ring and a helical filament. The scroll ring example shows that resonant drift pacing may cause collapsing rings to expand or expanding rings to collapse. The helical filament example demonstrates that it may be possible to have a stationary (i.e. non-expanding and non-collapsing) helical scroll when the filament tension and the resonant drift compensate each other.

The latter example provides a plausible explanation for the points of false resonance which we observed in Chapter 4.



## Chapter 6

# Resonant drift in a whole-ventricle anatomical model

In 2002 [76] Trayanova published data on the first attempt to realistically model defibrillation via single shock defibrillation in three spatial dimensions with realistic ventricular geometry. In this chapter we present, what is to our knowledge, the first attempt to realistically model low-energy defibrillation in three spatial dimensions with anatomically accurate ventricular geometry, using resonant drift pacing. To allow for possible comparisons with the work of Trayanova *et al* we chose our model setting similar to [76, 65, 75]. In Chapter 4 we saw that constant frequency forcing sometimes terminated the re-entry faster than resonant drift pacing. To see if this is also true in this model setting we also investigate the effect of constant frequency forcing.

Most previous simulation studies of resonant drift pacing have been limited to 2D. Here we use an anisotropic bidomain model of cardiac tissue with microscopic fluctuations to the intracellular conductivity, and realistic cellular kinetics. The cellular kinetics are described by the Beeler-Reuter-Drouhard-Roberge [28] ionic model modified for high amplitude shocks (see Appendix A). For the geometry of the ventricles, we use the UCSD finite element mesh of a rabbit ventricle [78]. Truncated exponential monophasic shocks, of 8 ms duration, were applied via two large planar electrodes located at the boundaries of a perfusing bath surrounding the ventricles.

## 6.1 Methodology

### 6.1.1 Governing equations

The bidomain model (2.14)-(2.15) of cardiac tissue is most widely used to study defibrillation-related phenomena [65]. We repeat the equations here for convenience

$$\begin{aligned} C_m \frac{\partial V_m}{\partial t} &= -I_{ion} + \frac{1}{\beta} \nabla \cdot (\sigma_i \nabla V_m) + \frac{1}{\beta} \nabla \cdot (\sigma_e \nabla \phi_e) + I_{trans}, \\ \nabla \cdot ((\sigma_i + \sigma_e) \nabla \phi_e) &= -\nabla \cdot (\sigma_i \nabla V_m) + I_e, \end{aligned}$$

where  $V_m = \phi_i - \phi_e$  is the transmembrane potential,  $\phi_i$  and  $\phi_e$  are the intracellular and extracellular potential distributions,  $\beta$  is the average cell's surface to volume ratio,  $C_m$  is the membrane capacitance per unit area,  $\sigma_i$  and  $\sigma_e$  are the intracellular and extracellular conductivity tensors respectively,  $I_e$  is the extracellular current,  $I_{ion}$  is the ionic current density through the membrane, and  $I_{trans}$  is zero.

If variations of  $\phi_e$  are negligible compared to  $\phi_i$ , or if the anisotropy ratios in both domains are the same, then the bidomain equations can be replaced by the simpler monodomain equation (see section 2.3.2),

$$C_m \frac{\partial V_m}{\partial t} = -I_{ion} + \frac{1}{\beta} \nabla \cdot (\sigma_m \nabla V_m),$$

where  $\sigma_m$  is the membrane's conductivity. To allow comparison with [76, 65, 75], for the ionic currents,  $I_{ion}$  we have used a modified [71, 25] version of the Beeler-Reuter-Drouhard-Roberge ionic model [12, 28]. An explanation of the parameters used in our simulations are given in Section 6.1.2.

### 6.1.2 Numerical methods and parameters

All simulations were performed by the Cardiac Arrhythmia Research Package (CARP) [81, 80, 63]. For the ionic current kinetics we use the Beeler-Reuter-Drouhard-Roberge [28] ionic model modified for high amplitude shocks by Skouibine *et al.* [71]. The complete model used in this study is described in Chapter 2 and listed in full in Appendix A.

To generate re-entry, we used a monodomain formulation with time step  $1 \mu s$ . For single shock defibrillation, resonant drift pacing, and constant frequency stimulation, a bidomain formulation was used throughout with time step  $10 \mu s$ .

As in the 2D bidomain study (see Chapter 3) we used simulated fluctuations of

the intracellular conductivities according to

$$\sigma_{ij} = \bar{\sigma}_{ij}(1 + F\eta), \quad (6.1)$$

where  $j = x, y, z$ . The fluctuation intensity was fixed to  $F = 0.5$  and  $\eta \in [-1, 1]$  are independent equidistributed random numbers. To investigate the effect of fluctuations on both single shock defibrillation and resonant drift pacing we tried setting  $F = 0.0$ .

As in [76, 65], we set the intracellular conductivities to  $\bar{\sigma}_{il} = 0.2 \text{ S/m}$  in the longitudinal plane, and  $\bar{\sigma}_{it} = 0.0135 \text{ S/m}$  in the transverse plane. The extracellular conductivities were set to  $\sigma_{el} = 0.3 \text{ S/m}$  in the longitudinal plane, and  $\sigma_{et} = 0.0315 \text{ S/m}$  in the transverse plane. In addition, we set  $\beta = 1400 \text{ cm}^{-1}$  and  $C_m = 1.0 \mu\text{F/cm}^2$  throughout.

For the geometry of the ventricles, we use the UCSD finite element mesh of rabbit ventricles [78]. The ventricles are placed in a surrounding bath with no-flux boundary conditions. The conductance of the perfusing bath was  $g_0 = 0.8 \text{ S/m}$ . The simulations presented in this chapter were calculated on the HPCx national supercomputing facilities [1].

Quantity	Value
Surface to volume ratio	$\beta = 1400 \text{ cm}^{-1}$
Membrane capacitance per unit area	$C_m = 1.0 \mu\text{F/cm}^2$
Extracellular conductivity tensor	$\sigma_e$
... in the transverse plane	$\sigma_{et} = 0.0315 \text{ S/m}$
... in the longitudinal plane	$\sigma_{el} = 0.3 \text{ S/m}$
Intracellular conductivity tensor	$\bar{\sigma}_i(1 + F\eta(x, y, z))$
... in the transverse plane	$\bar{\sigma}_{it} = 0.0135 \text{ S/m}$
... in the longitudinal plane	$\bar{\sigma}_{il} = 0.2 \text{ S/m}$
... fluctuation intensity	$F = 0.5$
... noise	$\eta(x, y, z) \in [-1, 1]$
Bath conductivity	$g_0 = 0.8 \text{ S/m}$
Time discretisation step	$\Delta t = 10 \mu\text{s}$

Table 6.1: Summary of numerical parameters for Chapter 6

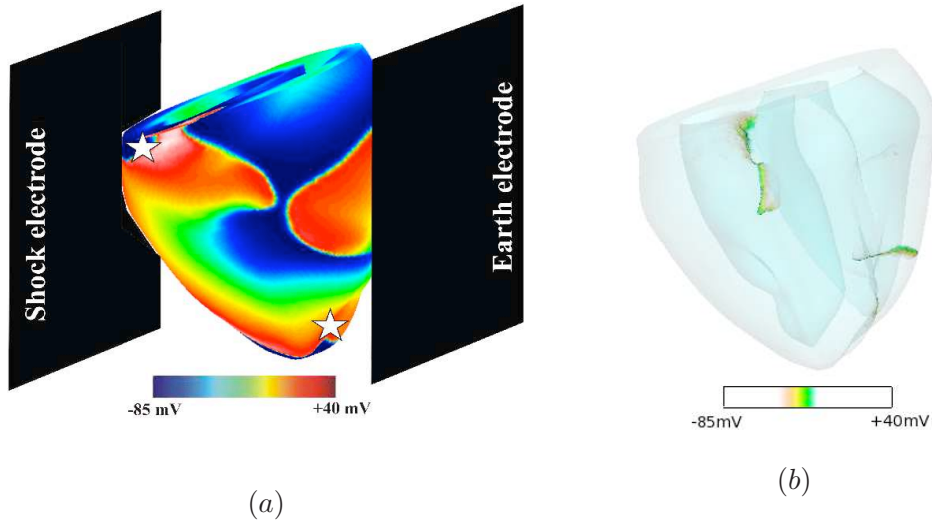


Figure 6.1: (a) Surface view of re-entry in the ventricles with illustration of the location of the shock electrodes. The location of the recording electrodes in the apex of the right ventricle and the base of the left ventricle are illustrated by a star. (b) Visualization of the filaments (yellow/green lines) in translucent ventricles.

### 6.1.3 Visualization

We used CARP’s transmembrane voltage  $V(x, y, z, t)$  output to visualize the results of simulations.

To visualize the surface potentials we used the colour-coding shown in Fig. 6.1(a). The same information was used to detect the scroll wave filaments. The wavefront at time  $t$  was defined as  $V_m = -60\text{mV}$ . Then the filament for that time were visualised as the parts of the wavefront which correspond to  $V_m$  at time  $t - 3\text{ms}$  within a certain range (see Fig. 6.1(b)).

To visualize drift, we used a “stroboscopic” method: we showed positions of the filament synchronized with the signals detected by the registration electrodes.

### 6.1.4 Generation of re-entry patterns

We used an S1-S2 protocol (see Fig. 6.2) to generate a re-entrant wave. An initial wavefront was initiated by stimulating nodes in the apex of the ventricles. After  $t = 140\text{ms}$ , the side of the ventricles were stimulated which causes re-entry due to the refractory period of the initial wavefront. Once re-entry was generated, we allowed evolution for 800 ms (about 11 periods of rotation) to make sure that the re-entry was sustained. We saved the state at  $t = 1000\text{ms}$  and used it as the initial conditions for our simulations.

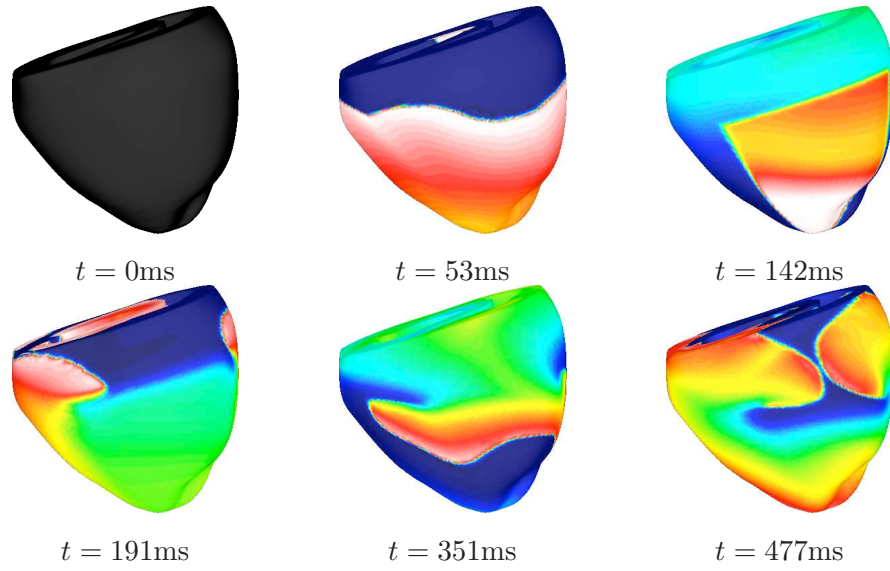


Figure 6.2: Generation of re-entry in rabbit ventricle

### 6.1.5 Single shock defibrillation procedure

Truncated exponential monophasic shocks of duration  $\Delta = 8$  ms were applied via two large planar electrodes located along the lateral faces of the conductive bath (see Fig 6.1(a)). Current was injected into, and withdrawn from, the conductive bath via the shock and earth electrodes respectively,

$$I_e(x, y, z, t) = A \exp\left(-\frac{(t - t_0)}{10}\right) \Theta(t - t_0) \Theta(t_0 + \Delta - t) [\chi_s(x, y, z) - \chi_e(x, y, z)].$$

Here  $\Theta()$  is the Heaviside step function,  $t_0$  is the time of the shock application, and  $\chi_s(x, y, z)$  and  $\chi_e(x, y, z)$  are equal to 1 within the shock and earth electrodes and equal to 0 otherwise.

We varied the shock amplitude until we found the value which terminated all re-entrant waves. A single shock was deemed successful if no re-entry was detectable at the moment 200ms after its end.

### 6.1.6 Resonant drift pacing procedure

Repetitive low-amplitude shocks of the same waveform and via the same *stimulating* electrodes as above were applied at the time moments determined by signals received via *registration* electrodes.

Two different locations for the registration electrodes were used: “point” electrodes  $0.02 \times 0.02 \times 0.02 \text{ cm}^3$  in the apex of the right ventricle and the base of the left ventricle (see Fig. 6.1).

A shock was applied immediately,  $t_{delay} = 0$ , when the average potential of the registration electrode exceeded  $-55$  mV.

With the understanding we now have from Chapter 3 about the possible ‘*loops*’ [56] which may occur, we introduce a delay  $t_{delay} = 20$  ms (about a third of the re-entry period) when the resonant drift pacing is unsuccessful.

To allow post-shock evolution, the registration electrodes were de-activated for a “blanking time”  $t_{blank} = 50$  ms after a shock application.

Resonant drift pacing was considered successful if all scrolls were terminated sooner than their self-termination time, 4000 ms.

### 6.1.7 Constant frequency stimulation procedure

In Chapter 4 we saw that in the Barkley model of excitable media, constant frequency forcing can sometimes terminate the scroll waves faster than resonant drift pacing. To investigate this effect in this anatomically accurate bidomain model of cardiac tissue, we use constant frequency shocks of the same waveform and via the same *stimulating* electrodes as described in section 6.1.5.

We chose the frequency of the shocks with the understanding which we now have of *resonant windows* (see Chapter 4 and [54]). We used;

- The mean frequency of the unperturbed re-entry  $\bar{\omega}_0$ . We allowed the unperturbed re-entry to evolve in the monodomain model, until it self-terminated after a further 4000 ms, and calculated  $\bar{\omega}_0$  by taking the mean frequency over the 4000 ms duration.
- The mean frequency of the perturbed re-entry  $\tilde{\omega}_0(A, \Omega)$ , which depends on the forcing amplitude  $A$ , and the forcing frequency  $\Omega$  [54]. By definition,  $\tilde{\omega}_0(0, \Omega) = \omega_0$  for any  $\Omega$ . We calculated  $\tilde{\omega}_0(A, \Omega)$  using data obtained in resonant drift pacing simulations.

Constant frequency stimulation was considered successful if all scrolls were terminated sooner than their self-termination time, 4000 ms.

## 6.2 Results

### 6.2.1 Single shock defibrillation results

We varied the strength,  $A$ , of the single shocks to find the threshold amplitude for terminating all re-entrant waves. If the shock amplitude was above the threshold, then all re-entry were annihilated immediately (see Fig. 6.3(a)). Shocks with amplitude below (but sufficiently close to) the threshold led to multiple wavebreaks (see Fig. 6.3(b)).

We found the single shock success threshold to be between  $28 \times 10^5 \mu\text{A}/\text{cm}^3$  and  $29 \times 10^5 \mu\text{A}/\text{cm}^3$  when  $F = 0.5$ . When we set the level of intracellular conductivity fluctuations to  $F = 0.0$  the single shock success threshold was found to be greater than  $100 \times 10^5 \mu\text{A}/\text{cm}^3$ .

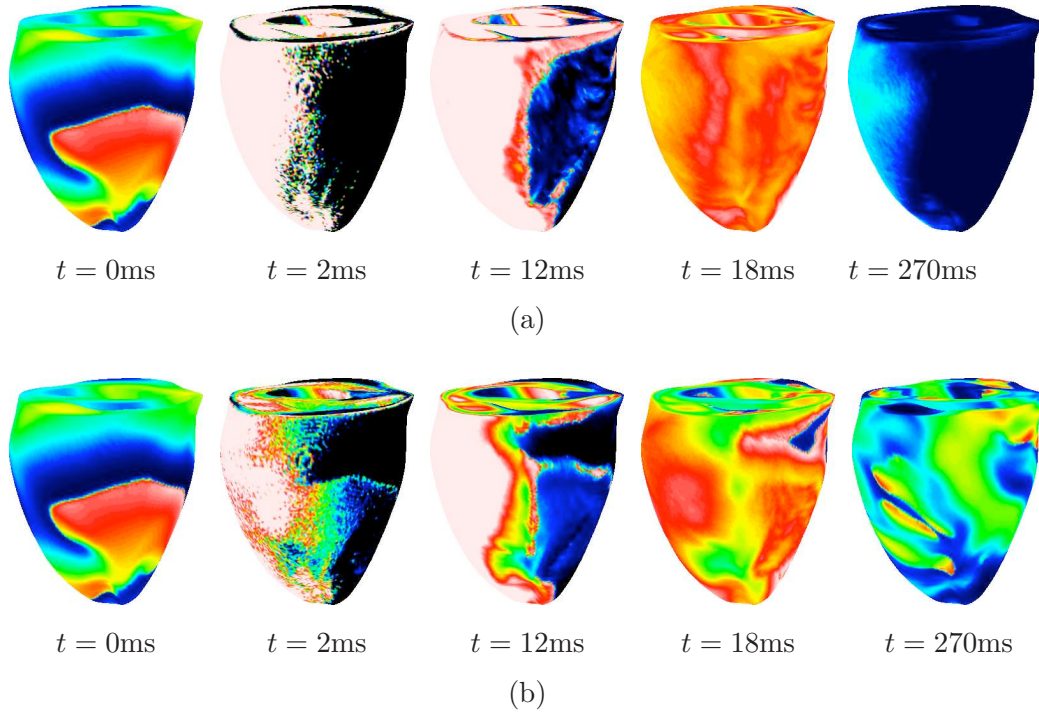


Figure 6.3: **Single shock defibrillation** in the rabbit ventricle: (a) Termination,  $A = 30 \times 10^5 \mu\text{A}/\text{cm}^3$  applied at time  $t = 1$ . (b) Breakup,  $A = 25 \times 10^5 \mu\text{A}/\text{cm}^3$  applied at time  $t = 1$ . The level of intracellular conductivity fluctuations was set to  $F = 0.5$ .

### 6.2.2 Resonant drift pacing results

Table 6.2 shows the termination times using resonant drift pacing when  $F = 0.5$ . We have observed that with the recording point located in the base of the left ventricle, we did not see termination for the amplitudes which we used. When the recording point was located in the apex of the right ventricle, resonant drift pacing was successful for shock amplitudes higher than  $2.5 \times 10^5 \mu\text{A}/\text{cm}^3$ .

A	Apex of right ventricle	Base of left ventricle
$1 \times 10^5 \mu\text{A}/\text{cm}^3$	> 4000 ms	> 4000 ms
$2 \times 10^5 \mu\text{A}/\text{cm}^3$	> 4000 ms	> 4000 ms
$2.5 \times 10^5 \mu\text{A}/\text{cm}^3$	1336 ms	> 4000 ms
$3 \times 10^5 \mu\text{A}/\text{cm}^3$	1216 ms	> 4000 ms
$3.5 \times 10^5 \mu\text{A}/\text{cm}^3$	1275 ms	> 4000 ms

Table 6.2: **Resonant drift pacing results:** Raw data showing whether each combination of shock amplitude and registration electrode location yielded termination. If termination was observed then the termination time is listed, otherwise we denote an unsuccessful termination within the allowed 4000 ms as ‘> 4000 ms’.

#### Apex location of registration electrode

Figure 6.4 presents images taken from a simulation of successful elimination of fibrillation, achieved in about  $t = 1.2$  s, after  $n = 30$  shocks of amplitude  $3 \times 10^5 \mu\text{A}/\text{cm}^3$ . The registration electrode is located near to the apex of the right ventricle.

Initially, two separate filaments exist. One connects the base of the ventricles to the inner ventricular wall (the ventricular septum) and the other curves around the apex of the right ventricle. After two shocks, the two individual filaments join together creating a single filament connecting the base of the ventricles to the outer ventricular wall near the apex of the right ventricle (which is close to the registration electrode). After 7 shocks have been applied, the ‘base end’ of this single filament starts to move down the inner ventricular wall whilst the ‘apex end’ of this filament remains relatively stationary. After a further 3 shocks, this single filament has reduced in length and now connects the inner wall near the apex of the right ventricle with the outer wall near the apex of the right ventricle. One further shock terminates this filament by drawing the two ends of the filament together, in turn shortening the filament until it collapses.



However, after the termination of the single filament a further 5 shocks are applied by the feedback algorithm. This is due to the wavefronts propagating past the registration electrode on their way to termination at the ventricular wall. Fig. 6.5 illustrates the final 343 ms of this simulation. Each shock in turn generates a small scroll wave on the side of the ventricle that the shock is applied. These newly generated filaments only survive for one rotation before collapsing. After the final shock, no new scroll wave is generated and so the feedback algorithm is not triggered to apply another shock.

We observed that when using the apex location for the registration electrode, resonant drift pacing is successful for shock amplitudes greater than  $2.5 \times 10^4 \mu\text{A}/\text{cm}^3$ .

### **Base location of registration electrode**

Figure (6.6) presents images taken from a simulation of resonant drift pacing with the registration electrode located at the base of the left ventricle. No termination was observed after 4000 ms which was enough time for 58 shocks of amplitude  $3 \times 10^5 \mu\text{A}/\text{cm}^3$ .

A possible reason for this particular simulation failing is the existence of a helical shaped filament. After 10 shocks, a helical filament has evolved which connects the base of the left ventricle (which is the location of the registration electrode) with the apex of the left ventricle. This helix persists, and its movement is limited, for the next 20 shocks. During these 20 shocks, additional scroll waves are generated. Eventually another scroll captures control of the feedback algorithm which causes shocks to be applied in resonance with this new scroll, and not anymore with the helix, allowing the helical filament to move. After 4000 ms filaments still exist so we stopped and considered this particular case to have failed. Perhaps, if the helix had not persisted we would have observed termination of all scrolls within the time allocated.

To highlight that what we observe is in fact a helical filament, Fig 6.7 shows the state of the system at time  $t = 1414\text{ms}$  but with the ventricle rotated at different angles.

We did not observe any successful terminations whilst using the registration electrode in the base of the left ventricle.

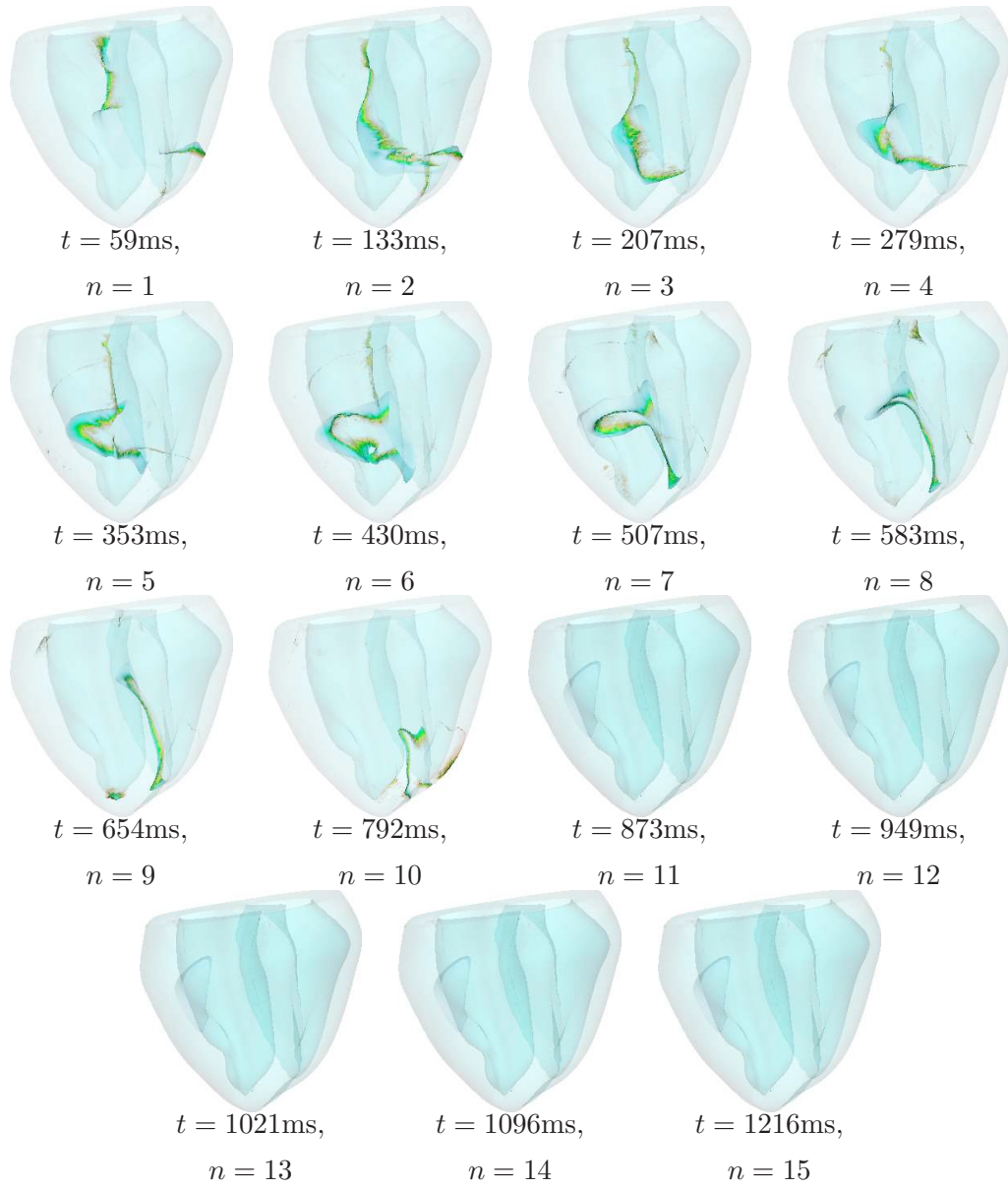


Figure 6.4: **Resonant drift pacing** in a rabbit ventricle with  $A = 3 \times 10^5 \mu\text{A}/\text{cm}^3$  and  $F = 0.5$ . The registration electrode is positioned in the apex of the right ventricle. The green lines represent the filaments and  $n$  denotes the number of shocks applied so far. For  $n = 11$  to  $n = 15$  there are no filaments but shocks are still being applied, see Fig 6.5 for an explanation of how further shocks are triggered.

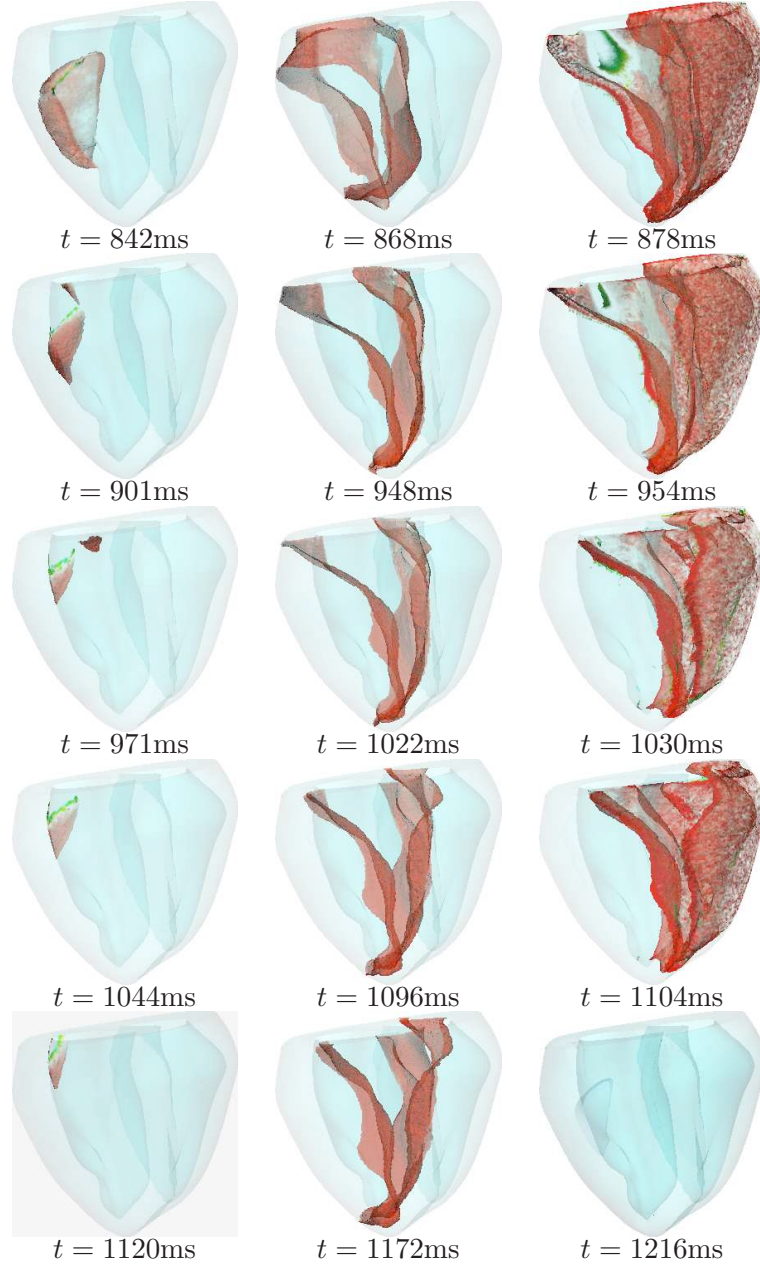


Figure 6.5: The final 343 ms of the simulation presented in Fig. 6.4. New wavefronts (shown in red) are generated by the shocks. These in turn trigger another shock as they pass the registration electrode. After each shock, a small filament is generated near the base of the right ventricle but quickly self terminates. Eventually, no new wavefronts are initiated by the shock.

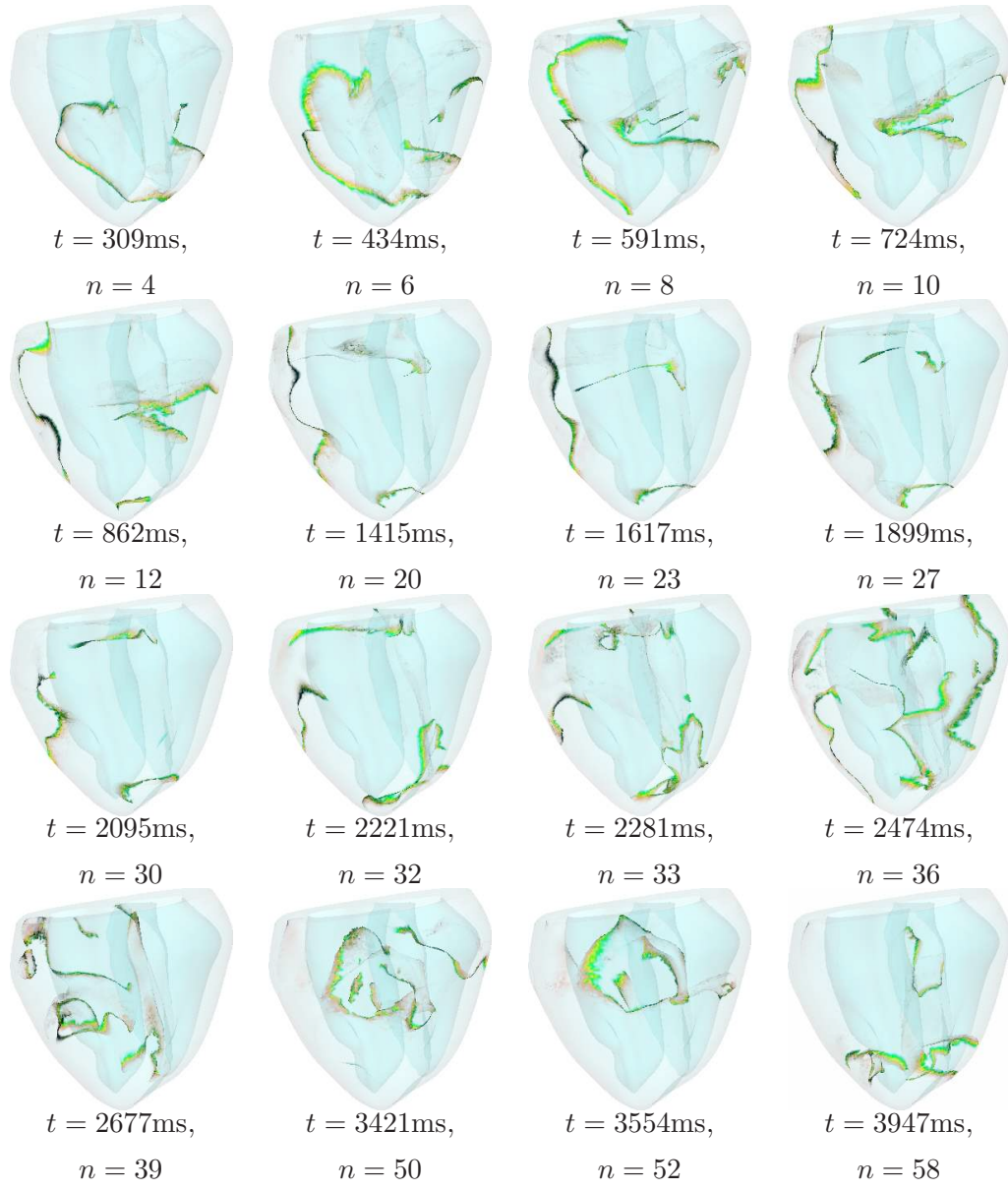


Figure 6.6: **Resonant drift pacing** of scroll waves in a rabbit ventricle with  $A = 3 \times 10^5 \mu\text{A}/\text{cm}^3$  and  $F = 0.5$ . The registration electrode is positioned in the base of the left ventricle. The green lines represent the filaments.  $n$  denoted the number of shocks applied so far.

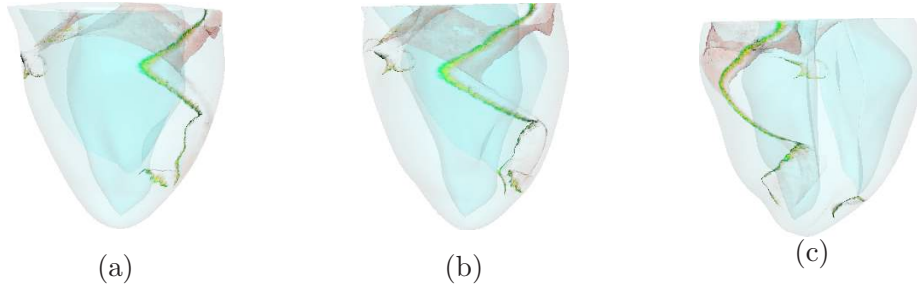


Figure 6.7: Helical filament in rabbit ventricles. This is the state  $t = 1415$  ms from Fig. 6.6 visualised from different angles.

### 6.2.3 Using a time delay to induce success

As discussed in Chapter 3, of all the mentioned parameters,  $t_{delay}$  is the easiest to change, and it may even be adjusted in real time, during pacing. We found in this earlier study that a change of the feedback delay may be used to discontinue an infinite loop even after it has already started.

To this if this would help in this three-dimensional model, we re-ran the simulation presented in Fig 6.6. Originally with  $t_{delay} = 0$  ms we observed the evolution of a helical filament which refuses to terminate. Now we increased  $t_{delay}$  to 20 ms at  $t = 1414$  ms. This allowed termination of all filaments after a further 13 shocks, see Fig 6.8.

### 6.2.4 Effect of conductivity fluctuations on resonant drift pacing

To investigate whether the fluctuation intensity effects the outcome of resonant drift pacing we set the fluctuation intensity to be zero  $F = 0.0$ , so that the intracellular conductivities remained constant,  $\sigma_{ij} = \bar{\sigma}_{ij}$ .

Fig. 6.9 shows the effect of applying resonant drift pacing with shock amplitude  $A = 3 \times 10^5 \mu\text{A}/\text{cm}^3$  where the registration electrode is located in the apex of the right ventricle. This simulation is equivalent to that depicted in Fig. 6.4 but here we have no conductivity fluctuations.

Termination is achieved in  $t = 1112$  ms using the same amplitude which was successful for resonant drift pacing with  $F = 0.5$ . Therefore it appears that the resonant drift pacing success threshold remains unchanged for different fluctuation intensities. For constant intracellular conductivity, we found the single-shock defibrillation success threshold to be at least  $A = 100 \times 10^5 \mu\text{A}/\text{cm}^3$ . This is more than 33 times higher than the resonant drift pacing success threshold.

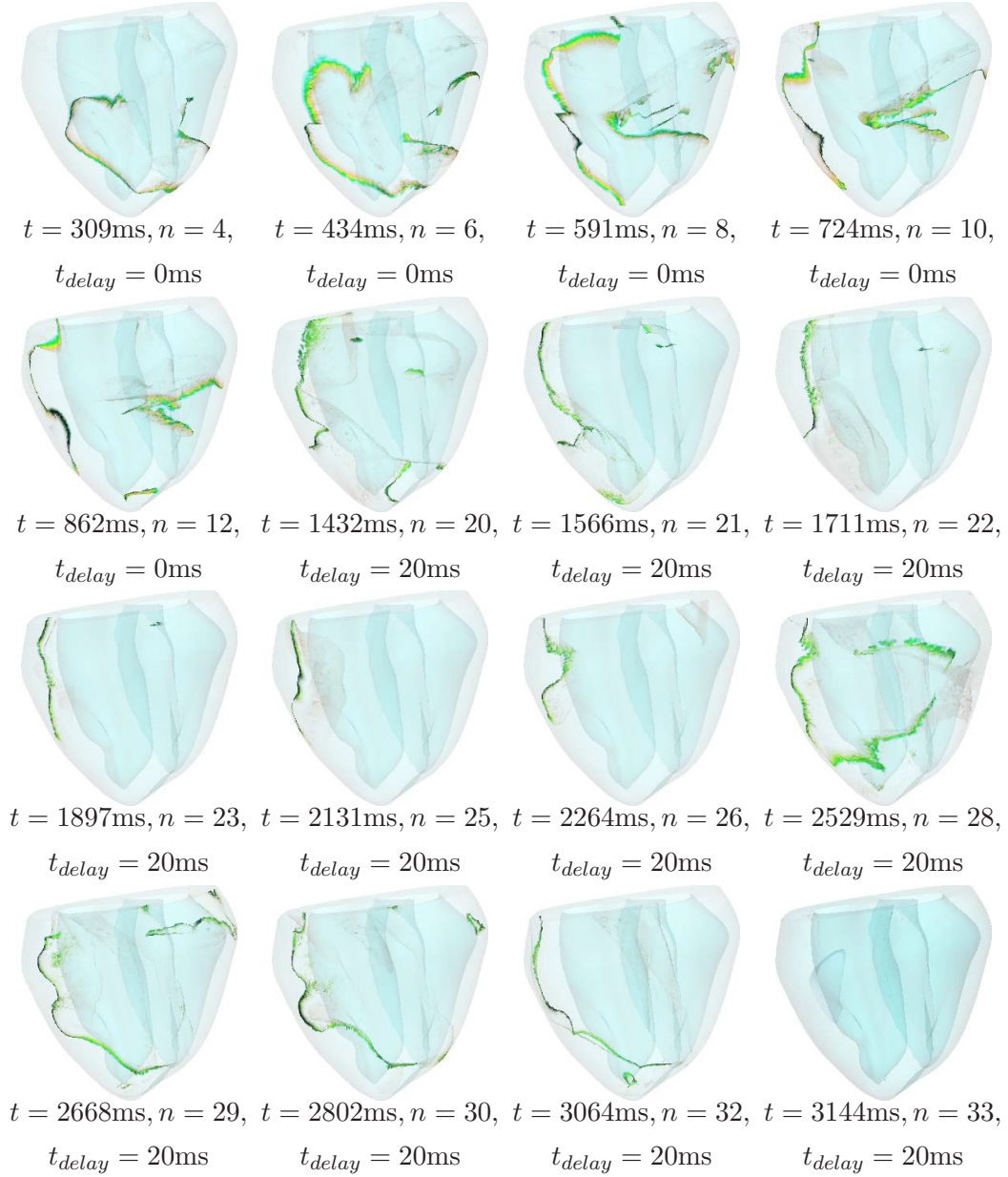


Figure 6.8: Using a **time delay** to induce success: we intervene the simulation from Fig. 6.6 at  $t = 1400\text{ms}$  and introduce a time delay  $t_{\text{delay}} = 20\text{ms}$ . After a further 14 shocks all re-entrant waves are terminated.



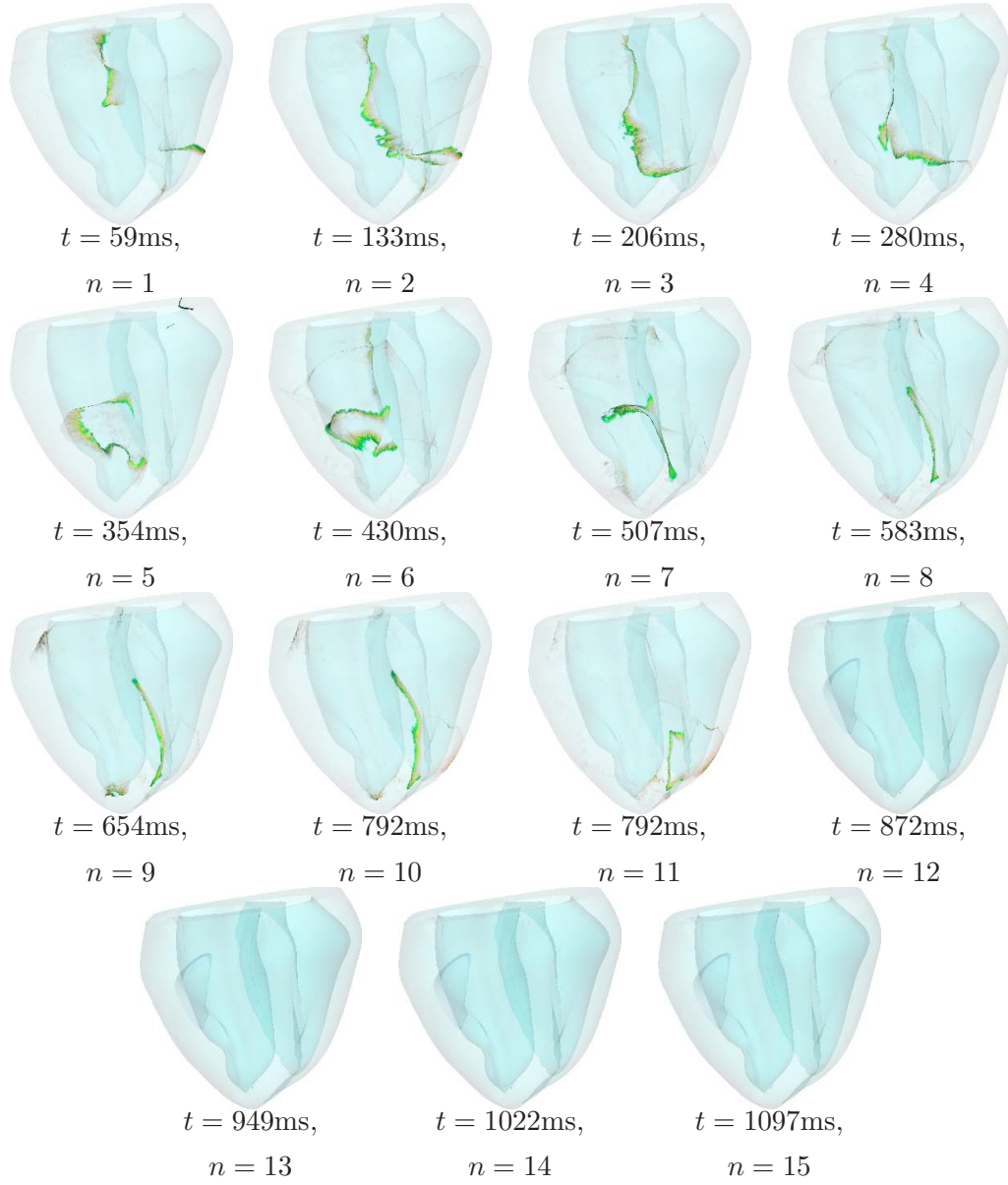


Figure 6.9: **Resonant drift pacing** in a rabbit ventricle with no conductivity fluctuations. This figure is equivalent to Fig. 6.4 but here we have set  $F = 0.0$ .

### 6.2.5 Constant frequency perturbation results

We calculated the mean frequency of the unperturbed re-entry  $\bar{\omega}_0$  by using the monodomain model to simulate the evolution of the re-entrant wave for a further 4000 ms. We found  $\bar{\omega}_0 = 67$  ms. To calculate the mean frequency of the perturbed re-entry  $\tilde{\omega}_0(A, \Omega)$  we used the data obtained from our resonant drift pacing simulations. We found that  $\tilde{\omega}_0(3 \times 10^6, \Omega) = 74$  ms when using the apex location for the registration electrode, and  $\tilde{\omega}_0(3 \times 10^6, \Omega) = 69$  ms when using the base location.

For shock amplitude  $A = 3 \times 10^6 \mu\text{A}/\text{cm}^3$  we did not observe termination of re-entry using any of the defined constant frequencies within  $t = 1216$  ms, which is the time taken for successful termination using resonant drift pacing with the same amplitude. Fig. 6.10 illustrates the simulation where we used the constant frequency  $\tilde{\omega}_0(3 \times 10^6, \Omega) = 74$  ms. In this example the filaments are moved about the ventricles in no particular direction. Termination was not observed after  $t = 1258$  ms.

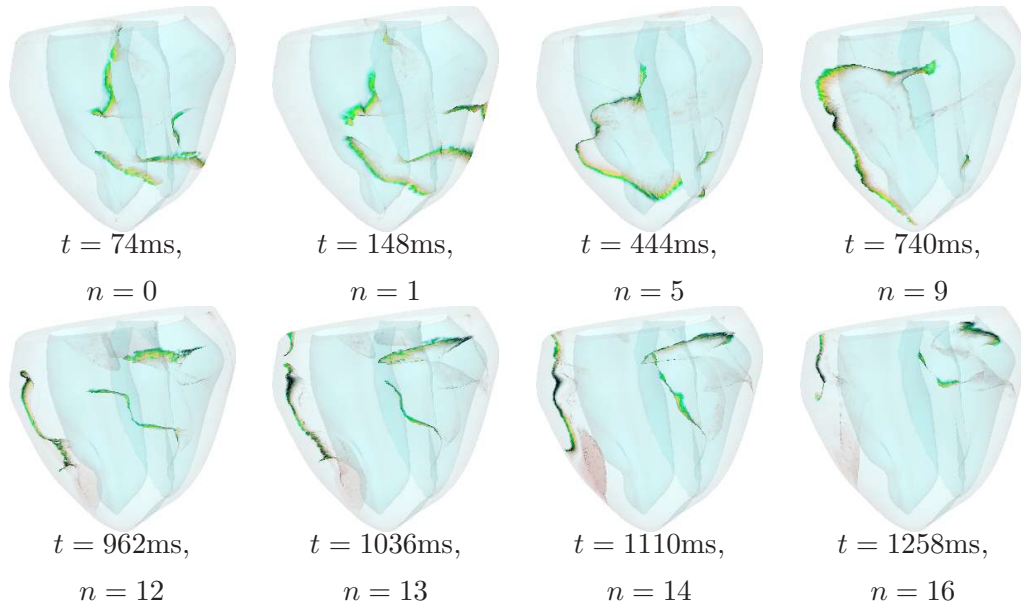


Figure 6.10: **Constant frequency stimulation** in the rabbit ventricle with shock amplitude  $A = 3 \times 10^5 \mu\text{A}/\text{cm}^3$ , frequency  $\tilde{\omega}_0(3 \times 10^6, \Omega) = 74$  ms, and  $F = 0.5$ . The green lines represent the filaments and  $n$  denotes the number of shocks applied so far. We do not observe complete termination of the re-entrant activity, just movement of the filaments to different regions of the ventricles.



### 6.3 Summary

The goal of this study was to investigate the effectiveness of using resonant drift pacing in an anatomically realistic, bidomain model, of a ventricle. The principle skepticism of experimentalists on the use of RDP as a method for low-energy defibrillation, was knowing where the inexcitable boundaries would be in the anatomy of a real heart. Experimentalists feared that if resonant drift was possible, then the re-entry would probably just move around the circumference of the ventricles. In this study we have used two locations for the registration electrode to observe the effect of resonant drift pacing.

In our simulations, resonant drift pacing can eliminate all re-entrant activity using shock amplitudes one order of magnitude lower than single shock defibrillation. Allowing 4s for low-energy re-entry termination, the required shock strength with resonant drift pacing is 12 times smaller than with single shock when  $F = 0.5$ , and at least 40 times smaller when  $F = 0.0$ . Success depends on the location of the registration electrode. It appears that when the registration electrode is positioned in the apex of the right ventricle, resonant drift pacing is the most effective. This is very convenient because current ICD's already position electrodes in the apex of the right ventricle to detect abnormal activity.

We did not observe any successful termination of re-entrant waves using constant frequency stimulation. This is in contrast to what we observed in Chapter 4 where for certain frequencies constant frequency stimulation terminated re-entry faster than resonant drift pacing. The observed difference could be due to the model or due to the vast amount of data which we obtained in Chapter 4.

Our data suggests that microscopic fluctuations of the intracellular conductivity have little effect on the outcome of resonant drift pacing. We also show that difficulties can occur when using resonant drift pacing. We found that when using the registration electrode in the base of the left ventricle, helical filaments can occur which fail to move under resonant drift pacing, allowing additional scroll waves to be generated from shocks. However, we have found that in this situation, adjusting the time delay  $t_{delay}$  between signal registration and shock application manages to overcome this difficulty and eventually terminated all re-entrant activity. Therefore, when difficulties occur, the value of  $t_{delay}$  can be varied during simulation, or in clinical practice, as an alternative to applying a high-energy single shock.

# Chapter 7

## Conclusions

In this Chapter I summarise the main findings in this thesis and suggest further directions of research.

### 7.1 Main results

#### **Resonant drift pacing in a bidomain model of cardiac tissue**

- In a bidomain model of cardiac tissue, with microscopic conductivity fluctuations, re-entrant waves can be annihilated using feedback-driven resonant drift pacing by directing the re-entry towards an inexcitable boundary, or towards each other.
- Termination using this approach is achieved, with high probability, at a fraction of the conventional shock strength.
- The direction of the drift can be managed by choosing the location of the registration electrodes and the time delay of the shock application.
- A line registration electrode positioned along the fibres is the most successful setup for resonant drift pacing in this model setting.
- Adjusting the time delay of shock application can successfully exit problematic loops (formed by the generation of new wavefronts from shock electrodes) and terminate all re-entrant waves.
- The level of intracellular conductivity fluctuations has little effect on the success or failure of resonant drift pacing.

## Resonant drift pacing in a three-dimensional monodomain model of excitable media

- In a three-dimensional monodomain model of excitable media, scroll wave turbulence can be annihilated using feedback-driven or constant frequency resonant drift pacing.
- Termination using this approach is achieved, with high probability, at a fraction of the conventional shock strength.
- The resonance between the constant frequency forcing and the scrolls is characterised not by a single resonant frequency, but by a resonant window which depends on the type of forcing and its amplitude.
- The fastest termination was achieved when the forcing was applied using either feedback-driven resonant drift pacing or with a constant frequency chosen within the resonant window.
- For lower amplitudes there exists a false resonance which is where formally defined resonant windows are abnormally extended towards higher frequencies but are not associated with fast and reliable termination.

## Theory of perturbed scroll waves

- Equations of motion for a perturbed general, twisted, scroll wave are developed.
- The equations are presented in both scalar and vector formats.
- These new equations of motion are applied to particular cases of scroll ring and helical shaped filament.
- The scroll ring example shows that resonant drift pacing may cause collapsing rings to expand or expanding rings to collapse.
- The helical filament example demonstrates that it may be possible to have a stationary (i.e. non-expanding and non-collapsing) helical scroll when the filament tension and the resonant drift compensate each other.

## Resonant drift pacing in a anatomically accurate bidomain model of cardiac tissue

- In an anatomically accurate bidomain model of cardiac tissue, with microscopic conductivity fluctuations, scroll waves can be annihilated using feedback-driven resonant drift pacing by directing the re-entry towards an inexcitable boundary.
- Termination using this approach is achieved, with high probability, at a fraction of the conventional shock strength.
- The direction of the drift can be managed by choosing the location of the registration electrodes.
- A point registration electrode positioned near the apex of the right ventricle is a more successful location than the base of the left ventricle.
- Adjusting the time delay of shock application can induce successful termination when resonant drift pacing fails.
- Feedback-driven resonant drift pacing preforms better than resonant constant frequency stimulation.
- Lowering the level of intracellular conductivity fluctuations dramatically increases the single shock success threshold. However, the fluctuation intensity has little effect on the success or failure of resonant drift pacing.

## 7.2 Clinical implications

In clinical practice, antitachycardia-pacing (ATP) is as efficient and as safe as single shock defibrillation for fast ventricular tachycardias up to 250 beats/min [83]. The exact mechanisms underlying success or failure of ATP are widely unexplored. Based on insights gained in this thesis it can be hypothesised that the electric field established by ATP interacts with a re-entrant wave and that with each pulse the organizing center of the re-entry is shifted in space. Since ATP relies on a fixed frequency (just like the constant frequency forcing used in Chapters 4, and 6), the induced drift is likely to be random. With resonant drift pacing, a core can be moved in any desired direction which may lead to termination within shorter time.

It is conceivable that low-energy defibrillation techniques, such as ATP, are in fact relying on resonant drift of the re-entry without realising it. Although the probability of ATP success is high, when it fails a single strong shock has to be applied. Our results show that if resonant drift pacing fails then introducing a time delay between the shock trigger and application can induce success.

Resonant drift pacing can potentially perform more efficiently than ATP due to the feedback mechanism. Therefore, resonant drift pacing could be applicable as a new approach for managing atrial or ventricular fibrillation.

### 7.3 Further directions of research

We hope that the data presented in this thesis will motivate experimentalists to test resonant drift pacing as a new approach for low-energy defibrillation. The use of numerical simulations (such as those presented in this thesis) may provide an invaluable tool in such studies. Following our presentation at Cardiosim 2008 [55], a leading ICD manufacturer *Sorin Group* [3] have already shown an interest in the results from this thesis.

Further directions of research include,

- Finding the optimum shock waveform and registration electrode geometries so that new wavefronts are not produced by stimulating shocks,
- Further investigating the optimum location for the recording point used by resonant drift pacing. We hypothesise that perhaps a line registration electrode (as used in Chapter 3) may also be the optimum form the ventricles,
- Developing the theory for resonant drift of multiple scroll waves - including scroll wave turbulence,
- Testing resonant drift-pacing through optical mapping studies and experiments using cell-cultures.

## Appendix A

# Modified Beeler-Reuter-Drouhard-Roberge model

Here we present the full modified Beeler-Reuter-Drouhard-Roberge model used in Chapter 6.

### Total transmembrane current

$$I_m = C_m \frac{\partial V_m}{\partial t} + i_{K_1} + i_{x_1} + i_{Na} + i_s + i_{ep}.$$

### Electroporation current

$$i_{ep} = g_p N(V_m, t) V_m,$$

where, the number of pores per unit area,  $N(V_m, t)$ , is governed by a first order differential equation

$$\frac{dN}{dt} = \alpha e^{\beta(V_m)^2} \left( 1 - \frac{N}{N_0} e^{-q\beta(V_m)^2} \right),$$

and the conductance  $g_p$  is modelled as an instantaneous function of transmembrane potential

$$g_p(V_m) = \frac{\pi h \sigma}{4} (e^{v_m} - 1) \left( e^{v_m} \frac{w_0 e^{(w_0 - n v_m)}}{w_0 - n v_m} - \frac{w_0 e^{(w_0 + n v_m)} + n v_m}{w_0 + n v_m} \right)^{-1},$$

where  $v_m$  is the non-dimensional transmembrane potential  $v_m \equiv V_m(e/KT)$ .

## Ionic currents

$$i_{K1} = 1.4 \frac{\exp(0.04[V_m + 85]) - 1}{\exp(0.08[V_m + 53]) + \exp[0.04(V_m + 53)]} + 0.07 \frac{V_m + 23}{1 - \exp[-0.04(V_m + 23)]},$$

$$\bar{i}_{x1} = \frac{0.8x_1(\exp[0.04(V_m + 77)] - 1)}{\exp[0.04(V_m + 35)]},$$

$$i_{Na} = m^3 h \bar{g}_{Na} (V_m - E_{Na}),$$

$$i_s = \bar{g}_s df(V_m - E_s),$$

where  $E_s = -82.3 - 13.0287 \ln[Ca]_i$  mS/cm<sup>2</sup>.

## Gating Variables

$$\frac{dy}{dt} = \alpha_y(1 - y) - \beta_y y, \quad y = x_1, m, h, d, f.$$

## Ionic current activation and inactivation gate rates

$$\alpha_d = 0.095 \frac{\exp[-0.01(V_m - 5)]}{\exp[-0.072(V_m - 5)] + 1} k,$$

$$\beta_d = 0.07 \frac{\exp[-0.017(V_m + 44)]}{\exp[-0.05(V_m + 44)] + 1} k,$$

$$\alpha_f = 0.012 \frac{\exp[-0.008(V_m + 28)]}{\exp[-0.15(V_m - 28)] + 1} k,$$

$$\beta_f = 0.0065 \frac{\exp[-0.06(V_m + 30)]}{\exp[-0.2(V_m + 30)] + 1} k,$$

$$\alpha_m = \begin{cases} 0.9 \frac{V_m + 42.65}{1 - \exp[-0.22V_m - 9.3830]}, & V_m < 100 \text{ mV} \\ 890.9437890 \frac{\exp[0.0486479V_m - 4.8647916]}{1 + 5.93962526 \exp[0.0486479V_m - 4.8647916]}, & V_m \geq 100 \text{ mV} \end{cases}$$

$$\beta_m = \begin{cases} 1.437 \exp[-0.085V_m - 3.37875], & V_m \leq -85 \text{ mV} \\ \frac{100}{1 + 0.4864082 \exp[0.2597504V_m + 22.0787804]}, & V_m > -85 \text{ mV} \end{cases}$$

$$\alpha_h = \begin{cases} 0.1 \exp[-0.193V_m - 15.37245], & V_m \leq -90 \text{ mV} \\ -12.0662845 - 0.1422598V_m, & V_m > -90 \text{ mV} \end{cases}$$

$$\beta_h = \frac{1.7}{1 + \exp[-0.095V_m - 1.9475]}$$

$$\alpha_{x_1} = \begin{cases} 0.0005 \frac{\exp[0.083V_m + 4.150]}{1 + \exp[0.057V_m + 2.850]}, & V_m < 400 \text{ mV} \\ 151.7994692 \frac{\exp[0.0654979V_m - 26.1871448]}{1 + 1.5179947 \exp[0.0654679V_m - 26.1871448]}, & V_m \geq 400 \text{ mV} \end{cases}$$

$$\beta_{x_1} = 0.0013 \frac{\exp[-0.06V_m - 1.20]}{1 + \exp[-0.04V_m - 0.80]}.$$

### Calcium concentration

$$\frac{d[Ca]_i}{dt} = \begin{cases} -10^{-7}i_s + 0.07(10^{-7} - [Ca]_i), & V_m < 200 \text{ mV} \\ 0, & V_m \geq 200 \text{ mV} \end{cases}$$

### Constants

Below is a table summarising the constants used in this modified Beeler-Reuter-Drouhard-Roberge model,

Quantity	Value
Membrane capacitance	$C_m = 1.0 \mu\text{F}/\text{cm}^2$
Rate constant of electroporation	$\alpha = 200.0 \text{ cm}^{-2}\text{ms}^{-1}$
Rate constant of electroporation	$\beta = 6.25 \times 10^{-5} \text{ mV}^{-2}$
Rate constant of electroporation	$q = 2.46$
Number of pores per unit area when $V_m = 0$	$N_0 = 1.5 \times 10^5 \text{ cm}^{-2}$
<i>continued on next page ...</i>	



... continued from previous page	
Quantity	Value
Membrane thickness	$h = 5.0 \text{ nm}$
Conductivity of aqueous solution in pores	$\sigma = 30.0 \text{ mS/cm}$
Energy barrier within pore	$w_0 = 5.25 \text{ kT}$
Relative entrance of length of pores	$n = 0.15$
Temperature	$T = 37^\circ \text{C}$
Boltzmann constant	$K = 1.38066 \times 10^{-20} \text{ mJ/K}$
Charge on an electron	$e = 1.6021765 \times 10^{-19} \text{ C}$
Slow inward current coefficient	$k = 8$
Na equilibrium potential	$E_{Na} = 40 \text{ mV}$
Na conductance	$g_{Na} = 15 \text{ mS/cm}^2$
S conductance	$g_{Na} = 15 \text{ mS/cm}^2$

Table A.1: Values of the constants used in our modified BRDR model

## Appendix B

# Modified Courtemanche model

Here we present the full modified Courtemanche model used in Chapter 3.

### Total transmembrane current

$$\begin{aligned} I_m = & C_m \frac{\partial V_m}{\partial t} + i_{Na} + i_{K1} + i_{to} + i_{Kur} + i_{Kr} + i_{Ks} + i_{Ca,L} \\ & + i_{p,Ca} + i_{NaK} + i_{NaCa} + i_{b,Na} + i_{b,Ca} + i_{K(ACH)} + i_{ep}. \end{aligned} \quad (B.1)$$

### Electroporation current

$$i_{ep} = G(V_m, t)V_m,$$

where

$$\frac{dG}{dt} = a \exp[b(V_m - V_{rest})^2](1 - \exp[-c(V_m - V_{rest})^2]).$$

### Intracellular concentrations

The intracellular concentrations of sodium  $Na^+$ , potassium  $K^+$ , and calcium  $Ca^{2+}$  are implemented through the equations

$$\begin{aligned} \frac{d[Na^+]_i}{dt} &= \frac{-3i_{NaK} - 3i_{NaCa} - i_{b,Na} - i_{Na}}{FV_i}, \\ \frac{d[K^+]_i}{dt} &= \frac{2i_{NaK} - i_{K1} - i_{to} - i_{Kur} - i_{Kr} - i_{Ks} - i_{b,K}}{FV_i}, \\ \frac{d[Ca^{2+}]_i}{dt} &= \frac{B1}{B2}, \end{aligned}$$

$$B1 = \frac{2i_{NaCa} - i_{p,Ca} - i_{Ca,L} - i_{b,Ca}}{2FV_i} + \frac{V_{up}(i_{up,leak} - i_{up}) + i_{rel}V_{rel}}{V_i},$$

$$B2 = 1 + \frac{[Trpn]_{max}K_{m,Trpn}}{([Ca^{2+}]_i + K_{m,Trpn})^2} + \frac{[Cmdn]_{max}K_{m,Cmdn}}{([Ca^{2+}]_i + K_{m,Cmdn})^2}.$$

The calcium concentration in release compartment and uptake compartment are given by the formulae

$$\begin{aligned} \frac{d[Ca^{2+}]_{up}}{dt} &= i_{up} - i_{up,leak} - i_{tr} \frac{V_{rel}}{V_{up}}, \\ \frac{d[Ca^{2+}]_{rel}}{dt} &= (i_{tr} - i_{rel}) \left[ 1 + \frac{[Csqn]_{max}K_{m,Csqn}}{([Ca^{2+}]_{rel} + K_{m,Csqn})^2} \right]^{-1}. \end{aligned}$$

**$Ca^{2+}$  buffers.**

$$\begin{aligned} [Ca^{2+}]_{Cmdn} &= [Cmdn]_{max} \frac{[Ca^{2+}]_i}{[Ca^{2+}]_i + K_{m,Cmdn}}, \\ [Ca^{2+}]_{Trpn} &= [Trpn]_{max} \frac{[Ca^{2+}]_i}{[Ca^{2+}]_i + K_{m,Trpn}}, \\ [Ca^{2+}]_{Csqn} &= [Csqn]_{max} \frac{[Ca^{2+}]_i}{[Ca^{2+}]_i + K_{m,Csqn}}. \end{aligned}$$

## Equilibrium potentials

The equilibrium potentials are calculated from the equation

$$E_X = \frac{RT}{zF} \log \frac{[X]_o}{[X]_i}, \quad X = Na, K, Ca^{2+}.$$

## Ionic currents and gating variables

The gating variables are calculated using

$$\frac{dy}{dt} = \frac{y_{\infty} - y}{\tau_y}, \quad y = m, h, j, o_a, o_i, u_a, u_i, x_r, x_s, d, f, f_{Ca}, u, v, w.$$

We will now explain how each of these ionic currents are modelled and give the values for the ionic conductances  $g_{ion}$  and the gate opening  $\alpha$  and closing rate constants  $\beta$  for the ionic channels.

## ACh dependent potassium current

$$i_{K(ACh)} = \left[ \frac{10}{1 + \frac{9.13652}{[ACh]^{0.477811}}} \right] \left[ 0.0517 + \frac{0.4516}{1 + \exp \left[ \frac{V_m + 59.53}{17.18} \right]} \right] (V - E_K).$$

**Fast sodium  $Na^+$  current.**

$$i_{Na} = g_{Na} m^3 h j (V_m - E_{Na}), \quad g_{Na} = 7.8,$$

The gate opening and closing rate constants for the  $Na^+$  channel are defined as

$$\alpha_m = \begin{cases} 0.32 \frac{V_m + 47.13}{1 - \exp[-0.1(V_m + 47.13)]}, \\ 0.32, \end{cases} \quad V_m = -47.13$$

$$\beta_m = 0.08 \exp(-V/11)$$

$$\alpha_h = \begin{cases} 0.135 \exp\left[\frac{-(V_m + 80)}{6.8}\right], \\ 0, \end{cases} \quad V_m \geq -40$$

$$\beta_h = \begin{cases} 3.56 \exp(0.07V_m) + 3.1 \times 10^5 \exp(0.35V_m), \\ \left[0.13 \left(1 + \exp\left(\frac{-(V_m + 10.66)}{11.1}\right)\right)\right]^{-1}, \end{cases} \quad V_m \geq -40$$

$$\alpha_j = \begin{cases} [-127140 \exp(0.2444V_m) - 3.474 \times 10^5 \exp(-0.04391V_m)] \frac{V_m + 37.78}{1 + \exp[0.311(V_m + 79.23)]}, \\ 0, \end{cases} \quad V_m \geq -40$$

$$\beta_j = \begin{cases} 0.1212 \frac{\exp(-0.01052V_m)}{1 + \exp[-0.1378(V_m + 40.14)]}, \\ 0.3 \frac{\exp[-2.535 \times 10^{-7}V_m]}{1 + \exp[-0.1(V_m + 32)]}, \end{cases} \quad V_m \geq -40,$$

where,

$$\tau_\phi = (\alpha_\phi + \beta_\phi)^{-1}, \quad \phi_\infty = \alpha_\phi \tau_\phi, \quad \text{for} \quad \phi = m, h, j.$$

**Inward rectifier  $K^+$  current.**  $i_{K1}$  was implemented based on the data available at the time and resting membrane resistance measurements. The current is described by

$$i_{K1} = \frac{g_{K1}(V_m - E_K)}{1 + \exp[0.07(V + 80)]}, \quad g_{K1} = 0.09.$$

**Transient outward  $K^+$  current.** The model implements  $i_{to}$  using the formula

$$i_{to} = g_{to} o_a^3 o_i (V_m - E_K), \quad g_{to} = 0.1652,$$

The gate opening and closing rate constants are

$$\begin{aligned} \alpha_{o(a)} &= 0.65 \left[ \exp \left( -\frac{V_m + 10}{8.5} \right) + \exp \left( -\frac{V_m - 30}{59.0} \right) \right]^{-1}, \\ \beta_{o(a)} &= 0.65 \left[ 2.5 + \exp \left( \frac{V_m + 82}{17.0} \right) \right]^{-1}, \\ \alpha_{o(i)} &= \left[ 18.53 + \exp \left( \frac{V_m + 113.7}{10.95} \right) \right]^{-1}, \\ \beta_{o(i)} &= \left[ 35.56 + \exp \left( -\frac{V_m + 1.26}{7.44} \right) \right]^{-1}, \end{aligned}$$

where

$$\begin{aligned} \tau_{o(a)} &= \frac{[\alpha_{o(a)} + \beta_{o(a)}]^{-1}}{K_{Q_{10}}}, & o_{a(\infty)} &= \left[ 1 + \exp \left( -\frac{V_m + 20.47}{17.54} \right) \right]^{-1}, \\ \tau_{o(i)} &= \frac{[\alpha_{o(i)} + \beta_{o(i)}]^{-1}}{K_{Q_{10}}}, & o_{i(\infty)} &= \left[ 1 + \exp \left( \frac{V_m + 43.1}{5.3} \right) \right]^{-1}. \end{aligned}$$

**Ultra-rapid  $K^+$  current.** The model implements  $i_{Kur}$  using the formulae

$$i_{Kur} = g_{Kur} u_a^3 u_i (V_m - E_K), \quad g_{Kur} = 0.005 + \frac{0.05}{1 + \exp [-(V_m - 15)/13]}$$

The gate opening and closing rate constants are

$$\begin{aligned} \alpha_{u(a)} &= 0.65 \left[ \exp \left( -\frac{V_m + 10}{8.5} \right) + \exp \left( -\frac{V_m - 30}{59.0} \right) \right]^{-1}, \\ \beta_{u(a)} &= 0.65 \left[ 2.5 + \exp \left( \frac{V_m + 82}{17.0} \right) \right]^{-1}, \\ \alpha_{u(i)} &= \left[ 1 + \exp \left( -\frac{V_m + 30.3}{9.6} \right) \right]^{-1}, \\ \beta_{u(i)} &= \exp \left( \frac{V_m - 158}{16} \right) \end{aligned}$$

where

$$\begin{aligned} \tau_{u(a)} &= \frac{[\alpha_{u(a)} + \beta_{u(a)}]^{-1}}{K_{Q_{10}}}, & u_{a(\infty)} &= \left[ 1 + \exp \left( -\frac{V_m + 30.3}{9.6} \right) \right]^{-1}, \\ \tau_{u(i)} &= \frac{[\alpha_{u(i)} + \beta_{u(i)}]^{-1}}{K_{Q_{10}}}, & u_{i(\infty)} &= \left[ 1 + \exp \left( \frac{V_m - 99.45}{27.48} \right) \right]^{-1}. \end{aligned}$$

**Rapid delayed  $K^+$  current.**

$$i_{Kr} = \frac{g_{Kr}x_r(V_m - E_K)}{1 + \exp\left(\frac{1+15}{22.4}\right)}k, \quad g_{Kr} = 0.0294,$$

where  $k = 9$  when using the modifications suggested by Xie [91], and  $k = 1$  otherwise.

The gate opening and closing rate constants are

$$\alpha_{x(r)} = 0.0003 \frac{V_m + 14.1}{1 - \exp\left(-\frac{V_m + 14.1}{5}\right)},$$

$$\beta_{x(r)} = 7.3989 \times 10^5 \frac{V_m - 3.3328}{\exp\left(\frac{V_m - 3.3328}{5.1237}\right) - 1},$$

where

$$\tau_{x(r)} = [\alpha_{x(r)} + \beta_{x(r)}]^{-1}, \quad x_{r(\infty)} = \left[1 + \exp\left(-\frac{V + 14.1}{6.5}\right)\right]^{-1}.$$

**Slow delayed  $K^+$  current.**

$$i_{Ks} = g_{Ks}x_s^2(V_m - E_K)k, \quad g_{Ks} = 0.129,$$

where  $k = 9$  when using the modifications suggested by Xie [91], and  $k = 1$  otherwise.

The gate opening and closing rate constants are

$$\alpha_{x(s)} = 4 \times 10^{-5} \frac{V_m - 19.9}{1 - \exp\left(-\frac{V_m - 19.9}{17}\right)},$$

$$\beta_{x(s)} = 3.5 \times 10^{-5} \frac{V_m - 19.9}{\exp\left(\frac{V_m - 19.9}{9}\right) - 1},$$

where

$$\tau_{x(s)} = \frac{1}{2}[\alpha_{x(s)} + \beta_{x(s)}]^{-1}, \quad x_{s(\infty)} = \left[1 + \exp\left(-\frac{V_m - 19.9}{12.7}\right)\right]^{-1/2}.$$

**L-type  $Ca^{2+}$  current.**

$$i_{Ca,L} = g_{Ca,L}f_{Ca}df(V_m - 65.0)k, \quad g_{Ca,L} = 0.1238,$$

where  $k = 0.65$  when using the modifications suggested by Xie [91], and  $k = 1$  otherwise. The gate opening and closing rate constants are

$$\tau_d = \frac{1 - \exp\left(-\frac{V + 10}{6.24}\right)}{0.035(V_m + 10) \left[1 + \exp\left(-\frac{V_m + 10}{6.24}\right)\right]},$$

$$\tau_f = 9 \left(0.0197 \exp[-0.0337^2(V_m + 10)^2] + 0.02\right)^{-1},$$

where

$$d_{\infty} = \left[ 1 + \exp \left( -\frac{V+10}{8} \right) \right]^{-1}, \quad f_{\infty} = \left[ 1 + \exp \left( \frac{V+28}{6.9} \right) \right],$$

$$\tau_{f(Ca)} = 2, \quad f_{Ca(\infty)} = \left( 1 + \frac{[Ca^{2+}]_i}{0.00035} \right)^{-1}.$$

**$Ca^{2+}$  pump current.**

$$i_{p,Ca} = g_{p,Ca(max)} \frac{[Ca^{2+}]_i}{0.0005 + [Ca^{2+}]_i}, \quad g_{p,Ca(max)} = 0.275$$

**$Na^+ - K^+$  pump current.**

$$i_{NaK} = i_{NaK(max)} f_{NaK} \frac{1}{1 + (K_{m,Na(i)}/[Na^+]_i)^{1.5}} \cdot \frac{[Na^+]_o}{[Na^+]_o + M_{m,K(0)}},$$

$$f_{NaK} = \left[ 1 + 0.1245 \exp \left( -0.1 \frac{FV}{RT} \right) + 0.0365 \sigma \exp \left( -\frac{FV}{RT} \right) \right]^{-1},$$

where

$$g_{NaK(max)} = 0.6, \quad \sigma = \frac{1}{7} \left[ \exp \left( \frac{[Na^+]_o}{67.3} \right) - 1 \right].$$

**$Na^+/Ca^{2+}$  exchanger.**

$$i_{NaCa} = \frac{\exp[\gamma VF/RT][Na^+]_i^3 [Ca^{2+}]_o - \exp[(1-\gamma)VF/RT][Na^+]_o^3 [Ca^{2+}]_i}{(K_{m,Na}^3 + [Na^+]_o^3)(K_{m,Ca} + [Ca^{2+}]_o \cdot (1 + k_{sat} \exp[(\gamma-1)VF/RT])},$$

where

$$g_{NaCa(max)} = 1600.0.$$

**Background  $Ca^{2+}$  current.**

$$i_{b,Ca} = g_{b,Ca}(V_m - E_{Ca}), \quad g_{b,Ca} = 0.00113.$$

**Background  $Na^{2+}$  current.**

$$i_{b,Na} = g_{b,Na}(V_m - E_{Na}), \quad g_{b,Na} = 0.000674.$$

## Saroplasmic reticulum calcium storage and release currents.

$$i_{rel} = k_{rel}u^2vw([Ca^{2+}]_{rel} - [Ca^{2+}]_i), \quad k_{rel} = 30$$

$$i_{tr} = \frac{1}{\tau_{tr}}([Ca^{2+}]_{up} - [Ca^{2+}]_{rel}), \quad \tau_{tr} = 180$$

$$i_{up} = \frac{i_{up(max)}}{1 + (k_{up}/[Ca^{2+}]_i)}, \quad i_{up(max)} = 0.005$$

$$i_{up,leak} = \frac{[Ca^{2+}]_{up}}{[Ca^{2+}]_{up(max)}} i_{up(max)}$$

where

$$\tau_u = 8.0, \quad u_\infty = \left(1 + \exp \left[ -\frac{F_n - 3.4175 \times 10^{-13}}{13.67 \times 10^{-16}} \right] \right)^{-1},$$

$$\tau_v = 1.91 + 2.09 \left(1 + \exp \left[ -\frac{F_n - 3.4175 \times 10^{-13}}{13.67 \times 10^{-16}} \right] \right)^{-1},$$

$$v_\infty = 1 - \left(1 + \exp \left[ -\frac{F_n - 6.835 \times 10^{-14}}{13.67 \times 10^{-16}} \right] \right)^{-1},$$

$$\tau_w = 6.0 \frac{1 - \exp \left( -\frac{V_m - 7.9}{5} \right)}{\left[ 1 + 0.3 \exp \left( -\frac{V - 7.9}{5} \right) \right] (V_m - 7.9)}$$

$$w_\infty = 1 - \left[ 1 + \exp \left( -\frac{V - 40}{17} \right) \right]^{-1},$$

$$F_n = 10^{-12} V_{rel} i_{rel} - \frac{5 \times 10^{13}}{F} (0.5 i_{Ca,L} - 0.2 i_{NaCa}).$$

## Constants

Below is a table summarising the constants used in this modified Courtemanche model,

Quantity	Value
Membrane capacitance	$C_m = 1.0\text{mF/cm}^2$
<i>continued on next page ...</i>	



... continued from previous page

Quantity	Value
Rate constant of electroporation	$a = 2.5 \times 10^{-3} \text{mS/cm}^2$
Rate constant of electroporation	$b = 2.5 \times 10^{-5} \text{mV}^{-2}$
Rate constant of electroporation	$c = 1.0^{-9} \text{mV}^{-2}$
Gas constant	$R = 8.3143 \text{JK}^{-1} \text{mol}^{-1}$
Temperature	$T = 310 \text{K}$
Faraday Constant	$F = 96.4867 \text{C/mmol}$
intracellular volume	$V_i = 13668 \mu\text{m}^3$
SR uptake compartment volume	$V_{up} = 1109.52 \mu\text{m}^3$
SR release compartment volume	$V_{rel} = 96.48 \mu\text{m}^3$
Extracellular $K^+$ concentration	$[K^+]_o = 5.4 \text{mM}$
Extracellular $Na^+$ concentration	$[Na^+]_o = 140.0 \text{mM}$
Extracellular $Ca^{2+}$ concentration	$[Ca^{2+}]_o = 1.8 \text{mM}$
Maximal $i_{Na}$ conductance	$g_{Na} = 7.8 \text{nS/pF}$
Maximal $i_{K1}$ conductance	$g_{K1} = 0.09 \text{nS/pF}$
Maximal $i_{to}$ conductance	$g_{to} = 0.1652 \text{nS/pF}$
Maximal $i_{Kr}$ conductance	$g_{Kr} = 0.0294 \text{nS/pF}$
Maximal $i_{Ks}$ conductance	$g_{Ks} = 0.129 \text{nS/pF}$
Maximal $i_{Ca,L}$ conductance	$g_{Ca,L} = 0.1238 \text{nS/pF}$
Maximal $i_{b,Ca}$ conductance	$g_{b,Ca} = 0.00113 \text{nS/pF}$
Maximal $i_{b,Na}$ conductance	$g_{b,Na} = 0.000674 \text{nS/pF}$
Maximal $i_{NaK(max)}$	$i_{NaK(max)} = 0.60 \text{pA/pF}$
Maximal $i_{NaCa(max)}$	$i_{NaCa(max)} = 1600.0 \text{pA/pF}$
Maximal $i_{p,Ca(max)}$	$i_{p,Ca(max)} = 0.275 \text{pA/pF}$
Maximal $i_{up(max)}$	$i_{up(max)} = 0.005 \text{mM/ms}$
Temperature scaling factor	$K_{Q10} = 3$
Voltage dependence parameter	$\gamma = 0.35$
Saturation constant	$K_{m,Na(i)} = 10 \text{mM}$
Saturation constant	$K_{m,K(o)} = 1.5 \text{mM}$
Saturation constant	$K_{m,Na} = 87.5 \text{mM}$
continued on next page ...	

... continued from previous page	
Quantity	Value
Saturation constant	$K_{m,Ca} = 1.38\text{mM}$
Saturation factor	$k_{sat} = 0.1$
Maximal release rate	$k_{rel} = 30\text{ms}^{-1}$
Half-saturation constant	$K_{up} = 0.00092\text{mM}$
Maximal concentration in myoplasm	$[Ca^{2+}]_{up(max)} = 15\text{mM}$
Maximal concentration in myoplasm	$[Cm\text{dn}]_{max} = 0.05\text{mM}$
Maximal concentration in myoplasm	$[Trpn]_{max} = 0.07\text{mM}$
Maximal concentration of SR release	$[Csqn]_{max} = 10\text{mM}$
Half saturation constant	$K_{m,Cm\text{dn}} = 0.00238\text{mM}$
Half saturation constant	$K_{m,Trpn} = 0.0005\text{mM}$
Half saturation constant	$K_{m,Csqn} = 0.8\text{mM}$

Table B.1: Values of the constants used in our modified Courtemanche model

# Appendix C

## Calculations from Chapter 5

### C.1 Reaction-diffusion system expressed in the filament frame of reference

Throughout Appendix C.1, I will use the subscript notation  $N_x, N_y$ , and  $N_z$  are the  $x, y$  and  $z$  components of the vector  $\mathbf{N}$  (and similar for other vectors). The notation  $\partial_s \mathbf{N}$  will represent the partial derivative of the vector  $\mathbf{N}$  with respect to  $s$ , etc.

Appendix C.1 shows details of the calculations from section 5.1.1.

#### C.1.1 The gradient operator $\nabla \alpha$

The first step in the derivation of the motion equations for the filament is to express the three dimensional gradient operator in the filament coordinate system  $(s, p, q, t')^T$ . Using the coordinate representation

$$\alpha(x\mathbf{i} + y\mathbf{j} + z\mathbf{k}) = \alpha(\mathbf{R}(s, t') + p\mathbf{N}(s, t') + q\mathbf{B}(s, t')),$$

where

$$\begin{aligned} x &= (\mathbf{R}(s, t') + p\mathbf{N}(s, t') + q\mathbf{B}(s, t')) \cdot \mathbf{i} \\ y &= (\mathbf{R}(s, t') + p\mathbf{N}(s, t') + q\mathbf{B}(s, t')) \cdot \mathbf{j} \\ z &= (\mathbf{R}(s, t') + p\mathbf{N}(s, t') + q\mathbf{B}(s, t')) \cdot \mathbf{k} \end{aligned}$$

one can define the Jacobian

$$\mathbf{J} = \frac{\partial(x, y, z)}{\partial(s, p, q)},$$

as

$$\mathbf{J} = \begin{pmatrix} \partial_s R_x + p\partial_s N_x + q\partial_s B_x & \partial_s R_y + p\partial_s N_y + q\partial_s B_y & \partial_s R_z + p\partial_s N_z + q\partial_s B_z \\ N_x & N_y & N_z \\ B_x & B_y & B_z \end{pmatrix},$$

where  $R_x$  is the  $x$  component of vector  $\mathbf{R} = (R_x, R_y, R_z)$  etc. By using the Frenet-Serret equations (5.3) - (5.6) this can now be expressed as follows

$$\mathbf{J} = \begin{pmatrix} \gamma_x & \gamma_y & \gamma_z \\ N_x & N_y & N_z \\ B_x & B_y & B_z \end{pmatrix}$$

where,

$$\begin{aligned} \gamma_x &= T_x + p(-\kappa T_x + \tau B_x) - q(\tau N_x) \\ \gamma_y &= T_y + p(-\kappa T_y + \tau B_y) - q(\tau N_y) \\ \gamma_z &= T_z + p(-\kappa T_z + \tau B_z) - q(\tau N_z) \end{aligned}$$

Since

$$\begin{pmatrix} \partial_s \alpha \\ \partial_p \alpha \\ \partial_q \alpha \end{pmatrix} = \mathbf{J} \begin{pmatrix} \partial_x \alpha \\ \partial_y \alpha \\ \partial_z \alpha \end{pmatrix}$$

we can say that the gradient operator becomes

$$\nabla \alpha = \mathbf{J}^{-1} \begin{pmatrix} \partial_s \alpha \\ \partial_p \alpha \\ \partial_q \alpha \end{pmatrix}$$

Therefore, to find  $\mathbf{J}^{-1}$  we must first express  $\mathbf{J}$  as follows

$$\mathbf{J} = \mathbf{K}[\mathbf{TNB}]^{-1} = \begin{pmatrix} 1 - \kappa p & -\tau q & \tau p \\ 0 & 1 & 0 \\ 0 & 0 & 1 \end{pmatrix} \cdot \begin{pmatrix} T_x & T_y & T_z \\ N_x & N_y & N_z \\ B_x & B_y & B_z \end{pmatrix}$$

then by using the fact that,

$$\mathbf{J}^{-1} = [\mathbf{TNB}]\mathbf{K}^{-1} = \begin{pmatrix} T_x & N_x & B_x \\ T_y & N_y & B_y \\ T_z & N_z & B_z \end{pmatrix} \cdot \mathbf{K}^{-1}$$

it is now left to find  $\mathbf{K}^{-1}$ ;

$$\begin{aligned} \mathbf{K}^{-1} &= \frac{1}{|\mathbf{K}|} \text{adj}(\mathbf{K}) \\ &= \frac{1}{(1 - \kappa p)} \begin{pmatrix} 1 & q\tau & -p\tau \\ 0 & 1 - \kappa p & 0 \\ 0 & 0 & 1 - \kappa p \end{pmatrix} \end{aligned}$$

and so,

$$\mathbf{J}^{-1} = \begin{pmatrix} \frac{T_x}{(1-\kappa p)} & \frac{T_x q \tau}{(1-\kappa p)} + N_x & \frac{-T_x p \tau}{(1-\kappa p)} + B_x \\ \frac{T_y}{(1-\kappa p)} & \frac{T_y q \tau}{(1-\kappa p)} + N_y & \frac{-T_y p \tau}{(1-\kappa p)} + B_y \\ \frac{T_z}{(1-\kappa p)} & \frac{T_z q \tau}{(1-\kappa p)} + N_z & \frac{-T_z p \tau}{(1-\kappa p)} + B_z \end{pmatrix}.$$

By using this equations for  $\mathbf{J}^{-1}$  we finally arrive at the equation for the gradient operator,

$$\nabla \alpha = \begin{pmatrix} \left( \frac{T_x}{(1-\kappa p)} \right) \partial_s \alpha & \left( \frac{T_x q \tau}{(1-\kappa p)} + N_x \right) \partial_p \alpha & \left( \frac{-T_x p \tau}{(1-\kappa p)} + B_x \right) \partial_q \alpha \\ \left( \frac{T_y}{(1-\kappa p)} \right) \partial_s \alpha & \left( \frac{T_y q \tau}{(1-\kappa p)} + N_y \right) \partial_p \alpha & \left( \frac{-T_y p \tau}{(1-\kappa p)} + B_y \right) \partial_q \alpha \\ \left( \frac{T_z}{(1-\kappa p)} \right) \partial_s \alpha & \left( \frac{T_z q \tau}{(1-\kappa p)} + N_z \right) \partial_p \alpha & \left( \frac{-T_z p \tau}{(1-\kappa p)} + B_z \right) \partial_q \alpha \end{pmatrix}.$$

which can be written in the simplified form as

$$\nabla \alpha = \mathbf{T} \frac{1}{(1-\kappa p)} \partial_s \alpha + \mathbf{T} \frac{q \tau}{(1-\kappa p)} \partial_p \alpha + \mathbf{N} \partial_p \alpha - \mathbf{T} \frac{p \tau}{(1-\kappa p)} \partial_q \alpha + \mathbf{B} \partial_q \alpha$$

or,

$$\nabla \alpha = \mathbf{T}(H\alpha) + \mathbf{N} \partial_p \alpha + \mathbf{B} \partial_q \alpha$$

where  $H\alpha$  is the first order differential operator,

$$\begin{aligned} H\alpha &= \frac{1}{(1-\kappa p)} (\partial_s \alpha + q \tau \partial_p \alpha - p \tau \partial_q \alpha) \\ &= \frac{1}{(1-\kappa p)} (\partial_s \alpha - \tau \partial_\theta \alpha) \end{aligned}$$

### C.1.2 The Laplacian $\Delta_3 \alpha$

The Laplacian can be written as follows

$$\Delta_3 \alpha = (\mathbf{T}H + \mathbf{N} \partial_p + \mathbf{B} \partial_q) (\mathbf{T}H\alpha + \mathbf{N} \partial_p \alpha + \mathbf{B} \partial_q \alpha).$$

Due to the orthogonality of  $\mathbf{N}$ ,  $\mathbf{T}$  and  $\mathbf{B}$  most terms will cancel from this equation.

The remaining terms are described below

$$\begin{aligned} \mathbf{T}(H(\mathbf{T}H\alpha)) &= \mathbf{T}(H\mathbf{T})(H\alpha) + \mathbf{T}\mathbf{T}(H(H\alpha)) \\ &= \mathbf{T} \left( \frac{1}{(1-\kappa p)} \partial_s T \right) (H\alpha) + HH\alpha \\ &= \mathbf{T} \left( \frac{1}{(1-\kappa p)} \kappa \mathbf{N} \right) (H\alpha) + HH\alpha \\ &= HH\alpha \end{aligned}$$

$$\begin{aligned}
\mathbf{T}(H(\mathbf{N}\partial_p\alpha)) &= \mathbf{T}(H\mathbf{N})\partial_p\alpha + \mathbf{T}\mathbf{N}(H\partial_p\alpha) \\
&= \mathbf{T}\left(\frac{1}{(1-\kappa p)}\mathbf{N}_s\right)\partial_p\alpha \\
&= \frac{\mathbf{T}}{(1-\kappa p)}(-\kappa\mathbf{T} + \tau\mathbf{B})\partial_p\alpha \\
&= \frac{-\kappa}{(1-\kappa p)}\partial_p\alpha
\end{aligned}$$

$$\begin{aligned}
\mathbf{N}\partial_p(\mathbf{N}\partial_p\alpha) &= \mathbf{N}\mathbf{N}\partial_p^2\alpha + \mathbf{N}(\partial_p\mathbf{N})(\partial_p\alpha) \\
&= \partial_p^2\alpha
\end{aligned}$$

$$\begin{aligned}
\mathbf{B}\partial_q(\mathbf{B}\partial_q\alpha) &= \mathbf{B}\mathbf{B}\partial_q^2\alpha + \mathbf{B}(\partial_q\mathbf{B})(\partial_q\alpha) \\
&= \partial_q^2\alpha
\end{aligned}$$

Hence, one can conclude that the Laplacian can be expressed as

$$\Delta_3\alpha = H(H\alpha) - \frac{\kappa}{(1-\kappa p)}\partial_p\alpha + \partial_p^2\alpha + \partial_q^2\alpha$$

### C.1.3 Time derivative

The next step in the derivation of the motions equations of a filament is to allow the new coordinate system to move in time. To do this we should include time in our coordinate transformation  $(x, y, z, t)^T \rightarrow (s, p, q, t')^T$ , where  $t = t'$ . Using the chain rule,

$$\begin{aligned}
\partial_{t'}\alpha &= (\partial_t\alpha)(\partial_{t'}t) + (\partial_{t'}x)(\partial_x\alpha) + (\partial_{t'}y)(\partial_y\alpha) + (\partial_{t'}z)(\partial_z\alpha) \\
&= \partial_t\alpha + (\nabla\alpha)(\partial_{t'}\mathbf{X}),
\end{aligned}$$

yields

$$\partial_{t'}\alpha = \partial_t\alpha + \left(\partial_{t'}\mathbf{R}(s, t') + p\partial_{t'}\mathbf{N}(s, t') + q\partial_{t'}\mathbf{B}(s, t')\right)(H\alpha\mathbf{T} + \mathbf{N}\partial_p\alpha + \mathbf{B}\partial_q\alpha).$$

Since  $\mathbf{N}\partial_t\mathbf{B} = \mathbf{B}\partial_t\mathbf{N}$  and  $\mathbf{B}\partial_t\mathbf{B} = \frac{1}{2}(B^2)_t = \frac{1}{2}\frac{d}{dt}(1) = 0$ , and by noticing that  $\mathbf{N}\partial_t\mathbf{B} = \mathbf{B}\partial_t\mathbf{N}$  and  $p\partial_q\alpha + q\partial_p\alpha = \partial_\theta\alpha$  we can express the required change in time derivatives as follows

$$\partial_t\alpha = \partial_{t'}\alpha - (H\alpha\mathbf{T})(\partial_{t'}\mathbf{X}) - (\partial_{t'}\mathbf{R})(\mathbf{N}\partial_p\alpha + \mathbf{B}\partial_q\alpha) - \mathbf{B}(\partial_{t'}\mathbf{N})(\partial_\theta\alpha).$$

## C.2 Existence equation for a rigidly rotating spiral wave

Throughout the remainder of Appendix C, we will use the notation  $\mathbf{N}_s$  to represent the partial derivative of the vector  $\mathbf{N}$  with respect to  $s$ , etc.

Appendix C.2 gives details of the calculations of the derivation of the equation for the existence of spiral waves used in section 5.1.2.

Consider the 2D reaction diffusion system in polar coordinates,

$$\mathbf{u}_t = \mathbf{D}\Delta_{r,\theta}\mathbf{u} + \mathbf{f}(\mathbf{u}), \quad (\text{C.1})$$

where  $\Delta_{r,\theta}\mathbf{u} = \mathbf{u}_{rr} + \frac{1}{r}\mathbf{u}_r + \frac{1}{r^2}\mathbf{u}_{\theta\theta}$ .

Spiral waves are a particular type of rotating solution, so to find them it is best to consider the unperturbed reaction diffusion system in a rotating coordinate system  $(\rho, \phi, \hat{t})$ . That is a coordinate system which rotates with a constant angular velocity  $\omega$  with respect to the laboratory coordinate system  $(r, \theta, t)$  where

$$(r, \theta, t)^T \rightarrow (\rho, \phi, \hat{t})^T$$

To write (C.1) in these new rotating coordinates  $\rho, \phi, \hat{t}$ , first consider any solution to have the form

$$\mathbf{u}(r, \theta, t) = \mathbf{Q}(\rho(r, \theta, t), \phi(r, \theta, t), \hat{t}(r, \theta, t)).$$

The unperturbed reaction diffusion system (C.1) can now be written in the rotating coordinate system as

$$\mathbf{Q}_{\hat{t}} = D\Delta_{\rho,\phi}\mathbf{Q} - \omega\mathbf{Q}_{\phi} - \mathbf{f}(\mathbf{Q}). \quad (\text{C.2})$$

From the above relations it follows that  $\Delta_{\rho,\phi} = \Delta_{r,\theta}$  so the subscript can be omitted.

One can say that a solution  $\mathbf{Q}(\rho, \phi, \hat{t})$  of (C.2) is a rigidly rotating spiral wave solution  $\mathbf{Q}(\rho, \phi, \hat{t}) = \mathbf{V}(\rho, \phi)$  if it does not depend on time,

$$\mathbf{Q}_{\rho} = \mathbf{0}.$$

That is, one can say that the following equation determines the existence of rigidly rotating spiral wave solutions to the reaction diffusion system

$$\mathbf{D}\Delta\mathbf{V} - \omega\mathbf{V}_{\phi} - \mathbf{f}(\mathbf{V}) = \mathbf{0}. \quad (\text{C.3})$$

### C.3 Orders of magnitude

To consider the orders of magnitude of terms in the equations from section 5.1.2 we use the ansatz from [19], regarding the order of magnitude of the terms in (5.11), and introduce a small scaling parameter  $\epsilon$ , so that

$$\begin{aligned}\mathbf{R}(s, t) &= \epsilon^{-1} \hat{\mathbf{R}}(\epsilon s, \epsilon^2 t) = \epsilon^{-1} \hat{\mathbf{R}}(\xi, \zeta), \\ \phi(s, t) &= \hat{\phi}(\epsilon s, \epsilon^2 t) = \hat{\phi}(\xi, \zeta).\end{aligned}$$

The following analysis uses the Frenet-Serret equations (5.3)-(5.6),

$$\epsilon \hat{\mathbf{R}}_{\xi\xi} = \kappa \mathbf{N}, \tag{C.4}$$

$$\epsilon^2 \hat{\mathbf{R}}_{\xi\xi\xi} = \kappa_s \mathbf{N} + \kappa(\tau \mathbf{B} - \kappa \mathbf{T}), \tag{C.5}$$

$$\begin{aligned}\epsilon^3 \hat{\mathbf{R}}_{\xi\xi\xi\xi} &= \kappa_{ss} \mathbf{N} + 2\kappa_s \tau \mathbf{B} - 2\kappa_s \kappa \mathbf{T} \\ &\quad + \kappa \tau_s \mathbf{B} - \kappa \kappa_s \mathbf{T} - \kappa \tau^2 \mathbf{N} + \kappa^3 (\kappa \mathbf{T} - \tau \mathbf{B}).\end{aligned} \tag{C.6}$$

Since  $\mathbf{R}, \mathbf{T}, \mathbf{N}$ , and  $\mathbf{B}$  are unit vectors they have order  $O(1)$ . By comparing coefficients in the equations (C.4), (C.5), and (C.6) one can deduce that  $\kappa$  and  $\tau$  have order  $\epsilon$ , and  $\kappa_s, \tau_s$ , have order  $\epsilon^2$ .



## C.4 Eigenvalues and eigenfunctions of $L$

Here we will deduce that  $\mathbf{V}_p$ ,  $\mathbf{V}_q$ , and  $\mathbf{V}_\theta$  are eigenfunctions of the linear operator  $L$ , each having eigenvalue 0, as introduced in section 5.1.2..

Begin with  $\mathbf{V}$  which is a solution of the unperturbed reaction diffusion system expressed in the filament frame of reference,

$$\mathbf{V}_t = \mathbf{D}\Delta_2\mathbf{V} + \mathbf{f}(\mathbf{V}). \quad (\text{C.7})$$

Differentiating (C.7) with respect to  $p$  yields

$$(\mathbf{V}_p)_t - \mathbf{D}\Delta\mathbf{V}_p - \mathbf{F}(V)\mathbf{V}_p = 0. \quad (\text{C.8})$$

Differentiating (C.7) with respect to  $q$  yields

$$(\mathbf{V}_q)_t - \mathbf{D}\Delta\mathbf{V}_q - \mathbf{F}(V)\mathbf{V}_q = 0. \quad (\text{C.9})$$

Differentiating (C.7) with respect to  $\theta$  yields

$$(\mathbf{V}_\theta)_t - \mathbf{D}\Delta\mathbf{V}_\theta - \mathbf{F}(V)\mathbf{V}_\theta = 0. \quad (\text{C.10})$$

In (C.8) and (C.9) the Laplacian is  $\Delta\alpha = (\alpha_{pp} + \alpha_{qq})$  and in (C.10) the Laplacian is  $\Delta\alpha = \left(\alpha_{rr} + \frac{1}{r}\alpha_r + \frac{1}{r^2}\alpha_\theta\right)$ .

It can now be deduced from (C.8), (C.9), and (C.10) that  $\mathbf{V}_p$ ,  $\mathbf{V}_q$ , and  $\mathbf{V}_\theta$  are all eigenfunctions of  $L$  and all have eigenvalue 0. Notice that since  $\mathbf{V}$  is a periodic function of time, so are  $\mathbf{V}_p$ ,  $\mathbf{V}_q$  and  $\mathbf{V}_\theta$ . Hence, they are eigenfunctions of the linear operator  $L$  (from (5.12)) in the space of  $\frac{2\pi}{\omega}$  periodic functions of time.

## C.5 Orthogonality of $\mathbf{Y}_i$ to $\mathbf{V}_j$

Appendix C.5 checks orthogonality of eigenfunctions introduced in section 5.1.3. We illustrate here one example only,

$$\begin{aligned}
\langle \tilde{\mathbf{Y}}_p, \tilde{\mathbf{V}}_q \rangle &= \left\langle \frac{1}{2} \left( e^{i(\omega\tilde{t}-\phi)} \tilde{\mathbf{Y}}_+ + e^{-i(\omega\tilde{t}-\phi)} \tilde{\mathbf{Y}}_- \right), \frac{1}{2i} \left( e^{i(\omega\tilde{t}-\phi)} \tilde{\mathbf{V}}_+ - e^{-i(\omega\tilde{t}-\phi)} \tilde{\mathbf{V}}_- \right) \right\rangle \\
&= \frac{1}{4i} \left\langle e^{i(\omega\tilde{t}-\phi)} \tilde{\mathbf{Y}}_+, e^{i(\omega\tilde{t}-\phi)} \tilde{\mathbf{V}}_+ \right\rangle + \frac{1}{4i} \left\langle e^{i(\omega\tilde{t}-\phi)} \tilde{\mathbf{Y}}_+, -e^{-i(\omega\tilde{t}-\phi)} \tilde{\mathbf{V}}_- \right\rangle \\
&\quad + \frac{1}{4i} \left\langle e^{-i(\omega\tilde{t}-\phi)} \tilde{\mathbf{Y}}_-, e^{i(\omega\tilde{t}-\phi)} \tilde{\mathbf{V}}_+ \right\rangle + \frac{1}{4i} \left\langle e^{-i(\omega\tilde{t}-\phi)} \tilde{\mathbf{Y}}_-, -e^{-i(\omega\tilde{t}-\phi)} \tilde{\mathbf{V}}_- \right\rangle \\
&= \frac{1}{4i} \langle \tilde{\mathbf{Y}}_+, \tilde{\mathbf{V}}_+ \rangle - e^{-2i(\omega\tilde{t}-\phi)} \frac{1}{4i} \langle \tilde{\mathbf{Y}}_+, \tilde{\mathbf{V}}_- \rangle \\
&\quad + e^{2i(\omega\tilde{t}-\phi)} \frac{1}{4i} \langle \tilde{\mathbf{Y}}_-, \tilde{\mathbf{V}}_+ \rangle - \frac{1}{4i} \langle \tilde{\mathbf{Y}}_-, \tilde{\mathbf{V}}_- \rangle \\
&= 0.
\end{aligned}$$

which is true because of the condition  $\langle \tilde{\mathbf{Y}}_i, \tilde{\mathbf{V}}_j \rangle = \delta_{ij}$  for  $i, j = +, -, 0$ . In deriving this we also used the rules

$$\begin{aligned}
\langle \alpha \mathbf{A}, \mathbf{B} \rangle &= \bar{\alpha} \langle \mathbf{A}, \mathbf{B} \rangle, \\
\langle \mathbf{A}, \alpha \mathbf{B} \rangle &= \alpha \langle \mathbf{A}, \mathbf{B} \rangle,
\end{aligned}$$

## C.6 Some coefficients of the motion equations are zero

Appendix C.6 contains the calculations showing that some coefficients from the motion equations (5.18)-(5.20) are zero.

$$a_2 = \langle \tilde{\mathbf{Y}}_p, \mathbf{D}\tilde{\mathbf{V}}_{\theta\theta} \rangle \text{ and } a_3 = \langle \tilde{\mathbf{Y}}_q, \mathbf{D}\tilde{\mathbf{V}}_{\theta\theta} \rangle$$

Using the relation

$$\tilde{\mathbf{Y}}_p + i\tilde{\mathbf{Y}}_q = 2e^{i(\omega\tilde{t}-\phi)}\tilde{\mathbf{Y}}_+(\rho, \tilde{\theta}),$$

and the above definition of the inner product (5.25),

$$\begin{aligned} a_2 + ia_3 &= 2 \int_{\tilde{t}-\frac{\pi}{\omega}}^{\tilde{t}+\frac{\pi}{\omega}} d\eta \oint d\tilde{\theta} \int_0^\infty \rho d\rho \left( e^{i(\omega\eta-\phi)} \tilde{\mathbf{Y}}_+(\rho, \tilde{\theta}) \cdot \mathbf{D}\tilde{\mathbf{V}}_{\theta\theta}(\rho, \tilde{\theta}) \right) \\ &= 2e^{-i\phi} \left[ \oint e^{i\omega\eta} d\eta \right] \cdot \left[ \int_0^\infty \rho d\rho \left( \tilde{\mathbf{Y}}_+(\rho, \tilde{\theta}) \cdot \mathbf{D}\tilde{\mathbf{V}}_{\theta\theta}(\rho, \tilde{\theta}) \right) \right] \\ &= 0. \end{aligned}$$

Here, we used the assumption the  $\phi$  is constant.

$$c_1 = \langle \tilde{\mathbf{Y}}_\theta, \mathbf{D}\tilde{\mathbf{V}}_p \rangle, \ c_2 = \langle \tilde{\mathbf{Y}}_p, \mathbf{D}\tilde{\mathbf{V}}_\theta \rangle \text{ and } c_4 = \langle \tilde{\mathbf{Y}}_q, \mathbf{D}\tilde{\mathbf{V}}_\theta \rangle$$

Similar arguments show that  $c_1 = 0$  and  $c_2 + ic_3 = 0$ .

$$d_1 = \langle \tilde{\mathbf{Y}}_\theta, p\tilde{\mathbf{V}}_\theta \rangle \text{ and } d_2 = \langle \tilde{\mathbf{Y}}_\theta, q\tilde{\mathbf{V}}_\theta \rangle$$

We have the following dependencies,

$$\begin{aligned} \tilde{\mathbf{Y}}_\theta &= \tilde{\mathbf{Y}}_\theta(\rho, \tilde{\theta}), \\ \tilde{\mathbf{V}}_\theta &= \tilde{\mathbf{V}}_0(\rho, \tilde{\theta}). \end{aligned}$$

In the scroll coordinate system, the polar coordinates  $p$  and  $q$  can be written as

$$\begin{aligned} p &= \rho \cos(\tilde{\theta} - \omega\tilde{t} + \phi), \\ q &= \rho \sin(\tilde{\theta} - \omega\tilde{t} + \phi), \end{aligned}$$

hence,

$$p + iq = \rho e^{i(\tilde{\theta} - \omega\tilde{t} + \phi)}.$$

Using the definition for the inner product (5.25),

$$\begin{aligned}
d_1 + id_2 &= \int_{\tilde{t}-\frac{\pi}{\omega}}^{\tilde{t}+\frac{\pi}{\omega}} d\eta \oint d\tilde{\theta} \int_0^\infty \rho^2 d\rho \left( e^{i(\tilde{\theta}-\omega\tilde{t}+\phi)} \tilde{\mathbf{Y}}_\theta(\rho, \tilde{\theta}) \cdot \tilde{\mathbf{V}}_0(\rho, \tilde{\theta}) \right) \\
&= e^{-i\phi} \left[ \oint e^{-i\omega\eta} d\eta \right] \cdot \left[ \oint d\tilde{\theta} \int_0^\infty \rho^2 d\rho \left( e^{i\tilde{\theta}} \tilde{\mathbf{Y}}_\theta(\rho, \tilde{\theta}) \cdot \tilde{\mathbf{V}}_0(\rho, \tilde{\theta}) \right) \right] \\
&= 0.
\end{aligned}$$

Here, we used the assumption the  $\phi$  is constant.

## C.7 Non-zero coefficients

Appendix C.7 contains the derivations of the coefficients (5.30).

$$a_1 = \langle \tilde{\mathbf{Y}}_\theta, \mathbf{D}\tilde{\mathbf{V}}_{\theta\theta} \rangle$$

Using the definition of the inner product (5.25),

$$\begin{aligned} a_1 &= \int_{\tilde{t}-\frac{\pi}{\omega}}^{\tilde{t}+\frac{\pi}{\omega}} d\eta \oint d\tilde{\theta} \int_0^\infty \rho d\rho \left[ \tilde{\mathbf{Y}}_\theta(\rho, \tilde{\theta}) \cdot \mathbf{D}\tilde{\mathbf{V}}_{\theta\theta}(\rho, \tilde{\theta}) \right] \\ &= \frac{2\pi}{\omega} \oint d\tilde{\theta} \int_0^\infty \rho d\rho \left[ \tilde{\mathbf{Y}}_\theta(\rho, \tilde{\theta}) \cdot \mathbf{D}\tilde{\mathbf{V}}_{\theta\theta}(\rho, \tilde{\theta}) \right] \end{aligned}$$

$$b_1 = \langle \tilde{\mathbf{Y}}_\theta, \mathbf{D}\tilde{\mathbf{V}}_\theta \rangle$$

Using a similar argument,

$$\begin{aligned} b_1 &= \int_{\tilde{t}-\frac{\pi}{\omega}}^{\tilde{t}+\frac{\pi}{\omega}} d\eta \oint d\tilde{\theta} \int_0^\infty \rho d\rho \left[ \tilde{\mathbf{Y}}_\theta(\rho, \tilde{\theta}) \cdot \mathbf{D}\tilde{\mathbf{V}}_\theta(\rho, \tilde{\theta}) \right], \\ &= \frac{2\pi}{\omega} \oint d\tilde{\theta} \int_0^\infty \rho d\rho \left[ \tilde{\mathbf{Y}}_\theta(\rho, \tilde{\theta}) \cdot \mathbf{D}\tilde{\mathbf{V}}_\theta(\rho, \tilde{\theta}) \right] \end{aligned}$$

$$b_2 = \langle \tilde{\mathbf{Y}}_p, \mathbf{D}\tilde{\mathbf{V}}_p \rangle \text{ and } c_3 = \langle \tilde{\mathbf{Y}}_q, \mathbf{D}\tilde{\mathbf{V}}_p \rangle$$

Using the identities

$$\begin{aligned} \tilde{\mathbf{Y}}_p + i\tilde{\mathbf{Y}}_q &= 2e^{i(\omega\tilde{t}-\phi)}\tilde{\mathbf{Y}}_+(\rho, \tilde{\theta}) \\ \tilde{\mathbf{V}}_p &= \frac{1}{2} \left( e^{i(\omega\tilde{t}-\phi)}\tilde{\mathbf{V}}_+(\rho, \tilde{\theta}) + e^{-i(\omega\tilde{t}-\phi)}\tilde{\mathbf{V}}_-(\rho, \tilde{\theta}) \right), \end{aligned}$$

the inner product (5.25) yields

$$\begin{aligned} b_2 + ic_3 &= 2 \langle e^{i(\omega\tilde{t}-\phi)}\tilde{\mathbf{Y}}_+(\rho, \tilde{\theta}), \mathbf{D}\tilde{\mathbf{V}}_x \rangle \\ &= \langle e^{i(\omega\tilde{t}-\phi)}\tilde{\mathbf{Y}}_+(\rho, \tilde{\theta}), \mathbf{D} \left( e^{i(\omega\tilde{t}-\phi)}\tilde{\mathbf{V}}_+(\rho, \tilde{\theta}) + e^{-i(\omega\tilde{t}-\phi)}\tilde{\mathbf{V}}_-(\rho, \tilde{\theta}) \right) \rangle \\ &= \langle e^{i(\omega\tilde{t}-\phi)}\tilde{\mathbf{Y}}_+(\rho, \tilde{\theta}), \mathbf{D}e^{i(\omega\tilde{t}-\phi)}\tilde{\mathbf{V}}_+(\rho, \tilde{\theta}) \rangle + \langle e^{i(\omega\tilde{t}-\phi)}\tilde{\mathbf{Y}}_+(\rho, \tilde{\theta}), \mathbf{D}e^{-i(\omega\tilde{t}-\phi)}\tilde{\mathbf{V}}_-(\rho, \tilde{\theta}) \rangle \end{aligned}$$

where we have

$$\begin{aligned} \langle e^{i(\omega\tilde{t}-\phi)}\tilde{\mathbf{Y}}_+(\rho, \tilde{\theta}), \mathbf{D}e^{i(\omega\tilde{t}-\phi)}\tilde{\mathbf{V}}_+(\rho, \tilde{\theta}) \rangle &= \langle \tilde{\mathbf{Y}}_+(\rho, \tilde{\theta}), \mathbf{D}\tilde{\mathbf{V}}_+(\rho, \tilde{\theta}) \rangle, \\ \langle e^{i(\omega\tilde{t}-\phi)}\tilde{\mathbf{Y}}_+(\rho, \tilde{\theta}), \mathbf{D}e^{-i(\omega\tilde{t}-\phi)}\tilde{\mathbf{V}}_-(\rho, \tilde{\theta}) \rangle &= 0, \end{aligned}$$

and so

$$\begin{aligned}
b_2 + ic_3 &= \langle \tilde{\mathbf{Y}}_+(\rho, \tilde{\theta}), \mathbf{D}\tilde{\mathbf{V}}_+(\rho, \tilde{\theta}) \rangle \\
&= \frac{2\pi}{\omega} \oint d\tilde{\theta} \int_0^\infty \rho d\rho \left[ \tilde{\mathbf{Y}}_+(\rho, \tilde{\theta}) \cdot \mathbf{D}\tilde{\mathbf{V}}_+(\rho, \tilde{\theta}) \right]
\end{aligned}$$

## C.8 Terms due to perturbation

Appendix C.8 contains the derivations of (5.31)-(5.33).

$$e_2 = \langle \tilde{\mathbf{Y}}_p, \mathbf{h} \rangle \text{ and } e_3 = \langle \tilde{\mathbf{Y}}_q, \mathbf{h} \rangle$$

Using the relations

$$\begin{aligned} \tilde{\mathbf{Y}}_p + i\tilde{\mathbf{Y}}_q &= 2e^{i(\omega\tilde{t}-\phi)}\tilde{\mathbf{Y}}_+(\rho, \tilde{\theta}), \\ \mathbf{h}(\tilde{t}) &= \mathbf{H}(\Omega\tilde{t} - \phi_*), \end{aligned}$$

the inner product (5.25) yields

$$\begin{aligned} e_2 + ie_3 &= \int_{\tilde{t}-\frac{\pi}{\omega}}^{\tilde{t}-\frac{\pi}{\omega}} d\eta \oint d\tilde{\theta} \int_0^\infty \rho d\rho 2e^{i(\omega\eta-\phi)}\tilde{\mathbf{Y}}_+(\rho, \tilde{\theta}) \cdot \mathbf{H}(\Omega\eta - \phi_*) \\ &= \left[ \int_{\tilde{t}-\frac{\pi}{\omega}}^{\tilde{t}-\frac{\pi}{\omega}} d\eta e^{i(\omega\eta-\phi)}\mathbf{H}(\Omega\eta - \phi_*) \right] \cdot Q, \end{aligned}$$

where

$$Q = \oint d\tilde{\theta} \int_0^\infty \rho d\rho \tilde{\mathbf{Y}}_+(\rho, \tilde{\theta}).$$

To proceed, assume that  $\phi$  varies only slowly in time and rescale the limits of integration,  $\eta = \tilde{t} + \xi$ ,  $\eta \in [\tilde{t} - \frac{\pi}{\omega}, \tilde{t} + \frac{\pi}{\omega}]$ ,  $\xi \in [-\frac{\pi}{\omega}, \frac{\pi}{\omega}]$ ,

$$\begin{aligned} e_2 + ie_3 &= e^{-i\phi} \left[ \int_{-\frac{\pi}{\omega}}^{\frac{\pi}{\omega}} d\xi e^{i\omega(\tilde{t}+\xi)}\mathbf{H}(\Omega\tilde{t} + \Omega\xi - \phi_*) \right] \cdot Q \\ &= e^{i(\omega\tilde{t}-\phi)} \left[ \int_{-\frac{\pi}{\omega}}^{\frac{\pi}{\omega}} d\xi e^{i\omega\xi}\mathbf{H}(\Omega\tilde{t} + \Omega\xi - \phi_*) \right] \cdot Q. \end{aligned}$$

For resonant drift we require  $\Omega - \omega = o(\epsilon)$  (i.e.  $\Omega + \epsilon\delta = \omega$ ,  $\delta = o(1)$ ). Therefore

$$e^{i\omega\xi} = e^{i\Omega\xi} + e^{i\epsilon\delta\xi} = e^{i\Omega\xi}(1 + o(\epsilon)).$$

Using this assumption, the integral can be written as follows

$$e_2 + ie_3 = e^{i(\omega\tilde{t}-\phi)} \left[ \oint d\xi e^{i\Omega\xi}\mathbf{H}(\Omega\tilde{t} + \Omega\xi - \phi_*) \right] \cdot Q.$$

Returning to the original variables,  $\xi = \eta - \tilde{t}$ ,

$$\begin{aligned} e_2 + ie_3 &= e^{i(\omega\tilde{t}-\phi)} \left[ \oint d\eta e^{i\Omega\eta} e^{-i\Omega\tilde{t}}\mathbf{H}(\Omega\eta - \phi_*) \right] \cdot Q \\ &= e^{i((\omega-\Omega)\tilde{t}-\phi)} \left[ \oint d\eta e^{i\Omega\eta}\mathbf{H}(\Omega\eta - \phi_*) \right] \cdot Q. \end{aligned}$$

Making a final change of variables, set  $\Omega\eta - \phi_* = \chi$ ,

$$\begin{aligned} e_2 + ie_3 &= \frac{1}{\Omega} e^{i((\omega-\Omega)\tilde{t}-\phi)} \left[ \oint d\chi e^{i(\chi+\phi_*)} p(\chi) \right] \cdot Q \\ &= \frac{1}{\Omega} e^{i((\omega-\Omega)\tilde{t}-\phi+\phi_*)} \left[ \oint d\chi e^{i\chi} p(\chi) \right] \cdot Q \\ &= \frac{1}{\Omega} e^{i(\beta-\phi)} H_1, \end{aligned}$$

where  $\beta = (\omega - \Omega)\tilde{t} + \phi_*$  and

$$H_1 = \left[ \oint d\chi e^{i\chi} \mathbf{H}(\chi) \right] \cdot \left[ \oint d\tilde{\theta} \int_0^\infty \rho d\rho \tilde{\mathbf{Y}}_+(\rho, \tilde{\theta}) \right].$$

$$e_1 = \langle \tilde{\mathbf{Y}}_\theta, h \rangle$$

Using the relations

$$\begin{aligned} \tilde{\mathbf{Y}}_\theta &= \tilde{\mathbf{Y}}_0(\rho, \tilde{\theta}), \\ \mathbf{h}(\tilde{t}) &= \mathbf{H}(\Omega\tilde{t} - \phi_*), \end{aligned}$$

the inner product (5.25) yields

$$\begin{aligned} e_1 &= \langle \tilde{\mathbf{Y}}_\theta, \mathbf{h} \rangle \\ &= \int_{\tilde{t}-\frac{\pi}{\omega}}^{\tilde{t}+\frac{\pi}{\omega}} d\eta \oint d\tilde{\theta} \int_0^\infty \rho d\rho \tilde{\mathbf{Y}}_0(\rho, \tilde{\theta}) \cdot \mathbf{H}(\Omega\eta - \phi_*) \\ &= \left[ \int_{\tilde{t}-\frac{\pi}{\omega}}^{\tilde{t}+\frac{\pi}{\omega}} d\eta \mathbf{H}(\Omega\eta - \phi_*) \right] \cdot \left[ \oint d\tilde{\theta} \int_0^\infty \rho d\rho \tilde{\mathbf{Y}}_0(\rho, \tilde{\theta}) \right]. \end{aligned}$$

Make a final change of variables,  $\Omega\eta - \phi_* = \chi$ ,

$$\begin{aligned} e_1 &= \frac{1}{\Omega} \left[ \oint d\chi \mathbf{H}(\chi) \right] \cdot \left[ \oint d\tilde{\theta} \int_0^\infty \rho d\rho \tilde{\mathbf{Y}}_0(\rho, \tilde{\theta}) \right] \\ &= \frac{H_0}{\Omega}, \end{aligned}$$

where

$$H_0 = \left[ \oint d\chi \mathbf{H}(\chi) \right] \cdot \left[ \oint d\tilde{\theta} \int_0^\infty \rho d\rho \tilde{\mathbf{Y}}_0(\rho, \tilde{\theta}) \right].$$



## C.9 Derivatives $\mathbf{N}_t$ and $\mathbf{B}_t$

Appendices C.9 and C.10 details the calculations from section 5.5. Firstly, the derivatives  $v_t$ ,  $\kappa_t$  will be required in what follows, I present their derivation here. The derivation for  $v_t$  requires the fact that  $v = |\mathbf{R}_\sigma|$  and that  $v\mathbf{T} = \mathbf{R}_\sigma$ , where parameter  $\sigma$  was introduced in section 5.4,

$$\begin{aligned}
v_t &= |\mathbf{R}_\sigma|_t \\
&= \frac{1}{2}((\mathbf{R}_\sigma)^2)^{-\frac{1}{2}} 2(\mathbf{R}_\sigma \cdot \partial_\sigma(\partial_t \mathbf{R})) \\
&= \frac{1}{v}(\mathbf{R}_\sigma \cdot (\mathbf{R}_t)_\sigma) \\
&= \frac{1}{v}(v\mathbf{T} \cdot (\mathbf{R}_t)_\sigma) \\
&= \mathbf{T} \cdot (\mathbf{R}_t)_\sigma \\
&= \mathbf{T} \cdot \left( b_2 \kappa \mathbf{N} + c_3 \kappa \mathbf{B} + \frac{H_1}{\Omega}(\Phi \cos \beta + \Psi \sin \beta) \right)_\sigma \\
&= \mathbf{T} \cdot \left( b_2 \kappa_\sigma \mathbf{N} + b_2 \kappa \mathbf{N}_\sigma + c_3 \kappa_\sigma \mathbf{B} + c_3 \kappa \mathbf{B}_\sigma + \frac{H_1}{\Omega}(\Phi_\sigma \cos \beta + \Psi_\sigma \sin \beta) \right),
\end{aligned}$$

since,

$$\begin{aligned}
\mathbf{N}_\sigma &= -v\kappa \mathbf{T} + v\tau \mathbf{B}, \\
\mathbf{B}_\sigma &= -v\tau \mathbf{N}, \\
\Phi_\sigma &= \mathbf{N}_\sigma \cos \phi - \mathbf{B}_\sigma \sin \phi, \\
\Psi_\sigma &= \mathbf{N}_\sigma \sin \phi + \mathbf{B}_\sigma \cos \phi.
\end{aligned}$$

By substitution and using the fact that  $\mathbf{T} \cdot \mathbf{N} = \mathbf{T} \cdot \mathbf{B} = 0$ ,

$$v_t = -b_2 \kappa^2 v - \frac{H_1}{\Omega} \kappa v \cos(\phi - \beta),$$

The derivative  $\kappa_t$  is found as follows

$$\begin{aligned}
\kappa \mathbf{N} &= \mathbf{T}_s, \\
\kappa_t \mathbf{N} &= (\mathbf{T}_s)_t - \kappa \mathbf{N}_t, \\
\kappa_t &= (\mathbf{T}_s)_t \cdot \mathbf{N} \\
&= \frac{H_1}{\Omega}((\tau_s - \phi_{ss}) \sin(\phi - \beta) - (\tau - \phi_s)^2 \cos(\phi - \beta) + \kappa^2 \cos(\phi - \beta)) \\
&\quad + b_2 \kappa_{ss} - c_3 \tau_s \kappa - 2c_3 \tau \kappa_s - b_2 \tau^2 \kappa + b_2 \kappa^3,
\end{aligned}$$

where  $(\mathbf{T}_s)_t$  is derived below.

## Derivatives of $\mathbf{R}$

From above

$$\mathbf{R}_t = b_2\kappa\mathbf{N} + c_3\kappa\mathbf{B} + \frac{H_1}{\Omega}(\Phi \cos \beta + \Psi \sin \beta).$$

Differentiate with respect to  $s$

$$\begin{aligned} (\mathbf{R}_t)_s &= \mathbf{N}_t b_2\kappa + \mathbf{N} b_2\kappa_s + \mathbf{B}_t c_3\kappa + \mathbf{B} c_3\kappa_s + \frac{H_1}{\Omega}(\Phi_s \cos \beta + \partial_s(\mathbf{T} \cdot \Phi) \sin \beta) \\ &= (\tau\mathbf{B} - \kappa\mathbf{T})b_2\kappa + \mathbf{N} b_2\kappa_s - \tau\mathbf{N} c_3\kappa + \mathbf{B} c_3\kappa_s \\ &\quad + \frac{H_1}{\Omega}[\mathbf{N}(\tau - \phi_s) \sin \phi \cos \beta + \mathbf{B}(\tau - \phi_s) \cos \phi \cos \beta - \kappa\mathbf{T} \cos \phi \cos \beta] \\ &\quad + \frac{H_1}{\Omega}[-\mathbf{N}(\tau - \phi_s) \cos \phi \sin \beta + \mathbf{B}(\tau - \phi_s) \sin \phi \sin \beta - \kappa\mathbf{T} \sin \phi \sin \beta]. \end{aligned}$$

The equation for  $(\mathbf{R}_t)_s$  reduces to

$$\begin{aligned} (\mathbf{R}_t)_s &= \mathbf{N} \left[ b_2\kappa_s - \tau c_3\kappa + \frac{H_1}{\Omega}(\tau - \phi_s) \sin(\phi - \beta) \right] \\ &\quad + \mathbf{B} \left[ c_3\kappa_s + \tau b_2\kappa + \frac{H_1}{\Omega}(\tau - \phi_s) \cos(\phi - \beta) \right] \\ &\quad - \mathbf{T} \left[ \kappa^2 b_2 + \frac{H_1}{\Omega} \kappa \cos(\phi - \beta) \right]. \end{aligned}$$

## Derivatives of $\mathbf{T}$

$$\mathbf{T}_t = (\mathbf{R}_s)_t = (\mathbf{R}_t)_s - v^{-1}v_t\mathbf{T},$$

hence

$$\begin{aligned} \mathbf{T}_t &= \mathbf{N} \left[ b_2\kappa_s - \tau c_3\kappa + \frac{H_1}{\Omega}(\tau - \phi_s) \sin(\phi - \beta) \right] \\ &\quad + \mathbf{B} \left[ c_3\kappa_s + \tau b_2\kappa + \frac{H_1}{\Omega}(\tau - \phi_s) \cos(\phi - \beta) \right]. \end{aligned}$$

Differentiate with respect to  $s$

$$\begin{aligned} (\mathbf{T}_t)_s &= \mathbf{N}_t \left[ b_2\kappa_s - \tau c_3\kappa + \frac{H_1}{\Omega}(\tau - \phi_s) \sin(\phi - \beta) \right] \\ &\quad + \mathbf{N} \left[ b_2\kappa_{ss} - c_3\tau_s\kappa - c_3\tau\kappa_s + \frac{H_1}{\Omega}((\tau_s - \phi_{ss}) \sin(\phi - \beta) + \phi_s(\tau - \phi_s) \cos(\phi - \beta)) \right] \\ &\quad + \mathbf{B}_t \left[ c_3\kappa_s + \tau b_2\kappa + \frac{H_1}{\Omega}(\tau - \phi_s) \cos(\phi - \beta) \right] \\ &\quad + \mathbf{B} \left[ c_3\kappa_{ss} + b_2\partial_s\tau\kappa + b_2\tau\kappa_s + \frac{H_1}{\Omega}((\tau_s - \phi_{ss}) \cos(\phi - \beta) - \phi_s(\tau - \phi_s) \sin(\phi - \beta)) \right]. \end{aligned}$$

Use the Frenet-Serret equations (5.3)-(5.6), and simplify

$$\begin{aligned}
(\mathbf{T}_t)_s &= \mathbf{N} \left[ b_2 \kappa_{ss} - c_3 \tau_s \kappa - 2c_3 \tau \kappa_s - b_2 \tau^2 \kappa \right. \\
&\quad \left. + \frac{H_1}{\Omega} ((\tau_s - \phi_{ss}) \sin(\phi - \beta) - (\tau - \phi_s)^2 \cos(\phi - \beta)) \right] \\
&\quad + \mathbf{B} \left[ c_3 \kappa_{ss} + b_2 \tau_s \kappa + 2b_2 \tau \kappa_s - c_3 \tau^2 \kappa \right. \\
&\quad \left. + \frac{H_1}{\Omega} ((\tau_s - \phi_{ss}) \cos(\phi - \beta) + (\tau - \phi_s)^2 \sin(\phi - \beta)) \right] \\
&\quad - \mathbf{T} \left[ b_2 \kappa \kappa_s - \tau c_3 \kappa^2 + \kappa \frac{H_1}{\Omega} (\tau - \phi_s) \sin(\phi - \beta) \right].
\end{aligned}$$

Changing the order of differentiation

$$\begin{aligned}
(\mathbf{T}_s)_t &= (v^{-1} \mathbf{T}_\sigma)_t \\
&= (v^{-1})_t \mathbf{T}_\sigma + v^{-1} (\mathbf{T}_\sigma)_t \\
&= -v^{-2} v_t \mathbf{T}_\sigma + v^{-1} (\mathbf{T}_\sigma)_t \\
&= (\mathbf{T}_t)_s - v^{-1} v_t \mathbf{T}_s \\
&= (\mathbf{T}_t)_s - v^{-1} v_t \kappa \mathbf{N} \\
&= (\mathbf{T}_t)_s + \mathbf{N} \left( b_2 \kappa^3 + \frac{H_1}{\Omega} \kappa^2 \cos(\phi - \beta) \right),
\end{aligned}$$

$$\begin{aligned}
(\mathbf{T}_s)_t &= \mathbf{N} \left[ b_2 \kappa_{ss} - c_3 \tau_s \kappa - 2c_3 \tau \kappa_s - b_2 \tau^2 \kappa + b_2 \kappa^3 \right. \\
&\quad \left. + \frac{H_1}{\Omega} ((\tau_s - \phi_{ss}) \sin(\phi - \beta) - (\tau - \phi_s)^2 \cos(\phi - \beta) + \kappa^2 \cos(\phi - \beta)) \right] \\
&\quad + \mathbf{B} \left[ c_3 \kappa_{ss} + b_2 \tau_s \kappa + 2b_2 \tau \kappa_s - c_3 \tau^2 \kappa \right. \\
&\quad \left. + \frac{H_1}{\Omega} ((\tau_s - \phi_{ss}) \cos(\phi - \beta) + (\tau - \phi_s)^2 \sin(\phi - \beta)) \right] \\
&\quad - \mathbf{T} \left[ b_2 \kappa \kappa_s - \tau c_3 \kappa^2 + \kappa \frac{H_1}{\Omega} (\tau - \phi_s) \sin(\phi - \beta) \right].
\end{aligned}$$

**Derivatives of N**

$$\begin{aligned}
\mathbf{N}_t &= (\kappa^{-1} \mathbf{T}_s)_t \\
&= -\kappa^{-2} \kappa_t \mathbf{T}_s + \kappa^{-1} (\mathbf{T}_s)_t \\
&= -\kappa^{-1} \kappa_t \mathbf{N} + \kappa^{-1} (\mathbf{T}_s)_t \\
&= -\kappa^{-1} (\mathbf{N} \cdot (\mathbf{T}_s)_t) \mathbf{N} + \kappa^{-1} (\mathbf{T}_s)_t.
\end{aligned}$$

Substituting in the equation for  $(\mathbf{T}_s)_t$  derived above yields

$$\begin{aligned}\mathbf{N}_t &= \mathbf{B}\kappa^{-1} \left( \frac{H_1}{\Omega} ((\tau_s - \phi_{ss}) \cos(\phi - \beta) + (\tau - \phi_s)^2 \sin(\phi - \beta)) \right. \\ &\quad \left. + c_3 \kappa_{ss} + b_2 \kappa \tau_s + 2b_2 \tau \kappa_s - c_3 \kappa \tau^2 \right) \\ &\quad - \mathbf{T} \left( \frac{H_1}{\Omega} (\tau - \phi_s) \sin(\phi - \beta) + b_2 \kappa_s - \tau c_3 \kappa \right).\end{aligned}$$

For the vector equations  $\Phi_t$  we need the product  $(\mathbf{N}_t \cdot \mathbf{B})$ ,

$$\begin{aligned}(\mathbf{N}_t \cdot \mathbf{B}) &= \kappa^{-1} \left( \frac{H_1}{\Omega} ((\tau_s - \phi_{ss}) \cos(\phi - \beta) + (\tau - \phi_s)^2 \sin(\phi - \beta)) \right. \\ &\quad \left. + c_3 \kappa_{ss} + b_2 \kappa \tau_s + 2b_2 \tau \kappa_s - c_3 \kappa \tau^2 \right).\end{aligned}$$

Differentiate  $\mathbf{N}_t$  with respect to  $s$ ,

$$\begin{aligned}(\mathbf{N}_t)_s &= \mathbf{B}_t \left[ c_3 \kappa^{-1} \kappa_{ss} + b_2 \tau_s + 2b_2 \tau \kappa^{-1} \kappa_s - c_3 \tau^2 \right. \\ &\quad \left. + \kappa^{-1} \frac{H_1}{\Omega} ((\tau_s - \phi_{ss}) \cos(\phi - \beta) + (\tau - \phi_s)^2 \sin(\phi - \beta)) \right] \\ &\quad + \mathbf{B} \left[ -c_3 \kappa_s \kappa^{-2} \kappa_{ss} + c_3 \kappa^{-1} \kappa_{sss} + b_2 \tau_{ss} + 2b_2 \tau_s \kappa^{-1} \kappa_s \right. \\ &\quad \left. - 2b_2 \tau \kappa_s \kappa^{-2} \kappa_s + 2b_2 \tau \kappa^{-1} \kappa_{ss} - 2c_3 \partial_s \tau \tau \right. \\ &\quad \left. - \kappa_s \kappa^{-2} \frac{H_1}{\Omega} ((\tau_s - \phi_{ss}) \cos(\phi - \beta) + (\tau - \phi_s)^2 \sin(\phi - \beta)) \right. \\ &\quad \left. + \kappa^{-1} \frac{H_1}{\Omega} ((\tau_{ss} - \phi_{sss}) \cos(\phi - \beta) - \phi_s (\tau_s - \phi_{ss}) \sin(\phi - \beta) \right. \\ &\quad \left. + 2(\tau_s - \phi_{ss})(\tau - \phi_s) \sin(\phi - \beta)) + \phi_s (\tau - \phi_s)^2 \cos(\phi - \beta) \right] \\ &\quad - \mathbf{T}_s \left[ b_2 \kappa_s - \tau c_3 \kappa + \frac{H_1}{\Omega} (\tau - \phi_s) \sin(\phi - \beta) \right] \\ &\quad - \mathbf{T} \left[ b_2 \kappa_{ss} - \tau_s c_3 \kappa - \tau c_3 \kappa_s + \frac{H_1}{\Omega} (\tau_s - \phi_{ss}) \sin(\phi - \beta) \right. \\ &\quad \left. + \frac{H_1}{\Omega} \phi_s (\tau - \phi_s) \cos(\phi - \beta) \right].\end{aligned}$$

Simplify using the Frenet-Serret equations,

$$\begin{aligned}(\mathbf{N}_t)_s &= -\mathbf{N} \left[ \kappa^{-1} \tau \frac{H_1}{\Omega} ((\tau_s - \phi_{ss}) \cos(\phi - \beta) + (\tau - \phi_s)^2 \sin(\phi - \beta)) \right. \\ &\quad \left. + \kappa \frac{H_1}{\Omega} (\tau - \phi_s) \sin(\phi - \beta) + c_3 \tau \kappa^{-1} \kappa_{ss} + b_2 \tau \tau_s + 2b_2 \tau^2 \kappa^{-1} \kappa_s \right. \\ &\quad \left. - c_3 \tau^3 + b_2 \kappa \kappa_s - \tau c_3 \kappa^2 \right] \\ &\quad + \mathbf{B} \left[ -c_3 \kappa_s \kappa^{-2} \kappa_{ss} + c_3 \kappa^{-1} \kappa_{sss} + b_2 \tau_{ss} + 2b_2 \tau_s \kappa^{-1} \kappa_s \right.\end{aligned}$$

$$\begin{aligned}
& -2b_2\tau\kappa_s\kappa^{-2}\kappa_s + 2b_2\tau\kappa^{-1}\kappa_{ss} - 2c_3\tau_s\tau \\
& -\kappa_s\kappa^{-2}\frac{H_1}{\Omega}((\tau_s - \phi_{ss})\cos(\phi - \beta) + (\tau - \phi_s)^2\sin(\phi - \beta)) \\
& +\kappa^{-1}\frac{H_1}{\Omega}((\tau_{ss} - \phi_{sss})\cos(\phi - \beta) - \phi_s(\tau_s - \phi_{ss})\sin(\phi - \beta) \\
& +2(\tau_s - \phi_{ss})(\tau - \phi_s)\sin(\phi - \beta)) + \phi_s(\tau - \phi_s)^2\cos(\phi - \beta)) \Big] \\
& -\mathbf{T} \left[ b_2\kappa_{ss} - \tau_sc_3\kappa - \tau c_3\kappa_s + \frac{H_1}{\Omega}(\tau_s - \phi_{ss})\sin(\phi - \beta) \right. \\
& \left. + \frac{H_1}{\Omega}\phi_s(\tau - \phi_s)\cos(\phi - \beta) \right].
\end{aligned}$$

Change the order of differentiation

$$(\mathbf{N}_s)_t = (\mathbf{N}_t)_s - v^{-1}v_t\tau\mathbf{B} + v^{-1}v_t\kappa\mathbf{T},$$

$$\begin{aligned}
(\mathbf{N}_s)_t &= -\mathbf{N} \left[ \kappa^{-1}\tau\frac{H_1}{\Omega}((\tau_s - \phi_{ss})\cos(\phi - \beta) + (\tau - \phi_s)^2\sin(\phi - \beta)) \right. \\
& +\kappa\frac{H_1}{\Omega}(\tau - \phi_s)\sin(\phi - \beta) + c_3\tau\kappa^{-1}\kappa_{ss} + b_2\tau\tau_s + 2b_2\tau^2\kappa^{-1}\kappa_s \\
& \left. -c_3\tau^3 + b_2\kappa\kappa_s - \tau c_3\kappa^2 \right] \\
& +\mathbf{B} \left[ -c_3\kappa_s\kappa^{-2}\kappa_{ss} + c_3\kappa^{-1}\kappa_{sss} + b_2\tau_{ss} + 2b_2\tau_s\kappa^{-1}\kappa_s \right. \\
& -2b_2\tau\kappa_s\kappa^{-2}\kappa_s + 2b_2\tau\kappa^{-1}\kappa_{ss} - 2c_3\tau_s\tau \\
& -\kappa_s\kappa^{-2}\frac{H_1}{\Omega}((\tau_s - \phi_{ss})\cos(\phi - \beta) + (\tau - \phi_s)^2\sin(\phi - \beta)) \\
& +\kappa^{-1}\frac{H_1}{\Omega}((\tau_{ss} - \phi_{sss})\cos(\phi - \beta) - \phi_s(\tau_s - \phi_{ss})\sin(\phi - \beta) \\
& +2(\tau_s - \phi_{ss})(\tau - \phi_s)\sin(\phi - \beta)) + \phi_s(\tau - \phi_s)^2\cos(\phi - \beta)) \\
& \left. +b_2\kappa^2\tau + \frac{H_1}{\Omega}\kappa\tau\cos(\phi - \beta) \right] \\
& -\mathbf{T} \left[ b_2\kappa_{ss} - \tau_sc_3\kappa - \tau c_3\kappa_s + \frac{H_1}{\Omega}(\tau_s - \phi_{ss})\sin(\phi - \beta) \right. \\
& \left. + \frac{H_1}{\Omega}\phi_s(\tau - \phi_s)\cos(\phi - \beta) + b_2\kappa^3 + \frac{H_1}{\Omega}\kappa^2\cos(\phi - \beta) \right].
\end{aligned}$$

## Derivatives of B

$$\begin{aligned}
\mathbf{B}_t &= -\tau^{-2}\tau_t\mathbf{N}_t + \tau^{-1}(\mathbf{N}_t)_t + (\tau\kappa_t - \kappa\tau_t)\tau^{-2}\mathbf{T} + \kappa\tau^{-1}\mathbf{T}_t \\
&= -\tau^{-2}((\mathbf{N}_t)_t \cdot \mathbf{B} + \kappa\mathbf{T}_t\mathbf{B})(\tau\mathbf{B} - \kappa\mathbf{T}) + \tau^{-1}(\mathbf{N}_t)_t + (\tau((\mathbf{T}_s)_t \cdot \mathbf{N}) \\
&\quad -\kappa((\mathbf{N}_t)_t \cdot \mathbf{B} + \kappa\mathbf{T}_t\mathbf{B}))\tau^{-2}\mathbf{T} + \kappa\tau^{-1}\mathbf{T}_t \\
&= -\tau^{-1}((\mathbf{N}_t)_t \cdot \mathbf{B})\mathbf{B} + \tau^{-2}\kappa((\mathbf{N}_t)_t \cdot \mathbf{B})\mathbf{T} - \tau^{-1}\kappa(\mathbf{T}_t \cdot \mathbf{B})\mathbf{B} + \tau^{-2}\kappa^2(\mathbf{T}_t \cdot \mathbf{B})\mathbf{T}
\end{aligned}$$

$$\begin{aligned}
& +\tau^{-1}(\mathbf{N}_t)_t + \tau^{-1}((\mathbf{T}_s)_t \cdot \mathbf{N})\mathbf{T} - \kappa\tau^{-2}((\mathbf{N}_t)_t \cdot \mathbf{B})\mathbf{T} - \kappa^2\tau^{-2}(\mathbf{T}_t \cdot \mathbf{B})\mathbf{T} + \kappa\tau^{-1}\mathbf{T}_t \\
= & -\tau^{-1}((\mathbf{N}_t)_t \cdot \mathbf{B})\mathbf{B} - \tau^{-1}\kappa(\mathbf{T}_t \cdot \mathbf{B})\mathbf{B} + \tau^{-1}(\mathbf{N}_t)_t + \tau^{-1}((\mathbf{T}_s)_t \cdot \mathbf{N})\mathbf{T} + \kappa\tau^{-1}\mathbf{T}_t,
\end{aligned}$$

and so

$$\begin{aligned}
\mathbf{B}_t = & -\mathbf{N}\kappa^{-1} \left( \frac{H_1}{\Omega}((\tau_s - \phi_{ss}) \cos(\phi - \beta) + (\tau - \phi_s)^2 \sin(\phi - \beta)) \right. \\
& \left. + c_3\kappa_{ss} + b_2\kappa\tau_s + 2b_2\tau\kappa_s - c_3\kappa\tau^2 \right) \\
& -\mathbf{T} \left( \frac{H_1}{\Omega}(\tau - \phi_s) \cos(\phi - \beta) + c_3\kappa_s + b_2\tau\kappa \right).
\end{aligned}$$

## C.10 Covariant form of the motion equations

We have already defined the following

$$\begin{aligned}\Phi &= \mathbf{N} \cos \phi - \mathbf{B} \sin \phi, \\ \Psi &= \mathbf{N} \sin \phi + \mathbf{B} \cos \phi.\end{aligned}$$

The first derivatives with respect to  $s$  are

$$\begin{aligned}\Phi_s &= -\kappa \mathbf{T} \cos \phi - (\phi_s - \tau) \Psi, \\ \Psi_s &= -\kappa \mathbf{T} \sin \phi + (\phi_s - \tau) \Phi.\end{aligned}$$

Taking the following scalar product yields the result for  $(\phi_s - \tau)$ ,

$$\begin{aligned}(\Psi \cdot \Phi_s) &= -\kappa(\Psi \cdot \mathbf{T}) \cos \phi - (\phi_s - \tau) \\ &= -(\phi_s - \tau),\end{aligned}$$

and so

$$(\Psi \cdot \Phi_s)^2 = (\phi_s - \tau)^2.$$

Consider the derivative  $\Phi_{ss}$ ,

$$\begin{aligned}\Phi_{ss} &= -\kappa_s \mathbf{T} \cos \phi - \kappa^2 \mathbf{N} \cos \phi + \kappa \mathbf{T} \phi_s \sin \phi - (\phi_{ss} - \partial_s \tau) \Psi - (\Psi \cdot \Phi_s) \kappa \mathbf{T} \sin \phi \\ &\quad - (\Psi \cdot \Phi_s)^2 \Phi.\end{aligned}$$

Take the dot product with  $\Psi$ ,

$$\begin{aligned}(\phi_{ss} - \tau_s) &= -(\Psi \cdot \Phi_{ss}) - (\Psi \cdot \mathbf{N}) \kappa^2 \cos \phi \\ &= -(\Psi \cdot \Phi_s) - \kappa^2 \cos \phi \sin \phi.\end{aligned}$$

This expression can be further simplified by using the derivative  $(\Psi_s \cdot \Phi_s) = (\Psi \cdot \Phi_s) + (\Psi \cdot \partial_s^2 \Phi)$ ,

$$(\phi_{ss} - \partial_s \tau) = -\Psi_s \cdot \Phi_s + (\Psi_s \cdot \Phi_s) - \kappa^2 \cos \phi \sin \phi,$$

since  $(\Psi_s \cdot \Phi_s) = \kappa^2 \cos \phi \sin \phi$ , it can be deduced that

$$(\phi_{ss} - \tau_s) = -(\Psi_s \cdot \Phi_s).$$

Using the relations  $(\Psi \cdot \mathbf{N}) = \sin \phi$  and  $(\Psi \cdot \mathbf{B}) = \cos \phi$ , we have

$$\begin{aligned}
\mathbf{T}(\tau\kappa \sin \phi - \kappa_s \cos \phi) &= \mathbf{T}(\tau\kappa(\Psi \cdot \mathbf{N}) - \kappa_s(\Psi \cdot \mathbf{B})) \\
&= \mathbf{T}(\Psi \cdot (\tau\kappa\mathbf{N} - \kappa_s\mathbf{B})) \\
&= \mathbf{T}(\Psi \cdot (\tau\kappa(-\mathbf{T} \times \mathbf{B}) - \kappa_s(\mathbf{T} \times \mathbf{N}))) \\
&= \mathbf{T}(\Psi \cdot (\mathbf{T} \times (-\tau\kappa\mathbf{B} - \kappa_s\mathbf{N}))).
\end{aligned}$$

It follows from the Frenet-Serret equations that  $\mathbf{R}_{sss} + \kappa^2\mathbf{T} = \tau\kappa\mathbf{B} + \mathbf{N}_t$ , and so

$$\mathbf{T}(\tau\kappa \sin \phi - \kappa_s \cos \phi) = -\mathbf{T}(\Psi \cdot (\mathbf{T} \times (R_{sss} + \kappa^2\mathbf{T}))).$$

Finally

$$\mathbf{T}(\tau\kappa \sin \phi - \kappa_s \cos \phi) = -\mathbf{R}_s(\Psi \cdot (\mathbf{R}_s \times \mathbf{R}_{sss})),$$

using the relations  $(\Phi \cdot \mathbf{N}) = \cos \phi$  and  $(\Phi \cdot \mathbf{B}) = -\sin \phi$ , we have

$$\begin{aligned}
\mathbf{T}(\tau\kappa \cos \phi + \kappa_s \sin \phi) &= \mathbf{T}(\tau\kappa(\Phi \cdot \mathbf{N}) - \kappa_s(\Phi \cdot \mathbf{B})), \\
&= \mathbf{T}(\Phi \cdot (\tau\kappa\mathbf{N} - \kappa_s\mathbf{B})).
\end{aligned}$$

Then as above we can deduce that

$$\mathbf{T}(\tau\kappa \cos \phi + \kappa_s \sin \phi) = -\mathbf{R}_s(\Phi \cdot (\mathbf{R}_s \times \mathbf{R}_{sss})).$$



# Bibliography

- [1] HPCx. <http://www.hpcx.ac.uk/>.
- [2] MPI. [http://en.wikipedia.org/wiki/Message\\_Passing\\_Interface](http://en.wikipedia.org/wiki/Message_Passing_Interface).
- [3] Sorin Group. <http://www.sorin.com/>.
- [4] K. A. Agladze, V. A. Davydov, and Mikhailov. An observation of resonance of spiral waves in distributed excitable media. *JETP Lett.*, 45(12):767–770, 1987.
- [5] F. Aguel, J. Eason, and N. Trayanova. Advances in modeling cardiac defibrillation. *Int. J. Bif. Chaos*, 13(12):3791–3802, 2003.
- [6] S. Alonso, R. Kahler, A. S. Mikhailov, and F. Sagues. Expanding scroll rings and negative tension turbulence in a model of excitable media. *Phys. Rev. E.*, 70:056201, 2004.
- [7] S. Alonso, F. Sagues, and A. S. Mikhailov. Taming Winfree turbulence of scroll waves in excitable media. *Science*, 299:1722–1725, 2003.
- [8] S. Alonso, F. Sagues, and A. S. Mikhailov. Periodic forcing of scroll rings and control of winfree turbulence in excitable media. *Chaos*, 16(2):023124, 2006.
- [9] S. Balay, K. Buschelman, W. D. Gropp, D. Kaushik, M. G. Knepley, L. C. McInnes, B. F. Smith, and H. Zhang. PETSc. <http://www.mcs.anl.gov/petsc>.
- [10] D. Barkley. A model for fast computer simulation of waves in excitable media. *Physica D*, 49:61–70, 1991.
- [11] D. Barkley and M. Dowle. Ezspiral and ezscroll. [http://www.warwick.ac.uk/~masax/Software/ez\\_software.html](http://www.warwick.ac.uk/~masax/Software/ez_software.html).

- [12] G. W. Beeler and H. Reuter. Reconstruction of the action potential of ventricular myocardial fibres. *J. Physiol.*, 268:177–210, 1977.
- [13] C. Bernard. *Introduction a l'étude de la Médecine Expérimentale*. Flammarion, Paris, 1865.
- [14] V. N. Biktashev. A three-dimensional autowave turbulence. *Int. J. Bif. Chaos*, 8(4):677–684, 1998.
- [15] V. N. Biktashev and A. V. Holden. Resonant drift of an autowave vortex in a bounded medium. *Phys. Lett. A*, 181:216–224, 1993.
- [16] V. N. Biktashev and A. V. Holden. Design principles of a low voltage cardiac defibrillator based upon. *Phys. Lett. A*, 181:216–224, 1994.
- [17] V. N. Biktashev and A. V. Holden. Control of re-entrant activity in a model of mammalian atrial tissue. *Proc. R. soc. Lond. B*, 260:211–217, 1995.
- [18] V. N. Biktashev and A. V. Holden. Resonant drift of autowave vortices in two dimensions and the effect of boundaries and inhomogeneities. *Chaos Solitons Fractals*, 5:575–622, 1995.
- [19] V. N. Biktashev, A. V. Holden, and H. Zhang. Tension of organizing filaments of scroll waves. *Phil. Trans. R. Soc. Lond. A.*, 347:611–630, 1994.
- [20] I. V. Biktasheva, D. Barkley, V. Biktashev, G. Bordyugov, and A. Foulkes. Computation of the response functions of spiral waves in active media. *Phys. Rev. E. (to appear)*, 2008.
- [21] G. Boriani, M. Biffi, P. Silvestri, C. Martignani, C. Valzania, I. Diemberger, C. Moulder, G. Mouchawar, M. Kroll, and A. Branzi. Mechanisms of pain associated with internal debrillation shocks: results of a randomized study of shock waveform. *Heart Rhythm*, 2(7):708–713, 2005.
- [22] M. Courtemanche, R. J. Ramirez, and S. Nattel. Ionic mechanisms underlying human atrial action potential properties: insights from a mathematical model. *Am J Physiol*, 275:H301–H321, 1998.
- [23] J. M. Davidenko, A. V. Pertsov, R. Salomosz, W. Baxter, and J. Jalife. Stationary and drifting spiral waves of excitation in isolated cardiac muscle. *Nature*, 355:349–351, 1992.

- [24] V. A. Davydov, V. S. Zykov, A. S. Mikhailov, and P. K. Brazhnik. Drift and resonance of spiral waves in active media. *Sov. Phys. Radiophys.*, 31:574–582, 1988.
- [25] K. A. DeBruin and W. Krassowska. Electroporation and shock-induced transmembrane potential in a cardiac fiber during defibrillation strength shocks. *Ann. Biomed. Eng.*, 26:584–596, 1997.
- [26] J. W. Demmel, S. C. Eisenstat, J. R. Gilbert, X. S. Li, and J. W. H. Jiu. A supernodal approach to sparse partial pivoting. *SIAM J. Matrix Analysis and Applications*, 20(3):720–755, 1999.
- [27] M. Dowle, R. M. Mantel, and D. Barkley. Fast simulations of waves in three-dimensional excitable media. *Int. J. of Bifurcation and Chaos*, 7:2529–2545, 1997.
- [28] J. Drouhard and F. A. Roberge. Revised formulation of the Hodgkin-Huxley representation of the sodium current in cardiac-cells. *Comp. Biomed. Res.*, 20(4):333–350, 1987.
- [29] I. R. Efimov, I. R. Aguel, Y. Cheng, B. Wollenzier, and N. Trayanova. Virtual electrode polarization in the far field: implications for external defibrillation. *Am. J. Physiol. Heart. Circ. Physiol.*, 279:H1055–H1070, 2000.
- [30] I. R. Efimov, Y. Cheng, D. R. Wagoner, T. Mazgalev, and P. J. Tchou. Virtual electrode-induced phase singularity: A basic mechanism of defibrillation failure. *Circ. Res.*, 82:918–925, 1998.
- [31] R. Fitzhugh. Impulses and physiological states in theoretical models of nerve membrane. *Biophys. J.*, 1:445–466, 1961.
- [32] E. I. Fredholm. Sur une classe d’equations fonctionnelles. *Acta Math.*, 27:365–390, 1903.
- [33] G. Gerisch. Periodic signals control pattern formation and cell aggregations. *Naturwissenschaften*, 58(9):430–438, 1971.
- [34] R. Gray and J. Jalife. Spiral waves and the heart. *Int. J. Bifurcation and Chaos*, 6:415–435, 1996.

- [35] R. Gray, J. Jalife, A. V. Panfilov, W. T. Baxter, C. Cabo, J. M. Davidenko, A. Pertsov, P. Hogeweg, and A. T. Winfree. Mechanisms of cardiac fibrillation. *Science*, 270:1222–1223, 1995.
- [36] C. S. Henriquez, J. V. Tranquillo, D. Weinstein, E. W. Hsu, and C. R. Johnson. *Cardiac electrophysiology from cell to bedside.*, pages 273–281. Saunders, Philadelphia, 2004.
- [37] A. L. Hodgkin and A. F. Huxley. A quantitative description of membrane current and its application to conduction and excitation in nerve. *J.Physiol.*, 117:500–544, 1952.
- [38] I. Idris and V. N. Biktashev. Critical fronts in initiation of excitation waves. *Phys. Rev. E.*, 176:021906, 2007.
- [39] I. Idris and V. N. Biktashev. An analytical approach to initiation of propagating fronts. *Phys. Rev. E. (to appear)*, 2008.
- [40] J. Jung, A. Heisel, R. Fries, and V. Kollner. Tolerability of internal low-energy shock strengths currently needed for endocardial atrial cardioversion - effect on atrial defibrillation threshold and pain perception. *The American Journal of Cardiology*, 80(11):1489–1490, 1997.
- [41] J. P. Keener. The dynamics of three-dimensional scroll waves in excitable media. *Physica D*, 31:296–276, 1988.
- [42] J. P. Keener and J. J. Tyson. The dynamics of helical scroll waves in excitable media. *Physica D*, 51:151–161, 1991.
- [43] J. P. Keener and J. J. Tyson. The dynamics of scroll waves in excitable media. *SIAM Review*, 34(1):1–39, 1992.
- [44] J. Kneller, R. Zou, E. Vigmond, Z. Wang, L. Leon, and S. Nattel. Cholinergic atrial fibrillation in a computer model of a two-dimensional sheet of canine atrial cells with realistic ionic properties. *Circ. Res.*, 90:E73–E87, 2002.
- [45] W. Krassowska. Effects of electroporation of transmembrane potential induced by defibrillation shocks. *Pacing Clin. Electrophysiol.*, 18:1644–1660, 1995.

- [46] V. Krinsky, V. N. Biktashev, and A. M. Pertsov. Autowave approaches to the cessation of autowave arrhythmias. *Ann. N.Y. Acad. Sci.*, 591:232–246, 1995.
- [47] L. J. Leon, F. A. Roberge, and A. Vinet. Simulation of two-dimensional anisotropic cardiac reentry: Effects of wavelength on the reentry characteristics. *Ann. Biophys. Mol. Biol.*, 69:387–403, 1998.
- [48] C. H. Luo and Y. Rudy. A model of the ventricular cardiac action potential. depolarization, repolarization, and their interaction. *Circ. Res.*, 68:1501–1526, 1991.
- [49] C. H. Luo and Y. Rudy. A dynamic model of the cardiac ventricular action potential. I. simulations of ionic currents and concentration changes. *Circ. Res.*, 74:1071–1096, 1994.
- [50] C. H. Luo and Y. Rudy. A dynamic model of the cardiac ventricular action potential. II. afterdepolarizations, triggered activity, and potentiation. *Circ. Res.*, 74:1097–1113, 1994.
- [51] R. E. McAllister, D. Noble, and R. W. Tsien. Reconstruction of the electrical activity of cardiac purkinje fibres. *J. Physiol.*, 251:1–59, 1975.
- [52] A. S. Mikhailov, A. V. Panfilov, and A. N. Rudenko. Twisted scroll waves in active 3-dimensional media. *Phys. Lett. A*, 109(5):246–250, 1985.
- [53] W. T. Miller and D. Geselowitz. Simulation studies of the electrocardiogram, I. the normal heart. *Circ. Res.*, 43(2):301–315, 1978.
- [54] S. W. Morgan, I. V. Biktasheva, and V. N. Bikatshev. Control of scroll wave turbulence using resonant perturbations. *Phys. Rev. E*, 78:046207, 2008.
- [55] S. W. Morgan, G. Plank, I. V. Biktasheva, and V. N. Bikatshev. Feedback control of resonant drift as a tool for low voltage defibrillation. *Europace*, 10(1):i140, 2008.
- [56] S. W. Morgan, G. Plank, I. V. Biktasheva, and V. N. Bikatshev. Low energy defibrillation in human atrial tissue: a simulation study. *Biophys. J.*, 96:1364–1373, 2009.

- [57] P. M. Nielson, B. H. Le Grice, I. J. Smaill, and P. J. Hunter. Mathematical model of geometry and fibrous structure of the heart. *Am. J. Physiol.*, 260:1365–1378, 1991.
- [58] D. Noble. A modification of the Hodgkin-Huxley equations applicable to Purkinje fibre action and pace-maker potentials. *J. Physiol.*, 160:317–352, 1962.
- [59] H. N. Pak, Y. B. Liu, H. Hayashi, Y. Okuyama, P. S. Chen, and S. F. Lin. Synchronization of ventricular fibrillation with real-time feedback pacing: implication to low-energy defibrillation. *Am. J. Physiol. Heart. Circ. Physiol.*, 285:2704–2711, 2003.
- [60] A. Panfilov, S. Muller, V. Zykov, and J. Keener. Elimination of spiral waves in cardiac tissue by multiple electric shocks. *Phys. Rev. E.*, 61(4):4644–4647, 2000.
- [61] A. Panfilov and A. N. Rudenko. Two regimes of the scroll ring drift in the three-dimensional active media. *Physica D*, 28:215–218, 1987.
- [62] G. Plank, L. J. Leon, S. Kimber, and E. Vigmond. Defibrillation depends on conductivity fluctuations and the degree of disorganization in reentry patterns. *J. Cardiovasc. Electrophysiology.*, 16:205–216, 2005.
- [63] G. Plank, M. Liebmann, R. Weber dos Santos, E. J. Vigmond, and G. Haase. Algebraic multigrid preconditioner for the cardiac bidomain model. *IEEE Trans. Biomed. Eng.*, 54(4):585–596, 2007.
- [64] M. Potse, B. Dube, J. Richer, A. Vinet, and R. M. Gulrajani. A comparison of monodomain and bidomain reaction-diffusion models for action potential propagation in the human heart. *IEEE Trans. Biomed. Eng.*, 53(12):2425–2435, 2006.
- [65] B. Rodriguez, J. C. Eason, and N. A. Trayanova. Differences between left and right ventricular anatomy determine the types of re-entrant circuits induced by an external electric shock. a rabbit heart simulation study. *Circ. Res.*, 97(2):168–175, 2005.
- [66] B. J. Roth. Action potential propagation in a thick strand of cardiac muscle. *Circ. Res.*, 68:162–173, 1991.

- [67] J. Schlesner, V. Zykov, H. Brandtstadter, I. Gerdes, and H. Engel. Efficient control of spiral wave location in an excitable medium with localized heterogeneities. *New Journal of Physics*, 10:015003, 2008.
- [68] O. H. Schmitt. *Biological information processing using the concept of interpenetrating domains*. Springer-Verlag, New York, 1969.
- [69] N. G. Sepulveda, B. J. Roth, and J. P. Wikswo Jr. Current injection into a two-dimensional anisotropic bidomain. *Biophys. J.*, 55:987–999, 1989.
- [70] K. Skouibine and W. Krassowska. Increasing the computational efficiency of a bidomain model of defibrillation using a time-dependent activating function. *Ann. Biomed. Eng.*, 28:772–780, 2000.
- [71] K. B. Skouibine, N. A. Trayanova, and P. K. Moore. Anode/cathode make and break phenomena in a model of defibrillation. *IEEE Trans. Biomed. Eng.*, 46(7):769–777, 1999.
- [72] E. A. Sobie, R. C. Susil, and L. Tung. A generalized activating function for predicting virtual electrodes in cardiac tissue. *Biophys. J.*, 73:1410–1423, 1997.
- [73] C. Stevens, E. Remme, I. J. LeGrice, and P. J. Hunter. Ventricular mechanisms is diastole: material parameter sensitivity. *J. Biomech.*, 36:737–748, 2003.
- [74] J. L. Sullivan, S. B. Melnick, F. W. Chapman, and G. Walcott. Porcine defibrillation thresholds with chopped biphasic truncated exponential waveforms. *Resuscitation*, 74(2):325–331, 2007.
- [75] N. Trayanova. Defibrillation of the heart: insights into mechanisms from modelling studies. *Exp. Physiol.*, 91(2):323–337, 2006.
- [76] N. Trayanova, J. Eason, and F. Aguel. Computer simulations of cardiac defibrillation: a look inside the heart. *Comput. Visual. Sci.*, 4(259-270), 2002.
- [77] L. Tung. *A bidomain model for describing ischemic myocardial D.C. potentials*. PhD Thesis, Massachusetts Institute of Technology, Cambridge, 1978.
- [78] F. J. Vetter and A. D. McCulloch. Three dimensional analysis of regional cardiac function: a model of rabbit ventricular anatomy. *Prog. Biophys. Molec. Biol.*, 69:157–183, 1998.

- [79] E. J. Vigmond, F. Aguel, and N. A. Trayanova. Computational techniques for solving the bidomain equations in three dimensions. *IEEE Trans. Biomed. Eng.*, 49:1260–1269, 2002.
- [80] E. J. Vigmond, M. Hughes, G. Plank, and L. J. Leon. Computational tools for modeling electrical activity in cardiac tissue. *J. Elec. Supp.*, 36:69–74, 2003.
- [81] E. J. Vigmond and G. Plank. Cardiac arrhythmia research package (CARP). <http://carp.meduni-graz.at>.
- [82] G. P. Walcott, R. G. Walker, A. W. Cates, W. Krassowska, W. M. Smith, and R. E. Ideker. Choosing the optimal monophasic and biphasic waveforms for ventricular defibrillation. *J. Cardiovasc. Electrophysiol.*, 6:737–750, 1995.
- [83] M. Wathen, P. J. DeGroot, M. O. Sweeney, A. J. Stark, M. F. Otterness, W. O. Adkisson, R. C. Canby, K. Khalighi, C. Machado, D. S. Rubenstein, and K. J. Volosin. Prospective randomized multicenter trial of empirical antitachycardia pacing versus shocks for spontaneous rapid ventricular tachycardia in patients with implantable cardioverter-defibrillators: Pacing fast ventricular tachycardia reduces shock therapies (PainFREE Rx II) trial results. *Circulation*, 110:2591–2596, 2004.
- [84] R. Webber dos Santos, G. Plank, S. Bauer, and E. J. Vigmond. Parallel multi-grid preconditioner for the cardiac bidomain model. *IEE. Trans. Biomed. Eng.*, 51(11):1960–1968, 2004.
- [85] J. P. Wikswo Jr., S. F. Lin, and R. A. Abbas. Virtual electrodes in cardiac tissue: a common mechanism for anodal and cathodal stimulation. *Biophys. J.*, 73:2195–2210, 1995.
- [86] A. Winfree. Spiral waves of chemical activity. *Science*, 175(4022):634–636, 1972.
- [87] A. Winfree. Scroll-shaped waves of chemical activity in three dimensions. *Science*, 181:937–939, 1973.
- [88] A. Winfree. Rotating chemical reactions. *Sci. Amer.*, 230:82–95, 1974.
- [89] A. Winfree. Electrical turbulence in three-dimensional heart muscle. *Science*, 266:1003–1006, 1994.



- [90] N. J. Wu, H. Zhang, H. P. Ying, Z. Cao, and G. Hu. Suppression of Winfree turbulence under weak spatiotemporal perturbation. *Phys. Rev. E*, 73:060901, 2006.
- [91] F. Xie, Z. Qu, A. Garfinkel, and J. N. Weiss. Electrical refractory period restitute and spiral wave reentry in simulated cardiac tissue. *Am. J. Physiol. Circ. Physiol.*, 283:H448–H460, 2001.
- [92] A. M. Zhabotinsky and A. N. Zaikin. Autowave processes in a distributed chemical system. *J. Theor. Biol.*, 40:45–61, 1973.
- [93] D. Zipes and J. Jalife, editors. *Cardiac electrophysiology from cell to bedside*. Saunders, Philadelphia, 2004.
- [94] V. S. Zykov and H. Engel. *Analysis and control of complex nonlinear processes in physics, chemistry and biology, volume 5 of World Scientific Lecture Notes in Complex Systems*. World Scientific, 2007.
- [95] V. S. Zykov, O. U. Kheowan, R. Orapin, and S. C. Muller. Instabilities of the resonance attractor for spiral waves in an excitable medium. *Phys. Rev. E*, 65:026206, 2002.
- [96] V. S. Zykov, A. S. Mikhailov, and S. C. Muller. Controlling spiral waves in confined geometries by global feedback. *Phys. Rev. Lett.*, 78(17):3398–3401, 1997.